Title

On the Dynamical Evolution of Alfvenic Turbulence in the Inner Heliosphere

Author

Sioulas, Nikolaos

Publication Date

2024

Peer reviewed|Thesis/dissertation

UNIVERSITY OF CALIFORNIA
Los Angeles

On the Dynamical Evolution of Alfvénic Turbulence in the Inner Heliosphere

A dissertation submitted in partial satisfaction
of the requirements for the degree
Doctor of Philosophy in Geophysics and Space Physics

by

Nikolaos Sioulas

2024

ABSTRACT OF THE DISSERTATION

On the Dynamical Evolution of Alfvénic Turbulence in the Inner Heliosphere

by

Nikolaos Sioulas
Doctor of Philosophy in Geophysics and Space Physics
University of California, Los Angeles, 2024
Professor Marco C.M. Velli, Chair

As the solar wind expands into the interplanetary medium, its turbulent nature changes dramatically. The synergy of the Parker Solar Probe, Solar Orbiter, and WIND missions is enabling hitherto impossible studies of plasma turbulence throughout the inner heliosphere, ranging from within the Alfvén region out to Earth's orbit at 1 astronomical unit (AU). Understanding the dynamic evolution and transport of turbulent fluctuations from the corona into the heliosphere is fundamental to heliospheric science and can offer insights into several important unresolved problems in the field, including the coronal heating mechanism, the acceleration and non-adiabatic expansion of the solar wind, and the scattering and acceleration of energetic particles by turbulent fluctuations. The principal scientific aim of this thesis is to harness these observations and provide robust observational constraints on theoretical models and numerical simulations of Alfvńic turbulence by offering insights into the statistical signatures of 3-D anisotropic MHD turbulence in the solar wind. Emphasis is placed on testing homogeneous phenomenological models of MHD turbulence informed by the principles of *critical balance* and *dynamic alignment* and assessing the extent to which the conjectures and predictions made by these models align with in-situ observations. By comparing our observations with the model predictions, we aim to understand how effects not accounted for in these models, but present in the solar wind—namely, inhomogeneity induced by the radial expansion, imbalance in the fluxes of counterpropagating wave packets, compressibility, and the spherically polarized nature of the magnetic field fluctuations—can affect the statistical properties of MHD turbulence.

In parallel, our study dissects the dynamics and radial evolution of coherent magnetic structures, elucidating their role in magnetic energy dissipation and the ensuing heating of the solar wind.

The dissertation of Nikolaos Sioulas is approved.

Eduardo Paulo Da Costa Alves

Vassilis Angelopoulos

Hao Cao

Marco C.M. Velli, Committee Chair

University of California, Los Angeles

2024

To Maria,

whose unwavering love and support,

despite the 6,711 miles that separate us,

have made this journey possible.

TABLE OF CONTENTS

LIST OF FIGURES

LIST OF TABLES

Acknowledgments

Over the past four years, I have experienced both the highest of highs and the lowest of lows. These experiences have been profoundly enriched by the companionship and unwavering support of those who have walked this path with me.

I am truly indebted to my friends who have always supported these endeavors—Βασίλη, Γιώργο, Δημήτρη, Παναγιώτη, Παντελή, Χρήστο, Ethan, Kyle, Lizet, and Mark. Your encouragement and support have been the bedrock of my journey.

To my family, thank you for always supporting my dreams, even when they did not always make sense. Μαρία, your unwavering support and love have been my anchor throughout this journey. Your encouragement and understanding have made the challenging moments bearable and the successes even more rewarding. I am deeply grateful for your presence in my life.

My deepest gratitude goes to my advisor, Professor Marco Velli. It has been an immense honor and privilege to be your student. Your guidance, wisdom, and unwavering support have been pivotal in my academic and personal growth. Marco, thank you for everything.

I am also profoundly grateful to my colleagues—Dr. Chen Shi, Professor Anna Tenerani, Dr. Trevor Bowen, Professor Loukas Vlahos, Dr. Angelos Vourlidas, Dr. Alfred Mallet, Professor Benjamin Chandran, Dr. Mihailo Martinovic, Dr. Silvio Cerri, Dr. Luca Sorriso-Valvo, and many others. Your invaluable assistance, time, and knowledge have greatly enhanced my research and understanding. Your contributions have been crucial to the completion of this thesis.

Special thanks to the members of my committee, Professor Vassilis Angelopoulos, Professor Hao Cao, and Professor Paulo Alves, for taking time out of their demanding schedules to read and evaluate this thesis. Your insightful feedback and guidance have

been instrumental in refining this work. Vassilis, thank you for always being honest with me, telling me what I needed to hear, even when I did not want to hear it. Your advice has been invaluable.

This journey would not have been possible without the collective support of my mentors, colleagues, friends, and family. Each of you has played a vital role in shaping the person I am today and the scholar I aspire to be. From the bottom of my heart, thank you.

VITA

2015–2019 B.S. in Physics, Aristotle university , Thessaloniki, Greece

2020–Present Ph.D. student in Geophysics and Space Physics, University of California, Los Angeles, USA

PUBLICATIONS

Stochastic Turbulent Acceleration in a Fractal Environment, **Sioulas** et al., 2020

Superdiffusive stochastic Fermi acceleration in space and energy , **Sioulas** et al., 2020

Statistical Analysis of Intermittency and its Association with Proton Heating in the Near-Sun Environment, **Sioulas** et al., 2022

Particle heating and acceleration by reconnecting and nonreconnecting current sheets, **Sioulas** et al., 2022

Magnetic Field Intermittency in the Solar Wind: Parker Solar Probe and SolO Observations Ranging from the Alfvén Region up to 1 AU, **Sioulas** et al., 2022

Preferential Heating of Protons over Electrons from Coherent Structures during the First Perihelion of the Parker Solar Probe , **Sioulas** et al., 2022

Magnetic field spectral evolution in the inner heliosphere, **Sioulas** et al., 2023

On the evolution of the Anisotropic Scaling of Magnetohydrodynamic Turbulence in the Inner Heliosphere, **Sioulas** et al., 2023

Higher-Order Analysis of Three-Dimensional Anisotropy in Imbalanced Alfvénic Turbulence, **Sioulas** et al., 2024

CHAPTER 1

Introduction

Plasma permeates the cosmos, constituting the predominant form of visible matter scattered across the vast expanses of space. Occupying the cores of stars, weaving through nebulae, spiraling within galactic arms, and enveloping planetary environments, plasma stands apart from the solid, liquid, and gaseous states by virtue of its ionization. This so-called fourth state of matter is characterized by a sea of freely moving electrons and ions, which endows it with extraordinary electrical conductivity, magneto-responsive behavior, and the capacity to generate and interact with electromagnetic fields.

The behavior of astrophysical and space plasmas is often examined through the lens of magnetohydrodynamics (MHD). MHD merges fluid mechanics with electromagnetism, treating plasma as a magnetofluid governed by both hydrodynamic and electromagnetic forces.

At the heart of astrophysical plasma dynamics lies MHD turbulence, a state of plasma defined by the chaotic, nonlinear interactions between magnetic fields and plasma flows. MHD turbulence drives complex energy transport and dissipation mechanisms, linking large-scale astrophysical phenomena with microscopic processes. A deeper understanding of MHD turbulence is crucial for explaining various unresolved astrophysical problems, such as the heating of stellar coronae, the generation of stellar winds, the acceleration of cosmic rays, and star formation. These insights offer a deeper understanding of the mechanisms that govern the universe's most energetic events and the evolution of cosmic structures.

The solar wind, a continuous stream of plasma emanating from the Sun, provides an accessible laboratory for studying MHD turbulence. Direct, in situ observations of the

solar wind allow for the testing and refinement of MHD theories. Insights from solar wind studies can be extrapolated to broader astrophysical contexts (Matthaeus and Velli, 2011).

A comprehensive understanding of the statistical properties of MHD turbulence is essential for elucidating a wide range of astrophysical phenomena. Significant theoretical progress in recent decades has aimed to align MHD turbulence theories with observational and numerical evidence (see reviews by Schekochihin et al., 2009a; Bruno and Carbone, 2013; Beresnyak, 2019; Schekochihin, 2022, and references therein). Nonetheless, many aspects of MHD turbulence remain to be explored (Chen, 2016a). For instance, much of our theoretical framework is based on homogeneous turbulence, which involves nonlinear interactions between small-amplitude, shear alfvénic wave packets traveling in (anti)parallel directions relative to a large-scale background magnetic field. These interactions lead to the fragmentation of wave packets and the cascading of energy toward larger perpendicular wavenumbers. However, these assumptions often fall short in the radially expanding solar wind, which is dominated by outgoing large-amplitude wave packets exhibiting characteristics similar to spherically polarized Alfvénic modes. Therefore, in situ observations that account for and quantify these effects are crucial for the development and refinement of theoretical models.

Recent observations from the Parker Solar Probe (PSP, Fox et al., 2016) mission offer an opportunity to test turbulence theory predictions through in-situ observations of pristine turbulence in the vicinity of the solar wind sources. Integrating these findings with data from spacecraft like Solar Orbiter (Solo, Müller et al., 2020), Wind (Wind, Lepping et al., 1995), will facilitate investigations into the dynamic radial evolution of turbulence within the inner heliosphere.

Through this thesis our aim is not only to enhance our understanding of solar wind dynamics but also to provide solid observational constraints for MHD turbulence theories and to elucidate the processes governing magnetic energy dissipation and plasma heating.

The outline of the thesis is as follows:

Before delving into MHD and MHD turbulence, Section 1.1 discusses some basic concepts underlying the dynamics of fluids and introduces fundamental ideas of the hydrodynamic turbulent cascade.

To explore MHD turbulence, it is essential to understand some fundamental concepts of plasma physics. Therefore, Section 1.2 provides an overview of key properties essential for characterizing laboratory and astrophysical plasmas. Following this, Section 1.3 presents an introductory discussion on the framework of homogeneous Magnetohydrodynamic turbulence. A brief review of in-situ turbulence observations is provided in Section 1.4. The research objectives and scope of thise thesis are summarized in Section1.5.

The novel results of this thesis are presented in Chapters 3 through 5. A summary of our results and a brief discussion of ongoing and future work are provided in Chapter 6.

1.1 Hydrodynamic Turbulence

To delve into the complex dynamics of turbulent plasmas, it is crucial to first understand the foundational principles of hydrodynamics. In this chapter, we will start by examining the fundamental equations governing fluid dynamics, focusing specifically on the Navier-Stokes equations

We will then explore how different flow regimes emerge based on the relative importance of nonlinear advection and viscous terms. Laminar flow is characterized by smooth, orderly motion, while turbulent flow exhibits chaotic, eddying behavior. Understanding these regimes is crucial for interpreting the various states fluids can exhibit under different physical conditions.

Finally, we will delve into the principles underlying turbulent flows. Our discussion will adopt a phenomenological perspective, drawing extensively from the Kolmogorov framework (Kolmogorov, 1941). This framework provides a statistical approach to understanding turbulence, emphasizing the energy cascade process and scale invariance.

1.1.1 Governing Equations

Hydrodynamics pertains to the study of fluid motion and the forces that both influence and result from such dynamics. It employs mathematical models that build upon principles from kinetic theory, which models fluids as assemblies of numerous interacting particles. Each particle population in a fluid is described by a distribution function $f_j(\boldsymbol{r}, \mathbf{v}, t)$ that describes the probability of finding a particle in a differential element at position $\boldsymbol{r}$ to $\boldsymbol{r} + d\boldsymbol{r}$ and velocity $\boldsymbol{v}$ to $\mathbf{v} + d\mathbf{v}$ at time t. The distribution function for each particle type must satisfy the normalization condition:

$$\int f_j(\boldsymbol{r}, \mathbf{v}, t)\, d^3\boldsymbol{r}\, d^3\mathbf{v} = N_j, \tag{1.1}$$

where N_j is the total number of particles of type j.

Under the assumptions that the number of particles within the system remains con-

served, Liouville's theorem—which states the conservation of phase space volume—leads to the Vlasov equation:

$$\frac{\partial f_j}{\partial t} + \boldsymbol{v} \cdot \nabla_{\boldsymbol{r}} f_j + \boldsymbol{a} \cdot \nabla_{\boldsymbol{v}} f_j = 0, \tag{1.2}$$

where $\boldsymbol{a}$ is the acceleration on each of the particles due to the forces acting on those particles. This differential equation governs the evolution of the distribution function in regimes where collisions are rare or negligible, we have thus dropped the collision term, $(\frac{\delta f_c}{\delta t})_c$.

The transition from a kinetic to a hydrodynamic description involves taking statistical moments of the distribution function $f_j(\boldsymbol{r}, \boldsymbol{v}, t)$ over velocity space. The j-th moment tensor $\mathcal{J}_j^i(\boldsymbol{r}, t)$ is defined by:

$$\mathcal{J}_j^i(\boldsymbol{r}, t) = \int \boldsymbol{v}^i f_j(\boldsymbol{r}, \mathbf{v}, t)\, d^3\mathbf{v}. \tag{1.3}$$

From these moments, one can derive macroscopic fluid properties, such as the number density n_j and mean velocity $\boldsymbol{u}_j$ for each particle type:

$$n_j = \int f_j\, d^3\boldsymbol{v}, \quad n_j \boldsymbol{u}_j = \int \mathbf{v} f_j\, d^3\mathbf{v}. \tag{1.4}$$

Application of these moment definitions to the Vlasov equation yields a set of conservation equations. The zeroth-order moment leads to the continuity equation, which reflects mass conservation:

$$\frac{\partial n_j}{\partial t} + \nabla \cdot (n_j \boldsymbol{u}_j) = 0, \tag{1.5}$$

and the first-order moment results in the momentum equation for an inviscid fluid, typically expressed in Eulerian form:

$$\frac{\partial \boldsymbol{u}_j}{\partial t} + (\boldsymbol{u}_j \cdot \nabla)\boldsymbol{u}_j = \frac{\nabla \cdot \boldsymbol{P}_j}{m_j n_j} + \mathbf{F}_j, \tag{1.6}$$

where $\mathbf{F}_j$ represents external forces per unit mass and assuming isotropic pressure and and incompressible flow, see 1.1.2, we can decompose the pressure tensor as $\boldsymbol{P}_j = m_j \int (\mathbf{v} - \boldsymbol{v})(\mathbf{v} - \boldsymbol{v}) f(\boldsymbol{r}, (\mathbf{v} - \boldsymbol{v}), t)\, d^3\boldsymbol{v} = -\boldsymbol{I}p + \nu \nabla \boldsymbol{v}$, the latter term is the stress tensor, containing the off-diagonal terms.

A significant challenge arises because any given n-order moment depends on the $n+1$-order moment. This means that a complete description of system would require an infinite number of moment equations to be derived from the Vlasov equation. For practical calculations a closure assumption is usually implemented. One common approach is to truncate the hierarchy by assuming that all moments $\mathcal{J}_j^i = 0$ for i exceeding a certain order. A widely used closure model employs a polytropic equation of state, typically defined by $p\rho^{-\gamma} = \text{const}$, where γ is the polytropic index.

1.1.2 Incompressible flows & the Reynolds number

For an incompressible fluid, the density ρ is constant, leading to the simplification that its time derivative is zero:

$$\frac{d\rho}{dt} = 0, \tag{1.7}$$

where $\frac{d\psi}{dt} = \frac{\partial \psi}{\partial t} + \boldsymbol{u} \cdot \nabla \psi$, is the material derivative, and $\boldsymbol{u}$ the flow speed. Substituting this condition into the continuity equation we can obtain a condition for incompressibility:

$$\nabla \cdot \boldsymbol{v} = 0 \tag{1.8}$$

In this case the Navier-Stokes equations for an incompressible fluid can thus be written as:

$$\frac{\partial \boldsymbol{v}}{\partial t} + (\boldsymbol{v} \cdot \nabla)\boldsymbol{v} = -\frac{1}{\rho}\nabla p + \nu \nabla^2 \boldsymbol{v}, \tag{1.9}$$

$$\nabla \cdot \boldsymbol{v} = 0, \tag{1.10}$$

where $\nu = \mu/\rho$ represents the kinematic viscosity.

To gain a deeper understanding of different flow regimes we can render the Navier-Stokes equations nondimensional. We introduce characteristic length and velocity scales, L and U, respectively. We define the nondimensional variables:

$$\boldsymbol{v}' = \frac{\boldsymbol{v}}{U}, \quad t' = \frac{tU}{L}, \quad \boldsymbol{r}' = \frac{\boldsymbol{r}}{L}, \quad p' = \frac{p}{\rho U^2} \tag{1.11}$$

Substituting these into the Navier-Stokes equations and simplifying, we find that the terms involving the viscosity becomes:

$$\frac{\mu}{\rho L U}\nabla^2 \boldsymbol{v} \tag{1.12}$$

The coefficient of the viscous term, $\mu/\rho LU$, can be rewritten as:

$$\frac{1}{Re} = \frac{\mu}{\rho L U} \tag{1.13}$$

The Reynolds (1883) number contrasts inertial forces against viscous forces within the fluid flow. Alternatively, R_e can be estimated as the ratio between the nonlinear advection and the viscous terms in Equation 1.9, $|(\boldsymbol{v} \cdot \nabla)\boldsymbol{v}|/|\nu \nabla^2 \boldsymbol{v}|$. Low Re indicates laminar flow, which is smooth and ordered, while high Re signifies turbulent flow, marked by chaotic and stochastic fluid motion.

Turbulent dynamics pose a significant challenge in our understanding of fluid dynamics[1]. A field that interects disciplines of theoretical physics, applied mathematics, and

[1]Chaos and turbulence share similar properties of unpredictability, but chaos is usually used as a term

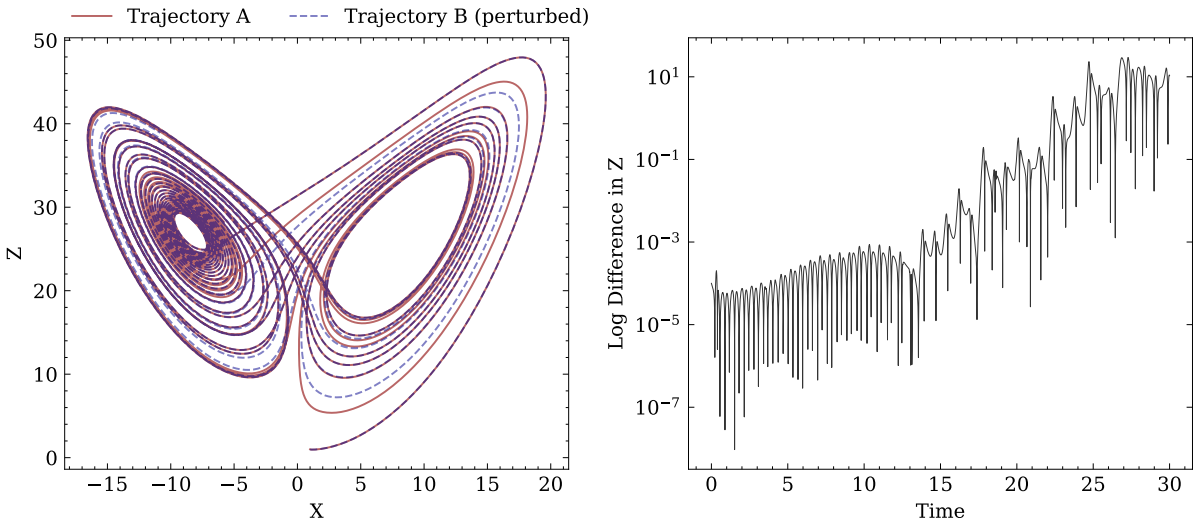

Figure 1.1: The Lorenz Attractor and Divergence of Trajectories. Panel (left) illustrates the two-dimensional projection of the Lorenz attractor, showing Trajectory A (solid line) and the perturbed Trajectory B (dashed line) in the X-Z plane, highlighting the sensitivity to initial conditions. THe right panel presents the logarithmic divergence of the z component between the two trajectories over time, exemplifying the 'butterfly effect' where small differences in starting conditions lead to exponential separation, a characteristic feature of chaotic systems.

engineering. In contrast to laminar flow, where fluid particles trace smooth, predictable trajectories, turbulent flow is marked by erratic and seemingly random movements. This unpredictability is not just a theoretical concern but also has significant practical implications, for example, in meteorology. The difficulty in precisely predicting weather patterns, particularly severe storms, highlights the challenges posed by turbulence. Even minor changes in initial conditions can lead to widely divergent outcomes, illustrating the so-called butterfly effect within chaotic systems, see e.g., Figure 1.4.

1.1.3 Stationarity, Ergodicity & the Power Spectral Tensor

The complexity of turbulence arises from its highly irregular, chaotic, and multiscale nature, involving a vast range of interacting eddies and vortices. This inherent complexity makes it nearly impossible to derive exact analytical solutions for turbulent flows. Consequently,

to describe a nonlinear system without too many degrees of freedom. Turbulence on the other hand has many degrees of freedom.

physicists resort to statistical descriptions, which allow them to characterize the average properties and probabilistic behavior of turbulence, thereby providing meaningful insights into its dynamics despite the absence of precise deterministic solutions.

An ensemble, denoted as $z(t)$, consists of various outcomes $z_j(t)$ of a random process, where $j = 1, 2, \ldots, M$. The properties of the random process are discerned by averaging over the entire ensemble of M possible functions $z_j(t)$. For a specific time t_0, the mean value μ_z, i.e., the first moment of the probability density function, is defined as

$$\mu_z(t_0) = \langle z(t_0) \rangle = \lim_{M \to \infty} \frac{1}{M} \sum_{j=1}^{M} z_j(t_0), \tag{1.14}$$

while the autocorrelation function R_z is given by

$$R_z(t_0, t_0 + \tau) = \langle z(t_0) z(t_0 + \tau) \rangle = \lim_{M \to \infty} \frac{1}{M} \sum_{j=1}^{M} z_j(t_0) \cdot z_j(t_0 + \tau), \tag{1.15}$$

where the $\langle \ldots \rangle$ operator denotes the ensemble average.

The sample function $z(t)$ is referred to as weakly stationary when both $\mu_z(t_0)$ and $R_z(t_0, t_0 + \tau)$ remain independent of time, i.e., $\mu_z(t_0) = \mu_z$ and $R_z(t_0, t_0 + \tau) = R_z(\tau)$. Strong stationarity, however, requires all higher-order moments and joint moments to also remain constant over time (Frisch, 1995). It is important to point out that if the sample function $z(t)$ is characterized by a Gaussian distribution, its higher-order odd moments vanish, while even moments are completely described by second-order moments. Therefore, in Gaussian processes, weak stationarity naturally implies strong stationarity, with the first moment and autocorrelation function fully characterizing the process.

Typically, conditions are imposed ensuring the equality between different averages, formally known as ergodicity. Ergodicity is a fundamental concept that allows a time average over a single sample function $z_j(t)$ to serve as an ensemble average over all states in phase space for a stationary process. This implies that all statistical information can be derived from one function. This property is particularly advantageous for experimental data collection, as it allows for adequate sampling of a stationary random process through

averaging over a single time series. In the solar wind, for example, Matthaeus and Goldstein (1982) have demonstrated that magnetic field fluctuations often exhibit characteristics of weakly stationary and ergodic processes, provided one accounts for intermittency by excluding coherent structures. They observed that the mean and autocorrelation function computed over a sub-interval converge to the values estimated for the entire interval after a few correlation times τ_c.

The two-point autocorrelation tensor for the velocity field is expressed as (Frisch, 1995):

$$R_v^{mn}(r) = \langle v_m(x) \cdot v_n(x+r) \rangle, \tag{1.16}$$

where indices $m, n = 1, 2, 3$ represent the different components of $\mathbf{v}$. In conditions of weak homogeneity where the mean field $\mathbf{v_0} = \langle v(x) \rangle = 0$, $R_v^{mn}(r)$ becomes independent of the position, x. Therefore, $R_v^{mn}(r)$ characterizes the structural correlation between different components of $\mathbf{v}$ as a function of distance r, averaged over an ensemble of two spatial points. Similarly, the velocity cross-correlation tensor is defined as:

$$R_{mn}^{uv}(r) = \frac{1}{2} \left(\langle u_m(x) \cdot v_n(x+r) \rangle + \langle v_m(x) \cdot u_n(x+r) \rangle \right). \tag{1.17}$$

The connection between autocorrelation tensor $R_{mn}(r)$ and the power spectral tensor $S_{mn}(k)$ is established by the one-dimensional Wiener-Khinchin theorem, stating that for a stationary process:

$$\tilde{E}_{mn}(k) = \iiint R_{mn}(r) \exp(-i \cdot k \cdot r) d^3 r. \tag{1.18}$$

For instance, the velocity field power spectral tensor is expressed as:

$$\tilde{E}_{mn}^{v}(k) = \langle \tilde{v}_m^*(k) \cdot \tilde{v}_n(k) \rangle, \tag{1.19}$$

where the asterisk denotes the complex conjugate, $\tilde{v}_m^*(k) = \tilde{v}_m(-k)$. The power-spectra

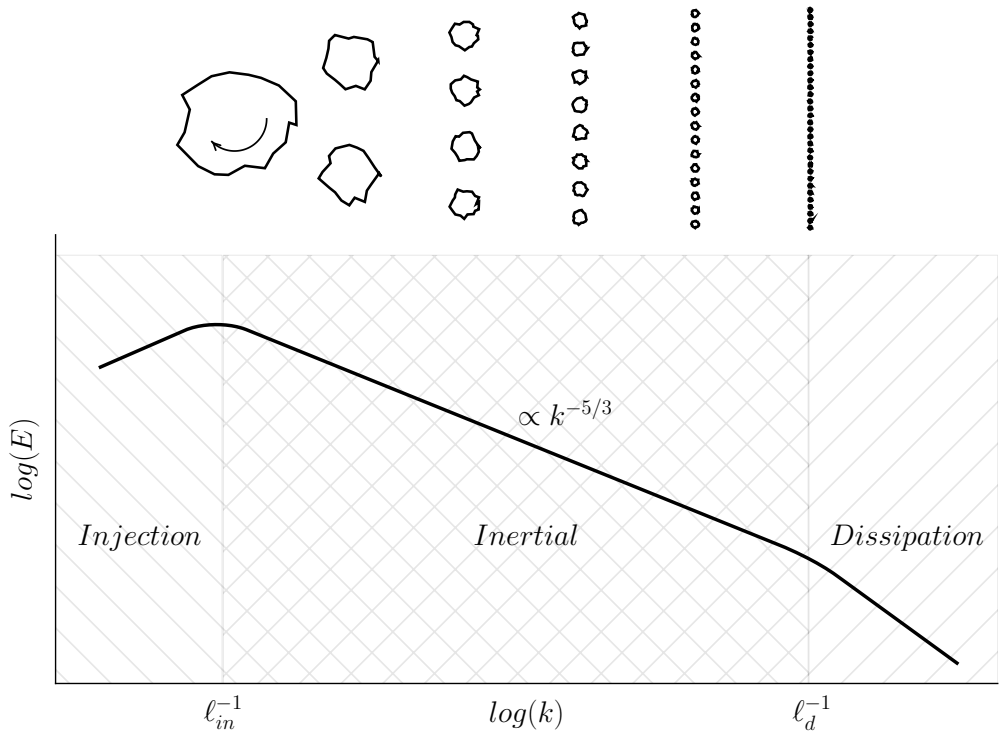

Figure 1.2: Representation of the energy spectrum in turbulent flows. The graph shows the distribution of energy across different scales of turbulence represented by wave number k. The peak at l_{in}^{-1} marks the energy injection scale, where energy is fed into the largest eddies. The $-5/3$ slope in the inertial subrange indicates the energy cascade due to the Kolmogorov spectrum, where energy transfers from larger to smaller eddies without significant loss until it reaches the dissipation scale at ℓ_d^{-1}. The visual insert of eddies demonstrates the process of energy transfer from larger to progressively smaller eddies, typical in turbulent flow.

can be obtained directly from the trace of the power spectral tensor, $\mathrm{Tr}\{\tilde{E}^v_{mn}(\mathbf{k})\} \equiv \sum_i \tilde{E}_{ii}$.

1.1.4 Phenomenology of the Inertial Range Turbulent Cascade

A hallmark of fully developed turbulence is an energy spectrum that spans a broad range of scales. We conceptualize a scenario in which physical quantities like energy are continuously injected at a large *energy injection scale* $\ell_{in} \sim 1/k \approx k_{in}$, with an injection rate ϵ_{in}. Through nonlinear, energy-conserving interactions, this energy is transferred across the spectrum towards smaller spatial scales at a rate ϵ_t, culminating in dissipation at the *dissipation scale* $k \approx k_d$, where energy is transformed into heat at a rate ϵ_d. In

steady-state turbulence, these rates of energy flux are equated. The scales between injection and dissipation are defined as:

$$\ell_{in} \gg \ell \gg \ell_d. \tag{1.20}$$

In this range, eddies are too large for viscosity to significantly influence and too small to be affected by large-scale inhomogeneities. This process is typically referred to as a *direct cascade*. However, under specific conditions, such as in purely 2D fluid turbulence, the cascade can reverse direction—from smaller to larger scales, a phenomenon known as an *inverse cascade*.

An important dynamical timescale in this system is the nonlinear *eddy turnover time*,

$$\tau_{nl} \sim \frac{\ell_m}{\delta v_n}, \tag{1.21}$$

defined as the time required for energy to transfer between consecutive scales ℓ_m and ℓ_{m+1}, with δv_n representing the velocity fluctuation amplitude at scale ℓ_m. For analytical purposes, we discretize the inertial range into logarithmically spaced scales:

$$\ell_0 > \ell_1 > \cdots > \ell_m, \quad \text{and thus} \quad k_0 < k_1 < \cdots < k_N, \tag{1.22}$$

where $\ell_m = 2^{-n=m}\ell_0$, and ℓ_0 is approximately equal to the system's largest scale L.

Kolmogorov proposed that the cascade process is complex enough for eddies to lose all memory of their past, and that their properties after each cascade step are random. A universal probability density function (PDF), $P(\delta u, \ell)$, is postulated to emerge over the inertial range. The velocity difference between non-proximate points is modeled as the sum of velocity differences over subintervals, supporting a Gaussian distribution assumption based on the central limit theorem. The validity of this assumption relies on the mutual independence among summands and comparable finite variances in the subinterval probability distributions (Feller, 1968).

Considering a global transfer energy rate ϵ that is independent of scale,

$$\epsilon \sim \frac{\delta v_n^3}{\ell_m}, \tag{1.23}$$

leads to the scaling relationship:

$$\delta v_n \sim \epsilon^{1/3} \ell_m^{1/3}. \tag{1.24}$$

Utilizing statistical moments of the PDFs, structure functions (SF^n):

$$SF_i^n(\ell) = \int_{-\infty}^{\infty} (\delta u_i)^n P(\delta u_i, \ell) d(\delta u_i), \tag{1.25}$$

where δu_i denotes longitudinal velocity increments, $\delta u_i = V_i(\boldsymbol{r} + \boldsymbol{\ell}) - V_i(\boldsymbol{r})$, Kolmogorov's similarity hypothesis yields:

$$SF_i^n(\ell) \sim \epsilon^{n/3} \ell^{\zeta^{K41}(n)}, \tag{1.26}$$

where $\zeta^{K41}(n) = n/3$, implying global scale invariance (self-similarity) of the fluctuations.

In addition, we derive the energy spectrum for isotropic turbulence, assuming a scalar wavenumber $k = \sqrt{k_x^2 + k_y^2 + k_z^2}$, and define the angle-integrated spectra as:

$$E = \int_0^{\infty} k\, E_k. \tag{1.27}$$

Equating the kinetic energy of eddies to the band-integrated Fourier spectrum gives:

$$\delta v_n^2 \sim k_n E_{k_n}, \tag{1.28}$$

from which we estimate:

$$E_k \sim \epsilon^{2/3} k^{-5/3}. \tag{1.29}$$

Finally, the dissipation scale within this framework, ℓ_d, can be identified as the point where nonlinear terms equate with diffusion terms, leading to $\ell_d v_\nu \approx \nu$, similar to the reasoning used in defining the Reynolds number, Re. Given that $v_k \sim \epsilon^{1/3} k^{-1/3}$, it follows that

$$\ell_d \sim \nu^{3/4} \epsilon^{-1/4}. \tag{1.30}$$

It is crucial to understand that this introduction is limited to incompressible hydrodynamics. The subsequent chapters will extend these concepts to address the generalizations necessary for anisotropic magnetohydrodynamic turbulence.

1.2 Basics of Plasmas

A notable feature of plasma is the significant mass difference between its components. Protons, the lightest ions, are nearly 2000 times heavier than electrons. This mass disparity profoundly influences the dynamics of plasma particles, which can exhibit a wide range of behaviors across different temporal and spatial scales. Understanding these dynamics requires the use of specific metrics, referred to as *plasma parameters*. In this section, I provide an overview of the fundamental concepts in plasma physics pertinent to the study of the solar wind and the subsequent research presented in this thesis. The discussion starts with the definition of plasma and the identification of its characteristic time and length scales.

Similar to hydrodynamics, modeling plasma dynamics often involves grappling with the intricacies of kinetic theory. This approach requires computing individual particle interactions, which is challenging due to the complexity of solving the Boltzmann or Vlasov equations analytically and numerically. Kinetic theory demands significant computational resources and sophisticated algorithms to account for the detailed behavior and interactions of particles.

To handle this complexity, the method of moments of the distribution functions is employed. This approach simplifies the microscopic specifics of individual particle states into macroscopic, measurable quantities like density, velocity, and pressure. This transition facilitates the use of fluid equations .

Even with this simplification, the resultant fluid models, such as the two-fluid model that distinguishes between ions and electrons, still embody a considerable degree of complexity. Within this framework, Magnetohydrodynamics (MHD) offers a further simplification by assuming nearly equal temperatures for ions and electrons and treating them as a single "fictitious" fluid. This approximation enables MHD to effectively integrate electromagnetic effects into fluid dynamics, creating a powerful tool for describing a broad spectrum of plasma behaviors across various conditions. Despite its simplifications, MHD remains highly effective in capturing a wide array of plasma dynamics, proving essential

for analyzing classical plasma regimes.

The derivation of MHD equations from kinetic theory requires an in-depth engagement with statistical mechanics and electromagnetic theory. This topic, while rich and expansive, is beyond the scope of this introductory section. Our objective in this section is to lay a foundational understanding that supports our study. This approach provides an accessible entry point into the complexities of MHD turbulence, tailored to our research needs. For those interested in a more thorough discussion, (Biskamp, 2003; Chiuderi and Velli, 2015) offer extensive insights into the subject.

1.2.1 Plasma parameters

The term "plasma" is derived from the Greek word $\pi\lambda\acute{\alpha}\sigma\mu\alpha$, meaning a substance that can be molded or shaped, was introduced in the scientific literature by Langmuir (1928) to describe ion and electron-rich regions around electrodes in equilibrium. Known as the "fourth state of matter," plasma forms under conditions conducive to the ionization of gases, a process triggered by energy input sufficient to overcome the electron binding energy, thus ionizing atoms. Such conditions are prevalent in various environments, including the cores of stars, Earth's ionosphere, and in controlled environments like tokamaks or other laboratory experiments.

Objects with mass, including charged particles in a plasma, follow Newton's laws of motion. When these particles travel at velocities significantly less than the speed of light, c, their dynamics are described by:

$$\boldsymbol{F}_{\text{total}} = \frac{d\boldsymbol{P}}{dt} = m\frac{d^2\boldsymbol{r}}{dt^2}, \tag{1.31}$$

where $\boldsymbol{F}_{\text{total}}$ denotes the total external force, $\boldsymbol{P}$ is momentum.

Charged particles moving with velocity $\boldsymbol{v}$, are subject to the Lorentz force:

$$\boldsymbol{F}_{\text{EM}} = q(\boldsymbol{E} + \boldsymbol{v} \times \boldsymbol{B}). \tag{1.32}$$

where $\boldsymbol{E}$ and magnetic field $\boldsymbol{B}$ are the macroscopic electric and magnetic fields that arise from possible external sources as well as from the presence and motions of all other particles. Therefore, while plasmas resemble neutral gases macroscopically, they differ microscopically due to the effects of these long-range interactions among the particles, leading to the collective behavior of the particles constituting the plasma. Quasineutrality is expressed as:

$$\sum_j n_j q_j \approx 0 \tag{1.33}$$

where q_j denotes the charge states of species j. This state is maintained by the long-range Coulomb force, ensuring global charge equilibrium which is crucial for the plasma's stability and unique properties.

The electric potential ϕ within plasmas is described by Poisson's equation:

$$\nabla^2 \phi = -\frac{\rho}{\varepsilon_0}, \tag{1.34}$$

with, ε_0, permittivity of free space, ρ, the charge density, comprising mainly free electrons and ions, and defined as $\rho = e(n_i - n_e)$. Assuming ions form a quasi-static background due to their significantly greater mass ($n_i = n_0$), the introduction of a test charge q_i perturbs the plasma, modeled by $\rho_{test} = q_i \delta(\boldsymbol{r})$.

At thermal equilibrium, the electron density's response to electrostatic potential follows the Boltzmann relation:

$$n_e = n_0 \exp\left(-\frac{e\phi}{k_B T_e}\right), \tag{1.35}$$

which simplifies to $n_e \approx n_0 \left(1 - \frac{e\phi}{k_B T_e}\right)$ under the condition $e\phi \ll k_B T_e$. This linear approximation, when inserted into Poisson's equation alongside the test charge term, yields:

$$\nabla^2\phi \approx \frac{e^2 n_0}{\varepsilon_0 k_B T_e}\phi + \frac{q_i \delta(\boldsymbol{r})}{\varepsilon_0}. \tag{1.36}$$

This leads to the identification of the **Debye length** λ_D, given by:

$$\lambda_D = \left(\frac{\varepsilon_0 k_B T_e}{e^2 n_0}\right)^{1/2}, \tag{1.37}$$

signifying the characteristic distance over which electric potentials are screened or attenuated in the plasma. Here ε_0 is the permittivity of free space, k_B the Boltzmann constant, T_e is the electron temperature in Kelvin.This naturally introduces the concept of the **Debye sphere**, a virtual sphere with a radius equal to the Debye length. Within this sphere, the electrostatic potential of a charged particle influences other charges, leading to a net screening effect. A collection of particles can be deemed a plasma if the particle count within a Debye sphere is substantially large. This can be quantified using the **plasma parameter**,

$$\Lambda = n_e \lambda_D^3 \gg 1 \tag{1.38}$$

In this thesis, our primary discussion revolves around collisionless plasmas, where the Coulomb **collision time**, denoted as $\tau_c = \frac{1}{\nu_c}$, ν_c the frequency of collisions among the particles, is considerably longer than any other typical temporal variation within the plasma.

In plasma physics, multiple characteristic frequencies are observed. The most fundamental frequency, indicating the oscillation frequency of a column of particles of a species, against the background plasma comprised of all other species, is the **plasma frequency** for a species s, expressed as:

$$\omega_{ps} = \left(\frac{n_j q_s^2}{m_j \epsilon_0}\right)^{\frac{1}{2}}. \tag{1.39}$$

The plasma frequency not only establishes a characteristic time scale ($\tau_p = 1/\omega_p$) that

differentiates plasma from neutral gases but also underscores the rapidity with which plasma responds to external disturbances, a fundamental aspect in the study of wave propagation and stability within plasma.

The Lorentz force leads to gyration motions, quantified by the **gyroradius** (r_L) and **gyrofrequency** (ω_c), which are critical for understanding particle confinement and the influence of magnetic fields on plasma behavior:

$$r_L = \frac{mv_\perp}{|q|B}, \tag{1.40}$$

$$\omega_c = \frac{|q|B}{m}, \tag{1.41}$$

emphasizing how particle energy and magnetic field orientation affect charged particle dynamics.

The **ion inertial length**, d_i, is given by

$$d_i = \frac{c}{\omega_{pi}}, \tag{1.42}$$

The ion inertial length characterizes the scale in plasma at which ions' inertia prevents them from reacting quickly to changes in the electric field, leading to their decoupling from the electrons. It marks the threshold below which the motion of electrons and magnetic field lines can be considered independent of ion motion.

We conclude by defining a critical parameter in plasma physics known as the **plasma beta**, β, which is the ratio of the thermal energy density to the magnetic energy density. It is given by:

$$\beta = \frac{nk_BT}{B^2/(2\mu_0)} \tag{1.43}$$

The value of β serves as an indicator of the dominant forces within the plasma. A $\beta \gg 1$ implies that thermal pressure is the dominating force over magnetic fields in

influencing plasma dynamics.

1.2.2 Difficulties of Resorting to Kinetic Theory

The Vlasov equation, see Section 1.1.1,

$$\frac{\partial f_j}{\partial t} + \boldsymbol{v} \cdot \frac{\partial f_j}{\partial \boldsymbol{r}} + \frac{q_j}{m_j} (\boldsymbol{E} + \boldsymbol{v} \times \boldsymbol{B}) \cdot \frac{\partial f_j}{\partial \boldsymbol{v}} = 0, \tag{1.44}$$

,

where we have subsituted the acceleration term using Equation 1.32 in tandem with Maxwell's equations:

$$\nabla \cdot \boldsymbol{E} = \frac{\rho}{\epsilon_0}, \qquad \text{(Gauss's law)} \tag{1.45}$$

$$\nabla \cdot \boldsymbol{B} = 0, \qquad \text{(Solenoidal constraint)} \tag{1.46}$$

$$\nabla \times \boldsymbol{E} = -\frac{\partial \boldsymbol{B}}{\partial t}, \qquad \text{(Faraday's law)} \tag{1.47}$$

$$\nabla \times \boldsymbol{B} = \mu_0 \boldsymbol{J} + \frac{1}{c^2} \frac{\partial \boldsymbol{E}}{\partial t}, \qquad \text{(modified Ampére's law)} \tag{1.48}$$

consitute the Maxwell-Vlasov equations providing a complete system description of collisionless plasma dynamics. Here

$$\rho = \sum_j q_j \int f_j \, d^3\mathbf{v} \tag{1.49}$$

is charge density, and

$$\boldsymbol{J} = \sum_j q_j \int \mathbf{v} f_j \, d^3\mathbf{v}, \tag{1.50}$$

the current density.

While an idealized approach would involve tracking the motion and interactions of

each particle, considering both the external and self-generated electromagnetic fields, the complexity of such a task is prohibitive due to the vast number of particles typically present in a plasma. For instance, in a typical laboratory plasma, the number of particles can exceed 10^{18} per cubic meter, each interacting with one another through electromagnetic forces that vary both spatially and temporally.

Given this complexity and the significant computational resources required for a particle-by-particle simulation, plasma physicists often resort to more manageable statistical or fluid-like models. These models, such as Magnetohydrodynamics (MHD), treat plasma as a continuous fluid influenced by magnetic fields, providing practical yet insightful ways to study plasma dynamics. These approximations, while less precise than a fully kinetic description, still offer significant predictive power and understanding of plasma phenomena in a variety of settings.

1.2.3 Conditions for MHD Applicability and Limitations

The MHD equations integrate the principles of fluid dynamics with electromagnetic theory. They include the Navier-Stokes equations, modified for conductive fluids, Maxwell's equations for describing electromagnetic fields, and an equation of state that defines the system. These equations characterize the fluid's velocity vector $\boldsymbol{v}$, thermodynamic pressure p, and magnetic field vector $\boldsymbol{B}$. Within the framework of the single-fluid approximation, the plasma is considered a continuous medium. The utility of this approach is contingent upon several specific conditions, which are detailed as follows:

Even though the plasma that is macroscopically neutral we can still have currents $\boldsymbol{J}$ as long as the electrons move at an average velocity $\boldsymbol{v}^-$ that is different than the average velocities $\boldsymbol{v}^+$ of the ions,

$$-\boldsymbol{J} = n^+e^+\boldsymbol{v}^+ + n^-e^-\boldsymbol{v}^- = -n^-e^-\boldsymbol{v}^+ n^-e^-\boldsymbol{v}^-, \tag{1.51}$$

and subsequently,

$$\boldsymbol{J} = n^-e^-(\boldsymbol{v}^- - \boldsymbol{v}^+) = n^-e^-\boldsymbol{v}'_{rel}, \tag{1.52}$$

where $\boldsymbol{v}'_{rel}$ is the relative velocity of the electrons compared to the ions.

However, the relative velocity $\boldsymbol{v}'_{rel}$ of the electrons with respect to the ions is usually very small and therefore, in a first approximation, the plasma motion can be considered as the motion of a neutral fluid which due to of electrical neutrality and because $m^- << m^+$ is described by the following macroscopic parameters:

$$\begin{aligned} Velocity: \quad & \boldsymbol{v} = \frac{n^+m^+\boldsymbol{v}^+ + n^-m^-\boldsymbol{v}^-}{n^+m^+ + n^-m^-} = \frac{m^+\boldsymbol{v}^+ + m^-\boldsymbol{v}^-}{m^+ + m^-} \approx \boldsymbol{v}^+, \\ Density: \quad & \rho = n^+m^+ + n^-m^- = n^-(m^+ + m^-) \approx n^+m^+ = nm, \\ Pressure: \quad & P = P^+ + P^- = 2nkT \quad and \quad Temperature: \quad T = \frac{T^+ + T^-}{2}. \end{aligned}$$

This simplifies the problem, since we do not have to write separate equations for the ions and electrons.

In the ion frame of reference, the equation of motion of the electrons is written to a first approximation,

$$\frac{d\boldsymbol{v}'}{dt} = -e\left(\boldsymbol{E}' + \frac{\boldsymbol{v}'}{c} \times \boldsymbol{B}'\right) - m_e\boldsymbol{v}'\frac{\nu'}{\nu_c}, \tag{1.53}$$

where ν_c is the collision frequency of electrons with ions, while in the system of moving ions the fields are denoted are denoted with a prime. Assuming that the speed of the electrons is constant, $\boldsymbol{v}'_{rel} \approx const.$, we have a balance between the Lorentz force and the frictional force in the system of moving ions. For non-relativistic velocities $V/c << 1$,

$$\boldsymbol{v}'_{rel} \approx -\frac{e\boldsymbol{E}'}{m_e\nu_c}, \tag{1.54}$$

and consequently,

$$\boldsymbol{J}' = -en_e\boldsymbol{v}' = \sigma\boldsymbol{E}', \tag{1.55}$$

where the electrical conductivity is,

$$\sigma \approx \frac{n_e e^2}{m_e \nu_c}. \tag{1.56}$$

Finally, by substituting the expressions into the Ohm's law for non-relativistic velocities, we have

$$\boldsymbol{J}' = \boldsymbol{J}, \quad \boldsymbol{B}' \approx \boldsymbol{B}, \quad \boldsymbol{E}' \approx \left(\boldsymbol{E} + \frac{\boldsymbol{v}}{c} \times \boldsymbol{B}\right). \tag{1.57}$$

The basic physical assumptions of underlying the magnetohydrodynamic framework are:

1. **Low-Frequency, Long-Wavelength Approximation:** MHD is predicated on the assumption that the phenomena of interest manifest at frequencies and wavelengths satisfying

   $$\omega \ll \Omega_{\mathrm{ci}}, \quad \lambda \gg \rho_{\mathrm{i}}, \tag{1.58}$$

   where ω denotes the phenomena's frequency, Ω_{ci} the ion cyclotron frequency, and ρ_{i} the ion gyroradius. This allows MHD to eschew kinetic effects, concentrating on the fluid and electromagnetic dynamics.

2. **Quasi-Neutrality:** MHD assumes quasi-neutrality, positing that the plasma remains neutral on average, with electron and ion densities (n_{e} and n_{i}, respectively) being approximately equal over scales much larger than the Debye length λ_{D}, the characteristic length for charge separation:

   $$L \gg \lambda_{\mathrm{D}}. \tag{1.59}$$

3. **Collisionality:** The approximation presupposes sufficient collisionality to sustain a Maxwellian distribution, enabling electron and ion temperatures to equilibrate ($T_{\mathrm{i}} = T_{\mathrm{e}}$). This reflects a regime where energy exchange among particles is frequent,

justifying the application of fluid equations to describe plasma behavior.

4. **Neglect of Displacement Current:** Within the MHD context, Ampére's law often disregards the displacement current due to the non-relativistic velocities involved ($V^2 \ll c^2$), rendering this term insignificant for the dynamics at hand.

These conditions delineate MHD's domain of applicability By adhering to these assumptions, MHD offers a computationally viable and powerful approach for investigating a variety of plasma phenomena.

1.2.4 The ideal MHD Equations

Ideal MHD simplifies the dynamics of electrically conducting fluids under magnetic fields by assuming infinite electrical conductivity ($\sigma \to \infty$). This assumption leads to two primary simplifications: the electric field within the fluid is negated, implying that magnetic field lines move with the fluid (the "frozen-in" condition), and resistive effects are omitted, preventing magnetic field diffusion through the plasma. Additionally, Ideal MHD disregards viscous dissipation and thermal conduction, eliminating internal frictional forces and conductive heat transfer from the equations of motion and energy conservation, respectively.

The **Continuity Equation** already defined in Section 1.1.1. The **Momentum Equation**, a modification of the Navier-Stokes equation presented in Section 1.1.1 enriched by the Lorentz force term. It describes the forces acting on the fluid, accounting for both electromagnetic and hydrodynamic forces:

$$\rho \left(\frac{\partial \boldsymbol{v}}{\partial t} + \boldsymbol{v} \cdot \nabla \boldsymbol{v} \right) = -\nabla p + \boldsymbol{J} \times \boldsymbol{B}, \tag{1.60}$$

where p is the pressure, $\boldsymbol{J}$ is the current density, and $\boldsymbol{B}$ is the magnetic field. This equation underscores the direct coupling between fluid motion and electromagnetic fields.

The relationship between the electric field $\boldsymbol{E}$ and the current density $\boldsymbol{J}$ is described by Ohm's Law, given by:

$$\boldsymbol{J} = \sigma \boldsymbol{E}', \tag{1.61}$$

where σ represents the electrical conductivity of the fluid, and $\boldsymbol{E}'$ denotes the electric field as perceived in the fluid's comoving frame. If the fluid parcel is moving with velocity $\boldsymbol{v}$, applying the Lorentz transformation yields $\boldsymbol{E}' = \boldsymbol{E} + \boldsymbol{v} \times \boldsymbol{B}$. In scenarios where the conductivity is infinite ($\sigma \to \infty$), this simplifies to $\boldsymbol{E} = -\boldsymbol{v} \times \boldsymbol{B}$.

By employing Faraday's equation, see Eq. 1.47, we derive the **Induction Equation** of ideal MHD:

$$\frac{\partial \boldsymbol{B}}{\partial t} = \nabla \times (\boldsymbol{v} \times \boldsymbol{B}). \tag{1.62}$$

This equation reveals that in a perfectly conducting plasma, magnetic field lines behave as if they are frozen, permitting unobstructed flow along the magnetic field $\boldsymbol{B}$, whereas any flow perpendicular to $\boldsymbol{B}$ results in the displacement of these lines. Importantly, by taking it's divergence

$$\frac{\partial}{\partial t} \nabla \cdot \boldsymbol{B} = 0 \tag{1.63}$$

therefore the induction equation inherently incorporates the divergence-free condition of the magnetic field ($\nabla \cdot \boldsymbol{B} = 0$).

In addition, the current density $\boldsymbol{J}$ needs to be expressed in terms of the magnetic field $\boldsymbol{B}$. Utilizing the modified form of Ampére's law and incorporating Ohm's Law leads to an approximation of the electric field as $\boldsymbol{E} \approx \boldsymbol{v}_0 \boldsymbol{B}$, where $\boldsymbol{v}_0$ represents a typical velocity scale of the process. Considering the magnitudes of the terms in the Ampére's law, $\nabla \times \boldsymbol{B}$ and $\frac{1}{c^2} \frac{\partial \boldsymbol{E}}{\partial t}$, with the former proportional to $\frac{\boldsymbol{B}}{l_0}$ and the latter to $\frac{\boldsymbol{E}}{c^2 t_0}$, where l_0 and t_0 are characteristic spatial and temporal scales of the process, respectively. For non-relativistic processes where $\boldsymbol{v}_0 \ll c$, the first term is significantly greater than the latter, leading to a

simplified form:

$$\boldsymbol{J} = \frac{1}{\mu_0} \nabla \times \boldsymbol{B}. \tag{1.64}$$

However, to fully solve the system of MHD equations, a closure condition, such as an equation of state, is required to link the thermodynamic variables like pressure and temperature with the density and other state variables. This approach effectively models conducting fluids across a variety of astrophysical and laboratory scenarios, providing a robust framework for investigating fundamental plasma dynamics without the prohibitive complexity of a complete kinetic description.

Closure the ideal MHD equations typically involves an equation of state (EOS) that relates the plasma pressure to other macroscopic quantities like density and temperature. The most common choice for the EOS is the adiabatic or polytropic equation of state, which assumes that the process is reversible and no heat is exchanged with the environment, thus conserving entropy along fluid lines. This assumption leads to a relation of the form:

$$\frac{d}{dt}\left(\frac{p}{\rho^\gamma}\right) = 0, \tag{1.65}$$

where $\gamma = C_p/C_v$ is the adiabatic index (ratio of specific heats).

In deriving ideal MHD equations, the plasma is treated as a fluid under the assumption of sufficient collisionality to maintain local thermodynamic equilibrium (LTE), ensuring well-defined macroscopic quantities like pressure and temperature. However, this fluid description falls short in non-collisional or weakly collisional plasmas, common in many astrophysical settings, where particle mean free paths can be extensive.

To model these plasmas formally, one must resort to kinetic treatments (see e.g., Schekochihin et al., 2009b; Klein, 2013). Nevertheless, in a strongly magnetized plasma, the magnetic field exerts a dominant influence over the charged particles' motion. Charged particles gyrate around magnetic field lines with a characteristic radius known as the Larmor radius, ρ_l. This gyro-motion effectively restricts the particles in the direction perpendicular to the magnetic field, analogous to collisions, thereby contributing to a sort

of “magnetic collisionality.

This effect allows for a partial closure of the MHD equations. The analysis often employs an asymptotic expansion in terms of the small parameter ρ_l/L, where L is a characteristic scale length of the system, such as the length over which the magnetic field significantly changes. The assumption $\rho_l \ll L$ allows for a separation of scales between the microscopic motion of the particles (gyromotion) and the macroscopic (fluid-like) dynamics of the plasma.

Perpendicular dynamics are dominated by Alfvén waves, propagating through oscillations of the magnetic field lines without compressing the plasma. Conversely, parallel dynamics, unconfined by magnetic effects, resemble a traditional fluid with prominent sound wave activity.

In strongly magnetized plasmas ($\beta \ll 1$), where magnetic fields dominate collisionless dynamics along the field, incompressible MHD theory often provides an adequate description of the dynamics, even in low collisionality scenarios.

In summary, the complete set of ideal MHD equations can be succinctly expressed as follows:

$$\frac{\partial \rho}{\partial t} = -\nabla \cdot (\rho \boldsymbol{v}), \qquad \text{(Mass Continuity)} \tag{1.66}$$

$$\rho \frac{d\boldsymbol{v}}{dt} = -\nabla p - \nabla \frac{B^2}{2\mu_0} + \frac{1}{\mu_0} \boldsymbol{B} \cdot \nabla \boldsymbol{B}, \qquad \text{(Momentum)} \tag{1.67}$$

$$\frac{d}{dt}\left(\frac{p}{\rho^\gamma}\right) = 0, \qquad \text{(Energy)} \tag{1.68}$$

$$\frac{\partial \boldsymbol{B}}{\partial t} = (\boldsymbol{B} \cdot \nabla)\boldsymbol{v} - (\boldsymbol{v} \cdot \nabla)\boldsymbol{B}. \qquad \text{(Induction)} \tag{1.69}$$

In the momentum equation, the Lorentz force is separated into pressure and tension components using the relation $(\nabla \times \boldsymbol{B}) \times \boldsymbol{B} = -\nabla \frac{B^2}{2} + \boldsymbol{B} \cdot \nabla \boldsymbol{B}$. This separation highlights the magnetic influences through an isotropic pressure term and a field line tension part.

It is important to note that while the Lorentz force is inherently perpendicular to $\boldsymbol{B}$, both terms may still have components aligned with $\boldsymbol{B}$. This occurs because the parallel component of the tension term cancels out the parallel component of the magnetic pressure term. Additionally, we utilize the substitution $\nabla \times (\boldsymbol{v} \times \boldsymbol{B}) = (\boldsymbol{B} \cdot \nabla)\boldsymbol{v} - (\boldsymbol{v} \cdot \nabla)\boldsymbol{B}$. For further exploration and detailed derivations beyond this section, readers are referred to seminal texts such as Biskamp (2003); Chiuderi and Velli (2015).

1.2.5 MHD Waves

In this section, we delve into the propagation characteristics of fundamental MHD modes, which are crucial for understanding the dynamics of plasmas. The study of MHD waves is pivotal as they manifest the system's response to small perturbations, offering insights into how disturbances propagate through a plasma medium. Each wave type is characterized by a specific restoring force; in plasma environments, these forces are primarily derived from magnetic fields and thermal pressure. The different combinations of these restoring forces give rise to a diverse array of wave phenomena. Moreover, the nonlinear coupling of these modes can initiate a cascade of energy, transferring disturbances from larger to smaller scales. This energy cascade is essential for the redistribution of energy within the plasma, influencing both local and global plasma behaviors and playing a critical role in the overall stability and evolution of plasma systems.

We begin our analysis by linearizing the governing ideal MHD equations around a stationary, uniform background state. We introduce small sinusoidal perturbations of the form $e^{i(\boldsymbol{k}\cdot\boldsymbol{x}-\omega t)}$, denoted by lowercase letters (e.g., $\delta\rho$, δp, $\delta\boldsymbol{v}$, $\delta\boldsymbol{b}$). These perturbations are assumed to be significantly smaller than their respective unperturbed background values, indicated with a subscript zero. All nonlinearities are neglected in this linear approximation. The background magnetic field is assumed to be aligned along the z-direction, represented as $\boldsymbol{B_0} = B_0\hat{\boldsymbol{z}}$. In addition we assume that there is no large scale-flow, $V_0 = 0$. We replace spatial and temporal derivatives with wave number and frequency respectively:

$$\nabla \rightarrow i\boldsymbol{k}, \quad \frac{\partial}{\partial t} \rightarrow -i\omega, \tag{1.70}$$

The linearized MHD equations then take the form:

$$\omega\delta\rho = \rho_0 \boldsymbol{k}\cdot\delta\boldsymbol{v}, \tag{1.71}$$

$$\omega\delta p = c_s^2\rho_0 \boldsymbol{k}\cdot\delta\boldsymbol{v}, \tag{1.72}$$

$$\omega\delta\boldsymbol{v} = \boldsymbol{k}_\perp(\frac{\delta p}{\rho_0} + \frac{\boldsymbol{B}_0\cdot\delta\boldsymbol{b}}{2\mu_0\rho_0}) - \frac{\boldsymbol{B}_0\cdot\boldsymbol{k}}{\mu_0\rho_0}\delta\boldsymbol{b} \tag{1.73}$$

$$\omega\delta\boldsymbol{b} = \boldsymbol{B}_0(\boldsymbol{k}\cdot\delta\boldsymbol{v}) - (\boldsymbol{B}_0\cdot\boldsymbol{k})\delta\boldsymbol{v}, \tag{1.74}$$

here we have implicitly projected our equations along and transverse to $\boldsymbol{B}_0$, $\boldsymbol{k} = k_\perp\hat{\boldsymbol{e}}_\perp + k_{||}\hat{\boldsymbol{e}}_z$, $k_\perp = (k_x^2 + k_y^2)^{1/2}$. Solving these equations leads to the eigenvalue problem, formulated from the characteristic matrix $\boldsymbol{I}$:

$$\boldsymbol{I}\cdot\begin{pmatrix}\delta v_x\\ \delta v_y\\ \delta v_z\end{pmatrix} = 0, \tag{1.75}$$

where, $\boldsymbol{I}$ is defined as:

$$\boldsymbol{I} = \begin{pmatrix}\omega^2 - k_\parallel^2 V_a^2 & 0 & 0\\ 0 & \omega^2 - k_\perp^2 c_s^2 - k^2 V_a^2 & -k_\perp k_\parallel c_s^2\\ 0 & -k_\perp k_\parallel c_s^2 & \omega^2 - k_\parallel^2 c_s^2\end{pmatrix} \tag{1.76}$$

Existence of non-trivial solutions requires the determinant of the matrix in question to vanish. This condition yields the following dispersion relation:

$$\left[\omega^2 - k^2 V_a^2 cos^2\theta\right]\left[\omega^4 - \omega^2(c_s^2 + V_a^2)k^2 + k^4 c_s^2 V_a^2 cos^2\theta\right] = 0, \tag{1.77}$$

θ is the angle between the wave vector $\boldsymbol{k}$ and the magnetic field $\boldsymbol{B}_0$.

By analyzing the number of equations containing time derivatives, we deduce that the system typically exhibits seven modes. The entropy mode, a trivial solution, is characterized by

$$\omega = 0, \quad \delta\rho \neq 0, \quad \delta\boldsymbol{v} = (0, 0, 0). \tag{1.78}$$

Since $\omega = 0$, the phase speed $u = \omega/k$ also vanishes, indicating that the entropy mode does not propagate and remains stationary within the plasma. Contact discontinuities, for example, can be viewed as nonlinear manifestations of the entropy mode in MHD.

In considering the limit $c_s \to \infty$ within the incompressible framework, the term enclosed in parentheses on the left-hand side of Equation 1.2.5 must vanish. This leads to the derivation of the following dispersion relation:

$$\omega^2 = k^2 v_A^2 \cos^2\theta$$

for the so-called Alfvén (1942) waves. To determine the eigenvectors associated with these eigenvalues, we revisit our system of linearized equations. The equations of motion and induction are decomposed into their respective components:

$$\rho\frac{\partial\delta v_x}{\partial t} = -\frac{\partial\delta p}{\partial x} + \frac{B_0}{4\pi}\left(\frac{\partial\delta b_x}{\partial z} - \frac{\partial\delta b_z}{\partial x}\right), \tag{1.79}$$

$$\frac{\partial\delta v_z}{\partial t} = -\frac{\partial\delta p}{\partial z}, \tag{1.80}$$

$$\frac{\partial\delta v_y}{\partial t} = \frac{B_0}{4\pi}\frac{\partial\delta b_y}{\partial z}, \tag{1.81}$$

$$\frac{\partial\delta b_x}{\partial t} = B_0\frac{\partial\delta v_x}{\partial z}, \tag{1.82}$$

$$\frac{\partial\delta b_z}{\partial t} = -B_0\frac{\partial\delta v_x}{\partial x}, \tag{1.83}$$

$$\frac{\partial\delta b_y}{\partial t} = B_0\frac{\partial\delta v_y}{\partial z}, \tag{1.84}$$

highlighting that the y components of velocity and magnetic field are decoupled from the other components. It is thus possible to set $\delta v_x = \delta v_z = \delta b_x = \delta b_z = \delta p = \delta\rho = 0$ and still achieve a nontrivial solution for δv_y and δb_y. By combining the equations involving the y components, we derive the following equation:

$$\left(\frac{\partial^2}{\partial t^2} - v_A^2\frac{\partial^2}{\partial z^2}\right)(\delta b_y, \delta v_y) = 0, \tag{1.85}$$

This equation signifies the presence of an incompressible transverse wave mode that propagates along $\boldsymbol{B}_0$ at the Alfvén speed. The oscillations occur perpendicular to both the magnetic field and the direction of wave propagation, with the magnetic tension acting as the restoring force. Consequently, we can express:

$$\delta\boldsymbol{v}\cdot\boldsymbol{k} = 0, \quad \delta\boldsymbol{v}\cdot\boldsymbol{B}_0 = 0, \quad \delta\boldsymbol{v} = (0, \delta v_y, 0), \quad \frac{\delta b_y}{B_0} = \pm\frac{\delta v_y}{v_A}. \tag{1.86}$$

The latter relationship indicates an equipartition between kinetic and magnetic energy densities:

$$\frac{\delta b_y^2}{8\pi} = \frac{1}{2}\rho\delta v_y^2, \tag{1.87}$$

Returning now to the rest of the solutions, we utilize the phase speed to reformulate the term in the brackets on the left-hand side of Equation 1.2.5:

$$u^4 - u^2(c_s^2 + v_A^2) + c_s^2 v_A^2 \cos^2\theta = 0. \tag{1.88}$$

It is convenient to introduce the normalized speed:

$$\tilde{u} = \frac{u}{\sqrt{c_s v_A}}, \tag{1.89}$$

which simplifies the quartic equation to:

$$\tilde{u}^4 - \left(\frac{c_s}{v_A} + \frac{v_A}{c_s}\right)\tilde{u}^2 + \cos^2\theta = 0. \tag{1.90}$$

The resulting dispersion relation for these solutions is:

$$u^2 = \left(\frac{\omega}{k}\right)^2 = \frac{1}{2}(c_s^2 + v_A^2)\left[1 \pm \left(1 - 4\frac{\cos^2\theta}{b^2}\right)^{1/2}\right], \tag{1.91}$$

where $b = \frac{c_s}{v_A} + \frac{v_A}{c_s} \geq 2$.

These solutions characterize magnetosonic waves, which bear similarities to sound waves. They may be considered a natural extension of classical sound waves in a magnetized medium. In the absence of a magnetic field, they revert to isotropic sound waves. Unlike regular sound waves, however, the phase speed of magnetosonic waves depends on v_A, c_s, and θ, rendering them anisotropic due to the angular dependence of the phase velocity.

The mode associated with the branch of the solution with the positive sign is termed the *fast magnetosonic wave*, or more simply, the fast wave, while the second mode is known as the *slow magnetosonic wave*, or the slow wave. Substituting these solutions into Eq. 1.2.5, it follows that $\delta u_y = 0$, implying that the eigenvectors for these waves are $(\delta u_x, 0, \delta u_z)$. Moreover, for these waves, $\delta\boldsymbol{v} \cdot \boldsymbol{k} \neq 0$ and $\delta\boldsymbol{v} \cdot \boldsymbol{B}_0 \neq 0$. Consequently, these waves are linked with non-zero perturbations in both density and pressure of the plasma and longitudinal, involving both vertical and parallel motion relative to the original

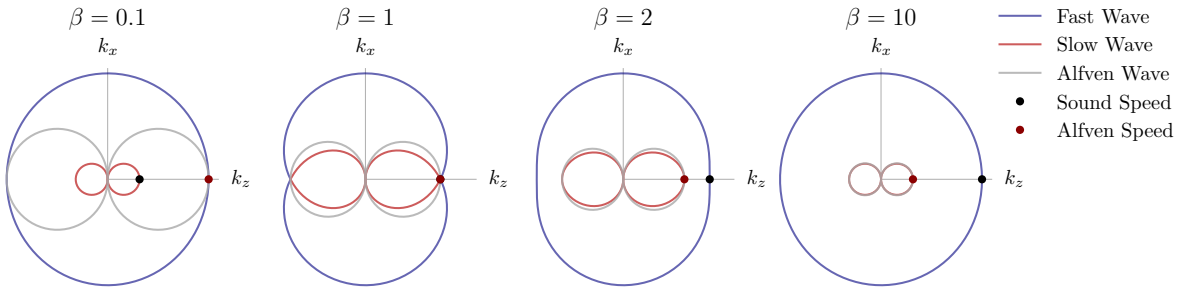

Figure 1.3: Friedrichs Diagrams, showing the phase speed plotted as a function of distance from the origin. These figures illustrate the relationship between the wave vector $\mathbf{k}$ and the magnetic field $\boldsymbol{B}_0$ by the angle with respect to the y-axis. In this representation, the parameter β is defined as $\beta = (c_s/v_A)^2$, where c_s is the sound speed, black dots, and v_A is the Alfvén speed, red dots.

magnetic field direction.

The difference between slow and fast waves can be better understood if we compare the signs of the perturbations in the gas pressure and the magnetic field. From the z component of the linearized momentum equation we have that perturbation in pressure is related to the speed of a magnetosonic wave as,

$$\omega \rho_0 v_z = kP \cos\theta. \tag{1.92}$$

It follows that the dispersion in the magnetic field is,

$$\delta\left(\frac{B_0^2}{8\pi}\right) = \frac{\boldsymbol{B}_0 \cdot \delta\boldsymbol{b}}{4\pi} = \frac{(\boldsymbol{k}\cdot\delta\boldsymbol{v})B^2 - (\boldsymbol{k}\cdot\boldsymbol{B}_0)(\boldsymbol{B}_0\cdot\delta\boldsymbol{v})}{4\pi\omega}. \tag{1.93}$$

Using the system of equation defined above we get:

$$\frac{\boldsymbol{B}_0\cdot\delta\boldsymbol{b}}{4\pi} = \rho V_a^2 - \frac{k^2 V_a^2 \cos^2\theta}{\omega^2}\delta p = \rho V_a^2\left(1 - \frac{k^2 C_s^2\cos^2\theta}{\omega^2}\right)\delta p. \tag{1.94}$$

Thus, we see that δp, $(\boldsymbol{B}_0\cdot\delta\boldsymbol{b}/4\pi)$, have the same sign if $v > c_s\cos\theta$, and opposite sign if $v < c_s\cos\theta$, where $v = \frac{\omega}{k}$ is the phase velocity. It can easily be shown that $v_f > c_s\cos\theta$ and $v_s < c_s\cos\theta$. So we conclude that in the fast magnetosonic wave the fluctuations of the thermal pressure of the gas and the magnetic pressure reinforce each

other. Whereas, in the slow magnetosonic wave, these fluctuations are opposed to each other, having opposite phases.

Finally, it is evident from Figure 1.2.5 that the behavior of the magnetosonic wave varies significantly depending on the plasma β regime and the wave vector $\boldsymbol{k}$ under consideration.

1.2.6 Incompressible MHD

In the preceding analysis, we have demonstrated that MHD facilitates the propagation of various modes, specifically shear Alfvén waves and compressible magnetosonic waves. For the remainder of this thesis, our primary focus will be on the Alfvén mode and its nonlinear generalizations. The dynamics of shear Alfvén waves are often analyzed within the framework of incompressible MHD theory (Biskamp, 2003).

To derive the incompressible MHD equations, we revisit the system of Equations 1.66 - 1.69. We enforce incompressibility in the system, as discussed in Section 1.1.1. Additionally, we introduce the total pressure, $\Pi = p + \frac{B^2}{2\mu_0}$, and disregard dissipative terms, based on the assumption that dissipation occurs predominantly at smaller spatial scales. Under these conditions, the ideal MHD equations simplify to:

$$\frac{\partial \boldsymbol{v}}{\partial t} = -\boldsymbol{v} \cdot \nabla \boldsymbol{v} - \frac{1}{\rho_0} \nabla \Pi + \frac{1}{\mu_0 \rho_0} \boldsymbol{B} \cdot \nabla \boldsymbol{B}, \tag{1.95}$$

$$\nabla \cdot \boldsymbol{v} = 0, \tag{1.96}$$

$$\frac{\partial \boldsymbol{B}}{\partial t} = (\boldsymbol{B} \cdot \nabla)\boldsymbol{v} - (\boldsymbol{v} \cdot \nabla)\boldsymbol{B}. \quad , \tag{1.97}$$

$$\nabla \cdot \boldsymbol{B} = 0. \tag{1.98}$$

It was Elssäser in 1950 who introduced a method to simplify these equations by defining the (Elsasser, 1950) variables

$$\boldsymbol{z}^{\pm} \equiv \boldsymbol{v} \pm \frac{1}{\sqrt{\mu_0 \rho_0}} \boldsymbol{B}, \tag{1.99}$$

which represent eigenfunctions of (Alfvén, 1942) waves propagating (anti)parallel to the background magnetic field ($\boldsymbol{B}_0$) at the Alfvén speed, $\boldsymbol{V}_a$. The governing equations for $\boldsymbol{z}^{\pm}$ are then:

$$\frac{\partial \boldsymbol{z}^{+}}{\partial t} = -\boldsymbol{z}^{-} \cdot \nabla \boldsymbol{z}^{+} - \frac{\nabla \Pi}{\rho_0}, \tag{1.100}$$

$$\frac{\partial \boldsymbol{z}^{-}}{\partial t} = -\boldsymbol{z}^{+} \cdot \nabla \boldsymbol{z}^{-} - \frac{\nabla \Pi}{\rho_0}, \tag{1.101}$$

$$\nabla \cdot \boldsymbol{z}^{\pm} = 0. \tag{1.102}$$

Note that the total pressure Π is related to the $\boldsymbol{z}^{\pm}$ fields by incompressibility through:

$$\nabla^2 \Pi = -\sum_{i,j=1}^{3} (\partial_i z_j^{-})(\partial_j z_i^{+}) \tag{1.103}$$

This formulation of the incompressible MHD equations is advantageous for its symmetric nature. This form of the governing equations allows to generalize insights from linear waves to nonlinear wavepacket behavior, which prominently appear in MHD turbulence theories.

1.2.7 Alfvénic Wavepackets & the Alfvén Effect

Nonlinearities, as illustrated by the first term on the right-hand side of Equation 1.100, arise solely from interactions between oscillation modes with opposing cross-helicity signs (i.e., between $\boldsymbol{z}^{+}$ and $\boldsymbol{z}^{-}$). This feature permits a *nonlinear* extension of the linear Alfvén waves described by Equation (1.100). To facilitate this analysis, we consider a scenario where even in the nonlinear regime, a uniform background field, constant in space and time and placed be along the z-direction, can be identified by averaging out the fluctuations.

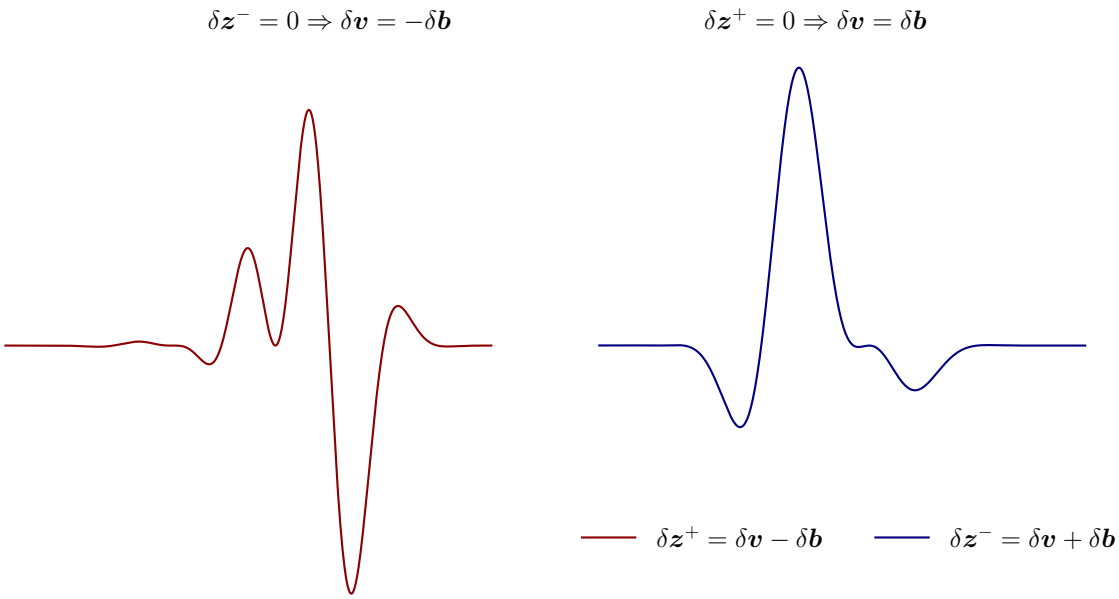

Figure 1.4: Arbitrary form wave packets propagating without distortion parallel and antiparallel to the local magnetic field $\boldsymbol{B}_0$, at the Alfvén speed, $\boldsymbol{V}_a$.

In addition we asume no fluid motions. We thus have:

$$\boldsymbol{B}_0 = B_0 \hat{\boldsymbol{z}}, \ \boldsymbol{v}_0 = 0 \tag{1.104}$$

Contrary to the linear analysis in Section 1.2.5, the fluctuations here are considered to be of arbitrary magnitude and perturbations in the Elsässer fields can be expressed as:

$$\boldsymbol{z}^{\pm} = \boldsymbol{z}_0^{\pm} \pm \delta \boldsymbol{z}_1^{\pm}, \tag{1.105}$$

where $\boldsymbol{z}_0^{\pm} = \pm v_A \hat{\boldsymbol{z}}$. The governing equations, in terms of the new variables, become

$$\delta \boldsymbol{z}_1^{\mp} \cdot \nabla \boldsymbol{z}_1^{\pm} \pm v_A \frac{\partial \delta \boldsymbol{z}_1^{\pm}}{\partial z} = \delta \boldsymbol{z}_1^{\mp} \cdot \nabla \delta \boldsymbol{z}_1^{\pm} - \frac{\nabla \Pi}{\rho_0}, \tag{1.106}$$

$$\nabla \cdot \boldsymbol{\delta z_1}^{\pm} = 0. \tag{1.107}$$

These nonlinear extensions of the Alfvén wave represent Alfvén wave packets of

arbitrary form propagating nondispersively (anti)parallel to $\boldsymbol{B}_0$, provided that the right-hand side (RHS) of the Equation 1.106 vanishes. As already discussed this happens when only unidirectional wave packets are present, for example, when $\delta \boldsymbol{z}_1^+ = 0$, indicating no spatial overlap between oppositely moving packets. In this case, the nonlinear cross-term $(\delta \boldsymbol{z}_1^+ \cdot \nabla)\delta \boldsymbol{z}_1^-$ vanishes and the equations simplify to:

$$\frac{\partial \delta \boldsymbol{z}_1^-}{\partial t} - v_A \frac{\partial \delta \boldsymbol{z}_1^-}{\partial z} = 0, \tag{1.108}$$

$$0 = \nabla \cdot \boldsymbol{\Pi}. \tag{1.109}$$

It is evident that if at a given time, $t = t'$, $\delta \boldsymbol{z}_1^\pm = 0$ and $\delta \boldsymbol{z}_1^\mp = \boldsymbol{f}(x, y, z)$ are present, the solution is given by $\delta \boldsymbol{z}_1^\mp = \boldsymbol{f}(x, y, z \mp v_A t)$ and $\delta \boldsymbol{z}_1^+ = 0$. The coupling of small-scale velocity and magnetic fluctuations by the large-scale background magnetic field, $\boldsymbol{B}_0$, underpins the *Alfvén effect*.

Conversely, inertial or energy-conserving interactions[2] between counterpropagating wave packets activate the nonlinear terms in Equation 1.106. This leads to the fragmentation of the wave packets and drives the energies E^+ and E^- toward smaller, perpendicular scales (Iroshnikov, 1963; Kraichnan, 1965). As the cascade reaches ion scales, energy is converted into heat through collisionless dissipation mechanisms.

We conclude this section by discussing two fundamental conservation laws relevant to ideal incompressible MHD.

Taking the inner product of the momentum equation with $\rho \boldsymbol{v}$ and combining it with the induction equation, after considering the inner product of the latter with $\boldsymbol{B}/\mu_0$, we can establish the conservation law for the total energy density, $\mathcal{E} = \frac{\rho_0 v^2}{2} + \frac{B^2}{2\mu_0}$. This is expressed through the following equation:

[2]In the absence of viscoresistive effects, collisions between two oppositely traveling wave packets are elastic; they do not result in an energy exchange. While their shape may become elongated along $\boldsymbol{B}_0$ due to shearing, the energy content of each packet remains constant.

$$\frac{\partial}{\partial t}\mathcal{E} + \nabla \cdot \left[\left(\frac{\rho_0 v^2}{2} + p \right) \boldsymbol{v} + \frac{1}{\mu_0} (\boldsymbol{B} \times (\boldsymbol{v} \times \boldsymbol{B})) \right] = 0. \tag{1.110}$$

The energy flux within this equation incorporates the advected energy flux, in addition to the Poynting flux, $\boldsymbol{E} \times \boldsymbol{B}/\mu_0$. This conservation law indicates that the total energy integrated over the plasma volume remains constant under ideal conditions.

Additionally, the conservation of cross-helicity, $\mathcal{H}$, represented by the volume integral $\mathcal{H} = \int \boldsymbol{v} \cdot \boldsymbol{B}\, d\boldsymbol{x}$, is considered. This quantity, conserved in ideal MHD, emerges by taking the dot product of the momentum equation with $\boldsymbol{B}$ and combining it with the dot product of the induction equation with $\boldsymbol{v}$. Combining the two equations, we get:

$$\frac{\partial(\boldsymbol{v} \cdot \boldsymbol{B})}{\partial t} + \nabla \cdot \left[(\boldsymbol{v} \cdot \boldsymbol{B})\boldsymbol{v} + \frac{B^2 \boldsymbol{v}}{2\mu_0} - \frac{(\boldsymbol{v} \cdot \boldsymbol{v})\boldsymbol{B}}{2} \right] = 0. \tag{1.111}$$

Overall, the total energy

$$\mathcal{E} = E^+ + E^- = \int \rho \left(\frac{|\boldsymbol{v}|^2 + |\boldsymbol{b}|^2}{2} \right) d^3x, \tag{1.112}$$

and cross-helicity

$$\mathcal{H} = E^+ - E^- = \int \rho \boldsymbol{v} \cdot \boldsymbol{b}\, d^3x, \tag{1.113}$$

expressed in terms of the energy associated with fluctuations in $\boldsymbol{z}^\pm$, $E^\pm = \langle |\delta \boldsymbol{z}^\pm|^2 \rangle / 4$, are ideal (i.e., with zero viscosity and resistivity) invariants of the incompressible MHD equations. The ratio of these two ideal invariants defines the normalized cross-helicity

$$\sigma_c = \frac{\mathcal{H}}{\mathcal{E}}. \tag{1.114}$$

When the energy fluxes, denoted as $\epsilon^\pm$, in wave packets traveling in opposite directions differ, indicated by $\epsilon^+/\epsilon^- \neq 1$, the MHD system is *imbalanced*, $\sigma_c \neq 0$. This condition is very typical in the solar wind, where outwardly propagating modes usually dominate over

inwardly propagating ones.

It is evident that, in contrast to the energies of magnetic and velocity fields, the energy associated with each Elsässer field undergoes a conservative cascade. For this reason, the Elsässer fields are regarded as the fundamental variables in MHD.

1.3 MHD Turbulence

Space and astrophysical plasmas are typically magnetized and turbulent, exhibiting fluctuations across a broad range of scales where the energy spectrum adheres to a power-law scaling. Understanding the dynamics of these astrophysical systems necessitates comprehending the long-term behavior of wavepacket interactions, particularly their role in facilitating turbulent energy cascades and subsequent energy dissipation at the smallest scales. The slope of the turbulent energy spectrum, which emerges from these interactions, provides valuable insights into the physical mechanisms driving the turbulent cascade.

In recent years, there has been a shift towards phenomenological models of MHD turbulence. These models incorporate various assumptions about the physical mechanisms underlying the turbulent cascade to provide inertial-range scaling predictions consistent with numerical simulations and solar wind observations.

This section introduces the basic principles underlying our theoretical understanding of Alfvénic MHD turbulence. We outline the fundamental ideas behind state-of-the-art models and review the scaling theories of MHD turbulence from a historical perspective.

1.3.1 Isotropic MHD Turbulence: The Iroshnikov-Kraichnan Model

IK introduced a phenomenological model based on the coupling of small-scale velocity and magnetic fluctuations by the large-scale background magnetic field, $\boldsymbol{B}_0$. Based on the observation that non-linearities only arise between counterpropagating wavepackets Kraichnan posited that their interactions are weakened since the mean field transports the two modes away from each other in the linear propagation (or collision) time,

$$\tau_{\mathcal{A}} = \frac{\lambda}{v_A}. \tag{1.115}$$

Whereas distortions to the $z^{\pm}$ fluctuations occur on the dynamical time it takes for a turbulent perturbation of size λ to break up nonlinearly,

$$\tau_\lambda = \frac{\lambda}{\delta z_\lambda} \tag{1.116}$$

The ratio of this two dynamical timescales defines the nonlinearity parameter, $\chi \equiv \tau_\mathcal{A}/\tau_\lambda$. Kraichnan argued that the non-linear interactions are weak such that $\chi \ll 1$, and that the resulting energy transfer rate at a given scale ϵ is limited by the linear time. This implies $\epsilon \propto \tau_l$.

In the limit of weak turbulence, $\chi \ll 1$, energy transfer to smaller scales occurs fractionally upon each collision, with weak nonlinear effects accumulating over timescales significantly longer than the wave period. As a result of a single collision, the change in amplitude is proportional to the interaction time, $\Delta\delta z_\lambda/\delta z_\lambda \sim \chi \ll 1$. Successive collisions are uncorrelated, limited to the duration of the interactions, and add up with random phases. Under the assumption that collisions accumulate in a manner akin to a standard random walk, we can estimate the number of collisions for the small perturbations to build up to order unity as $n_\lambda \sim (\delta z_\lambda/\Delta\delta z_\lambda)^2 \sim (\tau_\lambda/\tau_\mathcal{A})^2 \gg 1$. As a result the cascade time is given by:

$$\tau_c \sim n_\lambda \tau_\mathcal{A} \sim \frac{(\tau_\lambda)^2}{\tau_\mathcal{A}}. \tag{1.117}$$

We can understand that when compared to the hydrodynamic phenomenological model of K41, the spectral transfer in this framework is reduced by a factor of $\tau_\mathcal{A}/\tau_\lambda$ owing to the limited strength of the interaction exhibited by Alfvén waves. Therefore, we can estimate the spectral energy flux as

$$\epsilon \sim \frac{\delta z_\lambda^4 \, \tau_\mathcal{A}}{\lambda^2}. \tag{1.118}$$

Similar to the K41 phenomenology, we can obtain the Iroshnikov-Kraichnan (IK) spectrum through $\delta z_\lambda^2 \sim k\, E_k$ (where $k \sim \lambda^{-1}$),

$$E_k \sim (\epsilon\, v_A)^{1/2}\, k^{-3/2}. \tag{1.119}$$

1.3.2 Weak Anisotropic MHD Turbulence

While isotropy is normally justified in HD, a background magnetic field is usually present in most astrophysical and space plasmas. In fact the guide field need not be an external static field, but can also be the field in the large-scale energy-containing eddies. As opposed to mean velocity fields, $\boldsymbol{V}_0$, magnetic fields cannot be eliminated via Galilean transformations of the MHD equations resulting in strongly anisotropic turbulent dynamics (Montgomery and Turner, 1981) (see also reviews by Schekochihin et al., 2009a; Chen, 2016a, and references therein). In particular, conservation of energy and momentum during three wave resonant interactions

$$\begin{aligned} \boldsymbol{p} + \boldsymbol{q} &= \boldsymbol{k}, \\ \omega_p + \omega_q = \omega_k \quad &\Rightarrow \quad -p_\parallel + q_\parallel = k_\parallel \quad \Rightarrow \quad q_\parallel = k_\parallel, \quad p_\parallel = 0, \end{aligned}$$

more specifically, a wave - 2D perturbation interaction, (see, Montgomery and Matthaeus, 1995), allows power to cascade down to smaller scales perpendicular to $\boldsymbol{B}_0$, resulting in a two-dimensionalization of the turbulence spectrum in a plane transverse to the locally dominant magnetic field while at the same time inhibiting spectral energy transfer along the direction parallel to the field making the turbulence cascade anisotropic (Shebalin et al., 1983).

A multitude of observational and numerical studies have investigated the manifestations of anisotropy in the presence of an energetically significant mean magnetic field e.g., (Belcher and Davis Jr., 1971; Matthaeus et al., 1990; Bieber et al., 1996; Maron and Goldreich, 2001; Weygand et al., 2009; Beresnyak and Lazarian, 2010; Osman et al., 2012; Wicks et al., 2013a; Chandran and Perez, 2019; Pine et al., 2020; Bandyopadhyay and

McComas, 2021; Zank et al., 2022; Sioulas et al., 2022b; Chhiber, 2022; Dong et al., 2022). A comprehensive overview of the various forms of anisotropy can be found in (Horbury et al., 2012).

To derive the anisotropic version of the IK we would thus have to account for the fact that the cascade is inhibited parallel cascade along the $\boldsymbol{B}_0$. Other than that, the assumptions made in the Section 1.3.1 hold. More specifically, we consider a system that is excited at the scale l in a statistically steady and isotropic fashion such that $\delta z_l \ll v_A$ in the weak turbulence regime, $\chi \ll 1$, in the limit of balanced turbulence. Once again, collisions, are uncorellated, adding up with random phases, limited to the duration of the interactions and accumulate in a random-walk fashion. While the definition of the eddy turnover time, Eq. 1.116 holds, the absence of cascade along z, implies that *the Alfvén time is scale-independent* and should be redefined:

$$\tau_{\mathcal{A}} = \frac{l}{v_A}. \tag{1.120}$$

Since we are in the $\chi \ll 1$ regime, non-linear effects accumulate slowly and the deformation during a single collision is given by

$$\frac{\Delta \delta z_\lambda}{\delta z_\lambda} \sim \chi \ll 1. \tag{1.121}$$

Thus, following the same process described is Sec. 1.3.1, we can estimate, based on the equation for the energy flux

$$\delta z_\lambda \sim \left(\frac{\epsilon v_A}{l}\right)^{\frac{1}{4}} \lambda^{\frac{1}{2}} \tag{1.122}$$

which yields an inertial-range energy spectrum of

$$E_{k_\perp} \sim \left(\frac{\epsilon v_A}{l}\right)^{\frac{1}{2}} k_\perp^{-2}, \tag{1.123}$$

1.3.3 Strong MHD Turbulence: Critical Balance

An initial state of globally weak turbulence is often unstable, and the intrinsic anisotropy of the energy cascade inevitably develops smaller perpendicular scales that are strongly turbulent with nonlinear effects present at the leading order. More specifically, the number of collisions required for $\Delta\delta z_\lambda/\delta z_\lambda \sim 1$, decreases as the cascade proceeds to smaller scales

$$n_\lambda \sim \frac{\lambda}{l}\left(\frac{v_A}{\delta z_l}\right)^2. \tag{1.124}$$

This implies that the turbulent cascade progressively strengthens towards smaller scales. The weak turbulence cascade, while transferring energy to smaller scales, where τ_{nl} is shorter, saws the seeds of its own destruction. At sufficiently small scales the assumptions required for the weak turnulence regime to hold will no longer be satisfied. More specifically, at sufficiently small scales, $\chi \sim 1$, and only a small number of the order of $n_\lambda \sim 1$ collisions with another wave packet of comparable size will be required for a fractional change in wave amplitude $\Delta\delta z_\lambda \sim \delta z_\lambda$. This limits he spectral range in which the spectrum $E_{k_\perp} \sim k_\perp^{-2}$ applies. Such a transition was observed in balanced MHD shell-model simulations (Verdini and Grappin, 2012) and 3D incompressible MHD simulations (Meyrand et al., 2016).

The case of strong turbulence was addressed by (Higdon, 1984) and (Goldreich and Sridhar, 1995), hereafter GS95. GS95 expanded upon the idea that fluctuations in any two planes perpendicular to the mean field can remain correlated only if an Alfvén wave can propagate between them in less time than their perpendicular decorrelation time (see also, Maron and Goldreich, 2001; Schekochihin et al., 2009b). This leads to the implication that the dynamics of the inertial range in incompressible MHD turbulence are governed by wavevector modes in a "critical balance" (CB) state, i.e., characterized by a near-equal balance between the two dynamically important timescales, essentially achieving $\chi \sim 1$. Since the perturbation frequency ω has a lower bound due to an uncertainty relation $\omega\tau_c > 1$, the cascade is forced to remain in the $\chi \sim 1$ regime.

Under the assumption of negligible cross helicity, which suggests identical statistical properties for counterpropagating wavepackets, this implies that the parallel and perpendicular wavevectors follow the scaling law

$$k_{\parallel} \sim \frac{\epsilon^{1/3}}{v_A} k_{\perp}^{2/3} \sim k_{\perp}^{2/3}, \tag{1.125}$$

Defining an anisotropic energy spectrum $E(k_{\parallel}, k_{\perp})$, the fluctuation amplitude at a scale is given by

$$\delta z_{k_{\perp}}^2 \sim k_{\perp}^{-2/3} \sim k_{\parallel}^{-1} \sim \int_k^{\infty} E(k_{\parallel}, k_{\perp}) k_{\perp} \, dk_{\perp} \, dk_{\parallel} \tag{1.126}$$

for which one-dimensional power spectra for total energy scale can be shown to scale as

$$E(k_{||}) \propto k_{||}^{-2} \tag{1.127}$$

along the background magnetic field

$$E(k_{\perp}) \propto k_{\perp}^{-5/3} \tag{1.128}$$

across the background magnetic field.

At this point it is important to stress that the causality argument used to justify the long parallel coherence lengths hinges on the ability of Alfvenic perturbations to propagate along the magnetic field. However, anisotropy in turbulence represents a local property that relies on both the position and scale. The turbulent fluctuations at a given scale ℓ are greatly influenced by the local mean magnetic field of a size that ranges between $3 - 5\ell$ (Cho and Vishniac, 2000; Podesta, 2009; Gerick et al., 2017). More specifically, a wavepacket at perpendicular scale λ cannot distinguish between a larger wavepacket of size few times its scale, and the static background magentic field field $\boldsymbol{B}_0$. Thus, it will propagate along the local field, thereby $\boldsymbol{B}_{\ell}$ and so it is along the local field that the

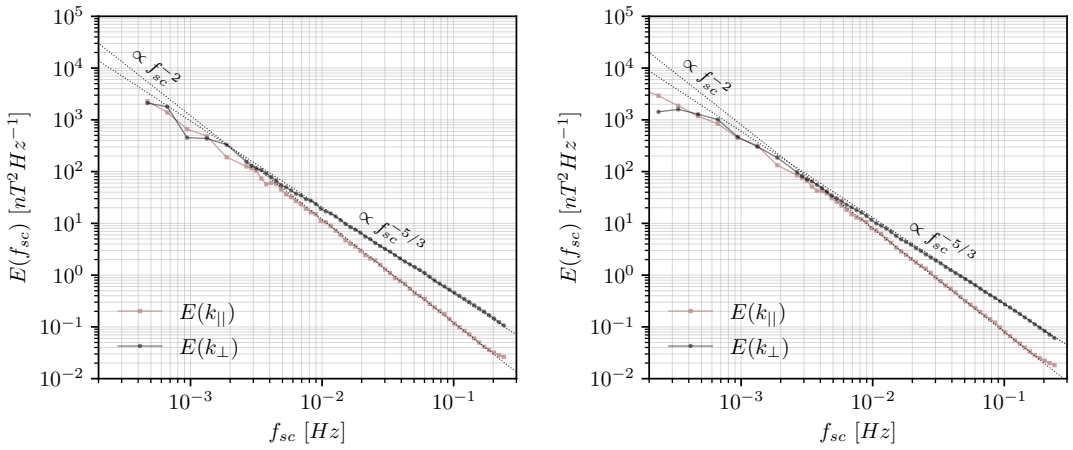

Figure 1.5: Power spectra for the perpendicular (black lines, $\theta_{VB} \geq 80°$) and parallel (red lines, $\theta_{VB} \leq 10°$) components of the magnetic field time series reproduced from (Horbury et al., 2008) shown in panel (a), and from (Wicks et al., 2010) shown in panel (b). In both cases, the inertial range scalings are in good agreement with the predictions of the CB model of balanced MHD turbulence. To estimate the anisotropic spectra a scale-dependent background magnetic field is first estimated, allowing estimate of the scale-dependent angle between the magnetic field and velocity timeseries to be calculated. Through conditional averaging, the wavelet spectra are then estimated in the two limiting cases.

arguments based on this propagation will apply. In assessing the dominant scale of the background magnetic field, two methodologies are predominantly employed, utilizing the global and local frames (Cho and Vishniac, 2000; Maron and Goldreich, 2001). For a detailed exploration of the consequences associated with defining the magnetic field either globally, thereby $\boldsymbol{B}_0$, or locally, denoted as $\boldsymbol{B}_\ell$, interested readers are encouraged to refer to (Chen et al., 2011; Matthaeus et al., 2012; Gerick et al., 2017).

The GS95 model is directly applicable to the Reduced MHD approximation (RMHD), where the background magnetic field $\boldsymbol{B}_0$ is significantly stronger than the fluctuating amplitudes (Kadomtsev and Pogutse, 1967; Strauss, 1976; Oughton et al., 2017). The latter are restricted to a plane orthogonal to $\boldsymbol{B}_0$. Despite $\delta\boldsymbol{b}_\perp \ll \boldsymbol{B}_0$, nonlinear effects are retained at the leading order. This is achieved by excluding all high-frequency fluctuations $\tau_a \leq \tau_{nl}$. Consequently, fluctuations within the RMHD approximation inherently satisfy the condition $\chi \geq 1$ (Oughton and Matthaeus, 2020). In this case, nonlinear interactions along the mean field may be completely neglected, allowing the nonlinear evolution to

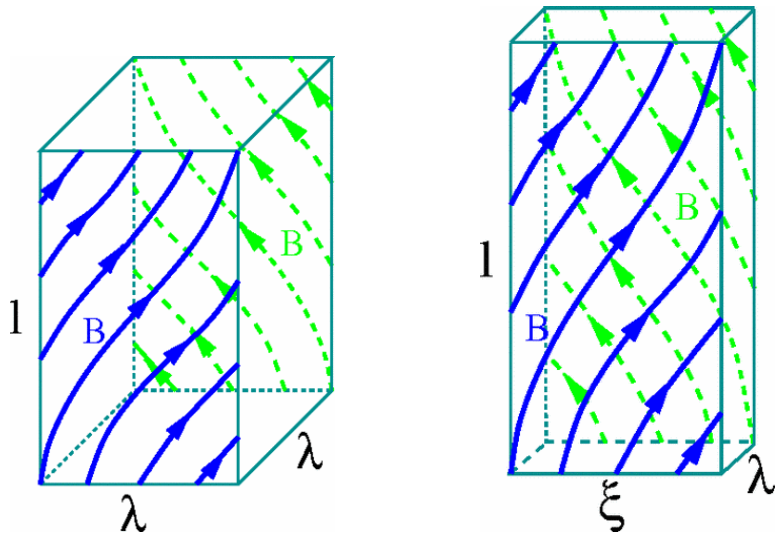

Figure 1.6: Eddies consistent with (left) the GS95, (right) 3D-anisotropic eddies consistent with the B06 model. In this case coherence lengths in the three physicaly important directions are characterized by $\ell_{||} \gg \xi \gg \lambda$, where, $\lambda/\xi \sim \sin\theta_{\perp}^{ub}$. Here, ξ represents the coherence length in the fluctuations direction, $\delta\boldsymbol{b}$. This figure is adapted from (Boldyrev, 2006) [reprinted with permission from (Boldyrev, 2006), copyright (2006) by the American Physical Society

adhere to the 2D incompressible MHD equations in planes orthogonal to $\boldsymbol{B}_0$[3].

1.3.4 Strong MHD Turbulence: Scale Dependent Dynamic Alignment

While the core principle of the GS95 model, namely CB, was shown to be consistent with numerical simulations of homogeneous, (in)compressible MHD turbulence, the inertial range scaling perpendicular to $\boldsymbol{B}_\ell$ was observed to be closer to -3/2 (Maron and Goldreich, 2001; Müller et al., 2003; Müller and Grappin, 2005)[4]. Additionally, numerical simulations revealed a tendency for magnetic and velocity fluctuations in the field-perpendicular plane to align with each other within a small, scale-dependent angle (Beresnyak and Lazarian, 2006a).

To reconcile the noted discrepancy, (Boldyrev, 2005, 2006), henceforth B06, proposed

[3]Note, however, that the RMHD approximation encompasses essential elements of the physics of three-dimensional incompressible MHD (Dmitruk et al., 2005; Oughton et al., 2017)

[4]Recent higher resolution simulations further support this finding (Perez et al., 2012; Verdini and Grappin, 2015; Mallet et al., 2016; Dong et al., 2022; Shi et al., 2023a)

a phenomenological model linking the emergence of local imbalance (Dobrowolny et al., 1980; Matthaeus et al., 2008a) with the scale-dependent dynamic alignment (SDDA) in the polarizations of $\delta\boldsymbol{b}_\perp$ and $\delta\boldsymbol{v}_\perp$, towards smaller scales, $\theta_\perp^{ub} \sim \delta b/v_A \propto \lambda^{1/4}$. Drawing on geometrical considerations, B06 suggests that the observed increase in alignment at smaller scales is linked to both a depletion of nonlinearities and simultaneous development of local anisotropy in the plane perpendicular to $\boldsymbol{B}_\ell$. In this framework turbulent eddies are identified as 3D-anisotropic structures, characterized by $\ell_{||} \gg \xi \gg \lambda$, where, $\lambda/\xi \sim \sin\theta_\perp^{ub}$. Here, ξ represents the coherence length in the direction of $\delta\boldsymbol{b}$. B06 predicts three distinct scaling laws in the inertial range: $E(k_\xi) \propto k_\xi^{-5/3}$, $E(k_\lambda) \propto k_\lambda^{-3/2}$, and $E(k_{\ell_{||}}) \propto k_{\ell_{||}}^{-2}$.

A substantial body of numerical studies on homogeneous MHD turbulence has provided evidence supporting the scale-dependence of certain alignment measures across a sizable portion of the inertial range (Mason et al., 2006; Perez et al., 2012, 2014; Mallet et al., 2015; Chandran et al., 2015; Cerri et al., 2022). However, concerns have been raised suggesting that the observed alignment may be a finite-range effect intrinsically linked to dynamics occurring at the outer scale (Beresnyak, 2012). For instance, Beresnyak (2012) interpret these signatures based on the idea that MHD turbulence is much less local in k-space compared to hydrodynamic turbulence (see, e.g., Beresnyak, 2011; Schekochihin, 2022). Consequently, the driving mechanism does not fully replicate the properties of the inertial range, and the transition to asymptotic statistics is broad, causing many quantities to appear scale-dependent as they adjust to the asymptotic regime. Moreover, the B06 model has faced criticism for violating the rescaling symmetry of the RMHD equations (Beresnyak, 2012). As a result, an ongoing debate persists regarding whether this numerical evidence accurately reflects the scale-dependent dynamic alignment angle in the asymptotic state of the inertial range (Beresnyak, 2012; Perez et al., 2014).

1.3.5 Intermittency

The fundamental building blocks of turbulence are fluctuations or eddies, which undergo a cascade process, successively splitting into smaller structures. This cascade facilitates

the transfer of energy from large, outer scales to smaller scales until it is ultimately dissipated as heat at the smallest scales. A critical question is how the fluctuating energy is distributed among these spatial scales within this turbulent cascade.

The phenomenological models discussed thus far are anisotropic but retain elements of an idealized Richardson cascade, implicitly assuming that the number of eddies created at each stage of the cascade is sufficient to fill the system's volume uniformly. In a self-similar system, the statistical properties of turbulent fluctuations are invariant across different scales within the inertial range. However, this idealized view of self-similarity does not fully capture the complexities observed in real-world turbulent flows. For example, it is impossible to obtain a true power law distribution for the energy spectra over all scales, as the total energy

$$\mathcal{E} = \int_0^\infty Ck^{-\alpha}\, dk = Ck^{1-\alpha}\Big|_0^\infty \tag{1.129}$$

must necessarily diverge at small k for $\alpha > 1$ and large k for $\alpha < 1$ (Frisch, 1995).

Early studies of (M)HD turbulence revealed that probability density functions (PDFs) of fluctuations tend to display increasingly non-Gaussian behavior at progressively smaller scales (Batchelor et al., 1949; Burlaga, 1991; Sorriso-Valvo et al., 1999). Moreover, the spatial inhomogeneity of energy dissipation is expected to alter the scaling exponents of field increments with respect to length scales ℓ. While the fundamental approach to studying intermittency involves examining the PDFs of the dissipation rate, based on Kolmogorov's refined similarity hypothesis (KRSH) (Kolmogorov, 1962), local averages of dissipation rate are related to the scale-dependent increments of the velocity field. Thus, intermittency is reflected in the PDFs of field increments, showing an increasing divergence from a Gaussian distribution (i.e., PDFs display fatter tails) as smaller scales are involved (Castaing et al., 1990; Frisch, 1995). This behavior, often referred to as multifractal, violates the concept of global scale invariance, a key assumption of the K41 theory.

For increment scale ℓ, the highr-order moments of the field fluctuations are expected

to display a power-law dependence, $S_\psi^q(\ell) \propto \ell^{\zeta(q)}$. Thus, after the moments are calculated, power-law fits may be applied on the curves over different ranges of spatial scales to obtain the scaling exponents ζ_q of the structure functions. Based upon the assumptions that the statistical properties of the turbulent fields are locally homogeneous and isotropic, i.e., the energy dissipation rate within the inertial range is constant on average, both the K41 theory (Kolmogorov, 1941) in hydrodynamics, as well as, the Iroshnikov-Kraichnan (Iroshnikov, 1963) model for MHD turbulence predict a linear scaling of $\zeta(q)$ with order q in the fully developed regime, where $\zeta_q = q/3$, and $\zeta_q = q/4$ respectively.

However, as denoted by Landau (Oboukhov, 1962; Kolmogorov, 1962), irregularity of energy dissipation is expected to alter the scaling exponents of field increments with ℓ. More specifically, in the case where ϵ statistically depends on scale due to the mechanism that transfers energy from larger to smaller eddies, ϵ should be replaced by ϵ_ℓ and Equation 2.0.8 should be recast to

$$S_\psi^q \sim \langle \epsilon_\ell^{q/3} \rangle \ell^{q/3}. \tag{1.130}$$

Expressing $\epsilon_\ell^{q/3}$ via a scaling relation with ℓ we obtain

$$\langle \epsilon_\ell^{q/3} \rangle \sim \ell^{\tau_q/3} \tag{1.131}$$

and thus

$$S_\psi^q \sim \ell^{\zeta(q)}, \tag{1.132}$$

where, $\zeta(q) = q/3 + \tau_q/3$ is generally a nonlinear function of q. Thus, when the scaling exponents ζ_q of the structure functions are considered, the different local subsets of fractal dimension within a turbulent field are reflected on the departures from the linear scaling. This departure implies a process characterized by "multifractal" statistics and intermittency, i.e., the concentration of the energy into smaller volumes of space at smaller scales (Frisch, 1995).

Another way understand intermittency, is to model the turbulent cascade as an effort

of the system to approach thermal equilibrium (Matthaeus et al., 2015). At shorter time scales, local turbulent relaxation may occur, giving rise to local correlations in MHD. The borders of such regions will typically not be relaxed but rather remain in a dynamic state, leading to local nonlinear interactions and processes such as magnetic reconnection or various types of instabilities. These boundaries correspond to coherent structures (CSs) , which in the case of the solar wind, could be either of coronal origin being passively advected by the SW (Borovsky, 2021), or generated locally as an intrinsic feature of the ongoing nonlinear turbulent relaxation process (Matthaeus and Montgomery, 1980; Veltri, 1999; Greco et al., 2010; Matthaeus and Velli, 2011; Matthaeus et al., 2015; Chandran et al., 2015; Howes, 2015). Intermittency is associated with a fractally distributed population of small-scale CSs, superposed on a background of random fluctuations (Isliker et al., 2019; Chhiber et al., 2020b; Sioulas et al., 2020a). Even though CS represent a minor fraction of the entire dataset (Osman et al., 2012; Sioulas et al., 2022), CSs account for a disproportionate amount of magnetic energy dissipation, and have been shown to strongly influence the heating and acceleration of charged particles (Karimabadi et al., 2013; Osman et al., 2012; Tessein et al., 2013a; Bandyopadhyay et al., 2020; Qudsi et al., 2020; Lemoine, 2021; Sioulas et al., 2022c).

Over the past few decades several authors have put forward theoretical arguments to account for the intermittency effect (Gurland and Tripathi, 1971a; Frisch et al., 1978; She and Leveque, 1994; Grauer et al., 1994; Politano and Pouquet, 1995; Ruzmaikin et al., 1995; Horbury and Balogh, 1997a; Müller and Biskamp, 2000; Boldyrev, 2002).

1.3.6 SDDA as an Intermittency Effect

The theory of SDDA has been advanced by Chandran et al. (2015, hereafter, CSM15), refining it in a manner that aligns SDDA with the rescaling symmetry of RMHD. In their interpretation, alignment emerges as an intermittency effect, resulting from the mutual shearing of Elsässer fields during the imbalanced collisions ($\delta z^{\pm} \gg \delta z^{\mp}$) of counterpropagating wave packets. In formulating the model, they proposed two archetypal

types of alfvénic interactions: imbalanced ($\delta \boldsymbol{z}^{\pm} \gg \delta \boldsymbol{z}^{\mp}$) and balanced ($\delta \boldsymbol{z}^{\pm} \sim \delta \boldsymbol{z}^{\mp}$). The first involves occasional "balanced" interactions, $\delta \boldsymbol{z}^{-} \approx \delta \boldsymbol{z}^{+}$, where the amplitude of the wavepackets is reduced by a factor of $0 \leq \beta \leq 1$, yet their length scale remains unchanged. Consequently, the amplitude of a fluctuation at scale λ resulting from such balanced collisions can be expressed as follows:

$$\delta \boldsymbol{z}_{\lambda}^{\pm} = \delta \bar{z} \beta^{q}. \tag{1.133}$$

Here, $\delta \bar{z}$ is the initial fluctuation amplitude at the injection scale L, and q is the number of balanced collisions expected as the fluctuation evolves from scale L to λ. The value of q is presumed to follow a Poisson distribution:

$$P(q) = \frac{e^{-\mu} \mu^{q}}{q!}, \tag{1.134}$$

where μ is the scale-dependent mean value of q. The "typical" fluctuation amplitude that best characterizes the bulk of the volume is

$$\delta \boldsymbol{z}_{\lambda}^{*} = \delta \bar{z}. \tag{1.135}$$

On the contrary, for "imbalanced", $\delta \boldsymbol{z}^{\pm} \gg \delta \boldsymbol{z}^{\mp}$, collisions, the amplitudes of the fluctuations remain constant while the mutual shearing of the interacting wave packets leads to the rapid cascading of the subdominant field to smaller scales. This occurs as it rotates into alignment with the dominant field, notably without distorting their amplitudes. As a result, the sub-dominant field is sheared into alignment and its perpendicular scale λ reduces.

Assuming that the most intense coherent structures in MHD turbulence –specifically, those with $q = 0$– are 3D anisotropic current sheets with a volume filling factor $f_{cs} \propto \lambda$, this leads to a straightforward relation for the scaling exponents:

$$\zeta^{CSM15}(n) = 1 - \beta^n. \tag{1.136}$$

Consequently, at any given scale, wave packets subjected to fewer balanced collisions are characterized by larger amplitudes, resembling three-dimensional anisotropic current sheet structures (see also Howes, 2015; Mallet and Schekochihin, 2017). With the incorporation of SDDA, the nonlinear timescale is defined as $\tau_{nl}^{\pm} \sim \lambda/(\delta z^{\mp} \sin\theta^z)$, wherein θ^z denotes the angle between the fluctuations of the Elsässer variables in the plane perpendicular to the magnetic field, $\delta z_{\perp}^{\pm}$. By focusing solely on the scenario of zero cross helicity, CSM15 deduce a value for $\beta \approx 0.691$. This implies that $\zeta_n \to 1$ as $n \to \infty$.

(Mallet and Schekochihin, 2017) (hereafter, MS17) formulated a statistical model of RMHD turbulence grounded in three principal concepts: critical balance, dynamic alignment, and intermittency. To substantiate their model, they put forth four conjectures based on physical reasoning: (a) the fluctuation amplitudes adhere to an anisotropic log-Poisson distribution (Chandran et al., 2015; Zhdankin et al., 2016); (b) the structures at small scales are 3D anisotropic with a sheet-like morphology (Boldyrev, 2006; Howes, 2015); (c) the scale-independence of the critical balance parameter, inclusive of dynamic alignment, within the inertial range (Mallet et al., 2015); (d) a consistent energy flux across parallel scales in the inertial range (Beresnyak, 2015). The model offers predictions for scaling in the perpendicular, parallel, and fluctuation directions:

For the perpendicular direction:

$$\zeta_{\lambda}^{MS17}(n) = 1 - \beta^n, \tag{1.137}$$

for the parallel direction:

$$\zeta_{\ell_{||}}^{MS17}(n) = 2(1 - \beta^n), \tag{1.138}$$

and for the fluctuation direction:

$$\zeta_{\xi}^{MS17}(n) = \frac{n(1-\beta^n)}{n/2+1-\beta^n}, \tag{1.139}$$

where $\beta = 1/\sqrt{2}$. A more practical discussion of the model is presented in (Schekochihin, 2022).

1.4 Solar Wind: In-situ Observations.

The Sun, through nuclear fusion in its core, extending up to approximately 0.3 solar radii ($R_\odot \sim 7 \times 10^5$ km), converts hydrogen into helium at temperatures around 15 million Kelvin. Surrounding the core, the radiation zone spans from 0.3 to 0.7 $R_\odot$, beyond which lies the convection zone. Here, convection occurs when the temperature gradient surpasses the adiabatic gradient, which measures how temperature decreases in an adiabatically expanding material. The tachocline, a thin layer about 0.05 $R_\odot$ thick at the interface between the radiation and convection zones, plays a crucial role in magnetic field generation and the Sun's differential rotation.

The photosphere, the Sun's visible surface about 150-200 km thick, maintains a temperature of approximately 5,800 K. The solar atmosphere consists of the chromosphere, the transition region, and the corona. The chromosphere heats up to around 20,000 K, whereas the transition region sees temperatures escalating rapidly from 2×10^4 K to 10^6 K over just 30 km. The corona, observable during total solar eclipses, reaches temperatures of millions of degrees, significantly hotter than the underlying photosphere. The magnetic field, driven by convective motions within the photosphere, is essential in this heating process. The debate on the *coronal heating* problem focuses on the specific mechanisms that transfer, store, and dissipate this energy to the corona. The corona itself, lacking a defined boundary, gradually transitions into interplanetary space as the solar wind.

Table 1.1: Characteristic length scales in the solar wind at 1 AU.

Scale	Length	Definition
L	1 AU	Characteristic size of the system
$\lambda_{\mathrm{mfp,p}}$	1 AU	Proton collisional mean free path
d_p	100 km	Proton inertial length
ρ_p	80 km	Proton gyro-radius
λ_e	10 m	Electron Debye length

Parker (1958) theorized that the lack of hydrostatic equilibrium in the solar corona, due to its high thermal pressure, could drive the solar plasma to expand hydrodynamically into space at hypersonic velocities. Solar magnetic field lines, embedded in the moving

plasma, would also extend outward, a phenomenon described as a "frozen-in" magnetic field. This results in the magnetic field being twisted into spiral shapes in the ecliptic plane, forming what is known as the Parker spiral. The Parker spiral angle, $\phi_{r,B}$, which is the angle of inclination of the magnetic field lines relative to the radial direction from the Sun, is described by the equation:

$$\tan(\phi_{r,B}) = \frac{B_\phi}{B_r} = -\frac{\Omega \sin(\theta)(R_{\text{eff}} - R)}{U_r},$$

where B_ϕ and B_r are the azimuthal and radial components of the magnetic field, respectively, Ω is the angular velocity of the Sun, θ is the colatitude, R_{eff} is the effective co-rotation radius (typically 10–20 solar radii) (Bruno and Carbone, 2013), and U_r is the radial velocity of the solar wind. At a distance of 1 AU, the Parker spiral angle $\phi_{r,B}$ is approximately 45°. Further exploration of the mechanisms behind solar wind generation can be found in Chapter 5 of (Russell et al., 2016).

Initially met with skepticism, Parker's theory gained acceptance following *in situ* observations from Mariner II (Neugebauer and Snyder, 1966), which provided direct evidence of a steady stream of ionized particles from the Sun, confirming Parker's predictions.

It is now well-established that low-frequency Alfvénic motions in the lower solar corona possess sufficient energy to initiate and sustain the solar wind, a weakly collisional, supersonically expanding stream of charged particles that carries photospheric magnetic field lines into interplanetary space, forming a magnetized sphere of hot plasma known as the heliosphere.

Solar wind properties in the inner heliosphere vary due to the diversity of solar coronal sources, affecting plasma density, velocity, and temperature. This variability is influenced by the phase of the solar cycle, large-scale gradients, proximity to the heliospheric current sheet (HCS), and large-scale velocity shear in the solar wind (Bruno and Carbone, 2013, and references therein).

The data collected by the Helios mission, spanning from the solar minimum in 1976

to the solar maximum in the early 1980s, provided crucial insights into the distinct characteristics of solar wind streams. These streams are significantly differentiated by their outflow speeds, manifesting as fast and slow solar wind streams. Slow wind streams are characterized by lower proton temperatures and higher densities and exhibit more variable properties compared to their faster counterparts (Marsch and Tu, 1990a). Due to these pronounced differences, a classification system for solar wind was established in previous decades, categorizing it into three distinct types (see e.g., McComas et al., 1998). These categories are:

- **Fast wind** (500-800 km s^{-1}) - characterized by low-density and originating from open field lines in coronal holes.
- **Slow wind** (300-500 km s^{-1}) - more variable and higher density, emanating from open streamers, loops, and active regions.
- **Transient structures** - encompassing eruptive events such as coronal mass ejections (CMEs) during solar maximum.

Recently, the traditional dichotomy between fast and slow solar winds has come under scrutiny. This reevaluation is driven by the increased detection of Alfvénic slow solar wind streams, which exhibit many characteristics commonly associated with fast winds, particularly in regions closer to the Sun (D'Amicis and Bruno, 2015; D'Amicis et al., 2021).

This leads to non-WKB (Wentzel-Kramers-Brillouin) reflections due to linear couplings with large-scale inhomogeneities, providing necessary sunward components for activating the non-linear term in Equation 1.100 and inducing a turbulent cscade of the fluctuating energy (Velli et al., 1989; Iroshnikov, 1963; Kraichnan, 1965).

Turbulence is increasingly recognized as a significant contributor to the non-adiabatic expansion and acceleration of the solar wind (Matthaeus and Velli, 2011). In-situ observations suggest that the ion temperature, T_p, and electron temperature, T_e, of the solar wind decrease as functions of radial distance, $T_p \sim r^{-\gamma_p}$ and $T_e \sim r^{-\gamma_e}$, with

indices $0.5 \lesssim \gamma_p \lesssim 1$ and $0.3 \lesssim \gamma_e \lesssim 0.7$ respectively, indicating a slower decay than predicted by spherical symmetric adiabatic expansion models (Richardson et al., 1995; Stansby et al., 2018; Maksimovic et al., 2005; Boldyrev et al., 2020).

TO summarize, though only a small fraction $\sim 5 \times 10^{-5}$ of the Sun's overall energy output occurs via coupling to magnetized plasma, the latter interaction is responsible for the very existence of the Heliosphere and all the dynamic high-energy manifestations occurring therein, including interactions with the Earth and planetary magnetospheres. Traditionally, the coupling of magnetic fields in the solar atmosphere (photosphere through corona), solar wind, and solar wind – magnetosphere interactions have been studied independently, depending on the type of observational data available. The multi-spacecraft exploration of the interacting Sun - Earth system has reached new frontiers, with measurements reaching into the inner heliosphere and corona with Parker Solar Probe (PSP) and Solar Orbiter (SO)

1.4.0.1 Reduced Spectra & Taylor's Hypothesis

Before proceeding with a review of recent literature and discussing some of the statistical properties of MHD turbulence in the solar wind, it is important to address the framework through which we interpret spacecraft measurements.

In the study of turbulent flows, the ideal experimental setup would capture snapshots of flow properties in three dimensions at each instant in time. However, practical limitations often preclude this, due to constraints in experimental capabilities. The spatial resolution of measurements is limited by the number of sensors and their distribution across the observed region. Although several missions, such as Cluster, Themis, and MMS, have provided multi-point measurements (Escoubet et al., 2001; Angelopoulos, 2008; Burch et al., 2016), the in-situ solar wind observations considered in this work are restricted to single-point measurements.

Given that the spacecraft data analyzed in this study consist of temporal measurements in a reference frame that is in relative motion with respect to the turbulent plasma, certain

assumptions are necessary to interpret the temporal variations of measured quantities in terms of their corresponding spatial and temporal variations in the plasma frame.

An appropriate method is required to relate the frequency of waves in the plasma rest frame (ω_p) to the observed frequency measured onboard the spacecraft (ω_{sc}) and to translate this information into spatial information about waves and turbulence. This is typically achieved by employing Taylor's hypothesis (Taylor, 1938), thereby TH. In essence, Taylor's hypothesis, or the "frozen-in-flow" hypothesis, asserts that the timescale over which the characteristics of the studied modes change is much longer than the duration it takes for the spacecraft to traverse them, implying that they remain static in the reference frame moving with the large-scale flow, $\boldsymbol{v}_{sw}$. For instance, if the value of a field measured by the spacecraft at time t is $\boldsymbol{\psi}_{\rm sc}(t)$ and $\boldsymbol{\psi}_{sw}(\boldsymbol{r})$ denotes the value of the field in the solar-wind frame, assumed to be static, then:

$$\boldsymbol{\psi}_{\rm sc}(t) = \boldsymbol{\psi}_{sw}(\boldsymbol{r}_0 - \boldsymbol{v}_{sw}t). \tag{1.140}$$

In this context, the spectrum of modes measured by a spacecraft moving with velocity $\boldsymbol{V}_{sc}$ consists of a set of Doppler-shifted fluctuations. The equation relating ω_{sc} to ω_p is given by:

$$\omega_{\rm sc} = \omega_p + \boldsymbol{k} \cdot (\boldsymbol{v}_{sw} + \boldsymbol{v}_{\boldsymbol{sc}}), \tag{1.141}$$

where the phase speed of the waves is given by $\boldsymbol{v}_{ph} = \omega/k$, with $\boldsymbol{k}$ as the wavevector. Assuming that $v_{sc} \ll v_{sw}$, which is typical for measurements at 1 AU, we obtain:

$$\omega_{\rm sc} = \omega_p + k v_{sw} \cos\theta_k, \tag{1.142}$$

where the second term accounts for the frequency arising from the advection of a spatial fluctuation with wavevector $\boldsymbol{k}$ past the spacecraft. This indicates that the validity of TH depends on both the phase speed and the propagation angle of the modes with respect to the solar wind flow, and holds when $\cos\theta_k$, $|\omega_p| \ll |k v_{sw} \cos\theta_k|$ (Matthaeus

and Goldstein, 1982).

By considering typical plasma parameters at 1 AU, an order of magnitude analysis reveals that the solar wind speed v_{sw} is significantly greater than the thermal or Alfvén speed - given that the dominant fluctuations are non-compressive with traits akin to large-amplitude Alfvén waves. Therfore, the solar wind flow is both Alfvénic ($M_a = V_{\rm R}/V_a \gg 1$), typically $M_a \approx 10$. Considering that typical spacecraft speeds satisfy $v_{sc} \ll v_{sw}$, TH is, in principle, valid for low-frequency, MHD fluctuations.

For this reason, temporal scales may be converted to spatial scales through

$$\ell = -v_{sw}\tau, \tag{1.143}$$

where τ is the temporal lag.

However, at high frequencies, the solar wind exhibits fast/magnetosonic fluctuations, often appearing in the 0.1-10.0 Hz range near 1 AU. Their phase speeds can be comparable to or a significant fraction of the solar wind speed, $|\omega| \gtrsim |\boldsymbol{k} \cdot \boldsymbol{v}_{sw}|$. In such cases, the wave phase speed becomes prominent, and TH may be violated.

Therefore, the auto-correlation tensors we defined in Section 1.1.1 are only determined along a single direction defined by the flow past the spacecraft. A full Fourier decomposition is impossible, and instead, only reduced spectra can be measured (Matthaeus and Goldstein, 1982). If r_1 is the direction of flow past the spacecraft, only $R_{mn}(r_1, 0, 0)$ can be calculated. In this case we can estimate the reduced power spectral tensor as:

$$\tilde{E}^{(r)}_{mn}(k_1) = \int dr_1 R_{mn}(r_1, 0, 0) \exp(-ik_1 r_1). \tag{1.144}$$

Due to the inherent ambiguity associated with spatiotemporal evolution captured through single point measurements, the energy observed at the spacecraft frequency f_{sc} encompasses spectral components from various wave numbers:

$$\tilde{E}^{(r)}_{mn}(f_{sc}) = \iiint d^3\boldsymbol{k}, \tilde{E}_{mn}(\boldsymbol{k})\delta(2\pi f_{sc} - \boldsymbol{k}\cdot\boldsymbol{v}_{sw}) \tag{1.145}$$

(Fredricks and Coroniti, 1976). For a uniform flow and assuming a two-dimensionally anisotropic wave vector, we can estimate the power-spectrum as:

$$\tilde{E}^{(r)}_{mn}(f_{sc}) = \int d^3k\, \tilde{E}_{mn}(\boldsymbol{k})\delta(2\pi f_{sc} - k_{\parallel} v_{sw}\cos\theta_{Bv} - k_{\perp} v_{sw}\sin\theta_{Bv}). \tag{1.146}$$

Using this decomposition it is possible to obtain the field perpendicular and field parallel spectra in the limits where the angle between the mean magnetic field direction and the flow direction is $\theta_{Bv} \to 90°$, and, $\theta_{Bv} \sim 0°$, respectively (Horbury et al., 2008).

1.4.0.2 Taylor's Hypothesis: What happens closer to the Sun?

In contrast to 1 AU measurements, the validity of TH is threatened closer to the Sun. This is because as PSP approaches the Alfvén surface, where $M_a \sim 1$, the solar wind speed decreases becoming comparable, or even dropping bellow the alfvén speed, $v_{sw} v_a$. In this case the conventional version of Taylor's hypothesis does not in general apply. In recent years several modifications to TH have been proposed to quantify and account for these effects (Howes et al., 2014; Klein et al., 2014; Klein et al., 2015; Bourouaine and Perez, 2019; Perez et al., 2021; Zank et al., 2022)

In the following we provide a vulgarized version of the analysis presented in (Klein et al., 2015) who derived a modified version of TH that applies to outwardly propagating non-compressive modes satisfying the conditions pertaining to alfvén waves, Section 1.2.5. The dynamics of these non-compressibe fluctuations can be studied in the framework of the (Heinemann and Olbert, 1980) equations

$$\frac{\partial \boldsymbol{\xi}^{\pm}}{\partial t} + (\boldsymbol{v}_{sw} \pm \boldsymbol{v}_A) \cdot \nabla \boldsymbol{\xi}^{\pm} - \left(\frac{\boldsymbol{v}_{sw} \pm \boldsymbol{v}_A}{2v_A} \right) \frac{dv_A}{dr} \boldsymbol{\xi}^{\mp} = -(\boldsymbol{z}^{\mp} \cdot \nabla \boldsymbol{\xi}^{\pm})_{nc}, \tag{1.147}$$

where,

$$(\boldsymbol{z}^{\mp} \cdot \nabla \boldsymbol{\xi}^{\pm})_{nc} = \boldsymbol{z}^{\mp} \cdot \nabla \boldsymbol{\xi}^{\pm} - \left(\frac{1 \pm \eta^{1/2}}{\eta^{1/4}} \right) \frac{\nabla p_{\rm tot}}{\rho_0}.$$

Here, the subscript "nc" denotes "non-compressive modes, and,

$$\boldsymbol{\xi}^{+} = \left(\frac{1 + \eta^{1/2}}{\eta^{1/4}} \right) \boldsymbol{z}^{+}, \quad \boldsymbol{\xi}^{-} = \left(\frac{1 - \eta^{1/2}}{\eta^{1/4}} \right) \boldsymbol{z}^{-}, \tag{1.148}$$

are the Heinemann-Olbert variables,

$$\eta \equiv \frac{\rho_0}{\rho_a} = \frac{v_A^2}{v_{sw}^2}, \tag{1.149}$$

with ρ_a the reference density, and v_{sw} the flow velocity.

Focusing on strongly imbalanced intervals, $z^+ \gg z^-$, which is usually the norm close to Sun, implies that $\xi^- \ll \xi^+$, and in addition that ξ^-/ξ^+ is much smaller than z^-/z^+. Therefore, we can write $(1/u_a)du_a/dr \sim r^{-1}$. It follows

$$|(\boldsymbol{v_{sw}} + \boldsymbol{v_A}) \cdot \nabla \boldsymbol{\xi}^{+}| \gg |(\boldsymbol{v_{sw}} + \boldsymbol{v_A})/(2u_a)(du_a/dr)\boldsymbol{\xi}^{-}|,$$

and, Equation 1.147 may be written as

$$\frac{\partial \boldsymbol{\xi}^{+}}{\partial t} + (\boldsymbol{v_{sw}} + \boldsymbol{v_A}) \cdot \nabla \boldsymbol{\xi}^{+} = -(\boldsymbol{z}^{-} \cdot \nabla \boldsymbol{\xi}^{+})_{nc}.$$

To account for the motion of the spacecraft, we now apply a reference frame transformation from an inertial frame centered on the sun to the spacecraft reference frame with position $r' = r - \int v_{sc} dt$ and time $t' = t$. We can rewrite the previous equation as

$$\frac{\partial \boldsymbol{\xi}^+}{\partial t'} + \boldsymbol{U_{tot}} \cdot \nabla' \boldsymbol{\xi}^+ = -(\boldsymbol{z}^- \cdot \nabla' \boldsymbol{\xi}^+)_{nc},$$

where, $\boldsymbol{U_{tot}} = \boldsymbol{v_{sw}} + \boldsymbol{v_A} - \boldsymbol{v_{sc}}$.

We now seek to find the conditions under which nonlinear term can be negated. The $\boldsymbol{z}^- \cdot \nabla' \boldsymbol{\xi}^+$, $(\boldsymbol{v_{sw}} + \boldsymbol{v_A}) \cdot \nabla' \boldsymbol{\xi}^+$ terms account for variations of $\boldsymbol{\xi}^+$ orthogonal and parallel to $\boldsymbol{B}_0$, respectively. Therefore, the condition

$$|(\boldsymbol{v_{sw}} + \boldsymbol{v_A}) \cdot \nabla' \boldsymbol{\xi}^+| \gg |\boldsymbol{z}^- \cdot \nabla' \boldsymbol{\xi}^+|,$$

is not always satisfied despite, $v_{sw} + v_A \gg z^-$. This is because the perpendicular gradients in $\boldsymbol{\xi}^+$ could be larger than the longitudinal ones. On the other hand, the spacecraft velocity $\boldsymbol{v_{sc}}$ has a nonzero perpendicular component $\boldsymbol{v}_{sc,\perp} \equiv \boldsymbol{v_{sc}} - (\hat{b} \cdot \boldsymbol{v_{sc}})\hat{b}$, that becomes increasingly important as PSP approaches the perihelion of it's orbit. As a result, the term $\boldsymbol{v_{sc}} \cdot \nabla' \boldsymbol{\xi}^+$ greatly exceeds $\boldsymbol{z}^- \cdot \nabla' \boldsymbol{\xi}^+$ in magnitude when $v_{sc,\perp}$ satisfies:

$$v_{sc,\perp} \gg z^-.$$

This is the case at the perihelion of the orbit where the perpendicular component of the spacecraft velocity attains a very large value, $v_{sc,\perp} \approx 200$ km s^{-1}. In this case Equation 1.4.0.2 can be approximated to first order as:

$$\frac{\partial \boldsymbol{\xi}^+}{\partial t'} + U_{\text{total}} \cdot \nabla' \boldsymbol{\xi}^+ = 0,$$

where,

$$\boldsymbol{U}_{\text{total}} = \boldsymbol{v_{sw}} + \boldsymbol{v_A} - \boldsymbol{v_{sc}}.$$

This expression is equivalent to TH but modified to take into account the spacecraft

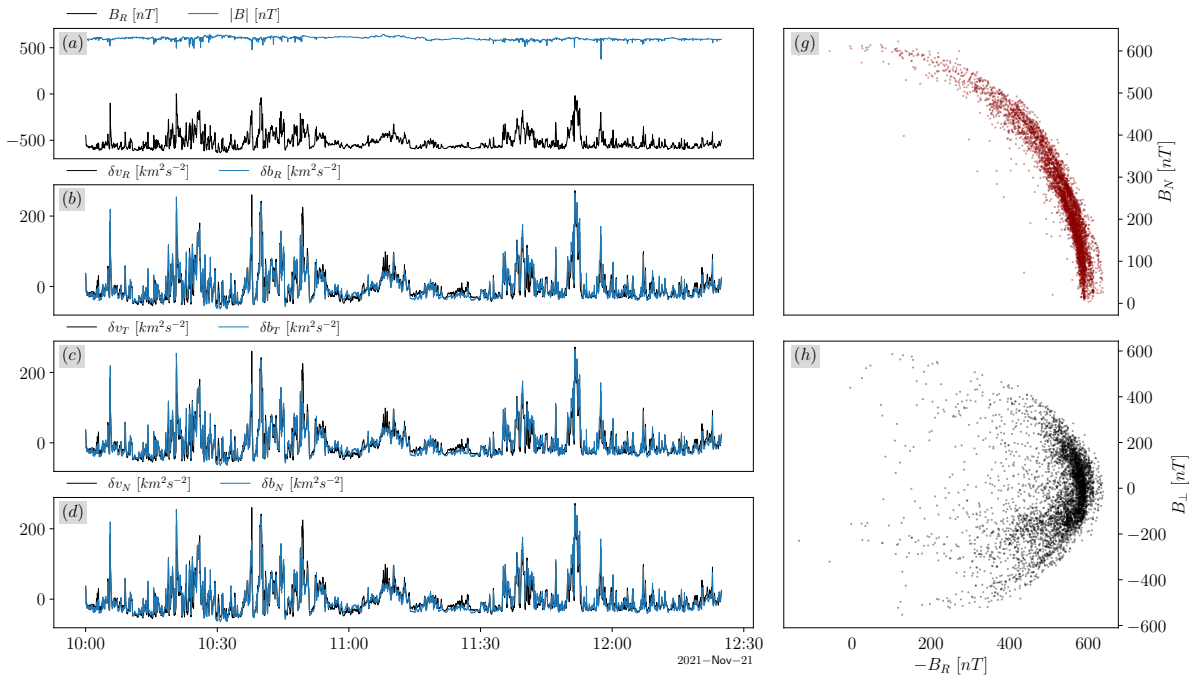

Figure 1.7: Near-Sun, $R \approx 13.4 R_\odot$, PSP measurements illustrating the highly alfvénic and spherically polarized nature of the fluctuations. While the fluctuations in the components are strong, with several switchbacks evident within the interval, the local magnetic field magnitude remains fairly constant. Left: scatterplot of the radial B_R and normal B_N magnetic field components in RTN. Right: radial B_R vs. orthogonal fluctuations $B_\perp$.

motion and mode propagation. This implies that that the frequency spectrum of ξ^+ in the spacecraft frame may be estimated as

$$\tilde{E}^{(\xi^+)}_{mn}(f_{sc}) = \iiint d^3\boldsymbol{k}, \tilde{E}^{\xi^+}_{mn}(\boldsymbol{k})\delta(2\pi f_{sc} - \boldsymbol{k}\cdot\boldsymbol{U}_{total}) \tag{1.150}$$

1.4.1 Transport of turbulent Fluctuations in the Expanding Solar Wind

Mechanisms that are not fully understood, possibly involving photospheric motions or magnetic reconnection, lead to a predominance of anti-sunward propagating waves, $\delta\boldsymbol{z}^+ \gg \delta\boldsymbol{z}^-$, a condition known as "imbalance." As the solar wind expands into the heliosphere, it carries a wide spectrum of magnetic field and plasma fluctuations (Coleman, 1968; Belcher and Davis Jr., 1971). These fluctuations encompass both incompressible and compressible motions, with the former contributing at least 90% of the total energy

(Klein et al., 2011). The study of the transport of these fluctuations in an inhomogeneous flow such as the solar wind is a necessary first step to understanding the more general question of the heating and acceleration of mechanically driven stellar winds (Velli et al., 1991; Velli, 1993).

In an expanding medium, the wave energy density $\mathcal{E} = \frac{1}{2}\rho\delta u^2$ is not a conserved quantity because wave pressure does work on the flow. Instead, in the absence of dissipation, the conserved quantity is the wave action, $\mathcal{S} = \mathcal{E}/\omega$, where $\mathcal{E}$ is the wave energy density and ω is the intrinsic wave frequency (i.e., in the plasma rest frame). The theory of wave action conservation (Witham, 1965; Bretherton and Garrett, 1968) is based on the WKB approximation. In this framework, the length scale over which the underlying medium is changing is much larger than the wavelength of the modes under study, allowing one to discard wave reflection due to coupling of the outgoing wave to the large-scale inhomogeneities. The following conservation law may then be derived:

$$\frac{\partial \mathcal{S}}{\partial t} + \nabla \cdot (v_g \mathcal{S}) = 0, \tag{1.151}$$

where $\boldsymbol{v_g}$ is the radial component of the group velocity. This conservation law can be generalized to include finite wavelength effects, thereby going beyond the WKB framework (Heinemann and Olbert, 1980; Grappin and Velli, 1996a).

The conservation of the flux $\mathcal{S}$ of the wave action across a spherical surface is given by:

$$u^2 \frac{(U + V_a)^2}{U V_a} = const. \tag{1.152}$$

For purely outwardly propagating, arbitrary amplitude Alfvénic structures, characterized by a constant magnetic field magnitude, the WKB (Wentzel-Kramers-Brillouin) approximation (Jacques, 1977) anticipates amplitude maxima at the Alfvén critical point. Beyond the Alfvén critical point, for $V_a < U$, where $U \sim U_0$ is nearly constant and $U_0 \gg V_a$, the amplitude exhibits a decay described by:

$$\delta u^2 \sim U/(\boldsymbol{v_{sw}} + \boldsymbol{v_A})^2 \propto R^{-3}, \tag{1.153}$$

implying that, since for an Alfvén wave the fluctuating magnetic field $\delta\boldsymbol{B}$ is related by $\delta\boldsymbol{B}/\sqrt{4\pi\rho} = \pm\boldsymbol{u}$, the wave energy decays as $u^2 \sim R^{-1}$.

Strong deviations from this prediction are indicative of other effects such as a nonlinear cascade (Bavassano et al., 1982). The conservation principle for wave action can be extended to the non-WKB limit, where the coupling between counter-propagating modes, influenced by background inhomogeneities, becomes significant. With these non-WKB effects considered, one can expect the turbulence amplitude to reach its absolute maximum within the Alfvén surface (Cranmer and van Ballegooijen, 2005; Verdini and Velli, 2007).

As Alfvén waves propagate through the heliosphere, the decreasing Alfvén speed results in the growth of normalized magnetic-field amplitudes to nonlinear magnitudes, $\delta B/B_0 \sim 1$. Unlike linearized Alfvén waves discussed in Section 1.2.5, these structures retain a parallel $\delta B_{||}$ component. Therefore these structures are not purely transverse to $\boldsymbol{B}_0$ but exhibit spherical polarization, meaning the magnetic field vector traces a sphere of constant radius $|\boldsymbol{B}_0 + \delta\boldsymbol{b}| = const.$ (Barnes and Hollweg, 1974; Bruno et al., 2001; Matteini et al., 2014).

As a result, in-situ near-Sun solar wind reveal that embedded within this turbulent spectrum of Alfvénic fluctuations is a population of radial-field reversals, or *switchbacks* whose amplitude is large enough for the magnetic field to bend backward on itself (Horbury et al., 2018; Bale et al., 2019; Tenerani et al., 2023). This results in a local reversal of the field's polarity and a corresponding jet in radial velocity (Matteini et al., 2014). Switchbacks display traits akin to spherically polarized, high-amplitude Alfvén waves. The origins of switchbacks remain a subject of ongoing discussion. There are generally three main theories: they may be produced and injected at coronal heights, for instance through interchange reconnection (Fisk and Kasper, 2020; Drake et al., 2021; Bale et al., 2021a); they could result from large-scale velocity shears, possibly due to coronal jets or the movement of magnetic footpoints across different source regions of fast and slow streams

(Landi et al., 2006); or they might form continuously in situ as a result of expansion and nonlinear processes.

Comprehending the dynamical evolution of fluctuations and switchbacks is crucial. This not only sheds light on the formation of switchbacks from the broader spectrum of turbulent fluctuations but also offers insight into their potential role in the turbulent cascade in the solar wind.

A first attempt in this direction was made in Tenerani et al. (2021). In this work, we investigated the radial evolution of switchbacks using data from PSP, Helios, and Ulysses. We demonstrated that large-scale Alfvénic fluctuations follow WKB decay, but the subset of switchbacks evolves as a separate population, with the radial component decaying as $\delta B_r^2 \sim R^{-4}$—faster than WKB decay—allowing them to maintain an approximately constant magnetic field magnitude. This result was interpreted as the saturation of amplitudes and could be due to coupling with compressible modes or dispersive waves that prevent relative amplitudes from becoming arbitrarily large. Furthermore, we found that the radial evolution of the occurrence rate of switchbacks in the solar wind is size-dependent, with larger switchbacks increasingly predominant at greater distances.

On the other hand, small-scale fluctuations were found to fall off with radial distance faster than predicted (see also Bavassano et al., 1982). In general, deviations from the WKB prediction indicate additional mechanisms that can accelerate or slow the dissipation of the waves, usually due to nonlinear coupling, instabilities (e.g., parametric decay instability) (Pruneti and Velli, 1997; Del Zanna et al., 2001; Réville et al., 2018; Chandran, 2018), and other effects, which can result in the preferential decay of certain components. For example, expansion preferentially reduces the radial magnetic field with respect to transverse components across all scales (Dong et al., 2014). This aspect is included in the Expanding Box Model (EBM) (Velli et al., 1992; Grappin et al., 1993; Grappin and Velli, 1996b), which describes a locally homogeneous plasma parcel advected by the expanding solar wind. Finally, it was shown by Matteini et al. (2024) that the tendency of magnetic field fluctuations in the solar wind to evolve towards a state of spherical polarization imposes constraints on the radial component's rms fluctuations,

leading to a decay described, particularly at large scales, by $b_r \sim \boldsymbol{b}/2B$ (see also Squire et al., 2020; Mallet et al., 2021).

1.4.2 The Solar Wind as a Testbed for Turbulence Theories

Linear couplings of the outgoing waves with the large-scale inhomogeneity result in non-WKB reflections (Velli et al., 1989), providing the sunward propagating component necessary for the activation of the non-linear term in Equation 1.100, leading to the emergence of a turbulent character (Iroshnikov, 1963; Kraichnan, 1965).

Alfvénic turbulence is widely regarded as the primary paradigm for explaining many observed properties of the solar wind (Matthaeus and Velli, 2011). Consequently, over the past few decades, the solar wind has served as a testbed (Coleman, 1968; Bavassano et al., 1982; Marsch and Tu, 1990b; Sorriso-Valvo et al., 1999; Mangeney, 2001a; Bruno et al., 2003; Salem et al., 2009; Horbury et al., 2008; Podesta, 2009; Chen et al., 2012, 2013; Verdini et al., 2018; Bowen et al., 2018a; Chen et al., 2020) for evaluating models of homogeneous incompressible magnetohydrodynamic turbulence (Goldreich and Sridhar, 1995; Lithwick et al., 2007; Chandran, 2005; Boldyrev, 2006; Chandran, 2008; Perez and Boldyrev, 2009a; Podesta and Bhattacharjee, 2010; Chandran et al., 2015; Mallet and Schekochihin, 2017; Schekochihin, 2022).

The magnetic spectrum of the solar wind, influenced by various physical processes across different scales, displays several segments each characterized by a power-law dependence over wavenumber, $E(\kappa) \propto \kappa^{-\gamma}$. At the largest scales, a spectral break delineates the inertial from the injection scales, typically showing a κ^{-1} dependence. This feature is prevalent in fast solar wind streams, shifting to larger scales with increasing heliocentric distance, though it is not always observed in the slow solar wind (Bruno and Carbone, 2013, and references therein).

At intermediate scales, non-linear interactions among counterpropagating wavepackets channel energy preferentially towards smaller scales perpendicular to $\boldsymbol{B}_0$. This range exhibits a steepening of the spectrum with indices, γ, varying between 3/2 to 5/3

(Bavassano et al., 1982; Marsch and Tu, 1990b; Matthaeus and Goldstein, 1982; Chen et al., 2020; Shi et al., 2021; Telloni et al., 2021). At ion scales, kinetic processes dominate, leading to further steepening of the spectrum and the conversion of turbulent energy into plasma heat through mechanisms such as ion cyclotron damping and kinetic Alfvén waves (Dmitruk et al., 2004; TenBarge and Howes, 2013; Karimabadi et al., 2013).

Over recent decades, our understanding of solar wind turbulence has significantly advanced, thanks to a combination of in-situ observations, theoretical developments, and numerical studies (see reviews by Matthaeus and Velli, 2011; Chen, 2016b; Bruno and Carbone, 2013; Schekochihin, 2022, and references therein). Despite this progress, several key questions remain unresolved. These include the overall decrease of the Alfvénic character of the fluctuations (Roberts et al., 1987; Chen et al., 2020; D'Amicis et al., 2019), the tendency of large-amplitude fluctuations to maintain a state of spherical polarization (Belcher and Davis Jr., 1971; Matteini et al., 2014), the origin and evolution of coherent structures in the inner heliosphere (Bruno et al., 2003; Borovsky, 2008; Greco et al., 2012a) and their impact on magnetic energy dissipation and plasma heating (Osman et al., 2012; Chasapis et al., 2015), the differential evolution in the inertial range scalings of magnetic field and velocity fluctuations (Shi et al., 2021), the large excess of energy observed in the magnetic field fluctuations over that in the velocity field fluctuations (Roberts et al., 1987; Grappin et al., 1991; Chen et al., 2013; D'Amicis and Bruno, 2015; Shi et al., 2021), often associated with anomalously steep magnetic field spectra (Bowen et al., 2018b), the role of compressible fluctuations in the turbulent cascade (Hnat et al., 2005), the inertial range anisotropic scalings of the fluctuations (Horbury et al., 2008; Wicks et al., 2010), the role of imbalance in the fluxes of counterpropagating wavepackets (Podesta and Borovsky, 2010; Wicks et al., 2011; Chen et al., 2013; Bowen et al., 2023) and their scale-dependent dynamic alignment (Podesta, 2009; Bowen et al., 2021), and finally the role of radial expansion and the breaking of the background magnetic field symmetry (Verdini et al., 2018, 2019).

The Parker Solar Probe (PSP; Fox et al., 2016) and Solar Orbiter (SolO; Müller et al., 2020) missions offer a unique opportunity to address these challenges by tracing the solar

wind from its early acceleration to its journey through the inner heliosphere (Velli et al., 2020a). Their complementary observations across various heliospheric distances hold the promise of providing new insights into solar wind dynamics, potentially shedding light on longstanding questions in solar and space physics.

Relation of MHD Turbulence Phenomenologies to Solar Wind Turbulence

The phenomenological MHD turbulence models discussed in Section 1.3 focus on the dynamics of small amplitude (toroidal) Alfvén modes, neglecting potential couplings with compressive fluctuations (e.g., Cho and Lazarian, 2003; Chandran, 2005; Chandran, 2018), within the context of globally *balanced*, homogeneous MHD turbulence. Therefore, while the higher-order scaling predictions offered by these models align reasonably well with numerical simulations of forced, homogeneous, and balanced reduced MHD turbulence (Chandran et al., 2015; Mallet et al., 2016; Palacios et al., 2022), their applicability to the solar wind is questionable. This uncertainty arises because solar wind turbulence is inhomogeneous, affected by spherical-expansion (Heinemann and Olbert, 1980; Velli et al., 1991), often characterized by non-vanishing cross helicity (D'Amicis et al., 2021) and includes a non-negligible fraction ($\sim 10\%$) of compressive and longitudinal fluctuations (Howes et al., 2012; Klein et al., 2012). To add to the above concerns, theoretical treatment of MHD turbulence is often performed in the limit of small-amplitude fluctuations. In contrast, solar wind turbulence typically displays a predominance in the flux of outwardly propagating fluctuations over inwardly directed ones (Roberts et al., 1987; D'Amicis et al., 2021). In addition, the predominant fluctuations in the solar wind are consistent with large amplitude ($\delta\boldsymbol{b} \sim \boldsymbol{B}_0$) Alfvén waves. These waves are not purely transverse to $\boldsymbol{B}_0$ but exhibit spherical polarization, meaning the magnetic field vector traces a sphere of constant radius $|\boldsymbol{B}_0 + \delta\boldsymbol{b}| = const.$ (Barnes and Hollweg, 1974; Bruno et al., 2001; Matteini et al., 2014). Recent Parker Solar Probe observations reveal that MHD turbulence in the vicinity of solar wind sources is permeated by abrupt radial-field reversals, or *switchbacks* that display traits akin to spherically polarized, high-amplitude Alfvén waves. The generation mechanism of switchbacks, whether from processes near the solar surface or in-situ during the expansion of the solar wind, remains under debate (Squire et al., 2020),

with latest observations indicating an absence of full magnetic reversals in sub-alfvénic, $v_{sw}/v_a \leq 1$, where v_{sw} the bulk solar wind speed, intervals (Akhavan-Tafti, unpublished). Furthermore, the dominance of this Alfvénic state diminishes as the heliocentric distance increases suggesting a potential connection between the dissipation of finite amplitude Alfvénic fluctuations and the acceleration and heating of the solar wind (Chen et al., 2020; Shi et al., 2021; Sioulas et al., 2022a; Dunn et al., 2023).

Finally, the dynamics of the solar wind are influenced not just by the mean field direction, but also by the radial axis along which the solar wind expands (Völk and Aplers, 1973). This aspect has been illuminated by numerical simulations using the Expanding Box Model (EBM) (Grappin et al., 1993; Grappin and Velli, 1996b), which demonstrate that expansion preferentially reduces the radial component of the magnetic field across all scales, confining fluctuations to a plane orthogonal to the radial direction (Dong et al., 2014). Given these considerations, the extent to which phenomenological models of homogeneous, Alfvénic turbulence can accurately capture the unique characteristics of the solar wind remains an active area of debate (Bowen et al., 2021). This aspect is further explored in Chapter5.

1.5 Research Objectives & Outline.

The thesis is comprised of three sections. The main scientific objectives of each section can be summarized as follows:

1. **Evolution of Alfvén Wave and Turbulence in the inner heliosphere.**

    - How do anisotropic signatures, like inertial range scalings and power-anisotropy, of MHD turbulence develop within the inner Heliosphere?
    - What are the physical mechanisms underlying the dynamic evolution?

2. **Dynamical evolution of coherent structures and their role on plasma heating.**

    - How do coherent magnetic structures, form and evolve in the solar wind?
    - How do the effects of expansion and spherical polarization affect their evolution as compared to homogeneous MHD ?
    - What is the contribution of coherent structures to magnetic energy dissipation and plasma heating?

3. **Higher-Order analysis of 3D anisotropic Alfvénic turbulence.**

    - How do predictions and conjectures of MHD turbulence models grounded in CB and SDDA principles fair against in-situ observations?
    - What are the effects of compressibility, intermittency, imbalance, and solar wind expansion on the 3D anisotropic statistical signatures of MHD turbulence?

CHAPTER 2

Analytical Tools, and Methods

2.0.1 Fourier Transform and Estimation of Power-Spectral Densities

The Fourier transform serves as a mathematical technique that breaks down a time-domain function (signal) into its individual frequency components. For a continuous-time signal $x(t)$, the Fourier transform $\tilde{X}(f)$ is expressed as:

$$\tilde{X}(f) = \int_{-\infty}^{\infty} x(t) e^{-j2\pi ft}\, dt \tag{2.1}$$

This integral transforms the time-domain signal $x(t)$ into the frequency-domain representation $\tilde{X}(f)$, where f denotes the frequency.

In practical scenarios, signals are often discrete rather than continuous. When a signal is discretized, we use the Discrete Fourier Transform (DFT) to analyze its frequency content. If we sample a continuous signal $x(t)$ at regular intervals Δt, we obtain a discrete signal $x[n] = x(n\Delta t)$. The DFT of this discrete signal is given by:

$$[k] = \sum_{n=0}^{N-1} x[n] e^{-j2\pi kn/N} \tag{2.2}$$

where N is the total number of samples, and k ranges from 0 to $N-1$. The DFT is not merely an approximation but a precise computation of the discrete signal's frequency content. However, the frequency resolution is limited by the sampling interval Δt and the total number of samples N. The frequency resolution is defined as:

$$\Delta f = \frac{1}{N\Delta t} \tag{2.3}$$

One significant consequence of discrete sampling is spectral leakage, which occurs when the signal contains frequencies that do not align with the DFT's frequency bins. This misalignment causes energy to spill into adjacent bins, leading to inaccurate frequency representation.

The Nyquist frequency is a critical concept in sampling theory. It is defined as half the sampling rate and represents the highest frequency that can be accurately sampled without aliasing. If the sampling rate is f_s, then the Nyquist frequency f_N is:

$$f_N = \frac{f_s}{2} \tag{2.4}$$

The computational expense of the DFT is another consideration. The direct computation of the DFT requires $O(N^2)$ operations, which can be computationally intensive for large N. However, the Fast Fourier Transform (FFT) algorithm significantly reduces this complexity to $O(N \log N)$, making it more practical for large datasets.

To estimate the Power-Spectral Density (PSD) of a signal, we leverage the total energy of the signal in real space. For a continuous signal $x(t)$, the total energy E is given by:

$$E = \int_{-\infty}^{\infty} |x(t)|^2 \, dt \tag{2.5}$$

Parseval's theorem states that the total energy of the signal in the time domain is equal to the total energy in the frequency domain:

$$\int_{-\infty}^{\infty} |x(t)|^2 \, dt = \int_{-\infty}^{\infty} |\tilde{X}(f)|^2 \, df \tag{2.6}$$

For discrete time series, Parseval's theorem can be expressed as:

$$\sum_{n=0}^{N-1} |x[n]|^2 = \frac{1}{N} \sum_{k=0}^{N-1} |\tilde{X}[k]|^2 \tag{2.7}$$

This relationship allows us to compute the PSD, which represents how the signal's

power is distributed across different frequencies.

The Wiener-Khinchin theorem connects the PSD to the autocorrelation function of the signal. The autocorrelation function $R_{xx}(\tau)$ of a signal $x(t)$ is defined as:

$$R_{xx}(\tau) = \int_{-\infty}^{\infty} x(t)x^*(t+\tau)\,dt \tag{2.8}$$

The theorem states that the Fourier transform of the autocorrelation function yields the PSD:

$$\tilde{R}_{xx}(f) = \tilde{S}_{xx}(f) \tag{2.9}$$

where $\tilde{S}_{xx}(f)$ is the PSD of $x(t)$.

2.0.2 Continous Wavelet Transform (CWT)

The Continuous Wavelet Transform (CWT) is a signal processing technique that offers a robust alternative to the Fourier Transform. Unlike the Fourier Transform, which decomposes a signal into infinite-duration sinusoidal components, the CWT employs wavelets—localized waveforms of finite energy and zero mean. This localization in both time and frequency allows the wavelet transform to capture both temporal and spectral information simultaneously, making it highly suitable for analyzing non-stationary signals where the frequency content varies over time.

A wavelet is characterized by its finite duration and complex structure, differentiating it from the infinite sinusoids used in Fourier analysis. The finite-energy property ensures that the wavelet has a bounded duration, while the zero-mean condition ensures that it oscillates around zero, providing both high and low-frequency information. This dual localization enables the wavelet to adapt to different scales, providing a multi-resolution analysis of the signal.

The process of wavelet transformation begins with the selection of a mother wavelet, denoted as ψ_0. The mother wavelet is a prototype function that generates daughter

wavelets through scaling and translation operations. A daughter wavelet, ψ, at scale s and position u, is obtained by stretching or compressing the mother wavelet, retaining its shape while adjusting its frequency and duration. Mathematically, this is expressed as:

$$\psi_{s,u}(t) = \frac{1}{\sqrt{s}}\psi_0\left(\frac{t-u}{s}\right) \tag{2.10}$$

Here, the factor $\frac{1}{\sqrt{s}}$ ensures that the energy of the wavelet remains constant across different scales, maintaining the same total energy as the mother wavelet. The parameter s controls the scale of the wavelet, determining whether it captures high-frequency, short-duration components (small s) or low-frequency, long-duration components (large s).

The Continuous Wavelet Transform of a signal $x(t)$ with respect to the mother wavelet ψ_0 is defined as:

$$W_x(s,u) = \int_{-\infty}^{\infty} x(t)\frac{1}{\sqrt{s}}\psi_0^*\left(\frac{t-u}{s}\right)dt \tag{2.11}$$

In this equation, ψ_0^* represents the complex conjugate of the mother wavelet. The CWT decomposes the signal $x(t)$ into wavelet coefficients $W_x(s,u)$, which provide a measure of the signal's similarity to the wavelet $\psi_{s,u}$ at different scales and positions.

Parseval's theorem for the wavelet transform states that the total energy of a signal $x(t)$ can be expressed in the wavelet domain as:

$$E = \int_{-\infty}^{\infty} |x(t)|^2 dt = \frac{2}{c_\psi}\int_0^{\infty}\int_{-\infty}^{\infty} |W_x^\psi(s,\tau)|^2 \frac{ds\,d\tau}{s^2} \tag{2.12}$$

where c_ψ is the admissibility constant, defined as:

$$c_\psi = \int_{-\infty}^{\infty} \frac{|\Psi_0(\omega)|^2}{\omega} d\omega \tag{2.13}$$

For the Morlet wavelet, $c_\psi \approx 0.776$. Hence, $|W_x^\psi(s,\tau)|^2$ represents the wavelet energy spectrum, indicating the relative contribution to the signal energy for a specific scale s

and time shift τ.

The conversion from scale to a Fourier pseudo-frequency for a Morlet wavelet is given by:

$$f = \frac{\omega_0 + \sqrt{\omega_0^2 + 2}}{4\pi s} \approx \frac{\omega_0}{2\pi s} \tag{2.14}$$

where ω_0 is the central frequency of the Morlet wavelet.

To estimate the Power Spectral Density (PSD) using the CWT, we utilize the wavelet coefficients $W_x(s, \tau)$. The PSD provides information about the distribution of power across different frequency components of the signal. The PSD at a specific pseudo-frequency f can be estimated using the following expression derived from Parseval's theorem:

$$E(f, \tau) = \frac{2T_s}{c_\psi f_0} \left| W_x^\psi(f, \tau) \right|^2 \tag{2.15}$$

where T_s is the sampling period, $f_0 = \omega_0/2\pi$, and $W_x^\psi(f, \tau)$ are the wavelet coefficients corresponding to the pseudo-frequency f.

2.0.3 Estimating Conditional Power Spectra

Anisotropy in turbulence represents a local property that relies on both the position and scale. The turbulent fluctuations at a given scale ℓ are greatly influenced by the local mean magnetic field of a size that ranges between $3 - 5 \cdot \ell$ (Gerick et al., 2017). To analyze anisotropy, wavelet analysis has proven to be a useful technique as it allows signal decomposition into components that are localized both in time and wavelet scale. Recently, the continuous wavelet transform (CWT) has been extensively utilized to estimate the power of magnetic field fluctuations as a function of the direction of the local mean magnetic field (Podesta, 2009; Wicks et al., 2010). For a discrete set of measurements such as the time series of the i-th component of the magnetic field B_i, where $i = R,\ T,\ N$ and resolution δt , the wavelet transform is defined as:

$$\omega_i(\ell,\ t_n) = \sum_{j=0}^{N-1} B_i(t_j)\psi^*(\frac{t_j - t_n}{\ell}), \tag{2.16}$$

where ψ^* denotes the conjugate of the Morlet mother wavelet, and $\psi(t) = \pi^{-1/4}[e^{i\omega_0 t} - e^{-\frac{\omega_0^2}{2}}]e^{-\frac{t^2}{2}}$. The parameter w_0, representing the frequency of the wavelet, is set equal to $w_0 = 6$. The transformation from the dilation scale, ℓ, to the physical spacecraft frequency, f_{sc}, is given by:

$$f_{sc} = \frac{w_0}{2\pi\ell\Delta t}, \tag{2.17}$$

where, Δt represents the time interval between successive measurements. The power spectral density of the i-th component as a function of spacecraft frequency f_{sc} and the local, scale-dependent field/flow angle θ_{BV} can be estimated as:

$$F_{ii}(f_{sc},\ \theta_{BV}) = \frac{2\delta t}{N}\sum_{n=0}^{N-1} |\omega_i(\ell, t_n, \theta_{BV})|^2, \tag{2.18}$$

Here, N is the number of samples within the range $\theta_{j-1} \leq \theta_{BV} \leq \theta_j$, $\theta_j = 5^\circ \cdot j$, j=0, 1, ..., 18. At time t_n and wavelet scale ℓ, we estimate the angle θ_{BV} using the scale-dependent local mean magnetic field $\boldsymbol{B}_\ell$ and velocity field $\boldsymbol{V}_\ell$, where $\boldsymbol{V}$ represents the solar wind velocity in the spacecraft frame (Duan et al., 2021; Cuesta et al., 2022). To calculate the scale-dependent local mean of a field, $\boldsymbol{q}$, we use a Gaussian weighting scheme centered at t_n:

$$\boldsymbol{q}_\ell(t_n, \ell) = \sum_{m=0}^{N-1} \boldsymbol{q}_m\ exp\left(-\frac{(t_n - t_m)^2}{2\lambda^2\ell^2}\right), \tag{2.19}$$

where λ is a dimensionless parameter that determines the scaling of the average. To ensure the robustness of our findings, we investigated two distinct values of λ, specifically $\lambda = 1$ and $\lambda = 3$. Remarkably, the results obtained for both cases were comparable, exhibiting differences in spectral exponents of only 0.01-0.02 (see also Gerick et al., 2017). The parameter θ_{BV} was determined using two distinct methods: the non-scale

dependent time-to-time velocity field value $\boldsymbol{V}(t)$ and the scale-dependent value, $\boldsymbol{V}_\ell$. Our results indicates that the outcomes obtained from both techniques are practically indistinguishable, which validates the minimal impact of interpolating $\boldsymbol{V}$ at the time points of $\boldsymbol{B}$ or only considering $\boldsymbol{V}(t)$ (see also Verdini et al., 2018; Wang et al., 2022). Throughout the remainder of the study, we utilize $\boldsymbol{B}_\ell$ and $\boldsymbol{V}_\ell$ to estimate the θ_{BV} parameter considering the case where $\lambda = 3$. For intervals that are sampled at heliocentric distances greater than 0.5 AU and have a significant lack of plasma data, defined as having more than 10% of solar wind velocity measurements missing, the angle θ_{BR} is used. This angle represents the angle between $\boldsymbol{B}_\ell$ and the scale-dependent radial component of the magnetic field, denoted as $B_{R\ell}$. To determine the reliability and consistency of using θ_{BR} instead of θ_{BV}, both angles were evaluated for intervals with adequate plasma data. Our findings suggest that the anisotropic spectra remained almost unchanged for the majority of intervals, even when sampled as close as 0.3 au. The subsequent analysis examines the trace of the power spectral density, denoted as $F = \sum F_{ii}$. The range of θ_{BV} is restricted to be between 0° and 90° based on the symmetry of θ_{BV} around 90° (Chen et al., 2011).

To transform the PSD derived in the spacecraft-frame frequency $F(f_{sc},\ \theta_{BV})$ into a wavenumber spectrum expressed in physical units $E(\kappa^*,\ \theta_{BV})$, we employ Taylor's frozen-in hypothesis (Taylor, 1938).

2.0.4 Estimating 2-point & 5-point increments

Assuming the validity of (Taylor, 1938) hypothesis the 2-point increments for a field $\boldsymbol{\phi}$ at a specific spatial lag, where $\boldsymbol{\ell} = \tau \cdot \boldsymbol{V}_{sw}$ and $\boldsymbol{V}_{sw}$ represents the solar wind speed, can be estimated as:

$$\delta\boldsymbol{\phi} = \boldsymbol{\phi}(\boldsymbol{r} + \boldsymbol{\ell}) - \boldsymbol{\phi}(\boldsymbol{r}). \tag{2.20}$$

However, in the context of estimating five-point increments, Equation 2.0.4 necessitates a redefinition of $\delta\boldsymbol{\phi}$ to:

$$\delta\boldsymbol{\phi} = [\boldsymbol{\phi}(\boldsymbol{r}-2\boldsymbol{\ell}) - 4\boldsymbol{\phi}(\boldsymbol{r}-\boldsymbol{\ell}) + 6\boldsymbol{\phi}(\boldsymbol{r}) - 4\boldsymbol{\phi}(\boldsymbol{r}+\boldsymbol{\ell}) + \boldsymbol{\phi}(\boldsymbol{r}+2\boldsymbol{\ell})]/\sqrt{35}. \tag{2.21}$$

Using the 5-point method, one can estimate the scale-dependent increments of the magnetic field—in velocity units—as $\delta\boldsymbol{b} = \delta\boldsymbol{B}/(\mu_0\rho(t))^{1/2}$, where $\rho(t) = 1.16 m_p n_p(t)$, μ_0 is the permeability of free space, and m_p and n_p represent the proton mass and number density, respectively. The factor 1.16 accounts for alpha particles, assuming $n_a/n_p = 0.04$ (Podesta et al., 2009).

Additionally, we can estimate the scale-dependent increments in the velocity field, denoted as $\delta\boldsymbol{v}$. The perpendicular components of the increments are defined by

$$\delta\boldsymbol{\phi}_\perp = \delta\boldsymbol{\phi} - (\delta\boldsymbol{\phi}\cdot\hat{\boldsymbol{z}})\cdot\hat{\boldsymbol{z}}, \tag{2.22}$$

where, $\hat{\boldsymbol{z}} = \boldsymbol{B}_{\boldsymbol{\ell}}/|\boldsymbol{B}_{\boldsymbol{\ell}}|$, is a unit vector in the direction of the localy-defined scale-dependent background magentic field estimated as

$$\boldsymbol{B}_\ell = [\boldsymbol{B}(\boldsymbol{r}-2\boldsymbol{\ell}) + 4\boldsymbol{B}(\boldsymbol{r}-\boldsymbol{\ell}) + 6\boldsymbol{B}(\boldsymbol{r}) + 4\boldsymbol{B}(\boldsymbol{r}+\boldsymbol{\ell}) + \boldsymbol{B}(\boldsymbol{r}+2\boldsymbol{\ell})]/16. \tag{2.23}$$

Additionally, we can calculate the perpendicular components of the increments in the outwardly and inwardly propagating modes as follows:

$$\delta\boldsymbol{z}_\perp^{o,i} = \delta\boldsymbol{v}_\perp \mp \mathrm{sign}(\langle B_R\rangle)\delta\boldsymbol{b}_\perp, \tag{2.24}$$

where $\langle B_R\rangle$ represents a 30-minute rolling average of B_R, the radial component of the

magnetic field in RTN coordinates (Franz and Harper, 2002). This rolling average assists in determining the polarity of the radial magnetic field (Shi et al., 2021).

2.0.5 Acounting for Imbalance

The total energy $E_t = E^+ + E^-$ and cross-helicity $H_c = E^+ - E^-$, expressed in terms of the energy associated with fluctuations in $\boldsymbol{z}^\pm$, $E^\pm = \langle|\delta\boldsymbol{z}^\pm|^2\rangle/4$, are ideal (i.e., with zero viscosity and resistivity) invariants of the incompressible MHD equations. Elsässer imbalance can be quantified by the normalized cross-helicity, $\sigma_c = E_t/H_c$, which measures the relative fluxes of counterpropagating wavepackets in the system. In the context of solar wind turbulence, Elsässer imbalance is assessed by examining the relative magnitudes of inwardly and outwardly propagating Alfvén waves (Velli et al., 1991; Velli, 1993).

$$\sigma_c = \frac{2\langle\delta\boldsymbol{v}_\perp \cdot \delta\boldsymbol{b}_\perp\rangle}{\langle\delta\boldsymbol{v}_\perp^2\rangle + \langle\delta\boldsymbol{b}_\perp^2\rangle} \tag{2.25}$$

In addition, we consider the normalized residual energy, σ_r, to investigate the effects of Alfvénic imbalance. This metric evaluates the relative energy in kinetic and magnetic fluctuations:

$$\sigma_r = \frac{\langle\delta\boldsymbol{v}_\perp^2\rangle - \langle\delta\boldsymbol{b}_\perp^2\rangle}{\langle\delta\boldsymbol{v}_\perp^2\rangle + \langle\delta\boldsymbol{b}_\perp^2\rangle}. \tag{2.26}$$

2.0.6 Alignment Angles

Conventionally, the angle between perpendicular components of field fluctuations, $\delta\boldsymbol{\phi}_\perp$ and $\delta\boldsymbol{\psi}_\perp$, is estimated using:

$$\sin(\theta_\perp^{\phi\psi}) = \left\langle \frac{|\delta\boldsymbol{\phi}_\perp \times \delta\boldsymbol{\psi}_\perp|}{|\delta\boldsymbol{\phi}_\perp||\delta\boldsymbol{\psi}_\perp|} \right\rangle. \tag{2.27}$$

This definition applies to estimating the angle between the fluctuations of the Elsässer fields, $\delta\boldsymbol{z}_\perp^o$ and $\delta\boldsymbol{z}_\perp^i$, denoted as $\theta_\perp^z$, as well as the angle between $\delta\boldsymbol{u}_\perp$ and $\delta\boldsymbol{b}_\perp$, denoted

as $\theta_{\perp}^{ub}$.

An alternate definition of these angles is obtained by separately averaging the numerator and denominator, a method known as polarization intermittency (Beresnyak and Lazarian, 2006a):

$$\sin(\tilde{\theta}_{\perp}^{\phi\psi}) = \frac{\langle|\delta\boldsymbol{\phi}_{\perp} \times \delta\boldsymbol{\psi}_{\perp}|\rangle}{\langle|\delta\boldsymbol{\phi}_{\perp}||\delta\boldsymbol{\psi}_{\perp}|\rangle}. \tag{2.28}$$

This approach allows for the identification of "dynamically relevant" fluctuations, as the averaging procedure considers that, at a given λ, fluctuations with amplitudes near the rms value are primary contributors to turbulent dynamics (Mason et al., 2006).

CSM15 predicts $\tilde{\theta}_{\perp}^{z} \propto \lambda^{0.10}$ for the Elsässer field and $\tilde{\theta}_{\perp}^{ub} \propto \lambda^{0.21}$ for the magnetic-velocity field polarization intermittency, respectively.

2.0.7 Partial Variance of Increments

The boundaries of CSs are associated with spatial variations or reversals of the local magnetic field. In recent years, a variety of methods, suitable for the detection of sharp gradients in a turbulent field, have been proposed (Bruno et al., 1999; Hada et al., 2003; Khabarova et al., 2021; Pecora, F. et al., 2021). A convenient statistical tool to perform this study, is the Partial Variance of Increments PVI (Greco et al., 2008). The PVI method has been used in the past in a variety of space plasma environments to determine the portion of the data corresponding to the underlying CSs (Tessein et al., 2013a; Chasapis et al., 2015; Bandyopadhyay et al., 2020; Chhiber et al., 2020b; Vasko et al., 2022; Lotekar et al., 2022). Assuming the validity of Taylor's hypothesis (Taylor, 1938), the PVI index at time t, for lag $\ell = -V_{SW}\tau$, is given by (Greco et al., 2008):

$$I_{\psi}(t,\ell) \;=\; \frac{|\delta\boldsymbol{\psi}(t,\ell)|}{\sqrt{\langle|\delta\boldsymbol{\psi}(t,\ell)|^2\rangle}}, \tag{2.29}$$

where, $|\delta\boldsymbol{\psi}(t,\ell)|$ is the magnitude of the field vector increments (either 2-pt or 5-pt), and $\langle ...\rangle$ stands for an average over a suitably large window that is a multiple of the

estimated correlation time for the magnetic field. (Greco et al., 2018) have shown that as the PVI index increases, the identified events are more likely to be associated with Non-Gaussian structures that lay on the "heavy tails" observed in the PDF of scale-dependent increments, suggesting that coherent structures correspond to events of index $PVI \geq 2.5$. The most intense magnetic field discontinuities, such as current sheets and reconnection sites, can then be identified by further raising the threshold value to $PVI \geq 4$, and, $PVI \geq 6$, respectively (Servidio et al., 2009).

2.0.8 Structure Functions and Scaling Exponents

Another method for assessing intermittency in a time series is based on estimating a sequence of q^{th} order moments of the magnetic field increments. The physical significance of this method is founded on the susceptibility of higher-order moments to concentrations of energy dissipation related to coherent structures and, from KRSH to extreme values of the magnetic field increments. We can estimate the q^{th} order structure-function for a field $\boldsymbol{\psi}$ field through

$$S^q_{\psi}(\ell) = \langle [\delta\boldsymbol{\psi}(t,\ell)]^q \rangle_T, \tag{2.30}$$

where, $|\delta\boldsymbol{\psi}(t,\ell)| = (\sum_i \delta\psi_i^2)^{1/2}$, is the magnitude of the vector magnetic field increments, and $\langle ... \rangle_T$ stands for averaging over an interval of duration T. Fitting each component of $S^n_{\psi}(\ell)$ to a power law, $\propto \ell^{\zeta_n}$, facilitates the estimation of scaling exponents, ζ_n.

2.0.9 Scale Dependent Kurtosis

An intermittency-affected generic time series exhibits alternate intervals of very high activity followed by extended periods of quiescence. Thus, intermittency in a signal is manifested in the form of a decrease in the fraction of volume occupied by structures at

scale ℓ with decreasing scale. Thus, due to it's relationship to the scale dependent filling fraction $F(\ell)$ for structures through

$$K(\ell) \sim 1/F(\ell) \tag{2.31}$$

the Scale Dependent Kurtosis (SDK), defined as

$$K(\ell) = \frac{\langle |\delta \boldsymbol{\psi}|^4 \rangle}{\langle |\delta \boldsymbol{\psi}|^2 \rangle^2}, \tag{2.32}$$

can be utilized to characterize the intermittency of a statistically homogeneous signal (Frisch, 1995).

An increase in $K(\ell)$ with the involvement of smaller and smaller scales ℓ is indicative of a signal that exhibits activity over only a fraction of space, with the fraction decreasing with the scale ℓ under consideration. For a scalar that emerges from an additive random process subject to a central limit theorem (i.e., follows a Gaussian distribution), the SDK is independent of scale and attains a constant value $K(\ell) = 3$, indicating the self–similar character of the fluctuations. On the contrary, the PDFs of intermittent fluctuations progressively deviate from a Gaussian distribution (i.e., distributions display fat tails) at smaller scales (Frisch, 1995). As a result, intermittency in a generic timeseries is manifested in the form of a monotonically increasing SDK with the involvement of smaller spatial/temporal scales. Additionally, when comparing two different time series, the one for which SDK grows more rapidly will be considered as more intermittent. Note that in the case where SDK fluctuates around a value different from 3, fluctuations are still characterized as self–similar but not Gaussian (i.e., formally referred to as Super-Gaussian). In this case, the fluctuations are not considered intermittent. This can be better understood when considering the way PDFs of increments are modified with scale. For instance, one may consider increments of a field ϕ that follow a given scaling

$$\delta\phi_\ell = \langle |\phi(x+\ell) - \phi(x)| \rangle \sim \ell^h. \tag{2.33}$$

By introducing a change of scale, $\ell \to \kappa\ell$, where $\kappa > 0$, we get the following transformation

$$\delta\phi_{\kappa\ell} \sim \kappa^h \delta\phi_\ell. \tag{2.34}$$

According to this relationship, increments estimated at different scales, are characterized by the same statistical properties (Frisch, 1995)

$$PDF(\delta\phi_{\kappa\ell}) = PDF(\kappa^h \delta\phi_\ell). \tag{2.35}$$

This means that if κ is unique, the PDFs of the normalized increments (e.g., rescaled by their standard deviations), $\delta\phi_\ell(x) = (\phi(x+\ell) - \phi(x))/\langle(\phi(x+\ell) - \phi(x))^2\rangle^{1/2}$ collapses to a single PDF highlighting the self-similar (fractal) nature of the fluctuations. On the other hand, intermittency implies multifractality and, as a consequence, an entire range of values for κ. It is thus reasonable to expect that over the scales for which the PDF of increments collapse on to each other, the SDK will fluctuate around a constant value.

CHAPTER 3

Magnetic Field Spectral Evolution in the Inner Heliosphere

3.1 Plasma Parameters Underlying the Dynamic Evolution of the Magnetic Spectrum in the Inner Heliopshere

This section is based on work published in (Sioulas et al., 2023a)

3.1.1 Introduction

As discussed in Section 1.3 MHD turbulence phenomenologies predict different power-law exponents depending on prevailing characteristics of turbulence, such as spatial wave-number anisotropy (Goldreich and Sridhar, 1995, 1997), intermittency (Chandran et al., 2015), and the scale-dependent correlation between velocity and magnetic field (Boldyrev, 2006). The variability of solar wind turbulence properties in the inner heliosphere reflects the diversity of solar coronal sources, which modulate the density, velocity, temperature, and ion composition of the plasma. Consequently, several factors, including the role played by large-scale gradients (Velli et al., 1989; Chandran and Perez, 2019), the proximity to the heliospheric current sheet (Chen et al., 2021; Shi et al., 2022b), the presence of magnetic field switchbacks (Martinović et al., 2021; Bourouaine et al., 2020; Shi et al., 2022a), and large-scale velocity shear in the SW (Coleman, 1968), strongly influence the properties of turbulence, resulting in a wide range of spectral scalings.

By fitting the power spectrum within a constant range in the frequency domain, recent statistical studies of PSP data have revealed a non-evolving velocity spectral index close

to $-3/2$, independent of the radial distance from the Sun (Shi et al., 2021), while the magnetic field spectrum steepens from a $-3/2$ slope at ~ 0.2 AU to a $-5/3$ slope at ~ 0.6 AU (Chen et al., 2020; Shi et al., 2021).

However, it is natural to expect that the relative physical scale of fluctuations of a given frequency decreases as the solar wind expands. Two scales are crucial to understanding the radial evolution of turbulence in the solar wind: (1) the ion inertial scale, $d_i = V_A/\Omega_i$, and (2) the thermal ion gyroradius, $\rho_i = V_{th,i}/\Omega_i$, where $\Omega_i = (e|B|)/m_p$ is the proton gyrofrequency, e is the elementary charge, $|B|$ is the magnitude of the magnetic field, and m_p is the mass of the proton. With increasing heliocentric distance, both physical scales (d_i, ρ_i) increase (Cuesta et al., 2022b; Sioulas et al., 2022b).

Here, we aim to understand the radial evolution of magnetic turbulence and study the basic features of scaling laws for solar wind fluctuations in terms of properly normalized physical scales. High-resolution data from the Parker Solar Probe (PSP) (Fox et al., 2016) and Solar Orbiter (SO) (Müller et al., 2020), covering heliocentric distances 13 $R_\odot \lesssim R \lesssim$ 220 $R_\odot$, are utilized to investigate the radial evolution of the magnetic spectral index as a function of normalized wavenumber.

We show that closer to the Sun, the magnetic field power spectrum exhibits a poorly developed, i.e., extending over a limited range of scales, inertial range characterized by a $-3/2$ spectral index. The inertial range extends to larger and larger scales as the solar wind expands into the interplanetary medium, with the inertial range spectral index steepening towards a $-5/3$ value. We demonstrate that the rate at which the steepening occurs is strongly dependent on the magnetic energy excess and Alfvénicity of the fluctuations.

3.1.2 Data Selection and Processing

We analyzed magnetic field data from the Flux Gate Magnetometer (FGM) (Bale et al., 2016), as well as plasma moment data from the Solar Probe Cup (SPC) and Solar Probe Analyzer (SPAN), which are part of the Solar Wind Electron, Alpha, and Proton (SWEAP)

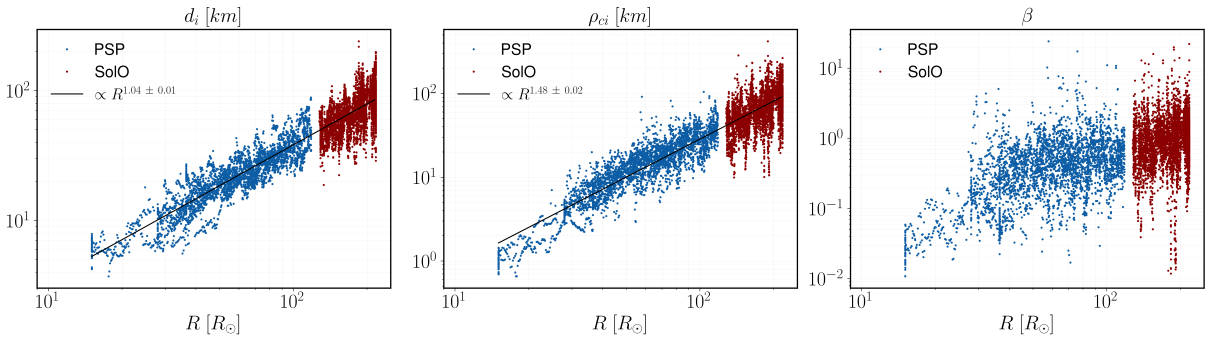

Figure 3.1: The radial evolution of (a) the ion inertial length d_i, (b) the ion gyroradiusρ_i, (c) ion plasma β

suite, collected between January 1, 2018, and June 15, 2022. This period encompasses the first twelve perihelia (E1-E12) of the PSP mission. SPC data were utilized for E1-E8, while SPAN data were used for E9-E12. When available, quasi-thermal noise-derived data (Moncuquet et al., 2020a) were preferred over SPAN or SPC data. Additionally, we considered magnetic field and particle moment measurements from the Magnetometer (MAG) instrument (Horbury et al., 2020), prioritizing burst data when available, and the Proton and Alpha Particle Sensor (SWA-PAS) (Owen et al., 2020) onboard the SO mission, collected between June 1, 2018, and March 1, 2022.

Intervals with quality flags indicating missing data $\geq 1\%$ and/or $\geq 10\%$ in the magnetic field and particle time series were omitted from further analysis. The remaining intervals were resampled linearly to the highest possible cadence based on their initial resolution. To eliminate spurious spikes, a Hampel filter (Davies and Gather, 1993a) was applied to the plasma time series.

Converting the spacecraft-frame frequency derived PSD, $F(f_{sc})$, to a wavenumber PSD, $E(\kappa)$, far from the Sun is possible using Taylor's hypothesis (TH) (Taylor, 1938), $\kappa = \frac{2\pi f_{sc}}{V_{SW}}$. This hypothesis becomes questionable when both the Alfvén velocity and the spacecraft velocity are comparable to the velocity of the solar wind. Therefore, a modified version of Taylor's hypothesis that accounts for both wave propagation and spacecraft velocity is adopted (Klein et al., 2015): in the above expression for κ, V_{sw} is replaced by $V_{tot} = |\boldsymbol{V}_{sw} + \boldsymbol{V}_a - \boldsymbol{V}_{sc}|$, where $\boldsymbol{V}_{sc}$ is the spacecraft velocity, and turbulence is assumed to be dominated by outwardly propagating Alfvén waves. Note that TH

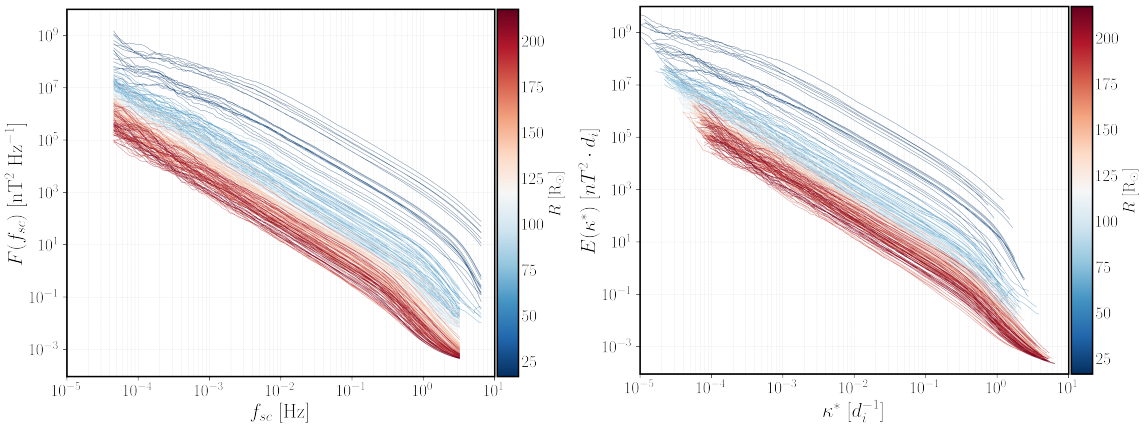

Figure 3.2: Magnetic field power spectrum, PSD at different heliocentric distances. The power-spectrum is shown, as a function of (a) spacecraft frequency; (b) wavenumber $k = \ell^{-1}$ in units of d_i

remained either moderately or highly valid for the majority of the time intervals examined, with only $\sim 1.53\%$ of the intervals under study exhibiting $M_A < 1.5$, including a number of sub-Alfvénic intervals during PSP $E_8 - E_{12}$ ($\sim 0.45\%$ of the entire dataset). Figure 5.8 illustrates the radial evolution of ion inertial length d_i, ion gyroradius ρ_i, and ion plasma β, which are quantities relevant to this study.

3.1.3 Results

3.1.3.1 Radial Evolution of magnetic field spectral index

We considered overlapping intervals of duration $d = 24$ hours, with the beginnings of adjacent intervals separated by 8 hours. For each interval, the Fourier trace power spectral density $F(f_{sc})$ was calculated, smoothed by averaging over a sliding window with a factor of 2, and transformed into a wavenumber spectrum expressed in physical units $E(\kappa^*)$ using the modified Taylor Hypothesis (TH):

$$E(\kappa^*) = \frac{V_{tot}}{2\pi \cdot \xi} F(f_{sc}) \ [nT^2 \cdot \xi],$$

where $\kappa^* = \kappa \cdot \xi = \frac{2\pi f_{sc}}{V_{tot}} \cdot \xi$, and $\xi = d_i, \rho_{ci}$.

The radial evolution of the power spectral density (PSD) as a function of spacecraft

frequency, normalized by d_i, is presented in Fig. 3.2a,b, respectively. Due to the expansion of the solar wind and the turbulent cascade, a decrease of approximately 4 orders of magnitude in magnetic power is observed with increasing heliocentric distance.

The spectral index α_B is obtained by taking a sliding window of one decade in the spacecraft-frame frequency (wavenumber) domain, over the smoothed spectra, and calculating the best-fit linear gradient in log-log space over this window. For clarity, ten radial bins have been used, and the median value of the spectral index as a function of frequency has been estimated for intervals that fall within the same bin. The color of the curve is keyed to the mean value of the distance R corresponding to the intervals within each bin. The results of this analysis are presented in Figure 3.3a. In the inertial range, an energy cascade rate that is independent of scale is expected, reflected in the power spectrum as a constant spectral index over this range of scales. Close to the Sun (dark blue line in Figure 3.3a), the inertial range is limited to a narrow range of frequencies ($2 \times 10^{-2} - 2 \times 10^{-1}$Hz). As the solar wind expands in the interplanetary medium: (1) a universal steepening (i.e., across all frequencies) is observed for the spectral index α_B at a constant f_{sc}; (2) the curves shift horizontally to lower and lower frequencies. As illustrated in Figure 3.3a, the frequency range over which the spectral index is constant migrates to the left while steepening with increasing distance, from $\alpha_B \approx -3/2$ to $\alpha_B \approx -5/3$. Similar behavior is observed at the largest scales. Closer to the Sun, for $f_{sc} \leq 2 \times 10^{-2}$ Hz, the spectrum becomes progressively shallower at lower frequencies and obtains a value of $\alpha_B \approx -1$ at $f_{sc} = 3 \times 10^{-4}$ Hz. As heliocentric distance increases, this low-frequency part of the spectrum gradually steepens, with all frequencies approaching a $-5/3$ scaling. Therefore, as the solar wind propagates outward, the inertial range of the spectrum develops gradually, extending from higher frequencies to progressively lower frequencies. Additionally, in accordance with (Duan et al., 2021), the ion scale break, which separates the inertial from the kinetic range, is observed to migrate to lower frequencies with distance.

To cast the results in terms of relevant physical scales, we considered the evolution of α_B into the wavenumber domain, normalizing by either the ion inertial length (d_i) or the

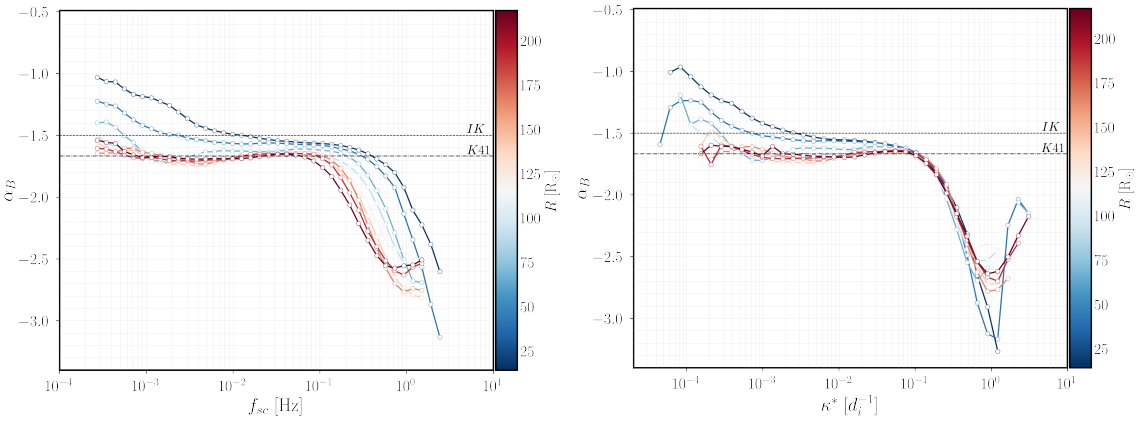

Figure 3.3: Evolution of magnetic field spectral index (α_B) as a function of distance, & (a) frequency in units of Hz (b) normalized wavenumber κ^* in units of d_i.

ion gyroradius (ρ_i).

The evolution of the spectral index as a function of distance (R) in the wavenumber domain normalized by d_i is illustrated in Figure 3.3b. It is readily seen that the vertical shifting of the curves to lower frequencies, observed in Figure 3.3a, has vanished: all the curves roll over at $\kappa d_i \approx 0.1$ and overlap at smaller scales. The normalization does not appear to have a substantial impact on the radial development of the spectral index at large scales, $\kappa^* \lesssim 8 \times 10^{-2}$, since a steepening closely resembling Figure 3.2a is obtained. On the other hand, as shown in Figure 3.2b, the small-scale break, demarcating the beginning of the transition region, $\kappa^* \approx 9 \times 10^{-2}$ (ρ_i^{-1}), does not show any remarkable evolution with distance and remains constant in physical space. We do not show plots using ρ_i as normalization because the spectra do not collapse as clearly into one curve at small scales, demonstrating that d_i is the more appropriate scale for such normalization.

3.1.3.2 Dependence of α_B on plasma parameters

To disentangle the spectral variation with distance from changes due to the differing plasma parameters of different solar wind streams the dependence of α_B on the normalized cross helicity σ_c, a measure of the relative amplitudes of inwardly and outwardly propagating Alfvén waves, and the normalized residual energy σ_r. The variation of α_B with V_{sw}, the ratio of magnetic to thermal pressure, $\beta \equiv n_p K_B T/(B^2/2\mu_0) \ll 1$, and the field/flow

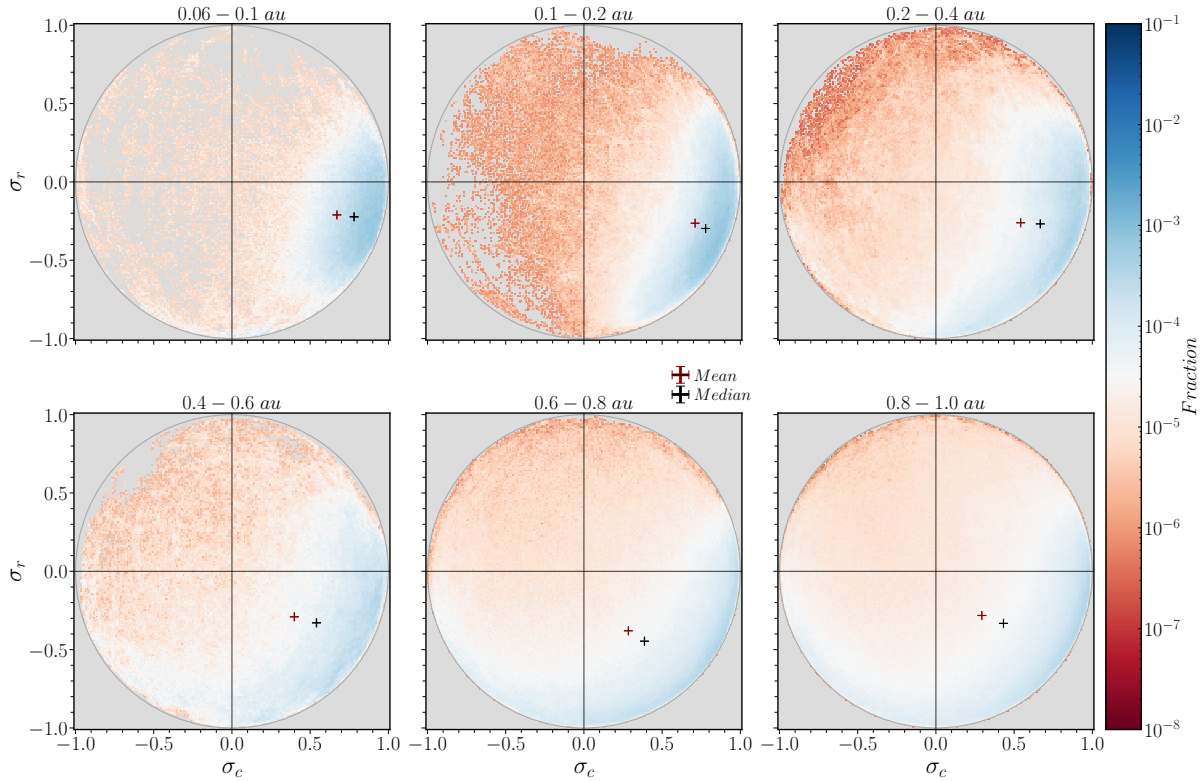

Figure 3.4: The joint distribution of normalized cross-helicity σ_c and normalized residual energy σ_r at different heliocentric distances.

angle Θ_{BV} was also examined. Though we do not focus on β, and Θ_{BV} here, we will comment on these in Section 3.1.4. The evolution of α_B is investigated by fitting the magnetic spectrum over a constant range ($10^{-3} - 3 \times 10^{-2}\ d_i^{-1}$). To ensure that the plasma parameters under study do not vary significantly within the interval the duration of intervals has been reduced to $d = 1$ hr.

3.1.3.3 Solar Wind Speed, V_{SW}

As shown in Figure 3.5a, Within 30 R_s, no significant differences in spectral index with solar wind speed are found with an inertial range scaling , $\alpha_B \approx -3/2$. As the solar wind expands, the dependence on solar wind speed becomes more evident: steepening occurs regardless of solar wind speed, but it is more efficient for slower solar wind streams. As a result, at $R \approx 1$ au, the dependence of the spectral index on speed is clear, with the spectral index being consistent with a K41 scaling in the fast wind and a steeper scaling

of ≈ -1.8 for the slowest winds. Categorizing the spectral index as a function of τ_{adv}, Figure 3.5b, instead of radial distance one finds that for $\tau_{adv} < 40Hrs$ no clear trend is observed for the spectral index as a function of wind speed. Beyond, this point, though steepening is monotonic with τ_{adv} at all wind speeds. Overall, lower speed intervals display a significant radial steepening as compared to faster winds that only display a slight steepening. Closer to the Sun, however, there seems to be no dependence on wind speed on the spectral index, suggesting that the spectra are initially similar regardless of the wind speed.

3.1.3.4 Normalized Cross Helicity, σ_c, & Normalized Residual Energy σ_r

The joint σ_c - σ_r distribution, estimated using 1 minute-long moving averages of the respective timeseries is presented in Figure 3.4. The median and mean value of σ_c and σ_r for each bin are also shown as red and black crosses respectively. The gray circle defines fluctuations with perfect alignment between velocity and magnetic field, given by $\sigma_c^2 + \sigma_r^2 = 1$. Closer to the sun (0.06-0.1 au) turbulence is highly Alfvénic, dominated by outwardly propagating waves ($\sigma_c \approx 0.85$), and in slight excess of magnetic energy ($\sigma_r \approx -0.15$). A small population of strongly magnetically dominated intervals characterised by very low alfvénic content (i.e., $\sigma_r \approx -1$, and $\sigma_c \approx 0$, mostly associated with heliospheric current sheet (HCS) crossings is also observed (see (Shi et al., 2022c)). At larger heliocentric distances the mean/median value of σ_c progressively decreases (Chen et al., 2020; Shi et al., 2021). Several mechanisms have been proposed to explain the diminishing dominance of outwardly propagating waves with increasing heliocentric distance due to wave reflection, including velocity shears (Roberts et al., 1992) and the parametric decay instability (Tenerani et al., 2017; Shoda et al., 2019). At 1au, σ_r is clearly more negative than in the near-Sun environment, but it does not show a clear trend with radial distance. In the distance range of 0.6-1 au, most of the data points are concentrated in the lower half, with a few intervals having slightly positive σ_r values. In addition, datapoints located in the bottom left quadrant are increasing with distance, indicating a radially decreasing dominance of waves propagating outward

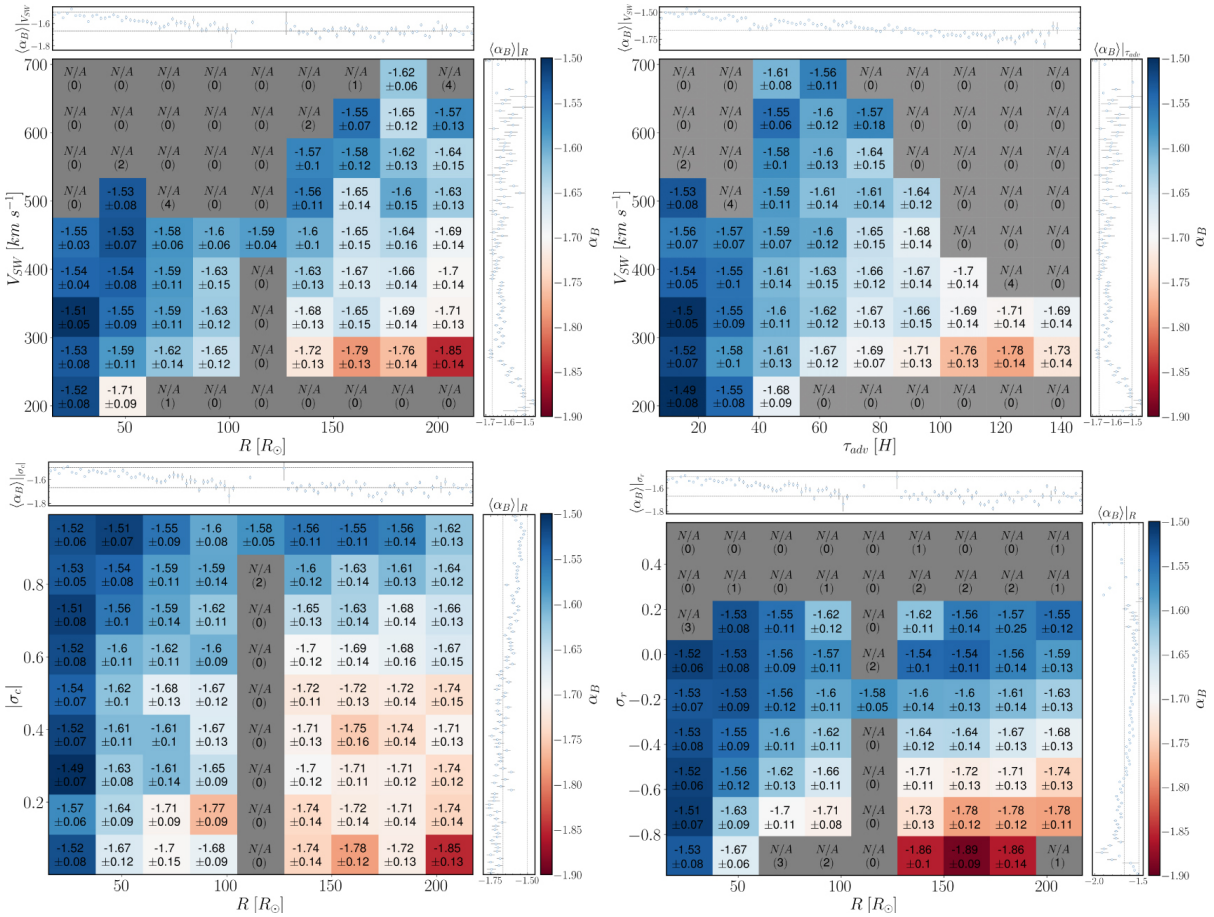

Figure 3.5: Magnetic field spectral index a_B as a function of V_{sw} and (a) heliocentric distance, (b) advection time τ_{adv}, as well as, a function of distance and (c) normalized cross helicity (σ_c), (d) normalized residual energy (σ_r)

The power-spectra of the fluctuating fields $\delta\boldsymbol{b}, \delta\boldsymbol{V}, \delta\boldsymbol{Z}_{o,i}$ have been obtained and both σ_c, and σ_r have been estimated by integrating the resulting spectra over a constant range ($10^{-3} - 5 \times 10^{-2}$ d_i^{-1}) in the wavenumber domain normalized by the ion inertial length. The dependence of the spectral index on $|\sigma_c|$ and σ_r as well as the radial distance (R) is presented in Figure 3.5c,d for σ_c and σ_r respectively. These show how highly alfvénic ($|\sigma_c| \approx 1$) and energetically equipartitioned intervals display little spectral evolution, while evolution to significantly steeper spectra is associated with low $|\sigma_c|$ and/or large magnetic energy excess, with the data at large distances consistent with 1 AU results (Chen et al., 2013; Bowen et al., 2018b).

3.1.4 Conclusions

Using *PSP* and *SO* data from the inner heliosphere we have analyzed 1) how the statistical signatures of turbulence evolve with heliocentric distance and (2) the plasma parameters driving the evolution.

Identifying a plasma scale that grows radially at the same rate as the high frequency break point is crucial for this study in order to anchor the spectrum in normalized wavenumber space and enable meaningful comparison between intervals sampled at different heliocentric distances. Since the high frequency break point exhibits a power-law radial dependence with a scaling exponent 1.08 ± 0.03 (Duan et al., 2021), then d_i which grows radially as $\propto R^{1.04\pm0.01}$ provides a better normalization than ρ_i which is characterized by a $\propto R^{1.48\pm0.02}$ radial scaling. It is important to emphasize that the goal here is not to find the quantity that has 1:1 correspondence with the high frequency break point. In fact, it is well known that intervals characterized by low ion β values exhibit a magnetic power spectral density that breaks at the ion inertial length (d_i), while high β intervals are characterized by a small scale break at the thermal ion gyroradius (ρ_i) (Chen et al., 2014a). Thus, the pinning of the power-spectrum at a constant κd_i scale, with increasing distance may be explained by the fact that plasma β values remain rather low in the inner heliosphere, see Figure 5.8. Another plasma scale that is correlated with the high frequency break point and should be considered by future investigations is the proton cyclotron resonance (Woodham, 2019a).

Additionally, our analysis indicates that closer to the Sun, the inertial range of the magnetic field power-spectrum is poorly developed i.e., the range of scales over which α_B remains constants is limited; its value is closer to $\alpha_B = -3/2$. As the solar wind expands into the interplanetary medium, the inertial range extends to progressively larger scales, while at the same time the inertial range spectral index steepens towards $\alpha_B = -5/3$.

We demonstrate that the rate at which α_B steepens is strongly dependent on the normalized residual energy and normalized cross helicity of the intervals under study. In particular, intervals with high alfvénic content ($|\sigma_c| \approx 1$), and equipartitioned in E_V-E_b

($\sigma_r \approx 0$) seem to retain their near-Sun scaling, and show a minor steepening with radial distance. In contrast, magnetically dominated and balanced intervals are observed to strongly steepen, resulting in anomalously steep inertial range slopes at 1 au, consistent with previous studies (Podesta, 2009; Bowen et al., 2018b).

While $|\sigma_c| \approx 1$ and $\sigma_r \approx 0$ values may be found in slow wind streams, especially closer to the sun, they are statistically less relevant than in fast winds (Shi et al., 2021). As a result, the occurrence of steeper spectral indices in slower wind streams may be attributed to the observed positive correlation between solar wind speed and $\sigma_c,\ \sigma_r$.

Intervals with large magnetic energy excess closer to the Sun do not display the steep spectra observed at 1 au, attributed by (Bowen et al., 2018b) to the correlation between magnetic coherent structures and highly negative σ_r values (Mininni and Pouquet, 2009). Recent studies (Sioulas et al., 2022b), suggest that magnetic field intermittency is strengthened with increasing heliocentric distance in the inner heliosphere, but no similar analysis has been conducted for the velocity field. However, velocity spectra do not display radial evolution (Shi et al., 2021) and exhibit a scaling of $a_v = -3/2$ at 1 au (Podesta and Borovsky, 2010). Based on our results, we expect that both the magnetic and velocity field spectra display a $-3/2$ scaling closer to the Sun, with the evolution of the magnetic spectrum related to the in-situ generation of magnetic coherent structures during expansion. A study of the evolution of α_B and a_v as a function of radial distance as well as intermittency is ongoing. Turbulence in the solar wind is anisotropic with respect to the mean magnetic field (see, e.g., reviews by Schekochihin et al., 2009a; Horbury et al., 2012; Oughton et al., 2015a, and references therein). Horbury et al. (2008); Osman et al. (2012) have shown that when the field/flow angle Θ_{BV} is $\Theta_{BV} = 90°$, then the inertial range range scales like either $\alpha_B \approx =5/3$, or sometimes $\approx =3/2$, consistent with a critical balance cascade and dynamical alignment models respectively. In the parallel direction, $\Theta_{BV} = 0°$, it is nearer $\alpha_B \approx -2$. In contrast, when a global magnetic field is utilized to estimate θ_{BV}, no anisotropy in the spectral index as a function of Θ_{BV} is observed (Tessein et al., 2009; Chen et al., 2011). Though it is not shown here, we find no correlation between Θ_{BV} and α_B, using a global magnetic field. A similar result was

obtained when considering the dependence of α_B on plasma β, suggesting that these two parameters are not related to the steepening of the spectrum. Further work to clarify the debate between a local, scale-dependent and global background magnetic field and it's role on the spectral evolution is presented in Chapter 3.2.

Our findings will help us gain a better understanding of how solar wind turbulence is generated and transported and will guide future models of solar wind turbulence.

3.2 On the Evolution of the Anisotropic Scaling of Magnetohydrodynamic Turbulence in the Inner Heliosphere.

This section is based on work published in (Sioulas et al., 2023b)

We analyze a merged Parker Solar Probe (PSP) and Solar Orbiter (SO) dataset covering heliocentric distances 13 $R_\odot \lesssim R \lesssim 220$ $R_\odot$ to investigate the radial evolution of power and spectral-index anisotropy in the wavevector space of solar wind turbulence. Our results show that anisotropic signatures of turbulence display a distinct radial evolution when fast, $V_{sw} \geq$ 400 $km\ s^{-1}$, and slow, $V_{sw} \leq$ 400 $km\ s^{-1}$, wind streams are considered. The anisotropic properties of slow wind in Earth orbit are consistent with a "critically balanced" cascade, but both spectral-index anisotropy and power anisotropy diminish with decreasing heliographic distance. Fast streams are observed to roughly retain their near-Sun anisotropic properties, with the observed spectral index and power anisotropies being more consistent with a "dynamically aligned" type of cascade, though the lack of extended fast-wind intervals makes it difficult to accurately measure the anisotropic scaling. A high-resolution analysis during the first perihelion of PSP confirms the presence of two sub-ranges within the inertial range, which may be associated with the transition from weak to strong turbulence. The transition occurs at $\kappa d_i \approx 6 \times 10^{-2}$, and signifies a shift from -5/3 to -2 and -3/2 to -1.57 scaling in parallel and perpendicular spectra, respectively. Our results provide strong observational constraints for anisotropic theories of MHD turbulence in the solar wind.

3.2.1 Introduction

In astrophysical systems such as stellar coronae, stellar winds, and the interstellar medium a large-scale magnetic field $\boldsymbol{B}_0$ is often present (Parker, 1979; Biskamp, 2003) and the fluctuations are typically observed to be mostly incompressible. Based on the weak interaction of oppositely moving Alfvénic wavepackets in a strong background magnetic field, $\delta v, \delta b \ll B_0$, i.e., assuming that the wave propagation, $\tau_A(\boldsymbol{\kappa}) = 1/|\boldsymbol{B} \cdot \boldsymbol{k}|$ is shorter than the nonlinear decay time $\tau_{nl}(\boldsymbol{\kappa}) \approx 1/(k \cdot \delta u_k)$, where δu_k is the average

velocity fluctuation at scales $\ell \sim 1/|\boldsymbol{k}|$, the turbulent cascade will be slowed relative to hydrodynamic turbulence (Iroshnikov, 1963; Kraichnan, 1965). Assuming homogeneity, isotropy, $\boldsymbol{B} \cdot \boldsymbol{k} \rightarrow B \cdot k$, and scale locality of the interactions, simple dimensional analysis then leads to the prediction of the inertial range omnidirectional power-spectrum, $E(k) \propto k^{-3/2}$. Magnetic fields, however, cannot be eliminated via Galilean transformations of MHD equations, as opposed to mean velocity fields, $\boldsymbol{V}_0$, resulting in strongly anisotropic turbulent dynamics (Montgomery and Turner, 1981) (see also reviews by Schekochihin et al., 2009a; Oughton et al., 2015b, and references therein). In particular, conservation of energy and momentum during wave-wave interactions (more specifically, a wave - 2D perturbation interaction, (see, Montgomery and Matthaeus, 1995)) allows power to cascade down to smaller scales perpendicular to $\boldsymbol{B}_0$, resulting in a two-dimensionalization of the turbulence spectrum in a plane transverse to the locally dominant magnetic field while at the same time inhibiting spectral energy transfer along the direction parallel to the field. (Shebalin et al., 1983; Ng and Bhattacharjee, 1996; Galtier et al., 2000).

Using in-situ observations in the solar wind (Horbury et al., 2008; Podesta, 2009; Chen et al., 2010) explored the dependence of the scaling index of the magnetic power spectrum's inertial range, α_B, on the field/flow angle θ_{BV}. An essential nuance in observing scale-dependent anisotropy involves the necessity of measuring parallel correlations along a local, scale-dependent mean magnetic field, $\boldsymbol{B}_\ell$, instead of the global mean magnetic field, as emphasized by (Cho and Vishniac, 2000; Gerick et al., 2017), (see also, review by Schekochihin, 2022, and references therein). The aforementioned studies suggest inertial range spectral indices of -2 and $-5/3$ for flow directions parallel ($\Theta_{BV} \approx 0^\circ$) and perpendicular ($\Theta_{BV} \approx 90^\circ$) to the mean magnetic field, respectively. These observations were interpreted as supporting evidence for the *critical balance* (CB) theory (Sridhar and Goldreich, 1994; Goldreich and Sridhar, 1995, 1997) [5], which is based on the conjecture that the inertial range dynamics of MHD turbulence with vanishing cross-helicity ($\sigma_c \approx 0$), later extended to imbalanced cascades (Lithwick et al., 2007), are governed by wavevector modes for which rough equality between $\tau_A(\boldsymbol{\kappa})$ and $\tau_{nl}(\boldsymbol{\kappa})$, $\tau_A(\boldsymbol{k}) \approx \tau_{nl}(|\boldsymbol{k}|)$ holds. As a result,

[5] Heavily influenced by the work of (Higdon, 1984)

the relationship between the parallel and perpendicular wavevectors follows an anisotropic scaling, $\kappa_{||} \sim \kappa_{\perp}^{2/3}$. Based on this scaling, we expect the magnetic fluctuation spectra to follow scalings of: $E(k_{\perp}) \propto k_{\perp}^{-5/3}$ and $E(k_{||}) \propto k_{||}^{-2}$. However, the *dynamic alignment* conjecture (Boldyrev, 2006; Mason et al., 2006; Perez and Boldyrev, 2009b) suggests that, as the energy cascades to smaller scales, velocity and magnetic field fluctuations in the plane perpendicular to $\boldsymbol{B}_{\ell}$ will align to within a smaller angle ϕ, resulting in weaker nonlinear interactions and a flatter perpendicular inertial range spectrum, $E(k_{\perp}) \propto k_{\perp}^{-3/2}$. In contrast, the field parallel spectrum remains unchanged, $E(k_{||}) \propto k_{||}^{-2}$. Other models of turbulence, such as the 2D plus slab model (Zank et al., 2020) lead to perpendicular and parallel spectra that can range between 5/3 and 3/2 in the perpendicular direction and 5/3 and 2 in the parallel direction.

As discussed in Section 3.1, recent observations from the Parker Solar Probe (PSP) and Solar Orbiter (SO) missions have provided the opportunity to investigate the radial evolution of turbulence in the inner heliosphere. It was shown that the inertial range of the magnetic spectrum grows with distance, progressively extending to larger spatial scales (Sioulas et al., 2022a) while at the same time steepening from a scaling of $\alpha_B = -3/2$ at approximately 0.06 au towards the Kolmogorov scaling of $\alpha_B = -5/3$ (Chen et al., 2020; Alberti et al., 2020; Telloni et al., 2021; Shi et al., 2021). The rate at which the spectrum steepens has also been found to be related to the Alfvénic content and magnetic energy excess of the fluctuations (Sioulas et al., 2022a). On the contrary, the spectral index of the velocity spectrum in the inertial range has consistently been found to be close to $\alpha_v = -3/2$, regardless of the distance from the Sun (Shi et al., 2021).

In this study, we aim to understand the radial evolution of anisotropic magnetic turbulence in the inner heliosphere. To do this, we analyze data from the PSP and SO missions covering heliocentric distances 13 $R_{\odot} \lesssim R \lesssim$ 220 $R_{\odot}$ using wavelet analysis. This technique allows us to decompose the magnetic field timeseries into scale-dependent background and fluctuations, and study the dependence of the turbulence properties on the field/flow angle θ_{BV}.

The rest of the paper is structured as follows: Section 3.2.2 presents the selection and

processing of the data. The results of this study are presented in Section 3.2.4, with a focus on high-resolution data obtained during the first perihelion of PSP in Subsection 3.2.4.1, and the radial evolution of magnetic field anisotropy investigated in Subsection 3.2.4.2. In Section 3.2.6, we compare our findings to previous relevant studies in order to advance our understanding of the topic and validate our conclusions. The discussion of the results and conclusions are provided in Sections 3.2.5 and 3.2.7, respectively.

3.2.2 Data Selection

As a first step, observations of PSP between January 1, 2018, and October 1, 2022, were collected, encompassing the first thirteen perihelia ($E1 - E13$) of the PSP mission. Level 2 magnetic field data from the Flux Gate Magnetometer (FGM) (Bale et al., 2016), as well as Level 3 plasma moment data from the Solar Probe Cup (SPC) for E1-E8, and the Solar Probe Analyzer (SPAN) from the Solar Wind Electron, Alpha and Proton (SWEAP) suite for E9-E13 (Kasper et al., 2016), were analyzed. Data from the SCaM product (Bowen et al., 2020a) obtained during E1 have also been analyzed and will be presented as a high-quality case study. The plasma data consists of moments of the distribution function computed on board the spacecraft, including the proton velocity vector $\boldsymbol{V}_p$, number density n_p, and temperature T_p. When available, electron number density data derived from the quasi-thermal noise from the FIELDS instrument (Moncuquet et al., 2020a) were preferred over SPAN or SPC data for estimating proton number density. In order to calculate the proton density from the electron density, charge neutrality must be considered, leading to a $\approx 4\%$ abundance of alpha particles. Therefore, electron density from QTN was divided by 1.08.

The second step involved obtaining magnetic field and particle measurements from the SO mission between June 1, 2018, to March 1, 2022. Magnetic field measurements from the Magnetometer (MAG) instrument (Horbury et al., 2020), have been analyzed using burst magnetic field data when available. Particle moments measurements for our study are provided by the Proton and Alpha Particle Sensor (SWA-PAS) onboard the

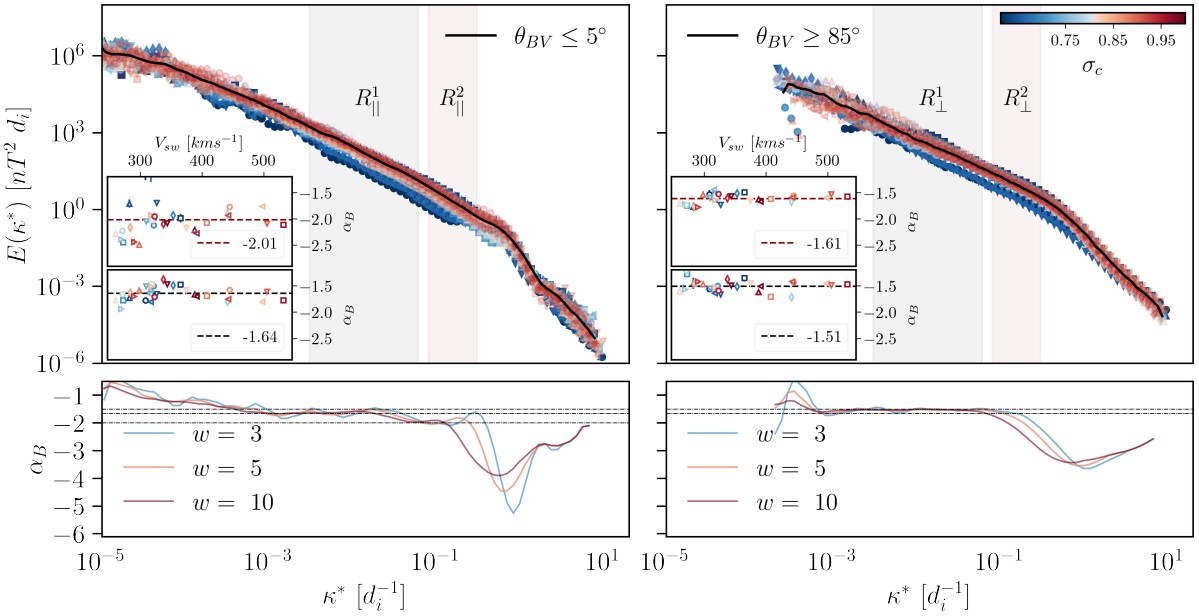

Figure 3.6: Averaged magnetic field power-spectrum (black solid line) for fluctuations parallel $\theta_{BV} \leq 5°$ (left panel) and perpendicular $\theta_{BV} \geq 85°$ (right panel) to the local magnetic field during the first perihelion of PSP (E1) estimated using SCaM data. The dependence of the spectra on normalized cross-helicity (σ_c) is also shown, with the color keyed to σ_c. The inset figures illustrate the spectral index α_B, at two different ranges of scales (bottom) $3 \times 10^{-3} - 5 \times 10^{-2} d_i$ and (top) $8 \times 10^{-2} - 2 \times 10^{-1} d_i$ as a function of solar wind speed and σ_c. The dashed horizontal lines indicate the mean value of α_B. The second row illustrates the local α_B, calculated over a sliding window of a factor of 3, 5, and 10 shown in cyan, orange, and red respectively. Horizontal dotted lines have also been added marking values $-3/2$, $-5/3$ and -2

Solar Wind Analyser (SWA) suite of instruments (Owen et al., 2020).

3.2.3 Data processing

Quality flags for the magnetic field and particle time series have been taken into account, and time intervals missing $\geq 1\%$ and/or $\geq 10\%$ in the magnetic field and particle time series have been omitted from further analysis. Additionally, the mean value of the cadence between successive measurements $\delta\tau$ in the magnetic field time series has been estimated for each of the selected intervals, and time intervals that were found to have a mean cadence of $\delta\tau \geq 250$ ms were discarded. Due to poor data quality, all PSP intervals exceeding $R \simeq 0.5$ au have also been discarded.

Spurious spikes in the plasma time series were eliminated by replacing outliers exceeding three standard deviations within a moving average window covering 200 points with their median values (Davies and Gather, 1993a).

3.2.4 Results

3.2.4.1 Case Study: SCaM Dataset, E1

The high-resolution data from the first perihelion of the PSP (R $\approx$ 0.17 au) from November 1 to November 11, 2018, was analyzed. A total of 33 intervals each with a duration of 12 hours were obtained and the power spectral density was estimated, with subsequent intervals overlapping by 50%. The analysis covered 18 bins of the θ_{BV} angle, but in the following, we will only focus on those bins closer to the parallel and perpendicular directions, with $\theta_{BV} \leq 5^{\circ}$ and $\theta_{BV} \geq 85^{\circ}$, respectively. It is worth noting that the second half of E1 displayed significantly different characteristics compared to the first half, with the solar wind exhibiting higher speeds and a greater number of magnetic switchbacks (Bale et al., 2019). It is well established that power spectra exhibit different characteristics when different solar wind speeds are considered due to the different types of fluctuations they transport (Borovsky et al., 2019). Specifically, the fast solar wind is highly Alfvénic and characterized by large-amplitude, incompressible fluctuations, while the slow wind is generally populated by smaller amplitude, less Alfvénic, compressive fluctuations, that include convected coherent structures (Bruno et al., 2003; Matteini et al., 2014; Shi et al., 2021; Sioulas et al., 2022b; Zhao et al., 2020). Consequently, the spectral variation due to the differing plasma parameters of the selected streams was investigated. More specifically, we considered the dependence of the PSD on the solar wind speed, V_{sw}, the normalized cross helicity σ_c:

, and the normalized residual energy σ_r. The magnetic field power-spectrum for fluctuations parallel $\theta_{BV} \leq 5^{\circ}$ and perpendicular $\theta_{BV} \geq 85^{\circ}$ to the local magnetic field, resulting from averaging all the respective spectra are presented in Figure 3.6. Individual spectra are also shown with the color of the curve keyed to σ_c. The fluctuation power

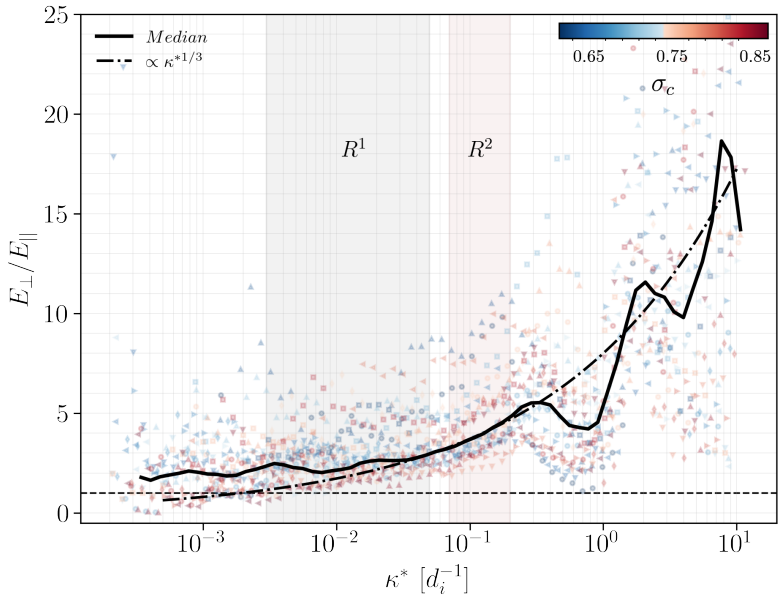

Figure 3.7: The anisotropy of the fluctuations described by the ratio of the perpendicular ($E_\perp$) to the parallel power ($E_{||}$). A horizontal black solid line has been added to indicate $E_\perp/E_{||} = 1$.

in the MHD range shows a positive correlation with σ_c, but this dependence vanishes in the transition region and kinetic scales. A similar trend was observed with σ_r and V_{sw}, not shown here. The results are consistent with (Vasquez et al., 2007), who found higher, MHD range, turbulence amplitudes associated with faster streams, as well as, (Pi et al., 2020) who showed that such dependence vanishes in the kinetic scales. The trend also vanishes at the large, energy injection scales, $\kappa d_i \leq 10^{-3}$, where the power spectrum is clearly dominated by parallel fluctuations. Focusing our attention on MHD scales, we can observe two distinct ranges, roughly $3 \times 10^{-3} - 5 \times 10^{-2} \kappa d_i$ and $8 \times 10^{-2} - 2 \times 10^{-1} \kappa d_i$, over which the PSD displays a clear power-law scaling. A light-black and red shade are used to indicate these regions in the figure, and we will thereby refer to them as $R^1_{||(\perp)}$, and $R^2_{||(\perp)}$. The power-law fitting has been applied to the PSD for the two ranges, and the bottom and top inset figures illustrate α_B as a function of V_{sw}. Note, that the color of the scatter plot is keyed to σ_c. Furthermore, horizontal lines have been added to indicate the average value of α_B. In the direction parallel to the mean field the PSD scales roughly like -5/3 and -2 in $R^1_{||}$ and $R^2_{||}$, respectively. For perpendicular fluctuations, only a minor difference may be observed between $R^1_\perp$ and $R^2_\perp$ which are characterized by a power-law

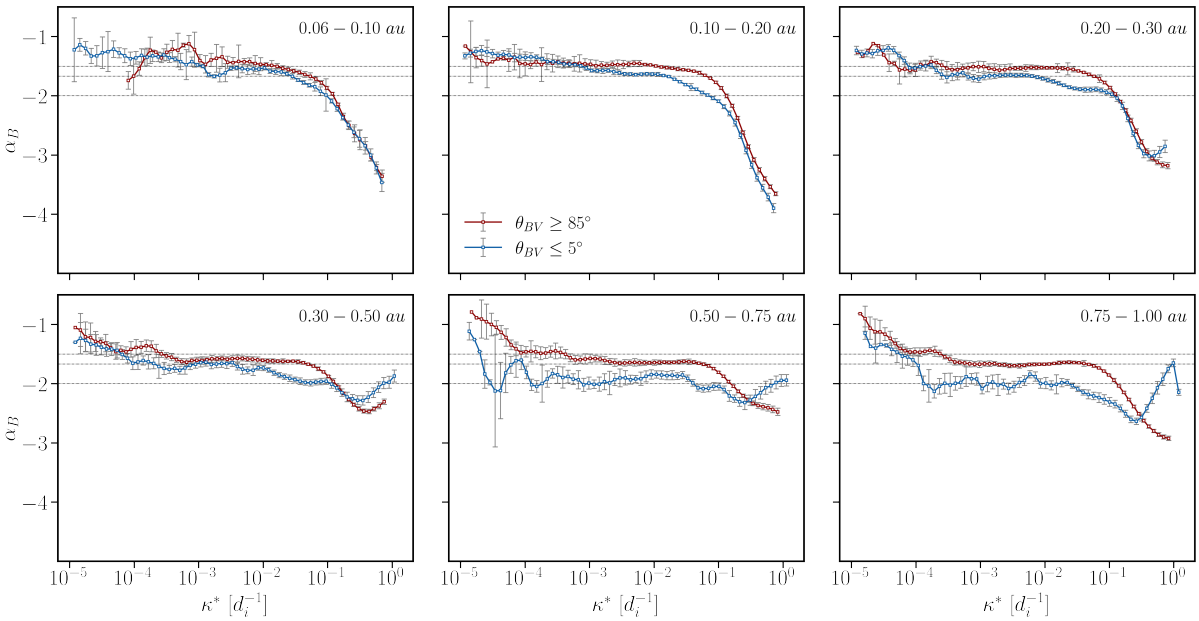

Figure 3.8: The local spectral index ($\alpha_B(\kappa^*)$) for fluctuations with $\theta_{BV} \leq 5°$ (blue), and $\theta_{BV} \geq 85°$ (red) at different heliocentric distances for slow streams, $V_{sw} \leq 400km\ s^{-1}$. The local spectral index was calculated for all selected intervals, and each curve corresponds to the mean of all intervals that fall inside the bins indicated in the legend. We focus on MHD scales, $\kappa d_i \leq 3 \times 10^{-1}$, because instrumental noise flattens the PSD with increasing distance, as discussed in Section 3.2.4.1.

scaling with index -3/2 and -1.57, respectively. The absence of a definitive correlation between α_B, V_{sw}, and σ_c, as reported in the study by (Sioulas et al., 2022a), could be ascribed to the relatively extended time intervals that were examined or the limited size of the sample, which, in this case, encompassed only 33 intervals.

When examining the local spectral index, $\alpha_B(\kappa^*)$, a similar pattern emerges. This is achieved by applying a sliding window of size $w = 3,\ 5,\ 10$ in κ^* over the spectra and calculating the best-fit linear gradient in log-log space over this window, shown in cyan, orange, and red, respectively, in the bottom panel of Figure 3.6. At smaller scales where $\kappa^* \geq 0.1 d_i^{-1}$, both parallel and perpendicular fluctuations display a steeper spectrum between the inertial and kinetic ranges. The scaling behavior observed in the transition and kinetic ranges is consistent with the findings reported by (Duan et al., 2021). Additionally, (Duan et al., 2021) report a scaling exponent of -2 for the parallel spectrum in the inertial range spanning $4 \times 10^{-1} - 2$ Hz, which corresponds to region

$R^2_{||}$ in our analysis. It is worth noting, however, that $R^2_{||}$ does not encompass the entire inertial range. Specifically, $R^1_{||}$ covers most of the MHD range and is characterized by a shallower scaling exponent, $\alpha_B \approx -5/3$. The two different MHD scalings persist in most of the intervals studied, suggesting that this may be a consistent feature of the solar wind power spectrum in the vicinity of the Sun.

We then analyzed the power anisotropy, defined as $E_\perp/E_{||}$ (Podesta, 2009), as a function of κ^*. The results of this analysis are displayed in Figure 3.7, where individual intervals are plotted as scatter points and binned based on their σ_c value. The median curve for each bin is shown and the color of each curve is keyed to σ_c. The median curve (black solid line) in Figure 3.7 is consistent with previous findings at larger heliocentric distances. Specifically, the curve exhibits a region of near isotropy for $kd_i \leq 10^{-3}$, which roughly corresponds to the roll-over to the f^{-1} range of the magnetic spectrum (see Figure 3.6). At smaller scales, the anisotropy becomes more noticeable and shows a power-law scaling that closely resembles the 1/3 value suggested by the CB conjecture. Therefore, a line with a scaling exponent of 1/3 was included in the figure as a point of reference. This $\kappa^{*1/3}$ scaling is observed within the range of $4 \times 10^{-2} - \ 3 \times 10^{-1}$ $[d_i^{-1}]$, which corresponds to region R^2 in Figure 3.6. Additionally, while the anisotropy increases at smaller scales until $\kappa d_i \ \approx 4 \times 10^{-1}$, there is a sudden but noticeable local minimum at around $\kappa d_i \ \approx 0.7$ followed by a local maximum at $\kappa d_i \ \approx 1.7$. Both the trough and peak are consistently observed across all intervals considered in this study. The local minimum may be caused by the bump observed in $E_{||}$ at $\kappa d_i \approx 0.06$, which coincides with the beginning of the transition region in $E_\perp$ (see Figure 3.6). This bump may suggest a local enhancement of energy that could be due to ion kinetic instabilities (Wicks et al., 2010). For a more comprehensive discussion of the double-peak structure in Figure 3.7a, see (Podesta, 2009).The results of this study differ from those of (Podesta, 2009) in that we observe an increase in anisotropy at smaller scales $\kappa d_i > 2$. As shown in Figure 7 of (Podesta, 2009), a rapid decrease in the power ratio is observed beyond the local kinetic scale maximum of approximately 1 Hz, which is attributed to the dissipation of kinetic Alfven waves (KAWs). However, as the spacecraft moves farther away from the

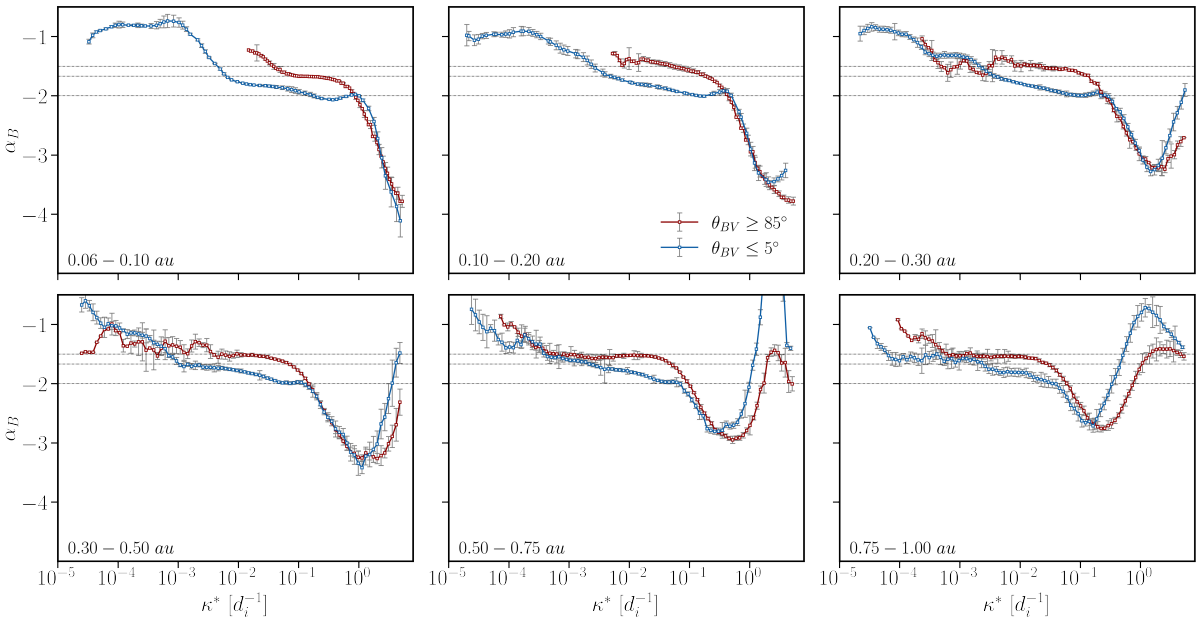

Figure 3.9: The local spectral index ($\alpha_B(\kappa^*)$) for fluctuations with $\theta_{BV} \leq 5°$ (blue), and $\theta_{BV} \geq 85°$ (red) at different heliocentric distances for fast streams, $V_{sw} \geq 400km\ s^{-1}$. The local spectral index was obtained for all selected intervals and each curve corresponds to the mean of all the intervals that fall inside the bins indicated in the legend.

sun, the amplitude of the fluctuations at kinetic scales is close to the noise floor of the magnetometer. This can lead to an artificial steepening of the power spectral density (PSD) caused by instrumental noise (Woodham, 2019b). The effect is particularly significant for $\alpha_B(\kappa^*)$ parallel, as most of the power in the solar wind is associated with perpendicular fluctuations. As a result, the parallel PSD systematically obtains lower values at MHD and kinetic scales and is therefore more likely to be affected by instrumental noise. On the other hand, the perpendicular PSD can remain intact. This can cause the parallel PSD to flatten out and the power ratio to decrease with decreasing scale. Considering that (1) the aforementioned paper uses magnetic field data from the STEREO mission (Acuña et al., 2008) at Earth-orbit, where the turbulence amplitude is lower compared to that observed by PSP's E1, and (2) the SCaM data product merges fluxgate and search-coil magnetometer measurements, allowing for magnetic field observations up to 1 MHz with an optimal signal-to-noise ratio, we attribute the discrepancy to instrumental noise that may have affected the parallel PSD in Figure 7 of (Podesta, 2009).

3.2.4.2 Radial Evolution of Spectral-index Anisotropy

In the following, we investigate the evolution of spectral index anisotropy with heliocentric distance. For this analysis we consider intervals sampled by the PSP and SO at distances between 0.06 - 1 au (see Section 4.1.3). Previous research has shown that the dominant orientation of fluctuation wavevectors in fast solar wind streams tends to be quasi-parallel to the local magnetic field, while in slow solar wind streams the dominant orientation is quasi-perpendicular (Dasso et al., 2005). In order to examine the distinct features of each type of stream and their potential impact on the development of anisotropy in the solar wind, a comprehensive visual analysis was undertaken to categorize the streams into two distinct groups: slow streams characterized by $V_{sw} \leq 400\ km/s$ and fast streams with $V_{sw} \geq 400\ km/s$. A comprehensive record of the chosen intervals can be accessed in MHDTurbPy

We shall begin by examining the evolution of slow streams, which comprise the majority of the samples collected from PSP and SO. To determine the local spectral index for each interval, we perform calculations in the direction parallel ($\theta_{BV} \leq 5°$) and perpendicular ($\theta_{BV} \geq 85°$) to the locally dominant magnetic field, utilizing a sliding window of size $w = 10$, following the methodology outlined in Section 3.2.4.1.

We then partitioned our intervals into six heliocentric bins and calculated the mean local spectral index for those intervals that fell within each bin. It should be noted that despite the spectra and local spectral indices being calculated at identical frequencies based on the interval duration and sampling frequency, the normalization process results in an irregular shift along the vertical axis. Consequently, we divided the complete range of κ^* into 100 bins, and computed the mean for all $\alpha_B(\kappa^*)$ values that fell within each bin, as described in (Němeček et al., 2021). It is worth noting that the size of the interval under consideration does not have a significant impact on the outcomes. This is true as long as a sizable statistical sample of fluctuations is taken into account at a given scale, in order to ensure the validity of the statistical analysis and produce accurate spectra (Dudok de Wit et al., 2013). Any intervals that exhibited noisy or otherwise unreliable

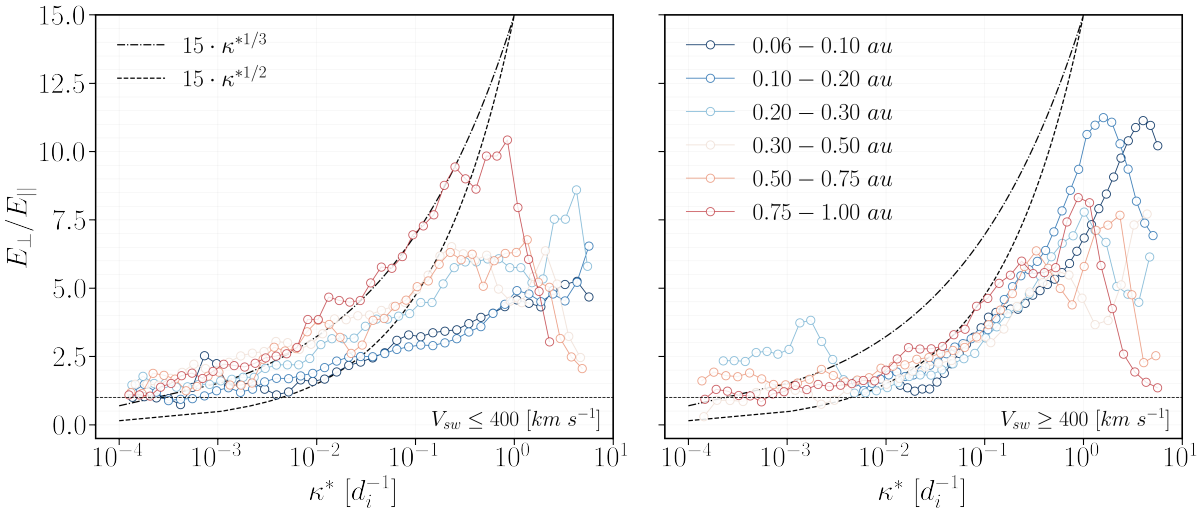

Figure 3.10: The radial evolution of the power anisotropy, represented by the ratio $E_\perp/E_{||}$, is depicted as a function of heliocentric distance for slow ($V_{sw} \leq 400\ km\ s^{-1}$) and fast ($V_{sw} \geq 400\ km\ s^{-1}$) streams. Six heliocentric-radius bins were utilized, and each curve represents the median of $E_\perp/E_{||}$ from all intervals that fall within each bin. The dashed ($y = 15 \cdot \kappa^{*1/2}$) and dashed-dotted ($y = 15 \cdot \kappa^{*1/3}$) lines were added as reference points, indicating consistency with "dynamically aligned" and "critically balanced" cascade, respectively.

spectra were excluded from subsequent analyses. However, it is important to note that such intervals made up only an inconsequential proportion of the overall dataset.

The radial size of each bin is shown in the legend of Figure 3.8. The slow wind local spectral indices, as a function of heliocentric distance, are shown in blue for perpendicular fluctuations, and in red for parallel fluctuations along with error bars indicating the standard error of the mean. The standard error is given by $\sigma_i/\sqrt{N}$, where σ_i is the standard deviation and N is the number of samples inside the bin, as described in (Gurland and Tripathi, 1971a). We focus our attention on MHD scales, $\kappa d_i \leq 3 \times 10^{-1}$, here simply because instrumental noise artificially steepens the PSD with increasing distance, as discussed in Section 3.2.4.1.

It is evident from Figure 3.8 that the spectral-index anisotropy of slow wind turbulence diminishes closer to the Sun. Within 0.1 au, both parallel and perpendicular spectra are characterized by a poorly developed inertial range, viz. the range of scales over which the spectral index is constant is limited to $3 \times 10^{-3} \lesssim \kappa d_i \lesssim 2 \times 10^{-2}$ with a scaling

exponent -1.47 ± 0.04 and -1.55 ± 0.05 for perpendicular and parallel fluctuations. At distances 0.1-0.2 au, two subranges (R^1 and R^2) emerge within the inertial range. The transition occurs at $\kappa d_i \approx 6 \times 10^{-2}$, and the scaling exponents in these ranges are similar to those shown in Figure 3.6. However, the steepened region R^2 is not as well defined in this case. Considering that the PSP was at a distance of 0.17 au during E1, we attribute this discrepancy to the fact that R^2 actually appears closer to 0.2 au. By shifting the left boundary of the bin towards 0.2 au, we confirmed this expectation as the steepened region displayed a parallel power-law scaling of -2 when the left boundary was shifted to approximately 0.15 au.

In R^1 both parallel and perpendicular spectra dynamically evolve with increasing distance and steepen towards -5/3, which in the case of the parallel spectrum occurs within 0.1 au. The steepening occurs in a scale-dependent fashion which results in R^2 extending to larger scales with distance. As a result, for distances exceeding 0.5 au, R^1 practically vanishes, and the power spectra are characterized by a power-law exponent that changes from $-5/3$ in the direction perpendicular to -2 in the direction parallel to the locally dominant mean field in good agreement with the predictions of "critical balance" theory. It should be noted that the analysis was iterated over bins of width 10°, yielding consistent outcomes. Notably, the obtained Power Spectral Densities (PSDs) for $\theta_{BV} \geq 80°$ or $\theta_{BV} \geq 85°$ exhibited indistinguishable scaling behavior across all distances. Conversely, a comparison of the PSDs obtained for $\theta_{BV} \leq 10°$ and $\theta_{BV} \geq 5°$ revealed marginally steeper scaling behavior in the latter case for the inertial range. Specifically, in the instance of slow solar wind intervals, when distances exceeded 0.5au, a consistent -2 scaling was observed for $\theta_{BV} \geq 5°$, whereas for $\theta_{BV} \geq 10°$, the scaling behavior obtained was closer to -1.89.

We next examined the evolution of fast streams ($V_{sw} \geq 400\ km\ s^{-1}$). It is important to consider that as the solar wind expands in the heliosphere, the local mean magnetic field vectors become increasingly oriented at larger angles relative to the radial direction. This radial trend causes sampling at 0.06 AU to be more quasi-longitudinal, and sampling at 1.0 AU to be more quasi-perpendicular. As parallel fluctuations decrease with increasing

distance, our ability to accurately estimate the low-frequency part of the parallel power spectrum is reduced. This effect makes the determination of the anisotropic scaling laws for high-speed streams in the ecliptic plane challenging, as there is insufficient data to make accurate measurements at low frequencies. While using longer records could resolve this issue, the limited lifetime of the streams restricts the length of the record. In an effort to address this issue, we imposed a minimum interval length that would allow for a large enough interval size but still enable us to gather a sufficient number of intervals for our statistical study. Specifically, for heliographic distances exceeding 0.3, and 0.5 au, we set the minimum interval size to 12 and 20 hours respectively. This resulted in a total of 274 intervals sampled across the inner heliosphere. The results of this analysis are presented in Figure 3.9. It is readily seen that the differences between fast and slow intervals are significant. When examining the lower frequencies, we observe that within 0.2 au, the energy injection range of the PSD is dominated by parallel fluctuations. In particular, a remarkably extended and relatively shallow range with $\alpha_B \approx -0.8$ is observed within 0.1 au, which steepens towards -1 with distance. This is particularly noteworthy as previous research has shown that Alfvén waves (AWs) can parametrically decay into slow magnetosonic waves and counter-propagating AWs (Galeev and Oraevskii, 1963a; Tenerani et al., 2017; Malara et al., 2022). This process may lead to the development of a $k_{||}^{-1}$ spectrum for outward-propagating AWs by the time they reach a heliocentric distance of 0.3 au in the fast solar wind (Chandran, 2018). For a more comprehensive investigation of the radial evolution of the lower-frequency part of the spectrum, see (Davis et al., 2023). Due to the issues with interval size that were discussed earlier, we do not attempt to interpret the evolution of the lower-frequency part of the spectrum beyond 0.3 au.

Focusing on MHD scales, we notice that the perpendicular PSD only extends up to $\kappa d_i \approx 10^{-2}$. This implies that fast streams in proximity to the Sun exhibit a nearly radial magnetic field at low frequencies. Interestingly, within 0.1 au, the scaling of the perpendicular spectrum is consistent with $-5/3$, but at larger distances, a scaling that is roughly consistent with $-3/2$, fluctuating between -1.49 to -1.55, is observed. This suggests that the MHD range spectral index of the perpendicular spectrum for fast

streams may not evolve in a consistent manner with increasing distance in the inner heliosphere. It is worth noting, however, that within 0.1 au, only four intervals with $V_{sw} \geq 400$ km/s were sampled by PSP. More data from fast streams near the Sun is needed to statistically confirm these findings. For parallel fluctuations, the inertial range scaling remains remarkably similar across all heliographic bins with the spectral index progressively steepening towards smaller scales from -5/3 towards -2, where a narrow range of scales over which the local spectral index obtains a constant value appears. In contrast to slow wind streams, the high-frequency point in fast wind streams does not remain anchored in a normalized wavenumber but gradually drifts towards larger scales with distance. This is an interesting finding that suggests the evolution of the high-frequency point is different between fast and slow wind streams and is discussed further in Section 3.2.5.

3.2.4.3 Radial Evolution of Power anisotropy

In this section we examine the radial evolution of the power anisotropy, represented by the ratio $E_{\perp}/E_{||}$, where $E_{\perp}$, $E_{||}$ the PSD for $\theta_{BV} \geq 85°$ and $\theta_{BV} \leq 5°$, respectively. To do this, we utilized the method described in Section 3.2.4.2 and calculated the mean of $E_{\perp}/E_{||}$ in six heliocentric bins. The results of this analysis are presented in Figure 3.10a for slow streams and Figure 3.10b for fast streams. According to theories based on "dynamical alignment', the inertial range scaling index should be 1/2 when considering $E_{\perp}/E_{||}$, while a slope of 1/3 is predicted by theories of "critical balance".

For slow wind streams, the power anisotropy becomes more significant with increasing distance, particularly at smaller scales (see Figure 3.10a). This suggests that the turbulence undergoes an anisotropic cascade, transporting the majority of its magnetic energy towards larger perpendicular wavenumbers. In contrast, fast streams show practically no significant radial trend, especially when taking into account the error bars (not shown here). As a result, even though the power anisotropy is more pronounced for fast winds closer to the Sun, at distances of around 1 au, the situation is reversed, and slow wind exhibits higher

values of $E_\perp/E_{||}$. In terms of anisotropic scaling, we observe that $E_\perp/E_{||}$ evolves in a manner similar to what was described in Subsection 3.2.4.2. Specifically, the scaling of $E_\perp/E_{||}$ for slow wind streams does not fit the predictions of any of the existing anisotropic theories closer to the Sun, but with increasing distance, it evolves towards a scaling that is consistent with CB theories. The situation is more complex for fast streams. In particular, for the bin closest to the Sun, the scaling of $E_\perp/E_{||}$ is closer to that predicted by CB theories ($\kappa^{*1/3}$), but for the rest of the bins, the scaling exponent fluctuates in the range between $1/2 - 1/3$. Additionally, the double peak structure discussed in Section 3.2.4.1 is also observed for most of the curves in this analysis, especially in fast wind intervals. In contrast to the data presented in Section 3.2.4.1, at smaller scales, the utilization of fluxgate magnetometer data leads to a significant impact of instrumental noise on the resulting curves, ultimately causing a marked decrease in the power ratio.

3.2.5 Discussion

Wavelet analysis of solar wind data obtained at heliocentric distances greater than 0.3 au has shown strong agreement between the anisotropic characteristics of magnetic turbulence and the predictions of the "critical balance" conjecture (Horbury et al., 2008; Wicks et al., 2010). However, (Podesta, 2009) cautioned that it would be premature to draw conclusions about the agreement of the scaling in the fast solar wind with any particular theory due to the large uncertainties of the scaling at the largest scales. It is worth noting that these studies either focused on high-speed streams or prolonged periods of both high-speed and slow streams(Horbury et al., 2008; Wicks et al., 2010; Wicks et al., 2013a; He et al., 2013). When extended intervals are considered, the PSD behavior will be practically determined by the fast sub-intervals since high-speed streams exhibit higher-amplitude magnetic fluctuations. Recent PSP measurements below 0.3 au have provided an unprecedented opportunity to study the nature of the solar wind in the vicinity of the solar wind sources. (Bandyopadhyay and McComas, 2021) have recently shown that large-scale fluctuations in the near-Sun solar wind are dominated by wavevectors quasi-parallel to the local magnetic field. (Zhao et al., 2022) also studied the radial dependence of this ratio by

grouping the available datasets into two catalogs according to the radial distance and found that the ratio between parallel and perpendicular fluctuations observed by PSP is about 50% : 50%.

Inertial range spectral anisotropy has been investigated by (Huang et al., 2022; Wu et al., 2022), who used slow solar wind data from E1 of PSP to show that the spectral indices are close to $-5/3$ and $-3/2$ in the parallel and perpendicular direction, respectively. (Wu et al., 2022) furhter conducted a comparative analysis of the anisotropic spectral properties of the slow wind stream observed by PSP during E1 and a fast wind stream with a solar wind speed $V_{sw} \approx 770 km/s$, which was sampled by Ulysses at 1.48 au. Their analysis led to the conclusion that the dynamical evolution of the inertial range scaling can be attributed to the existence of two sub-ranges in the inertial range. Specifically, the sub-range closer to the kinetic scales, 30-300 d_i, exhibits a radial steepening, while the sub-range at larger scales remained unchanged. As demonstrated by (Wu et al., 2022), the transition between the two ranges in question does not exhibit radial evolution, but rather remains constant in terms of κd_i. Nevertheless, the reliability of this finding is uncertain given the contrasting radial evolutions of fast and slow streams based on turbulence signatures, as reported by (Shi et al., 2021; Sioulas et al., 2022b; Sioulas et al., 2023a).

There are several significant questions that remain unanswered regarding the anisotropy of magnetic turbulence in the solar wind and its evolution as it propagates into the heliosphere. Firstly, it is unclear whether the anisotropy dynamically evolves with distance. Secondly, there is a need to investigate potential differences in spectral and power anisotropy between fast and slow streams, and if such differences exist, it is important to determine whether they evolve with distance. In the subsequent section, we endeavor to address these outstanding issues by comparing our findings with those of previous studies.

3.2.6 Review of Related Literature

3.2.6.1 Horbury et al. (2008) & Podesta (2009)

In our study, using data from PSP and SO, we estimated perpendicular inertial range spectral indices for the fast wind with values in the range of $[-1.49, \ -1.55]$. These values are slightly shallower than those reported in previous studies (Horbury et al., 2008; Podesta, 2009; Wicks et al., 2010) , which estimate values in the range of $[-1.55, \ -1.67]$. One possible reason for this discrepancy could be that the PSP and SO data were only collected in the ecliptic plane during the minimum and early rising phase of the Solar Cycle. It is known that solar wind conditions can vary significantly over the course of the Solar cycle, and it is possible that these variations could affect the observed scalings of the perpendicular spectra. In addition, due to the phase of the Solar Cycle, only a limited number of extended fast wind streams were collected. For example, PSP only sampled four intervals with $V_{sw} \geq 400$ km/s within 0.1 au. This limitation may affect the statistical significance of the results and make it difficult to accurately measure the anisotropic scaling laws for these streams at lower frequencies. As a result, it may be premature to draw firm conclusions about the agreement of the scaling in the fast solar wind sampled in the ecliptic plane by PSP and SO with any particular theory of anisotropic MHD turbulence.

3.2.6.2 Wicks et al. (2010)

Our results indicate that, when analyzing slow wind streams, normalizing the PSD with d_i allows us to fix the high-frequency break point, f_b, in normalized wavenumber space, as previously reported in (Sioulas et al., 2022a). However, for fast solar wind streams, f_b tends to shift towards larger κd_i as the distance increases. This phenomenon can be attributed to the fact that fast solar wind streams are characterized by higher proton temperatures (T_p) (Maksimovic et al., 2020; Shi et al., 2021; Shi et al., 2023b), which lead to higher plasma pressure and, consequently, higher plasma β values. The plasma β is defined as the ratio of thermal to magnetic pressure, $\beta \equiv n_p K_B T_p/(B^2/2\mu_0)$, and it is comparatively

higher in fast streams than in slow ones. It should be noted that the $V_{sw} - \beta$ correlation was verified, although it is not presented in this report. $2018_v echhaveshownthatthef_b$ of the magnetic PSD between inertial and kinetic scales correlates better with d_i when the intervals are characterized by $\beta < 1$ values, while high β intervals are characterized by a small scale break at the thermal ion gyroradius (ρ_i). In line with this, our analysis confirms the findings of (Wicks et al., 2010), who used five fast solar wind streams with $\beta > 1$ between 1.5 - 2.8 au and found that the small scale end of the inertial range seems to naturally scale with the ion gyroradius when normalized with ρ_i. Given that ρ_i grows radially as $\propto R^{1.48\pm0.02}$ (Sioulas et al., 2022a), we expect that f_b will display a similar radial trend for fast solar wind streams.

3.2.6.3 Wu et al. (2022)

The use of high-resolution data from E1 of PSP allowed us to confirm the existence of two sub-ranges (Telloni, 2022; Wu et al., 2022) within the inertial range. The transition occurs at $\kappa d_i \approx 6 \times 10^{-2}$ and signifies a shift from -5/3 to -2 scaling in the parallel spectra and from -3/2 to -1.57 scaling in the perpendicular spectra. The difference between the two ranges (R^1, R^2) is most apparent in the parallel spectrum and could signify a transition from weak to strong turbulence(Sridhar and Goldreich, 1994; Meyrand et al., 2016; Zank et al., 2020). It is important to note that the parallel spectral index we report here for $R^2_{||}$, $\alpha_B \approx -2$, is steeper than the one reported by (Wu et al., 2022). It is unlikely that the variations seen in the outcomes are due to the utilization of structure functions in the analysis carried out by (Wu et al., 2022). This is because we used second-order structure functions to confirm the anisotropic scaling. Nonetheless, it is feasible that the differences could be linked to the usage of better quality SCaM data in our research. In particular, Wu et al.'s parallel structure function in Figure 4b seems to become steeper at shorter timescales, but the limited cadence of around 1 Hz might prevent the clear detection of such scaling.

Moreover, it has been observed that there exist noteworthy differences between fast

and slow streams in terms of their anisotropic properties and dynamic evolution. Besides the distinctions noted in the evolution of the inertial range scaling, the high-frequency breakpoint displays a more rapid shift towards lower frequencies in the analysis of fast wind streams. These findings are at odds with the assertions put forth by (Wu et al., 2022) and emphasize the necessity of analyzing wind streams of comparable speeds for making meaningful comparisons.

3.2.7 Conclusions

We used a merged PSP and SO dataset to study the dynamic evolution of turbulence anisotropy in the inner heliosphere, focusing on understanding the differences in anisotropy observed between fast and slow wind streams. The main findings of our study can be summarized as follows:

For slow wind streams ($V_{sw} \leq 400\,\mathrm{km\ s^{-1}}$), we find:

(a1) Within 0.1 AU, the spectral index anisotropy of the inertial range vanishes, and the inertial range is confined to $3 \times 10^{-3} \lesssim \kappa d_i \lesssim 2 \times 10^{-2}$. The scaling exponents are -1.47 ± 0.04 and -1.55 ± 0.05 for perpendicular and parallel fluctuations, respectively. The power anisotropy ($E_\perp / E_\parallel$) is weaker compared to previous studies at 1 AU, and its inertial range scaling does not fit any predictions of anisotropic theories of turbulence.

(a2) At ≈ 0.15 AU, two inertial subranges (R^1 and R^2) emerge. The transition occurs at $\kappa d_i \approx 6 \times 10^{-2}$, signifying a shift from $-5/3$ to -2 and $-3/2$ to ≈ -1.6 scaling in parallel and perpendicular spectra, respectively.

(a3) Beyond this point, the power anisotropy strengthens monotonically with distance, indicating an anisotropic turbulent cascade that transports most of its magnetic energy towards larger perpendicular wavenumbers. Additionally, region R^2 extends towards smaller wavenumbers, gradually "consumin" region R^1. This process results in a scale-dependent steepening of the inertial range.

(a4) At distances exceeding 0.5 AU, region R^1 practically vanishes, and the power spectra are characterized by a power-law exponent that changes from $-5/3$ in the perpendicular direction to -2 in the parallel direction to the locally dominant mean field, in good agreement with the predictions of "critical balance" theory.

(a5) The rate at which the high-frequency breakpoint f_b of the magnetic power spectrum drifts to lower frequencies with distance scales naturally with the rate at which the ion inertial scale (d_i) grows with distance. In other words, the high-frequency point f_b remains anchored in κd_i.

For fast streams ($V_{sw} \geq 400\,\mathrm{km\ s^{-1}}$), we find:

(b1) Closer to the Sun, the energy injection range ($\kappa d_i \leq 10^{-3}$) of the spectrum is dominated by parallel fluctuations. Within 0.1 AU, this range exhibits an extended shallow region with a scaling index of ≈ -0.8. This region steepens towards -1 with increasing distance, providing evidence for the Parametric Decay Instability (PDI) as a generating mechanism for the $k_{\parallel}^{-1}$ spectrum in the fast solar wind (Chandran, 2018).

(b2) In MHD scales, the scaling of both the parallel and perpendicular spectra does not exhibit a clear radial trend. Within 0.1 AU, the scaling of the perpendicular spectrum is consistent with $-5/3$. Beyond 0.1 AU, the perpendicular spectral index fluctuates between -1.49 and -1.55. For parallel fluctuations, the inertial range scaling remains remarkably similar across all heliographic bins. The spectral index progressively steepens towards smaller scales from $-5/3$ towards -2, where a narrow range of scales over which the local spectral index obtains a constant value is observed.

(b3) Power anisotropy for fast streams does not seem to display a clear trend with distance. In terms of inertial range scaling, we find that fast streams are more consistent with the model based on "dynamical alignment" (Boldyrev, 2006) than the model based on "critical balance" (Goldreich and Sridhar, 1997), but the large uncertainties at lower frequencies make the statistical significance of this result questionable.

(b4) In agreement with (Wicks et al., 2010), the high-frequency point f_b remains

anchored in $\kappa\rho_i$.

A deeper understanding of anisotropy could be gained by considering the effect of intermittency on turbulence (Oboukhov, 1962), i.e., the concentration of fluctuation energy into smaller volumes of space at smaller scales. Recent research has demonstrated a connection between critical balance and dynamic alignment with intermittency (Chandran et al., 2015; Mallet and Schekochihin, 2017). Such results are presented in Chapter ref.

When analyzing turbulence in the inner heliosphere, where the Alfvén speed approaches and sometimes exceed the solar wind speed special care must be used in applying homogeneous turbulence theories and models to the observed characteristics. This is especially important for power anisotropies, as in addition to wave-number couplings, the couplings to large scale gradients both in the radial and transverse directions may be fundamental, with the solar corona, for example, acting to refract energy in fast mode polarization into regions of low Alfvén speed or even providing some total reflection. These couplings could also affect spectral slopes in the parallel and perpendicular directions in the nascent solar wind (Velli et al., 1991).

In conclusion, it is important to recognize the potential limitations of the current analysis, including the limited number of extended fast wind streams sampled by PSP and SO. These limitations may affect the statistical significance of the results and make it difficult to accurately determine the anisotropic scaling laws for these streams at lower frequencies. Therefore, it is advisable to continue collecting more samples from PSP and SO, particularly those of longer duration, to confirm the statistical significance of the findings. In addition, a more robust statistical analysis with longer intervals of data from Ulysses and Helios will be conducted to accurately determine the scaling of the anisotropy and its dependence on the heliocentric distance, phase of the solar cycle, and heliographic latitude.

CHAPTER 4

Intermittency: Dynamic Evolution and the Role of Magnetic Coherent Structures in Dissipation and Plasma Heating

4.1 Magnetic Field Intermittency in the Solar Wind: PSP and SolO Observations Ranging from the Alfvén Region out to 1 AU.

This section is based on work published in (Sioulas et al., 2022b)

4.1.1 Introduction

Even though the analysis of spectral properties, discussed in Chapter 3 can be informative, the second statistical moment of the probability distribution function of increments is only sufficient to fully characterize turbulence under the assumption of isotropic and scale-invariant fluctuations (Kolmogorov, 1962). In practice, these conditions are in principle violated in space and astrophysical systems.

The fundamental approach to studying intermittency involves the examination of the probability density functions (PDFs) of the dissipation rate. However, based on the Kolmogorov refined similarity hypothesis **KRSH** (Kolmogorov, 1962), local averages of dissipation rate are related to the scale-dependent increments of the velocity field. Thus, intermittency is reflected on the PDF of field increments in the form of an increasing divergence with respect to a Gaussian distribution (i.e., PDFs display fatter tails) as

increasingly smaller scales are involved (Castaing et al., 1990; Frisch, 1995). This behavior, often referred to as multifractal, violates the concept of global scale invariance, a key assumption of the K41 theory, giving rise to the concept of local scale invariance, i.e., turbulence is characterized by a diverse set of fractals with varying scalings.

The solar wind is an expanding medium. MHD fluctuations entering the super-Alfvénic wind in the trans-Alfvénic region, expected at $\sim 15 - 25 R_{\odot}$ (DeForest et al., 2018), are modified in terms of structure and scale as the SW expands into the interplanetary medium driven by the turbulent cascade, as well as, shear at stream interfaces (Roberts et al., 1992) and other transients (Shi et al., 2022b). It is, therefore, reasonable to expect that the statistical signatures of coherent structures evolve with heliocentric distance. Indeed, recent studies in the solar wind suggest a dynamic evolution of intermittency properties of MHD fluctuations indicating that the solar wind is an active turbulent medium involving both local and global dynamical processes that influence the higher-order statistics of fluctuations. (Bruno et al., 2003) have utilized Helios data to examine the radial evolution of intermittency utilizing the flatness (i.e., SDK hereafter) of the magnetic field. Their analysis indicates a different behavior for slow and fast wind intermittency. More specifically, slow wind ($V_{SW} \lesssim 500\ km \cdot s^{-1}$) was observed to display a higher degree of intermittency than the fast wind ($V_{SW} \gtrsim 600\ km \cdot s^{-1}$). Additionally, no radial dependence was observed for the slow wind, in contrast to an increase in intermittency with heliocentric distance for the fast solar wind. The distinct nature and radial evolution of intermittency were attributed to the different roles played by coherent non-propagating structures and by stochastic Alfvénic fluctuations for the two types of wind at different heliocentric distances. Turbulence in fast streams closer to the Sun is highly Alfvénic (i.e., the magnetic field and velocity fluctuations exhibit a high degree of correlation) and displays a self-similar (i.e., monofractal) character. However, during the expansion, due to nonlinear interaction amongst counter-propagating Alfvén waves, the fluctuations become decorrelated (Roberts et al., 1992; Chen et al., 2020; Shi et al., 2021) and the Alfvénic contribution, which tends to decrease intermittency because of its stochastic nature, is gradually depleted (Marsch and Liu, 1993). On the contrary,

advected structures tend to increase intermittency because of their coherent nature, while their relative contribution becomes more important with increasing heliocentric distance. As a result, the fractal nature of the magnetic field is modified, gradually approaching multifractal with increasing heliocentric distance. Slow wind does not show the same behavior since Alfvénic fluctuations have a less dominant role for this type of wind. The same line of reasoning was adopted by (Alberti et al., 2020; Telloni et al., 2021) to interpret the increasing deviation, with respect to the linear scaling expected from K41 theory, of the structure function scaling exponents , as well as, (Greco et al., 2012a) who, utilizing the PVI method, observed an increase in the fractional volume occupied by coherent in the inner heliosphere. More recently, (Parashar et al., 2019; Cuesta et al., 2022b) have examined the relationship between SDK and R_e, where R_e is the Effective Reynolds Number, to show that regions with lower R_e have on average lower kurtosis, at a fixed physical scale, suggestive of a less intermittent behavior. Even though Re is observed to decrease in the inner heliosphere, several effects overcome the relation of Re with intermittency, but at 1 au, a change of system dynamics begin to favor the effects from system size, resulting in progressively weaker intermittency at larger heliocentric distances, concurrent with a decreasing R_e.

During its first ten encounters with the Sun, the Parker Solar Probe (PSP) mission (Fox et al., 2016) has provided valuable measurements of solar wind particles and fields in the neighborhood of the solar wind sources. Aiming to approach the surface of the Sun by as close as 9.86 $R_\odot$, PSP offers unprecedented in-situ measurements in the vicinity of the Alfvén-zone, allowing us to study its influence on the evolution of spectral and intermittency properties of the field fluctuations (Kasper et al., 2021; Bandyopadhyay et al., 2022; Zhao et al., 2022). These observations will supplement simulations (Chhiber et al., 2022) and ultimately enable us to explore processes such as the heating of the solar corona and the acceleration of the solar wind in the vicinity of the Alfvén zone (Matthaeus and Velli, 2011). In conjunction with the recently launched Solar Orbiter *SolO* (Müller et al., 2020), the synergy of the two missions offers a unique opportunity to explore the connection between the Sun and the heliosphere (Velli et al., 2020b).

In this work, we are interested in understanding the radial evolution of inertial range MHD turbulence and studying the basic features of scaling laws for solar wind fluctuations. We start our investigation by examining the radial evolution of intermittency without accounting for the anisotropy introduced with respect to the alignment angle, Θ_{VB}. At a later stage, however, we show that accounting for anisotropy will complicate interpretation of the observations.

For the purposes of our analysis, high-resolution magnetic field and particle data from PSP and SolO covering heliocentric distances $13 \lesssim R \lesssim 220\ R_{\odot}$ are implemented. Our tools to study intermittency involve analytical methods such as the Partial Variance of increments (PVI), the scaling behavior of the high order moments of variations of the magnetic fields separated by a scale ℓ, or Structure Functions (SFs), and their respective scaling exponents, and finally the Scale Dependent Kurtosis (SDK) of the magnetic field.

The structure of this section is as follows: Section 4.1.2 presents the selection of data (PSP, Solar Orbiter) and their processing; The results of this study are presented in Section 4.1.4: In Subsection 4.1.4, the radial evolution of magnetic field intermittency is investigated, and in Subsection 4.1.5 the dependence of intermittency on plasma parameters is examined; A summary of the results along with the conclusions is given in Section 4.1.6.

4.1.2 Data Selection

A merged dataset of PSP and SolO observations is employed to study the radial evolution of magnetic field fluctuations in the inner heliosphere. In the first step, all available PSP observations from the period 2018-11-01 to 2022-02-22 (i.e., orbits 1 - 11) are collected. More specifically, Level 2 magnetic field data from the Flux Gate Magnetometer (FGM) (Bale et al., 2016), and Level 3 plasma moments from the Solar Probe Cup (SPC), as well as the Solar Probe Analyzer (SPAN) part of the Solar Wind Electron, Alpha and Proton (SWEAP) suite (Kasper et al., 2016), in the spacecraft frame, have been analyzed. Magnetic field data were obtained at a cadence of 4.58 samples per second ($\sim 0.218s$

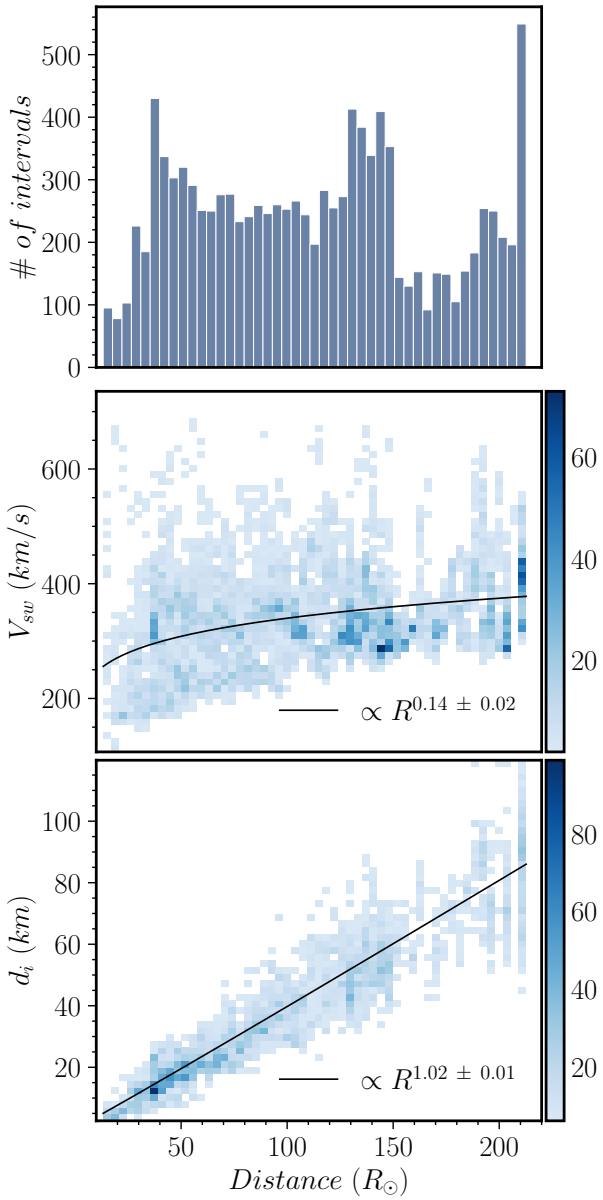

Figure 4.1: (a) Histogram showing the number of 5-hr intervals as a function of heliocentric distance (b) Joint distribution of SW speed V_{sw} vs heliocentric distance (R) (c) Joint distribution of ion inertial length d_i vs heliocentric distance(R) .

resolution). However, it was found that the higher cadence is mostly offered close to the perihelia of PSP, while for periods where PSP is further away from the Sun, the cadence is reduced to $0.42s$. For plasma moments, the cadence strongly depends on the interval studied, ranging from $0.218 - 0.874s$ during the encounters and to $\sim 27.9s$ at larger heliocentric distances for SPC, while for Span-i, the median cadence is ~ 3.5 for the encounters and $\sim 28s$ further away from the sun.

In the second step, magnetic field and particle data from the SolO mission from 2021-01-01 to 2021-12-01 are also employed. Magnetic field measurements from the Magnetometer (MAG) instrument (Horbury et al., 2020), downloaded from the ESA Solar Orbiter archive, have been utilized. Particle moment measurements for our study are provided by the Proton and Alpha Particle Sensor (SWA-PAS) onboard the Solar Wind Analyser (SWA) suite of instruments (Owen et al., 2020).

4.1.3 Data processing

In order to account for gaps in the magnetic field timeseries, the mean value of the cadence between successive measurements $\langle \delta\tau \rangle$ has been estimated for each interval. Subsequently, intervals have been divided into three classes (a) $\langle \delta\tau \rangle \leq 250ms$ (b) $\langle \delta\tau \rangle \leq 500ms$ (c) $\langle \delta\tau \rangle \geq 500ms$. For the first two classes of intervals magnetic field data have been linearly resampled to a cadence of $dt = 250ms$ and $dt = 500ms$ respectively, while the remaining intervals have been discarded. This decision was based on the observation that when resampling to $dt = 450ms$, the minimum spatial scale of $20d_i$ could not be achieved for a minor fraction of the intervals at distances $R \leq 20R_{\odot}$. To confirm that the different cadence does not affect the results of our study, the analysis was repeated by resampling all magnetic field data to $dt = 450ms$, with qualitatively similar results.

To obtain the plasma parameters from PSP, either SPAN or SPC data are utilized depending on the quality and cadence of the data for the interval. Subsequently, a Hampel filter was applied to all particle moments timeseries to eliminate spurious spikes and outliers exceeding three standard deviations from a moving average window spanning 200

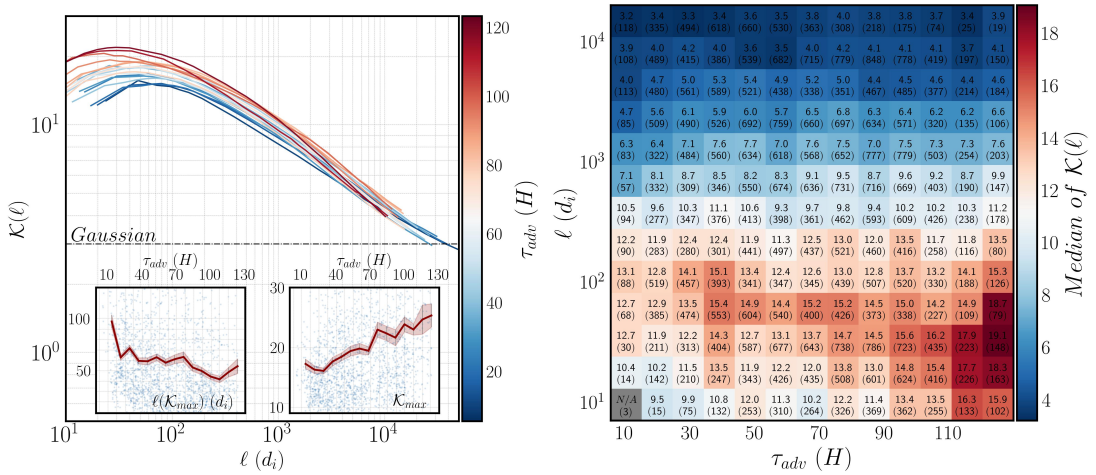

Figure 4.2: (a) Evolution of SDK with τ_{adv}. Each line represents the average of 100 intervals that fall within the same τ_{adv} bin. The inset scatter plots show (i) the scale, in units of d_i, at which the kurtosis attains the maximum value (ii) The maximum kurtosis value estimated for the individual 5H intervals. The binned mean of the two quantities is also shown with a red line. (b) Scale-dependent kurtosis of the magnetic field as a function of scale in units of ion inertial length d_i and SW convection time τ_{adv}. The numbers indicate the median value of kurtosis within each bin, and the bracketed numbers show the number of events within each bin.

points (Davies and Gather, 1993a). Finally, in order to maintain a sufficient statistical sample within any given interval, intervals that were found to have more than 5% of the values missing in the magnetic field or 10% in the particle timeseries have also been discarded. For the purposes of the SDK and SF's analysis, magnetic field and particle data have been divided into intervals of duration $d = 5\ hr$. On the other hand, due to the nature of the PVI analysis (i.e., our measure of intermittency is provided in the form of a timeseries) after PVI was estimated, data have been divided into intervals of duration $d = 15\ min$. The smaller duration intervals were chosen to mitigate the effects of mixing different types of solar wind, as well as to allow us to study intervals for which angle, Θ_{VB} is estimated.

Additionally, in an attempt to interpret the evolution of parameters that measure the evolution of intermittency, we attribute the differing behaviors in various samples of solar wind turbulence to the role played by the advection time of the solar wind defined as $\tau_{adv} = D_{SC}/V_{SW}$, where D_{SC} is the heliocentric distance of the spacecraft in units of km

and V_{SW} has units of $km\ H^{-1}$.

4.1.4 Radial evolution of magnetic field intermittency.

4.1.4.1 Scale Dependent Kurtosis (SDK).

In this section, we investigate the evolution of the magnetic field kurtosis as a function of lag and advection time of the solar wind. The SDK for the magnetic field magnitude was estimated for 3100 individual intervals of duration $d = 5$ hr. In Figure 4.2a the evolution of SDK as a function of advection time τ_{adv} of the solar wind is presented. To emphasize the trend, the average of 100 intervals that fall within the same τ_{adv} bin is estimated, and the mean value of τ_{adv} for each bin is reflected on the line color. At the largest scales, the kurtosis is near Gaussian, and no clear trend is observed. At smaller lags, $\ell \sim 5 \cdot 10^3 d_i$, the lines intersect and beyond this point separate. In particular, for $\ell \lesssim 5 \cdot 10^3 d_i$, an increase in kurtosis is observed with increasing τ_{adv}. For a more quantitative comparison, the evolution of the maximum value of the kurtosis (thereby K_{max}) as a function of τ_{adv} is presented on the right-hand side inset of Figure 4.2a. The blue dots indicate K_{max} estimated for individual intervals, and the red line is the binned mean of the same quantity. Uncertainty bars indicate the standard error of the sample, $\sigma_i/\sqrt{n}$, where σ_i is the standard deviation and n is the number of the samples inside the bin (Gurland and Tripathi, 1971b). Additionally, the spatial scale ℓ at which K_{max} is observed, i.e. $\ell(K_{max})$, expressed in units of d_i, is presented in the left inset figure. Even though there is a considerable scatter in the data, the maximum shifts towards smaller lags with increasing τ_{adv}. Moreover, as τ_{adv} increases, the peaks of SDK are progressively shifted to larger and larger values. As noted in the introduction, intermittency manifests itself as a growing kurtosis with decreasing spatial scale. Consequently, the increase of K_{max} indicates a radial strengthening in intermittency within the inner heliosphere. Figure 4.2 offers a different perspective on the evolution of SDK as a function of τ_{adv} for different spatial scales. The data points were binned according to ℓ, and τ_{adv}, and the median value inside each bin was calculated, which is reflected in the colors and written

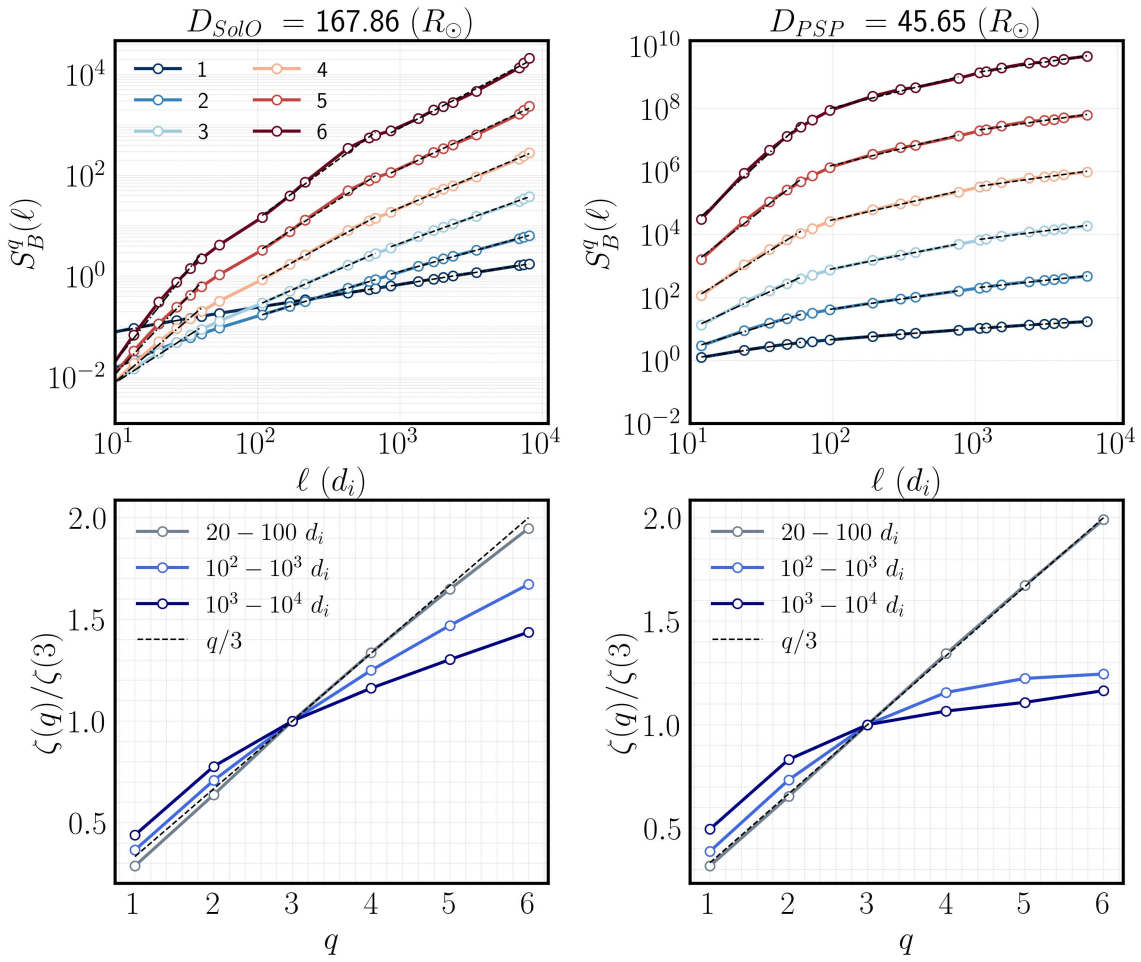

Figure 4.3: (a) Structure functions for $\delta\mathbf{B}$, as a function of spatial lags in units of the ion inertial length d_i, $S_B^p(\ell)$. Power-law fits applied to $S_B^p(\ell)$, in the range (a) $20 - 10^2 d_i$, (b) $10^2 - 10^3 d_i$ (c) $10^3 - 10^4 d_i$ are shown as a dashed-dotted and dashed line respectively. (b) The normalized resulting scaling exponents $\zeta(q)/\zeta(3)$ as a function of q. The K41 (q/3) linear scalings is also shown for comparison.

in the plot. The bracketed numbers in the plots are the number of data points inside each bin. Note that bins that include less than 10 data points have been discarded. From this figure, we can understand that at small lags, there is a clear upward trend as a function of τ_{adv}, whereas, for larger spatial scales, such trend becomes progressively less obvious.

4.1.4.2 Structure Functions (SFs).

A convenient way to describe the scaling variation of PDFs of the field fluctuations is by observing the deviation of the structure-function scaling exponents from the linear

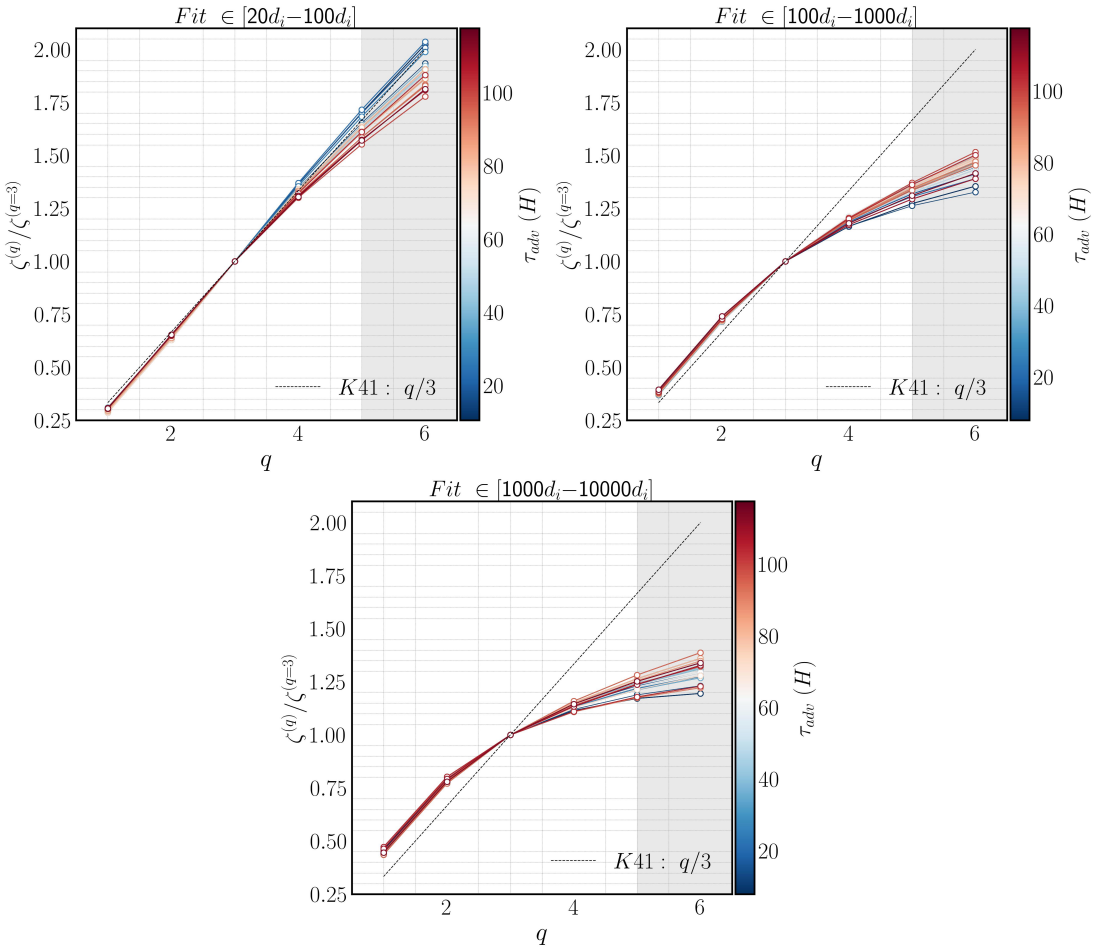

Figure 4.4: Normalized scaling exponents $\zeta(q)/\zeta(3)$ vs. q, as a function of advection time τ_{adv}. Each line represents the average of 100 intervals that fall within the same τ_{adv} bin. The scaling exponents have been obtained by applying a power-law fit on the structure functions ($S_B^q(\ell)$) within three different spatial ranges: (a) $[20d_i, 100d_i]$, (b) $[100d_i, 1000d_i]$, (c) $[1000d_i, 10000d_i]$. The K41 linear scaling is also shown with the black dashed line in all panels. The shaded area has been included to indicate moments that are not determined with reliable accuracy.

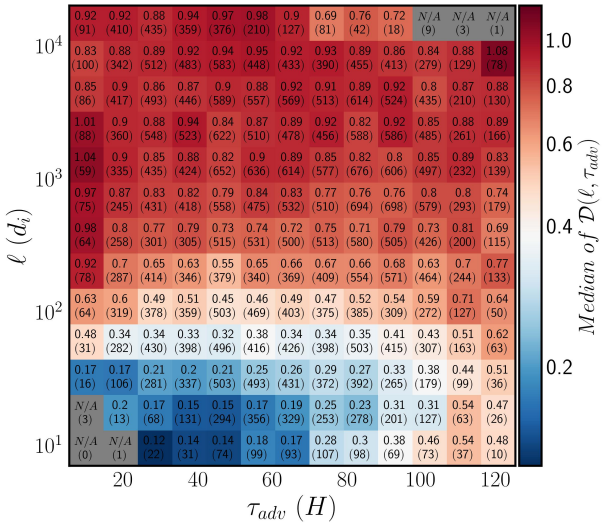

Figure 4.5: To further quantify the divergence from the linear scaling predicted by the K41 theory of isotropic turbulence, $z_{k41}^{(q)} = q/3$, and as a measure of intermittency at a given scale, the quantity $\mathcal{D}(\ell,\ \tau_{adv}) = (\sum(\frac{z(q,\ \ell)}{z(q=3,\ \ell)} - z_{k41}(q))^2)^{1/2}$ is presented. The data points were binned according to ℓ, and τ_{adv}, and the median value inside each bin was calculated, which is reflected in the colors and written in the plot. The bracketed numbers in the plots are the number of data points inside each bin. Note that bins, including less than 10 data points, were discarded.

dependence on the order.

We thus proceed by dividing $\zeta(q)$ for the different lag ranges by $\zeta(3)$ for the respective range. Two $d = 5$ hr-long intervals, sampled by PSP, and SolO, were randomly selected, and the structure functions $S_B^q(\ell)$ up to sixth order were calculated. Power-law fits have been applied on each q_{th} order structure-function in the ranges between $(20 - 10^2 d_i)$, $(10^2 - 10^3 d_i)$ and $(10^3 - 10^4 d_i)$ respectively. The resulting power-law exponents $\zeta(q)$ are presented in Figure 4.3. The same process was then repeated for each of the 3100 intervals, and $\zeta(q)/\zeta(3)$ as a function of q for the three different spatial scales is portrayed in Figure 4.4. It is important to note that the statistical accuracy of higher-order moments is affected by sample size. As a general rule, the highest order that can be computed reliably is $q_{max} = log(N) - 1$, where N is the number of samples (Dudok de Wit et al., 2013). In this case, since the majority of the intervals contain $N \sim 72000$ samples, we can estimate $q_{max} \approx 4$, meaning that higher-order statistics should be interpreted with caution. Consequently, a shaded gray area has been added to all the figures to indicate scaling

exponents recovered for moments that were determined with questionable accuracy.

In Figure 4.4a, the scaling exponents obtained by applying a best-fit linear gradient in log-log space over a window that spans between $(20 - 10^2 d_i)$ are shown. Over this range of spatial scales, which, roughly speaking, corresponds to the transition region (Bowen et al., 2020c), the scaling exponents obtain the highest observed values, indicating the presence of relatively stronger gradients in the magnetic field. Additionally, a roughly linear, i.e., monofractal, but super-Gaussian scaling at lower τ_{adv}, which after normalization with $\zeta(3)$, closely resembles the K41 predicted curve, is obtained. However, as τ_{adv} increases, the lines exhibit a more concave behavior at large q. This result is in qualitative agreement with the results obtained through the SDK method and suggests the strengthening of transition range intermittency as a function of the advection time. In the inertial range, $(10^2 - 10^3 d_i)$ the normalized scaling exponents exhibit a concave scaling that strongly deviates from the K41 curve and does not show a dependence on the advection time of the solar wind. As a matter of fact, the concave scaling is observed at all times, indicating that the inertial range fluctuations exhibit a multifractal character even in the vicinity of the Sun. A similar behavior (i.e., multifractal scaling that does not evolve radially) is observed at yet larger, nonetheless still inertial, scales between $(10^3 - 10^4 d_i)$.

To provide a quantitative context for the radial evolution of intermittency with respect to the advection time of the solar wind, the quantity $\mathcal{D}(\ell,\ \tau_{adv}) = (\sum(\frac{z(q,\ \ell)}{z(q=3,\ \ell)} - z_{k41}(q))^2)^{1/2}$ was estimated. This quantity is essentially the distance between two curves. The first curve corresponds to the scaling exponents $z(q,\ \ell)$ estimated for 5 hr-long intervals by applying a moving power-law fit to each of the structure functions up to order $q = 6$, normalized by $z(q = 3,\ \ell)$; the second curve corresponds to the K41 prediction for the scaling exponents $z_{k41}^{(q)}$). More specifically, the scaling exponents $\zeta(q,\ \ell)$ have been obtained by applying a moving power-law fit on each of the structure functions up to sixth order over a range of scales in the spatial domain $\ell \in [x_i, 3x_i]$, where x_i is the starting point of the power-law fit; Each scaling exponent, $\zeta(q, \ell)$, has been normalized by $z(q = 3, \ell)$ estimated over the same range of the respective interval. As a result, for a given interval and over a certain range of spatial scales, six normalized scaling exponents

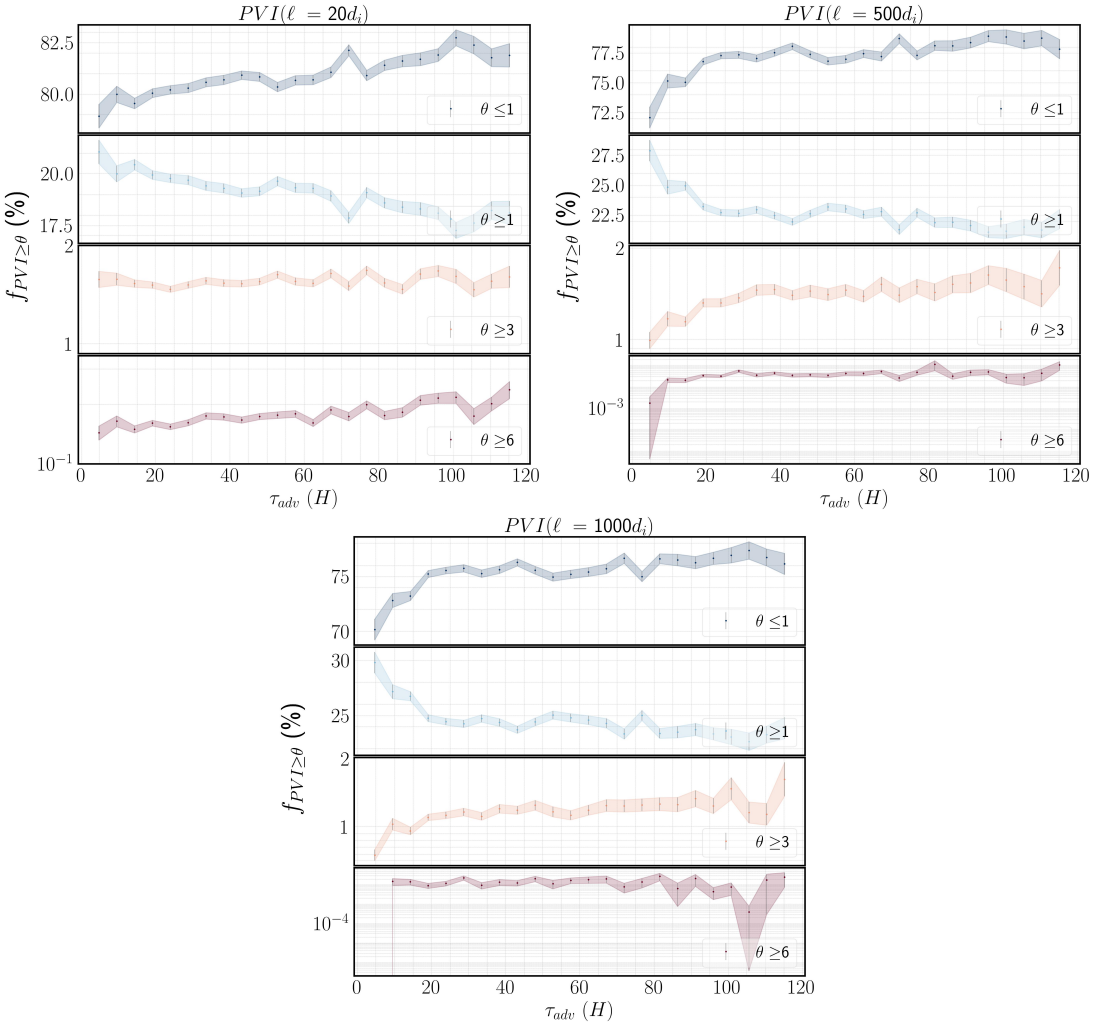

Figure 4.6: Binned mean of the fraction of datapoints with PVI value exceeding a given threshold ($f_{PVI\geq\theta}$, where $\theta = [1, 3, 6]$) shown as a function of advection time τ_{adv}, different thresholds are shown in different colors. Three spatial lags normalized to the ion inertial length d_i are considered, $\ell = 20,\ 500,\ 1000\ d_i$.

$\zeta(q, \ell)/z(q = 3, \ell)$ have been obtained. Subsequently, the square of the deviation from the K41 prediction, $z^{(q)}_{k41}$), was estimated. Finally, the square root of the sum for $q = 1, ..., 6$ was calculated resulting in $\mathcal{D}(\ell, \tau_{adv})$. By sliding the moving fit window over the spatial domain, several estimates of $\mathcal{D}(\ell, \tau_{adv})$ have been obtained for different spatial scales over the same interval. The process was then repeated for all the available 5 hr-long intervals. Data points were subsequently binned according to ℓ and τ_{adv}, and the median value of $\mathcal{D}(\ell,\ \tau_{adv})$ inside each bin was calculated, which is reflected in the colors. The results of this analysis are illustrated in Figure 4.4. The picture that emerges fits well with the

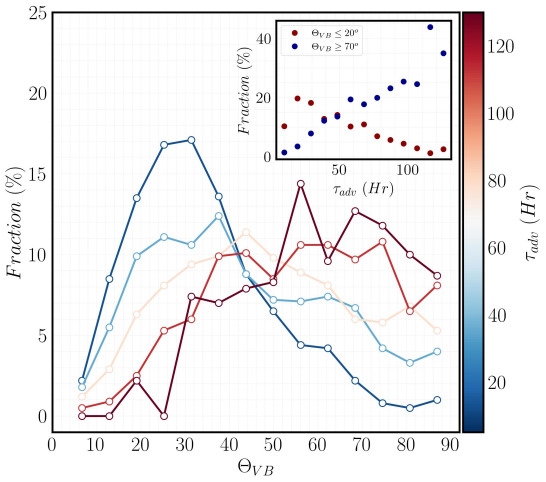

Figure 4.7: Five τ_{adv} bins are utilized to illustrate the fraction of Θ_{VB} angles for intervals that fall within each of the bins. Note that the alignment angle is constrained to lie in the range between 0° and 90°. For clarity, the inset figure shows the fraction of the dataset occupied by parallel ($\Theta_{VB} \leq$ 20°) and perpendicular intervals $\Theta_{VB} \geq$ 70°.

evolution of SDK (see Figure 4.2) since the general trend is towards stronger intermittency at larger τ_{adv} for $\ell \lesssim 100d_i$ and no dependence on the advection time for $\ell \gtrsim 100d_i$. Obviously, the statistical trend is heavily influenced by the higher-order moments. The normalized scaling exponents, which relate to the moments of order $q \leq 3$, remain almost linear (see Figure 4.4), hence contributing a negligible amount to the difference between the two curves. It is also important to note that the same process was repeated by only taking into account scaling exponents up to 4^{th} order, and the results were found to be qualitatively similar.

4.1.4.3 Partial Variance of Increments (PVI).

In this section, we examine the radial dependence of intermittency by considering the evolution of the fractional volume with respect to the overall fluctuations occupied by coherent structures identified by means of the PVI method. As suggested in (Greco et al., 2008), we consider a coherent structure any event for which the corresponding PVI index attains a value of $PVI > 2.5$. To estimate the PVI timeseries we follow the method outlined in Section 4.1.4.3 and employ non-overlapping 10 hr-long intervals sampled by PSP and SolO throughout the inner heliosphere. To ensure estimating the PVI on a

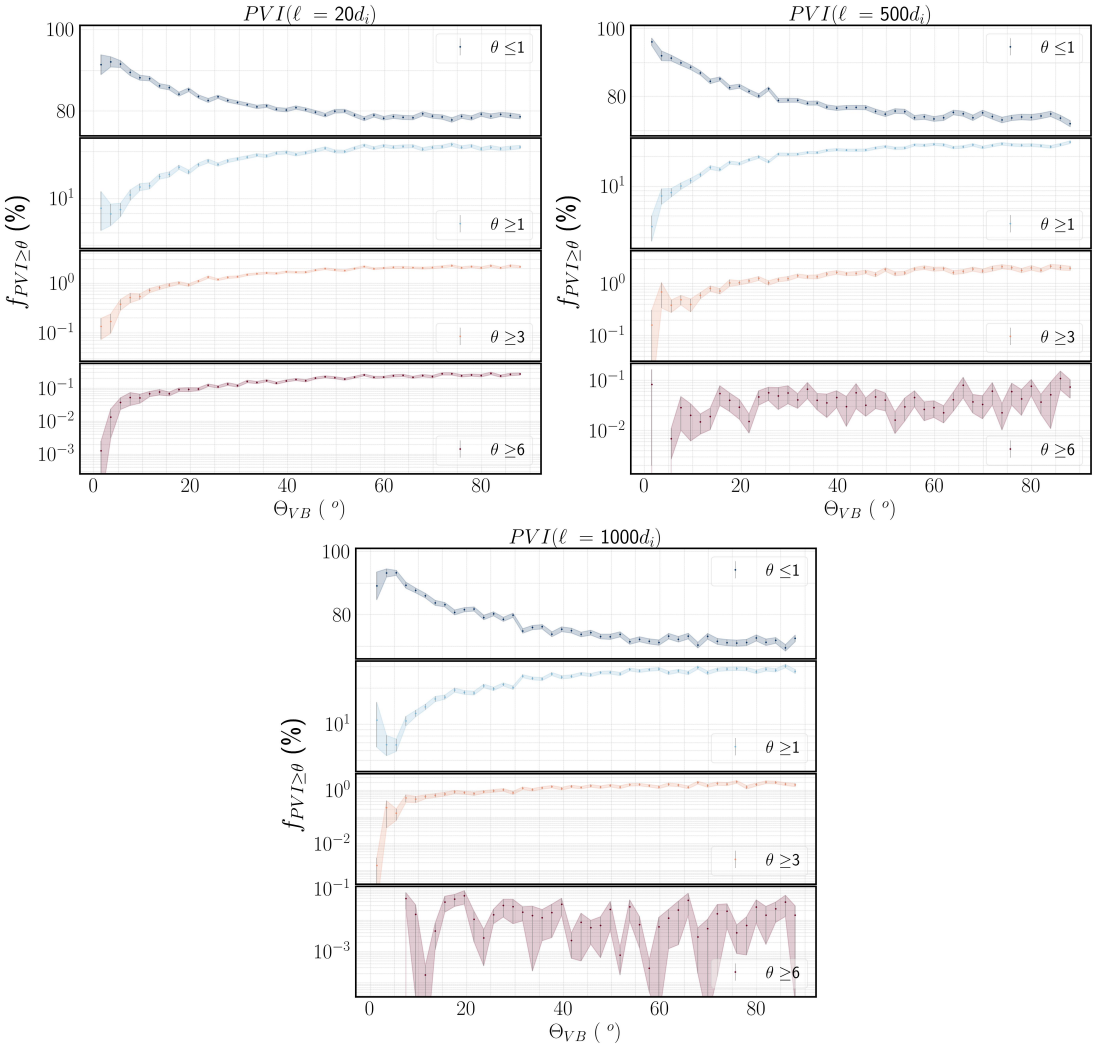

Figure 4.8: Binned mean of the fraction of PVI events $f_{PVI\geq\theta}$ (%), where $\theta = 1,\ 3,\ 6$ as a function of the angle between solar wind and background magnetic field Θ_{VB}. Three different lags are considered ($\ell = 1000,\ 500,\ 20\ d_i$). A total number of $n = 45$ bins have been used.

constant plasma scale, we adapt a lag normalized by the ion inertial length estimated at the respective interval (see Section. 4.1.4.3). After the PVI timeseries is estimated, data are further divided into 15-minute intervals, and the mean plasma advection time τ_{adv} for each interval is estimated. As a result of this process, a total number of $\sim 30,000$, intervals of duration $d = 15$ minutes are collected throughout the inner heliosphere. For a given interval, each data point is assigned a PVI value, and the fraction of the data points exceeding a certain PVI threshold $f_{PVI\geq\theta}$, where, $\theta = 1,\ 3,\ 6$, is estimated. In Figure 4.15a,b,c, we use 25 bins, to present the average value of $f_{PVI\geq\theta}$ per bin plotted against τ_{adv}, for PVI estimated with a lag of $\ell = 20,\ 500,\ 1000\ d_i$, respectively. Uncertainty bars indicate the standard error of the sample. It is readily seen that as we move to smaller spatial lags (i.e., going from right to left panel), the fractional volume occupied by the extreme events is increasing. This result is consistent with the elevated probability density of extreme events when the PDFs of the magnetic increments are considered and indicates the presence of large gradients in the magnetic field at the smaller scales. In Figure 4.15a, for lag $\ell = 20d_i$ and PVI greater than 3 ($f_{PVI\geq3}$, orange line), no clear trend is observed with τ_{adv}. This result introduces a paradox to our analysis as it seems to contradict the evolution of SDK at the smaller scales, shown in Figure 4.2a. However, when the evolution of $f_{PVI\geq6}$ with lag $\ell = 20d_i$ (red line, panel a) is considered, a clear upward trend as a function of τ_{adv} is observed. Thus, a natural hypothesis to explain the apparent contradiction is that the evolution of scale-dependent kurtosis (SDK) is dominated by the presence of the extreme events ($PVI \gtrsim 6$) that usually lay on the tails of the PDFs of normalized magnetic increments. Is easy to understand that the fluctuations characterized by a smaller PVI index, albeit accounting for the bulk of the distribution of data points, have a relatively minor contribution to the final SDK values; On the other hand, even though the high PVI value events occupy only a small fraction of the dataset, they can significantly impact the behavior of SDK, due to the susceptibility of the fourth-order moment, found in the numerator to extreme increments. The trend of $f_{PVI\geq6}$ is also consistent with the evolution of SDK at larger scales, shown in Figure 4.15b,c, as in both cases, the line practically remains flat as a function of τ_{adv}. A different

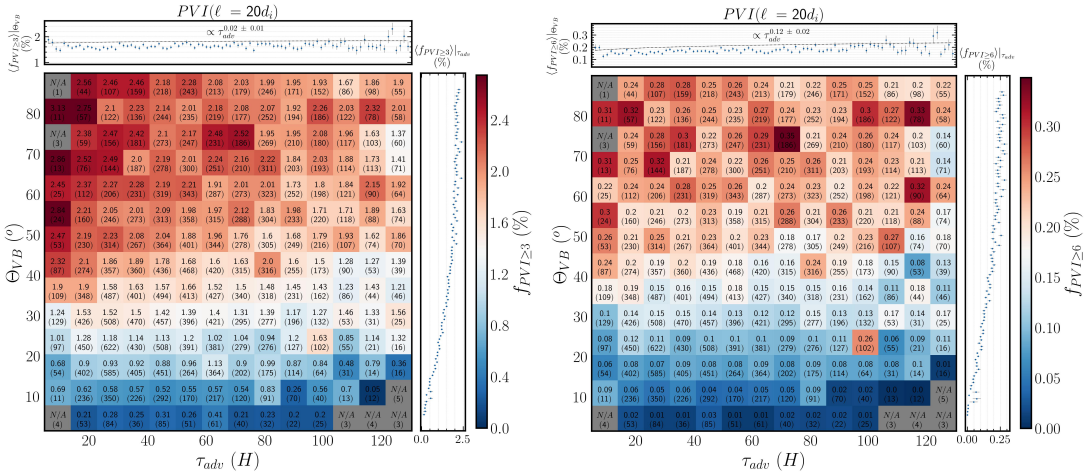

Figure 4.9: Binned mean of the fraction of datapoints with PVI value exceeding a given threshold, $f_{PVI\geq\theta}$, where $\theta = 3$ (left panel) and $\theta = 6$ (right panel) shown as a function of advection time τ_{adv} and Θ_{VB} angle. The PVI timeseries was estimated with a lag, $\ell = 20\ d_i$. The top subplot shows the averaged fraction of coherent structures, over Θ_{VB}, $\langle f_{PVI\geq\theta}\rangle|_{\Theta_{VB}}$. Power-law fits are also shown as black-dashed lines. Similarly, the right subplot shows the averaged fraction over τ_{adv}, $\langle f_{PVI\geq\theta}\rangle|_{\tau_{adv}}$.

trend is observed for $f_{PVI\geq 3}$, and $\ell = 500, 1000 d_i$. In both cases, an abrupt increase in $f_{PVI\geq 3}$ (yellow line) is observed up to $\sim 20 - 25$ hours. This feature is of particular importance, as it could be related to the crossing of PSP through the Alfvén region and is further discussed in Section 4.1.6. Beyond this point, a slight upward trend is observed at both lags for subsequent times. Another interesting feature in Figures 4.15a,b,c is the evolution of fluctuations with $PVI < 1$, as in all three cases a monotonic increase of $f_{PVI\leq 1}$ with τ_{adv} is observed. Since both $f_{PVI\leq 1}$ and $f_{PVI\leq 3}$ are following an upward trend, we can understand that the fluctuations in the $1 \lesssim PVI \lesssim 3$ are gradually getting depleted as the solar wind expands. In particular, for ℓ, the depletion process is gradual with a decrease of ≈ 2.5 %, observed between 5 and 130 hours. On the other hand, at the largest scales following an abrupt decrease of ≈ 5 % up to ≈ 25H, the $f_{PVI<1}$ practically remains constant over the ranges examined.

4.1.4.4 Angle between Solar Wind Flow and Magnetic Field Θ_{VB}

Two important factors need to be considered when studying the radial evolution of intermittency in the solar wind: (a) MHD turbulence in the solar wind has a well-known

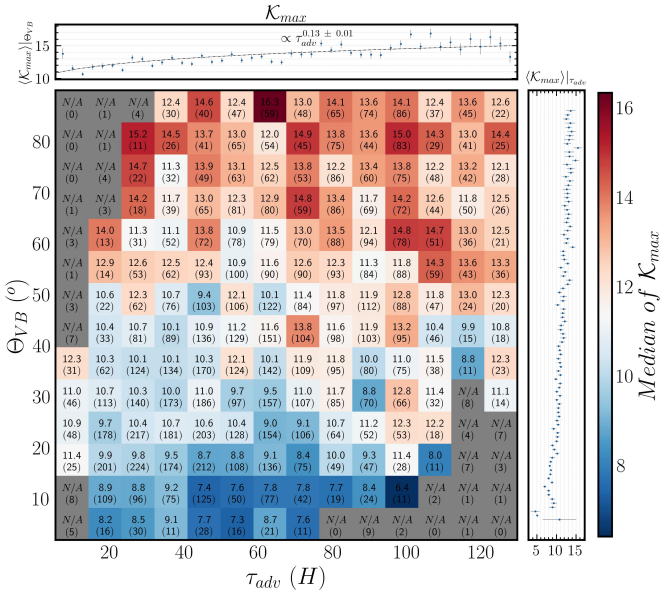

Figure 4.10: Scale-dependent kurtosis of the magnetic field as a function of Θ_{VB} and τ_{adv}. The numbers indicate the median value of kurtosis within each bin. The top subplot shows K_{max}, over Θ_{VB}, $\langle K_{max} \rangle|_{\Theta_{VB}}$. Power-law fits are also shown as black-dashed lines. Similarly, the right subplot shows the averaged fraction over τ_{adv}, $\langle K_{max} \rangle|_{\tau_{adv}}$.

tendency to develop and sustain several manifestations of anisotropy, e.g., wavevector anisotropy, variance anisotropy, etc. (Oughton et al., 2015). One of these is the anisotropy in magnetic field intermittency introduced by the presence of the background solar wind flow. For parallel intervals (i.e., $\Theta_{VB} \approx 0°$, or equivalently $\Theta_{VB} \approx 180°$), the statistical signature of the magnetic field fluctuations is that of a non-Gaussian globally scale-invariant process, in contrast to multi-exponent statistics observed when the local magnetic field is perpendicular to the flow direction (Horbury et al., 2008; Osman et al., 2012). (b) Because of the conservation of magnetic flux (Parker Spiral), the radial component of the magnetic field decreases faster than the transverse component.

Consequently, as radial distance increases, so does the number of perpendicular intervals. On the other hand, as shown in the inset of Figure 4.7, the fraction of parallel/anti-parallel intervals is monotonically decreasing. Therefore, for a complete understanding of the radial evolution of intermittency in the solar wind, an analysis that takes into account both τ_{adv} and Θ_{VB} is required. In this section, we examine the radial evolution of anisotropic intermittency by means of the PVI and SDK methods. As a first

step, the PVI method and the 15-min intervals are adapted. Having confirmed that the anisotropy is symmetric with respect to $\Theta_{VB} = 90°$, we proceeded by not distinguishing between parallel and anti-parallel directions. As a result, intervals with an estimated $\Theta_{VB}^{init} \geq 90°$ have been recast to $\Theta_{VB} = 180° - \Theta_{VB}^{init}$. We, therefore, require that the alignment angles lie within a range between 0° and 90° degrees. In Figures 4.8a,b,c, the fraction of PVI events at a given PVI threshold, $f_{PVI \geq \theta}$, is plotted against the Θ_{VB} angle for PVI estimated with lag $\ell = 20,\ 500,\ 1000\ d_i$, respectively. For clarity, data have been binned into 45 linearly spaced bins in the Θ_{VB} domain, and each dot indicates the mean value of $f_{PVI \geq \theta}$ within the bin. Error bars are also shown, indicating the standard error of the mean. For $\ell = 20 d_i$ (Figure 4.8a), the fraction of random fluctuations with $PVI < 1$ is rapidly decreasing as intervals with greater Θ_{VB} angles are considered. The opposite trend is observed in the fraction of magnetic increments with $PVI \geq 1$. As a matter of fact, the anisotropy grows stronger as higher PVI thresholds are considered. For instance, an increase in $f_{PVI \geq \theta}$ of at least one and two orders of magnitude is recovered between the lowest and highest Θ_{VB} angles for PVI thresholds $\theta = 3,\ 6$, respectively. Note, however, that regardless of the PVI threshold value, the increasing trend is halted at $\Theta_{VB} \approx 50°$. Beyond this point, no statistically significant differences in $f_{PVI \geq \theta}$ are observed at the largest Θ_{VB} angles. A similar degree of anisotropy, as a function of Θ_{VB}, is recovered for larger lags ($\ell = 500, 1000 d_i$) shown in Figure 4.8b,c, respectively. Note, however, a deviation from the trend for $f_{PVI \geq 6}$ indicating that the degree of anisotropy is lessened at progressively larger spatial scales.

In Figure 4.9, the evolution of anisotropic intermittency is examined as a function of τ_{adv}. For this reason, the data points were binned according to Θ_{VB} and τ_{adv}, and the mean value inside each bin was calculated, which is reflected in the colors and presented in the plot. The bracketed numbers in the plots are the number of data points inside each bin. Note that bins, including less than 10 data points, were discarded. In Figure 4.9a, the dependence of $f_{PVI \geq 3}$ as a function of Θ_{VB} and τ_{adv} for lag $\ell = 20 d_i$ is illustrated. Two major but contradicting conclusions can be drawn from this figure: (1) When the evolution of intervals that belong to the same Θ_{VB} bin is considered, a monotonic decrease

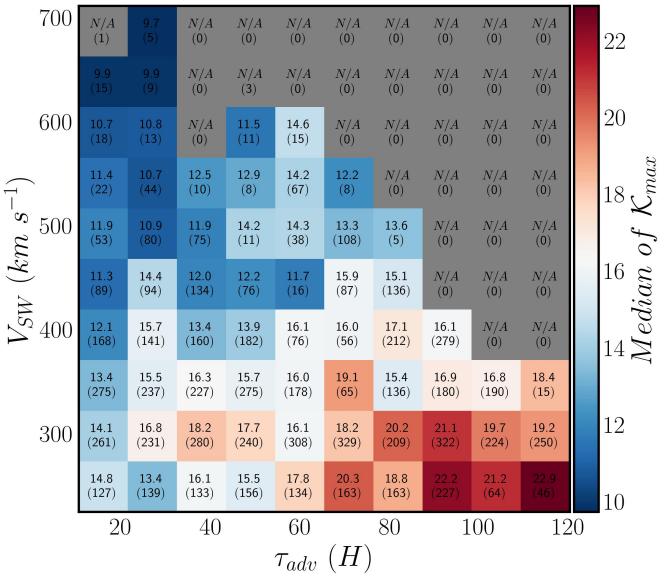

Figure 4.11: (a) Scale-dependent kurtosis of the magnetic field as a function of solar wind speed V_{SW} and SW advection time τ_{adv}. The numbers indicate the median value of kurtosis within each bin.

in $f_{PVI\geq 3}$ is observed for all Θ_{VB} rows. (2) The average $f_{PVI\geq 3}$, with regard to Θ_{VB}, shows a negligible, slightly positive trend as a function of τ_{adv}. This seemingly inconsistent result can be addressed by considering the radial evolution of the Parker spiral. Closer to the Sun, the solar wind speed and background magnetic field tend to be aligned, i.e., the intervals tend to concentrate around $\Theta_{VB} \sim 0°(180°)$. As we move further away from the Sun, this angle shifts towards the perpendicular direction, i.e., $\Theta_{VB} \sim 90°$. However, as shown in Figure 4.9, perpendicular intervals are typically associated with higher $f_{PVI\geq 3}$ values. Thus, despite the gradual decrease in the fraction of coherent structures with $PVI \geq 3$ as a function of τ_{adv} for a constant Θ_{VB} angle, on average, the fraction of the entire dataset shows signs of a very subtle increase. When considering the evolution of coherent structures of $PVI, \geq 6$, Figure 4.9b, a slightly different evolution may be noticed. In particular, not a clear trend is observed for intervals of constant Θ_{VB}. Additionally, as pointed out in Figure 4.8a the degree of anisotropy with regards to the Θ_{VB} angle is strengthened when higher PVI thresholds are considered. Therefore, by applying the same logic as outlined before for $PVI \geq 3$, we can explain the apparent increase in the fraction of coherent structures as a function of τ_{adv}.

We move on to examine the evolution of K_{max} as a function of τ_{adv} and Θ_{VB}. In order to mitigate the effects of mixing different types of solar wind, the duration of the intervals used has been reduced to $d = 30$ minutes. It is important to note that even though the radial trend of kurtosis is not affected (i.e., the maximum of the kurtosis is observed to increase with increasing τ_{adv} regardless of interval size), the curves are shifted vertically to larger values when larger averaging windows are considered. This may be attributed to the fact that by increasing the interval size, more and more extreme events are taken into consideration during the averaging process. Since these events have been shown to strongly affect the SDK, an increase of SDK for larger averaging windows is to be expected. The results of this analysis are illustrated in Figure 4.10. As expected, K_{max} follows a qualitatively similar trend with $f_{PVI\geq 6}$. More specifically, intervals for which the magnetic field and solar wind speed tend to be aligned exhibit lower K_{max} values. Moreover, no clear trend may be observed with τ_{adv} when examining intervals with a similar Θ_{VB}.

As a result of our analysis, it is apparent that understanding the physical mechanisms driving the evolution of intermittent properties in the magnetic field of the solar wind requires making a distinction between the effects of mixing strongly and less intermittently perpendicular and parallel intervals, respectively, as opposed to the evolution of turbulence during the expansion due to the local plasma dynamics.

4.1.5 Dependence of intermittency in plasma parameters.

4.1.5.1 Solar Wind Speed

In this section, the relationship between solar wind speed V_{SW} and magnetic field intermittency is investigated. Similarly to Section 4.1.4.4, to mitigate the effects of mixing different types of solar wind, the duration of the intervals used has been reduced to $d = 30$ minutes. Also, note that the intervals that are associated with fast solar wind $V_{SW} \gtrsim 600\ km\ s^{-1}$ comprise only a minor fraction of our dataset. Moreover, the majority of these intervals were observed during the latest perihelia of PSP and thus in proximity

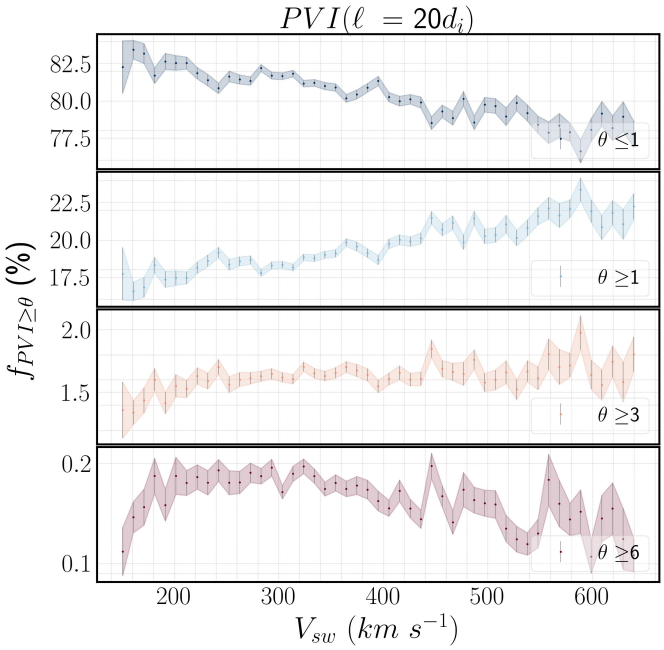

Figure 4.12: Fraction of datapoints with PVI value exceeding a given threshold, $f_{PVI \geq \theta}$, where $\theta = 1,\ 3, 6$ as a function of solar wind speed, V_{SW}.

to the Sun. Taking these arguments into account, we can understand that the study of the radial evolution of the fast wind is not feasible with our current dataset. Nevertheless, the study of intermittency properties as a function of V_{SW} is still possible since a considerable number of intervals with V_{SW} in the range 200 $km\ s^{-1} \lesssim V_{SW} \lesssim$ 600$km\ s^{-1}$ have been sampled by both PSP and SolO throughout the inner heliosphere. We begin our analysis by considering the relationship between K_{max} with τ_{adv} and V_{SW}, estimated for respective intervals. The results of this analysis are presented in Figure 4.11. In accordance with (Bruno et al., 2003; Weygand et al., 2006), we find that the kurtosis for the magnetic fluctuations in the slow solar wind exhibit higher peaks when compared to those of the fast solar wind. As a matter of fact, K_{max} almost monotonically decreases as a function of V_{SW} when intervals sampled at the same τ_{adv} column are considered. Additionally, regardless of the solar wind speed, K_{max}, increases as a function of τ_{adv}. This result comes in disagreement with (Bruno et al., 2003), as it indicates the radial strengthening of intermittency regardless of the solar wind speed.

Additionally, the relationship between the fractional volume occupied by coherent

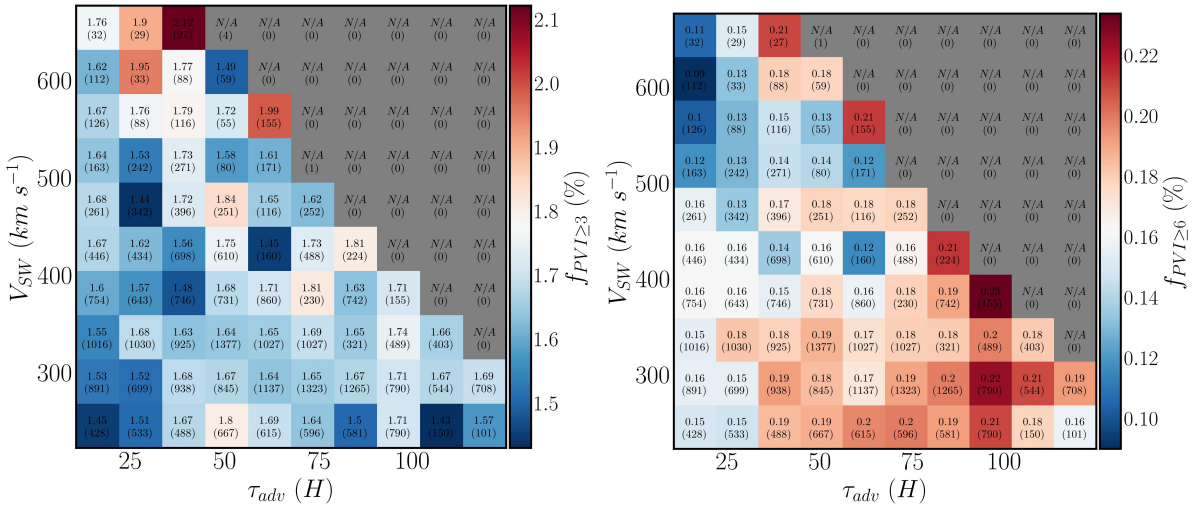

Figure 4.13: Fraction of datapoints with PVI value exceeding a given threshold, $f_{PVI\geq\theta}$, where (a) $\theta = 3$, (b) $\theta = 6$, as a function of V_{SW} and τ_{adv}. The numbers indicate the median value of $f_{PVI\geq\theta}$ and the bracketed numbers show the number of events within each bin.

structures, $f_{PVI\geq\theta}$, identified by using the PVI method, and V_{SW} is examined. The results of this analysis are illustrated in Figure 4.12, for PVI threshold $\theta = 1,\ 3,\ 6$. It is readily seen that fast solar wind is characterized by an elevated number density of magnetic increments with PVI index greater than unity, $\theta \geq 1$ (cyan line). Strictly speaking, and following the definition of

(Greco et al., 2008), only events of $PVI \gtrsim 2.5$ correspond to coherent structures and consequently strengthen the intermittent character of the magnetic fluctuations. However, this result is of interest as it was recently shown (Sioulas et al., 2022) that the number density of structures with PVI index greater than unity $f_{PVI\geq 1}$ is very strongly correlated with the temperature of protons T_p in the solar wind. At the same time, one of the clearest correlations between plasma parameters in the solar wind is the one between proton temperature with solar wind speed (Perrone et al., 2019). It is thus quite probable that events of PVI index greater than unity not only contribute to magnetic energy dissipation and the heating of the ambient plasma environment but at the same time are partly responsible for the acceleration of the solar wind. Moving on and considering the events of $\theta \geq 3$ (shown in yellow), a picture that contradicts our conclusions from the SDK analysis outlined earlier emerges. In particular, within the error bars, no statistically

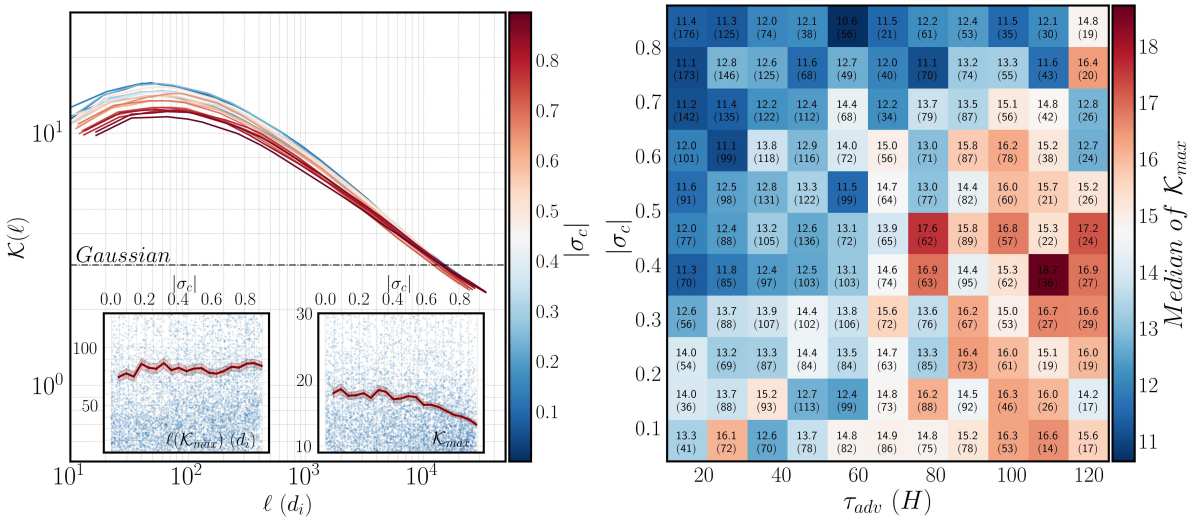

Figure 4.14: (a) Scale-dependent kurtosis of the magnetic field as a function of scale in units of ion inertial length d_i and SW advection time τ_{adv}. The numbers indicate the mean value of kurtosis within each bin. (b) Evolution of SDK with τ_{adv}. Each line represents the average of 100 intervals that fall within the same τ_{adv} bin. The inset scatter plots show (i) the scale, in units of d_i, at which the kurtosis attains the maximum value (ii) The maximum kurtosis value estimated for the individual 30-min intervals. The binned mean of the two quantities is shown (red line).

significant differences in the fractional volume occupied by coherent structures can be observed between fast and slow solar wind streams. As a matter of fact, one could even argue that a slight increase of $f_{PVI\geq 3}$ can be observed with increasing solar wind speed. A different picture emerges when we consider the highest PVI threshold $PVI \geq 6$. More specifically, $f_{PVI\geq 6}$ is progressively reduced when faster solar wind streams are considered. This result provides a natural explanation for the lower SDK peaks observed at faster solar wind streams since, as already discussed, the number density of PVI greater than 6 events, $f_{PVI\geq 6}$ is tightly correlated with K_{max}. We move on to investigate the evolution of $f_{PVI\geq\theta}$ as a function of V_{SW} and τ_{adv}. The results are presented in Figure4.13 for $PVI \geq 3$, and $PVI \geq 6$ respectively. For $PVI \geq 3$, though on average slightly higher values of $f_{fVI\geq 3}$, may be observed at greater τ_{adv}, there is, strictly speaking, not a clear horizontal trend. On the contrary, for $PVI \geq 6$, an increasing trend is observed for most of the rows (i.e., streams of similar solar wind speed) in qualitative agreement with the increasing K_{max} reported in Figure 4.12.

4.1.5.2 Normalized cross helicity.

In this section, the correlation between the normalized cross-helicity and intermittency, as indicated by the scale-dependent kurtosis (SDK) of the magnetic field magnitude, is examined. Note that for this analysis, the length of the interval has been reduced to $d = 30min$, to ensure that σ_c does not vary significantly within the interval. For each interval, the median of σ_c has been estimated, and intervals with standard deviation of σ_c greater than 0.2 have been discarded. In Figure 4.14a, the dependence of SDK as a function of $|\sigma_c|$ is illustrated. Note that each line corresponds to the average of 100 intervals that fall within the same $|\sigma_c|$ bin. As shown in the right inset figure, the maximum value of kurtosis is decreasing with increasing $|\sigma_c|$, indicating that Alfvénicity is negatively correlated with intermittency. However, it has been shown that the Alfvénic character of the field fluctuations in the solar wind strongly decreases with radial distance (Chen et al., 2020; Shi et al., 2021). Therefore, to distinguish between the effects of radial evolution and decrease in σ_c, we show in Figure 4.14b, the dependence of K_{max} as a function of $|\sigma_c|$ and τ_{adv}. It is readily noticed, that on average, highly Alfvénic intervals, exhibit lower K_{max} values. Nevertheless, it is evident that for a any $|\sigma_c|$ row in Figure 4.14, an increasing trend is observed for K_{max} at larger τ_{adv} values. The increase may be explained by the fact that there is still a mixing of parallel and perpendicular intervals outlined in Section 4.1.4.4.

4.1.6 Conclusions

This study has tried to address the following question: How do the statistical signatures of turbulence and intermittency evolve as the solar wind expands in the inner Heliosphere?

Intermittency lies at the heart of MHD turbulence in the solar wind. Thus, an improved understanding of its radial evolution can offer insights into some of the major open problems in the field of space physics, including the origins of the fluctuations and coherent structures observed in the solar wind; the influence of local and global dynamics in the evolution of the higher-order statistics; and ultimately into fundamental questions,

such as the generation, acceleration and adiabatic expansion of solar and stellar winds. For this purpose, we have analyzed high-resolution magnetic field and particle data from the first 11 orbits of the Parker Solar Probe mission, as well as Solar Orbiter observations, ranging from the vicinity of the Alfvén region ($R \approx 13.7\ R_{\odot}$) out to 1 au ($R \approx 215\ R_{\odot}$). Our study has been made possible by a variety of statistical tools, such as the Scale Dependent Kurtosis, the normalized scaling exponents of the Structure functions, and the PVI method that enable us to exploit the property of PDFs of intermittency affected magnetic fluctuations to be increasingly flared out at progressively smaller scales.

The main findings of our study can be summarized as follows:

(1) When methods utilizing higher-order moments are considered (e.g., SDK, SF_q), a strengthening of small-scale intermittency is observed with increasing advection time of the solar wind. Closer to the Sun, fluctuations of spatial scale $\ell \approx 20 - 10^2 d_i$, exhibit a monofractal-like but Super-Gaussian scaling that gradually evolves into multifractal as the solar wind expands into the interplanetary medium. Deeper in the inertial range, a multifractal scaling is observed that does not exhibit clear signs of radial evolution.

(2) The PVI method provides a different perspective on the evolution of intermittency. For lag $\ell = 20 d_i$, the fraction of the dataset occupied by coherent structures, $f_{PVI \geq 3}$, displays a very subtle upward radial trend, whereas a more obvious increase is observed for $f_{PVI \geq 6}$. At larger spatial scales $\ell = 5 \cdot 10^2,\ 10^3 d_i$, the opposite trend is observed as $f_{PVI \geq 6}$ is, within the error bars, independent of radial distance, while an increasing trend is observed for $f_{PVI \geq 3}$. It is important to note, however, that even though the trend remains positive at larger τ_{adv}, the biggest gain is observed for $\tau_{adv} \lesssim 35$ hrs.

In an effort to explain the disparity between SDK and PVI on the radial evolution of intermittency, the relationship between $f_{PVI \geq \theta}$ and the maximum values of SDK, K_{max} was examined. We have shown that the fractional volume of events with $PVI \geq 6$ is strongly correlated with K_{max}. In light of this result, we can understand that methods relying on the estimate of higher-order moments as a measure of intermittency will

mostly be affected by the extreme events that lie at the very tails of the distribution of increments. Such events are usually characterized by PVI values of the order of $PVI \gtrsim 6$ and constitute only a minor fraction $\lesssim 0.2\%$ of the fluctuations observed in the solar wind. As a result, higher peaks in SDK may still be observed at larger τ_{adv} even though $f_{PVI\geq 3}$ stays constant as long as $f_{PVI\geq 6}$ radially increases. However, to fully characterize the radial evolution of intermittency, one has to also take into account the evolution of coherent structures with $PVI \geq 3$, as these structures have been shown to dissipate a considerable amount of magnetic energy in the solar wind (Osman et al., 2012). In other words, a comprehensive analysis of the radial evolution of intermittency in the solar wind requires the use of lower-order moment-based methods, such as PVI.

(3) CSS can both decay and reform due to local plasma dynamics during the expansion, with in situ generation being more efficient at the larger scales (Figure 4.15). Nevertheless, the existence of passively advected coherent structures of Solar origin cannot be ruled out.

An observation that warrants a brief discussion is the abrupt increase incoherent structures of $PVI \geq 3$ at the largest spatial scales in the vicinity of the Alfvén region. Recently (Tenerani et al., 2021) have analyzed PSP, Helios, and Ulysses data to show that the evolution of the occurrence rate of Switchbacks in the solar wind is scale-dependent as the fraction of longer-duration switchbacks increases with radial distance, whereas it decreases for shorter switchbacks. The PVI method is agnostic to the nature of the discontinuities, meaning that coherent structures may be identified by PVI as long as there are strong gradients in the magnetic field. As a result, several types of coherent structures such as current sheets, vortices, reconnection exhausts, and switchbacks may be identified with the PVI method. In this sense, one contributing factor to the increasing fraction of the dataset occupied by coherent structures might be the increasing trend of longer-duration switchbacks associated with increasing solar wind advection times. At the same time, several mechanisms, including stream-stream dynamic interactions, parametric decay instability of large amplitude Alfvén waves, (e.g., Biskamp and Müller, 2000; Malara et al., 2001; Wan et al., 2009) might coexist simultaneously, resulting in the

generation of several types of CSS.

(4) In agreement with earlier studies, we identify a strong anisotropy in intermittency with respect to the angle between the background magnetic field and the solar wind flow. Intermittency is weaker at $\Theta_{VB} \approx 0^\circ$ and is progressively strengthened at larger angles. More specifically, peaks in the SDK (K_{max}) are shifted upward, and an increase is observed in the fraction of the dataset occupied by coherent structures ($PVI \geq 3$) when intervals with increasingly larger Θ_{VB} angles are considered. The anisotropy is more pronounced at higher PVI thresholds but becomes weaker at progressively larger spatial scales ;

(5) Even though at the smallest scales ($\ell = 20d_i$), the fraction of the dataset occupied by coherent structures ($PVI \geq 3$) radially decreases for intervals with fixed Θ_{VB}, on average (i.e., averaging over all Θ_{VB} bins at a given τ_{adv} column in Figure 4.9) the fraction of measured coherent structures increases in the inner Heliosphere. This is because closer to the Sun, the solar wind flow is statistically (anti)parallel to the magnetic field (i.e., $\Theta_{VB} \approx 0^\circ(180^\circ)$. However, due to the radial evolution of the Parker Spiral, the fraction of observed parallel intervals gradually decreases. Note that the changing fraction of parallel vs. perpendicular intervals is due to the limitations of the single-point measurements by PSP and the use of the Taylor hypothesis and not a reflection of the radial evolution of turbulence. Taking the Θ_{VB} anisotropy into account (see point (3)), we can understand that the mixing of highly intermittent perpendicular and relatively less intermittent parallel intervals blur the averaged behavior of the radial evolution of intermittency. Due to the fact that the anisotropy is stronger at a higher PVI threshold, the averaged fraction of events with $PVI \geq 6$ shows a more prominent positive radial trend with τ_{adv}. This increase is also reflected in K_{max}, as already discussed in (2).

(6) Solar wind of lower speed exhibits higher SDK peaks and is characterized by a higher fraction of $f_{PVI\geq 6}$ events. However, no statistically significant differences are observed in $f_{PVI\geq 3}$ as a function of solar wind speed. A strengthening of intermittency

with respect to the advection time τ_{adv} is observed regardless of solar wind speed. (see Figures 4.11, 4.12, 4.13)

(7) A negative correlation is observed between the absolute value of the normalized cross-helicity and intermittency of the magnetic field. That is, Alfvénic intervals statistically display lower levels of intermittency as indicated by the maximum value of the SDK. (see Figure 4.14)

As already discussed in point 4, the mixing of parallel and perpendicular intervals in the inner Heliosphere will result in a subtle radial increase in intermittency. However, perpendicular intervals are expected to progressively dominate with increasing heliocentric distance due to the conservation of magnetic flux (i.e., Parker Spiral). It is, therefore natural to expect that when the fraction of parallel intervals becomes statistically insignificant, the decreasing trend in the fraction of the dataset occupied by coherent structures will become apparent. Several observational studies have indicated that intermittency is expected to become progressively weaker with increasing heliocentric distance beyond 1AU (Parashar et al., 2019; Cuesta et al., 2022b). Based on our analysis, we propose that the decreasing trend in intermittency beyond 1AU can be attributed to the fact that the mixing effect is diminished due to the dominance of perpendicular intervals.

Finally, our results indicate that when it comes to analyzing the radial evolution of turbulence and intermittency, monitoring the changes in sampling direction is crucial. As the interplanetary magnetic field follows the Parker spiral, its angle with the spacecraft sampling direction will also vary as the distance from the Sun increases, which will then have an effect on measured turbulence characteristics. This effect needs to be disentangled from observations before the nature of the radial evolution of turbulence can be revealed. Previous studies using PSP data to analyze the radial evolution of intermittency have not taken this effect into consideration. However, our analysis indicates that obtaining such information is essential for understanding the more complex dynamics of the solar wind in the inner Heliosphere and can facilitate improvements to simulations of the solar wind (see also, Zhao et al., 2020; Chhiber et al., 2021b; Cuesta et al., 2022a).

As a final remark, we would like to caution the reader of a possible caveat to the current analysis. As PSP approaches the Sun, $\sim 10 - 15 R_{\odot}$, the spacecraft velocity can be similar to that of the solar wind $V_{sc} \sim V_{sw}$. As a result, the validity of the ergodic theorem is at best questionable (Matthaeus and Goldstein, 1982a) and could hinder our ability to perform statistical analysis that involves an ensemble averaging process (e.g. the estimate of moments of the field fluctuations). In any case, such intervals only make up a small portion of the entire dataset and should not affect the main conclusions of this section.

Our results will further the understanding of how CSs are generated and transported in the solar wind and will guide the development of future solar wind turbulence models.

4.2 Preferential Proton over Electron Heating from Coherent Structures & Statistical Analysis of Intermittency in the Near-Sun Environment

This section integrates findings from two published works (Sioulas et al., 2022; Sioulas et al., 2022)

4.2.1 Introduction

Observational and numerical studies indicate that plasma heating occurs in an intermittent fashion and suggest a statistical link between coherent magnetic field structures (CSs) and elevated temperatures (Osman et al., 2012; Chasapis et al., 2015; Yordanova et al., 2021; **?**). The intermittent character of turbulence can be attributed to a fractally distributed population of small-scale CSs, superposed on a background of random fluctuations that, despite occupying only a minor fraction of the entire dataset (Vlahos et al., 2008; Parashar et al., 2009; Osman et al., 2012; Wan et al., 2012; Sioulas et al., 2020a,b) can account for a disproportionate amount of magnetic energy dissipation, and heating of charged particles (Karimabadi et al., 2013; Sioulas et al., 2020a,b; Bandyopadhyay et al., 2020).

In this study, we aim to investigate the proton *vs.* electron heating in the nascent solar wind environment. For this reason, we analyze the Quasi-Thermal Noise (QTN) electron data and proton data from the Solar Probe Analyzer (SPAN) part of the Solar Wind Electron, Alpha, and Proton (SWEAP) suite (Kasper et al., 2016) form Parker Solar Probe mission (PSP) with the Sun (Fox et al., 2016). We examine the properties of proton and electron heating occurring within magnetic coherent structures identified by means of the Partial Variance of Increments (PVI) method. We show that on average, such events constitute $\approx 19\%$ of the dataset, though variations may occur depending on the plasma parameters. We show that the waiting time distribution (WT) of identified events is consistent across all six encounters following a power-law scaling at lower WTs. This result indicates that coherent structures are not evenly distributed in the solar

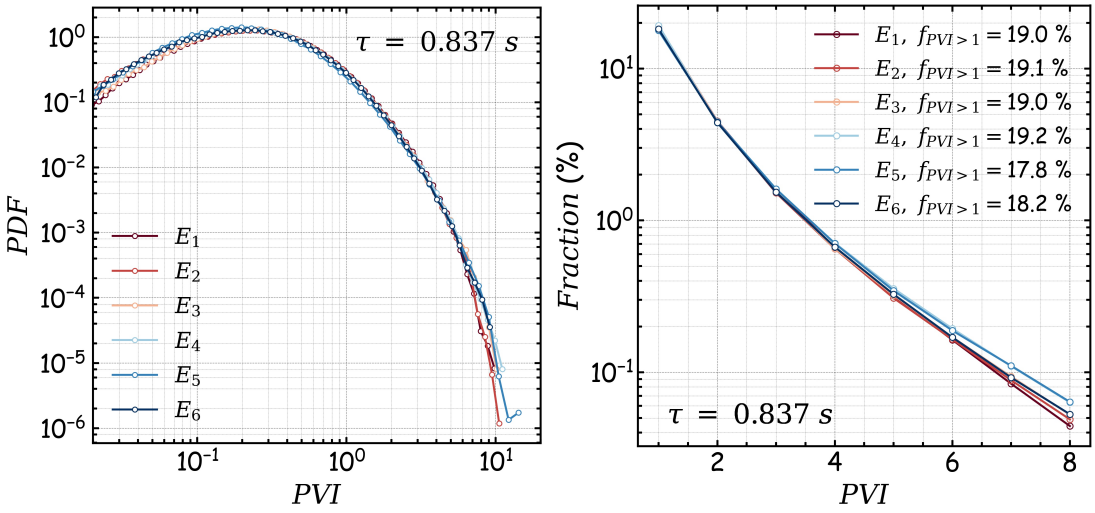

Figure 4.15: (a) PDFs of PVI for lag, $\tau = 0.837s$ (b) Fraction of PVI events exceeding a given threshold θ for $E_1 - E_6$.

wind but rather tend to be tightly correlated and form clusters. Statistically, regions of space with strong gradients in the magnetic field, $PVI \geq 1$, are associated with strongly enhanced proton but only slightly elevated electron temperatures. Our analysis indicates a heating mechanism in the nascent solar wind environment facilitated by a nonlinear turbulent cascade that preferentially heats protons over electrons.

The structure of this paper is as follows: Section 4.2.2 presents the selected data and their processing; In Section 4.2.3.2 we present the results of this study; Section 4.2.4 provides a summary of the results and conclusions.

4.2.2 Data

For the first part of this work we analyze data from first six encounters ($E_1 - E_6$) of PSP from 2018 to 2020, covering heliocentric distances $0.1 \lesssim R \lesssim 0.25$ au. We use magnetic field data from the FIELDS fluxgate magnetometers (Bale et al., 2016). To estimate the PVI time-series at time-lags, $\tau =$ 0.837 *seconds* magnetic field data have been resampled to a cadence of 0.837 *seconds* using linear interpolation. As outlined in Sec 2.0.7, in order to compute the variance, a moving average over a window that is a multiple of the correlation time is required. The correlation time can be estimated

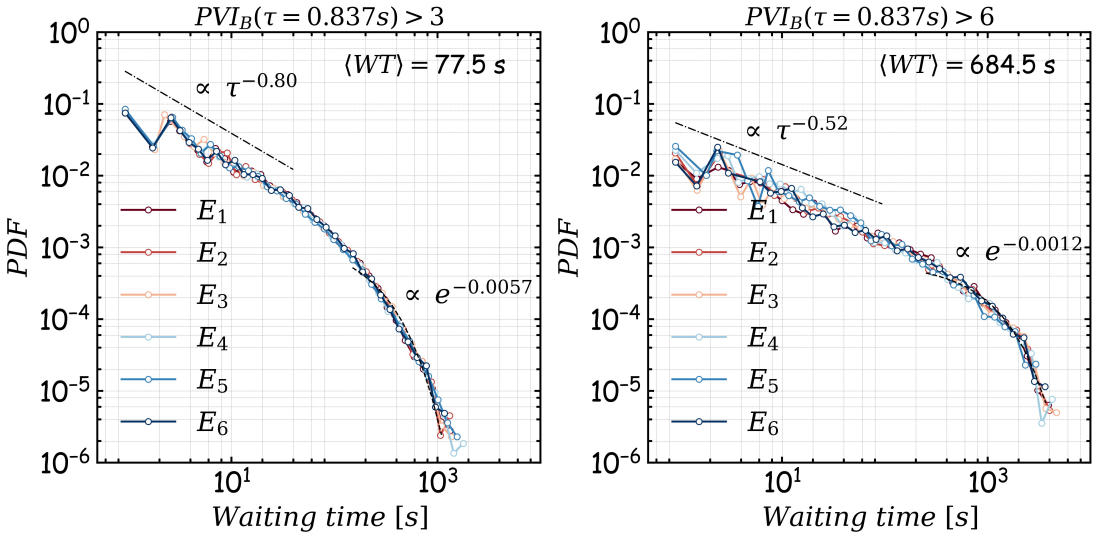

Figure 4.16: PDFs of WT between (a) $PVI > 3$, (b) $PVI > 6$ events for lag $\tau = 0.837$ *seconds*.

using the e-folding technique by considering the time it takes for the autocorrelation function to drop to e^{-1} of its maximum value (Matthaeus and Goldstein, 1982b; Krishna Jagarlamudi et al., 2019). For encounters $E_1 - E_6$, the correlation time was estimated to be between $500 \lesssim t \lesssim 2000$ *seconds*. Accordingly, we perform the ensemble averaging over a window of 8 hours for all six encounters. Several different averaging windows, ranging $2 - 12$ *hours* have been implemented, with qualitatively similar results on our analysis. Plasma data from Solar Probe Cup (SPC), part of the Solar Wind Electron, Alpha and Proton (SWEAP) suite (Kasper et al., 2016) have also been analyzed to obtain the bulk velocity and radial proton temperature/thermal speed measurements at ~ 0.837 *seconds* resolution. The radial temperature and bulk velocity time-series have been pre-processed to eliminate spurious spikes and outliers using the Hampel filter (Davies and Gather, 1993b). An important effect that should be taken into account when analyzing solar wind particle data is the anisotropy in the parallel ($T_{||}$) and perpendicular ($T_{\perp}$) temperatures with respect to the background magnetic field (Huang et al., 2020; Hellinger et al., 2011).

On the second, part, we focus solely first encounter E1 of PSP with the Sun, during the period November 1 - November 10, 2018. For magnetic field measurements, in order to obtain high-quality data without interference from instrumental noise, which could lead to

an artificial flattening of the power spectrum at the highest frequencies, we use the SCaM data product, which merges fluxgate and search-coil magnetometer (SCM) measurements from the FIELDS instrument (Bale et al., 2016) by making use of frequency-dependent merging coefficients, thus enabling magnetic field observations from DC to 1MHz with an optimal signal-to-noise ratio (Bowen et al., 2020a). Proton data were obtained from the Solar Wind Electron, Alpha, and Proton (SWEAP) suite (Kasper et al., 2016), and electron data derived from the Quasi-thermal noise from the FIELDS instrument (Moncuquet et al., 2020a). Note, that the same electron analysis was repeated by taking into account core temperature data fitted from the SPAN-e electron VDFS (Halekas et al., 2020), with qualitatively similar results.

In order to estimate the PVI timeseries, SCaM magnetic field data have been linearly interpolated to a cadence of $\delta\tau = 0.05$s. Subsequently, the PVI timeseries was estimated using an averaging window of duration $d = 8$ hours, which was several times the estimated correlation time of the magnetic field for E1 of PSP (Chhiber et al., 2020b). A lag of $\delta\tau = 0.05$s was used in estimating the PVI timeseries. Based on Taylor's hypothesis we can convert the temporal to spatial lag. We can then estimate the time-to-time ratio of the spatial lag to the ion inertial length to obtain the mean value of the spatial lag in units of the ion inertial length (d_i). The obtained d_i timeseries, not shown here, is in agreement with (Parashar et al., 2020). Therefore, the mean value of the spatial lag normalized in units of d_i value corresponds to $\tilde{\ell} \approx 0.76\ d_i$, with a standard deviation of $\pm 0.18\ d_i$. Note that the analysis was also carried out for various averaging times (from 1 to 12 hours) and it was observed to have minimal impact on the final result. Finally, the PVI time series was resampled to the electron timeseries cadence of 7 seconds, and proton timeseries cadence of ~ 28 seconds in a way such that for each interval the mean value of PVI in that interval was chosen. Note, that the same analysis was repeated by choosing the maximum value of PVI within each interval with qualitatively similar results.

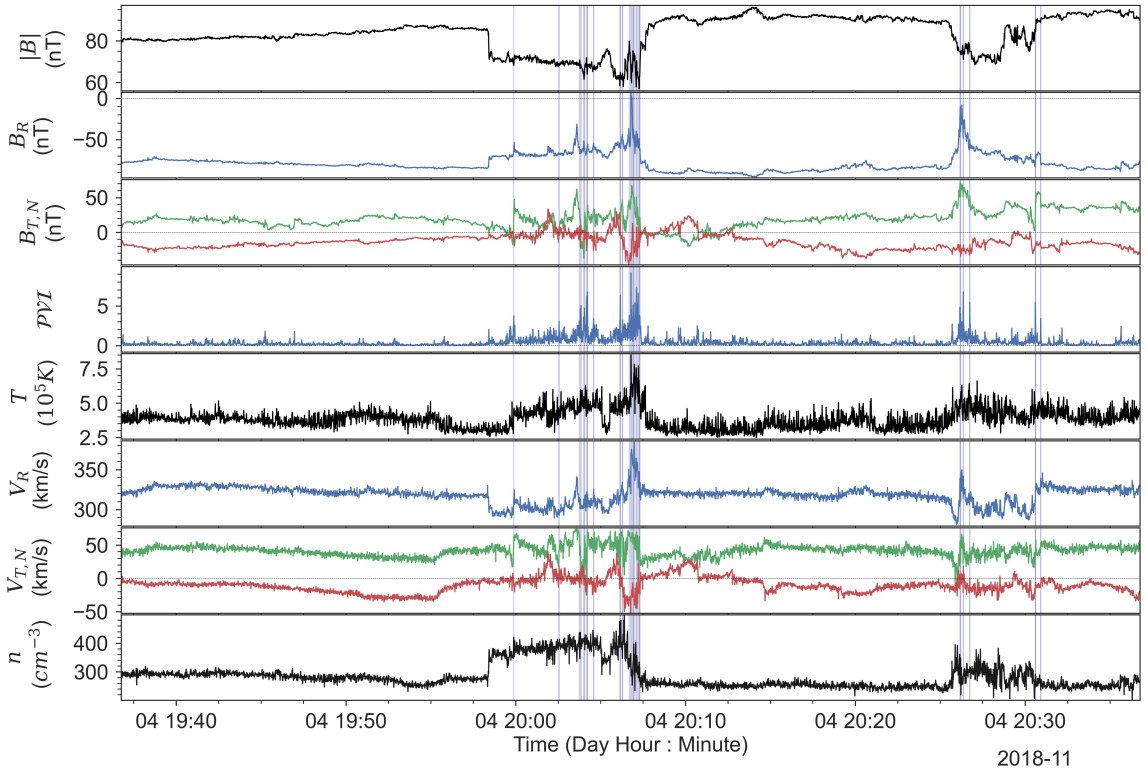

Figure 4.17: An example indicating clustering of intermittent structures associated with increased proton temperature. The shaded areas point to the location of $PVI \geq 3$ events. From top to bottom, the magnitude of the magnetic field $|B|$, the radial component of the magnetic field (B_R), the tangential and normal components of the magnetic field (B_T) and (B_N), in green and red respectively, the PVI time-series for lag, $\tau = 0.837$ *seconds* the temperature T, the radial component of the proton bulk velocity V_R, the tangential and normal components of the proton bulk velocity (V_T), and proton number density (n) are shown.

4.2.3 Results

4.2.3.1 Statistical properties of intermittent structures.

One of the major questions one has to address when studying intermittency is the nature of the physical processes that initiate the coherent structure production at the origin. Accordingly, in order to gain insight into the statistics of intermittent magnetic structures in the solar wind, we follow the process described in Sec. 2.0.7 to estimate the PVI time-series for time-lag, $\tau = 0.837$ *seconds*. In Fig. 4.15a we show the Probability Density Functions (PDFs) of PVI values. The most probable value is close to $\sim$ 0.3, indicating that the majority of the detected events can be characterized as non-intermittent. In Fig.

Figure 4.18: Binned average of radial proton temperature plotted against PVI (blue) along with the number of points per bin (red) for the first six encounters of PSP. Notice a rough upward trend in mean temperature at higher PVI bins.

4.15b, the fraction of the entire data-set occupied by PVI events exceeding the threshold $PVI > \theta$, is shown for $E_1 - E_6$.

Another method that can provide an insight into the statistics of the solar wind coherent structures is the Waiting Time (WT) distribution analysis. In the case of the PVI time-series, we define the waiting time as the time passed between the end and the start of two subsequent events for which the value of PVI stays above a threshold θ. Note, that PVI events have a finite duration. Therefore, subsequent times for which the PVI time-series stay above the threshold are considered as part of the same event. Also note that in order to maintain an adequate sample size, we have imposed a restriction on the minimum counts per bin. Consequently, bins with fewer than ten counts have been discarded. The waiting time interval is itself a new random variable, the distribution of which, is independent of the original random variable's distribution. A simple inspection of the distribution shape can then reveal whether or not the underlying mechanism can be classified as a random Poissonian-type of process, or it possesses "memory" indicating strong correlation and clustering. In the first case, the distribution is better described by an exponential, while in the latter distribution, scales like a power-law (Greco et al., 2009; Greco et al., 2010). Figs. 4.16a,b, show the PDF's of WT between intermittent PVI events with lag $\tau = 0.837$ *seconds* and threshold $\theta_1 = 3$, $\theta_2 = 6$, respectively, for the first six encounters. At lower WT's, the best fit analysis indicates that WT distributions are better described by a power-law. The index of the power-law fit attains values in the range $a \in [-0.8, -0.52]$, progressively getting softer as the threshold value, θ, increases. In contrast, for events further apart in time, the distribution is better described by an exponential. The change between power-law and exponential in the distribution can be interpreted as the breaking-point between *intercluster* and *intracluster* waiting times (Greco et al., 2010). This change seems to coincide with an ill-posed, due to the power-law nature of the distribution, mean value of WT, $\langle WT \rangle$ (Chhiber et al., 2020a). The WT

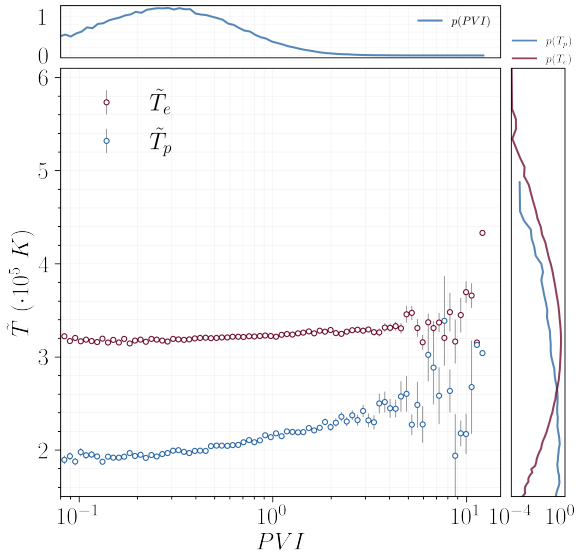

Figure 4.19: Binned mean of proton (T_p in blue) and electron temperature (T_e in red) plotted against PVI . Error bars are also shown indicating the standard error of the mean, $\sigma_i/\sqrt{n}$, where σ_i is the standard deviation of the samples inside the bin. The PDFs of the electron and proton temperature $p(T_e)$, $p(T_p)$ and the PVI index $p(PVI)$ are shown separately in red and blue on the top and right margin of the plot respectively.

distribution analysis was repeated by estimating the PVI time-series using a different time-lag, $\tau = 8.37, 83.7$ *seconds*, still sampling though, overtimes with 0.837 *seconds* cadence. The resulting waiting time distributions (not shown here) are once again remarkably similar between all six encounters and thus resemble the ones reported in (Chhiber et al., 2020a) for E_1. This provides a strong indication that high PVI valued coherent structures, are not evenly distributed within the solar-wind, but rather tend to be strongly correlated and form clusters, creating alternating regions of very low and very high magnetic field activity respectively (see also (Dudok de Wit et al., 2020; Chhiber et al., 2020a; Bale et al., 2021b)). One such example, out of the thousands of clustering events we were able to recover is presented in Fig. 4.17. To emphasize the clustering of coherent structures, blue, vertical lines have been added to indicate the location of events characterized by a magnetic PVI index, $PVI \geq 3$. Notice the elevated proton temperature at regions where coherent structures abound.

4.2.3.2 Electron vs. proton heating from intermittent structures.

We now focus on E1 and investigate the contribution of coherent structures, identified by means of the PVI method (see Section 4.2.2), to the heating of protons and electrons in the solar wind. The first step in this analysis is to interpret T_p as a function of PVI through binned statistics. Figure 4.19 shows the average proton (blue) and electron (red) temperature per bin using 100 PVI bins (i.e., $\langle T_p(\theta_i \leq PVI \leq \theta_{i+1})\rangle$, where θ_i is the PVI threshold) plotted against the center of the bin. Uncertainty bars are also shown indicating the standard error of the sample (Gurland and Tripathi, 1971a). In this case, the uncertainty is estimated as $\sigma_i/\sqrt{n}$, where σ_i is the standard deviation of the samples inside the bin. The PDFs of the electron and proton temperature $p(T_e)$, $p(T_p)$, as well as, the PDF of the PVI index $p(PVI)$ are shown separately in blue and red on the top and right margin of the plot. In agreement with previous studies (Osman et al., 2012; Yordanova et al., 2021; Sioulas et al., 2022c) a statistically significant positive correlation is observed with high PVI index and elevated T_p. Nevertheless, the limited number of observations for $PVI \geq 4$ results in high variability of T_p on the right-hand side of the figure. More specifically, the lowest observed PVI values, $PVI \sim 10^{-1}$, are associated with a proton temperature of $T_p \sim 4 \cdot 10^5$ K, while for $PVI \sim 4$ the proton temperature raises to $T_p \sim 4.6 \cdot 10^5$ K. On the other hand, for electrons, only a moderate positive statistical correlation is observed. In particular coherent structures characterized by a PVI index, $PVI \leq 1$, hardly change the electron temperature, while for higher PVI thresholds a rough statistical trend is observed. Note, that several bins with $PVI \sim 10$, usually associated with reconnection exhausts (Servidio et al., 2012), display considerably increased electron temperatures $T_e \geq 3.5 \cdot 10^5$ K. This could indicate that magnetic reconnection plays a major role in electron heating observed in the solar wind. However, further study is needed to identify these structures and determine whether magnetic reconnection is indeed responsible for the observed heating, and whether other mechanisms are involved.

To gain a deeper understanding of the relationship between the temperature of the solar wind, and magnetic field discontinuities, we estimate averages of T_j, where, $j = e,\ p$ the

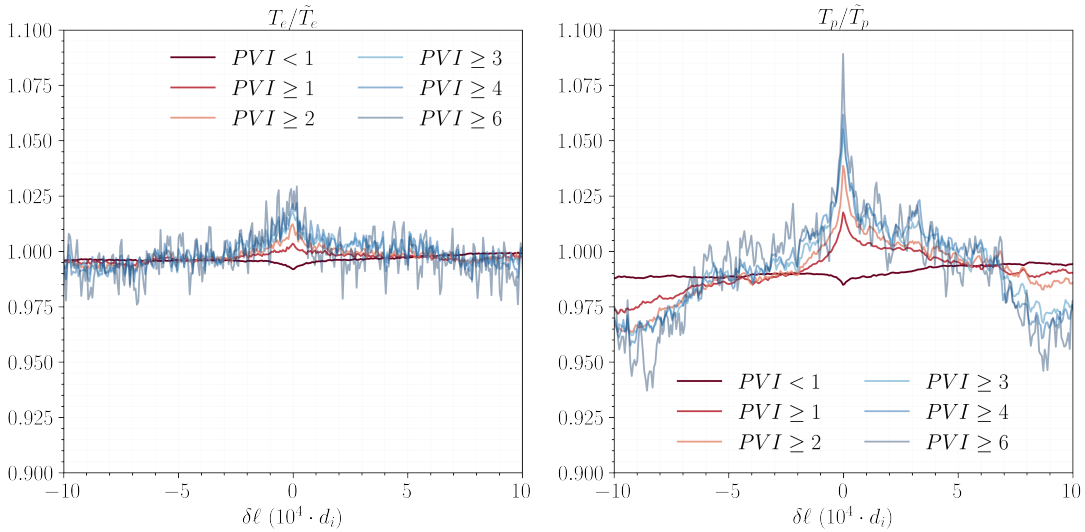

Figure 4.20: Average (a) T_e (b) T_p conditioned on the spatial lag, normalized to the ion inertial length d_i, estimate separation from PVI events that exceed a PVI threshold. Note that T_j, $j = e,\ p$ has been normalized by the average value $\tilde{T}_j$ within a window that spans $\delta\ell = 2 \cdot 10^5 d_i$ and is centered around the discontinuity under study.

temperature of electrons and protons respectively, constrained by the temporal separation between PVI events that belong to a given PVI bin. This can be formally expressed as (Tessein et al., 2013b; Sorriso-Valvo et al., 2018):

$$\langle T_j(\Delta t,\ \theta_i,\ \theta_{i+1})\rangle \ = \ \langle T_j(t_{PVI}\ + \Delta t)|PVI \geq \theta_i\rangle, \tag{4.1}$$

where, Δt is the temporal lag relative to the location of the main PVI event taking place at time t_{PVI}, and $\theta \ = \ [0,\ 1,\ 2,\ 3,\ 4,\ 6]$. Fig. 4.20 illustrates the conditional average of electron and proton temperature in the left and right panel respectively at different spatial lags. Note, that temporal lags have been converted to spatial lags, subject to the validity of Taylor's hypothesis (Taylor, 1938), $\ell = V_{SW}\Delta t$. For a direct comparison between different plasma environments and to cast our results in physically relevant units, spatial scales have been normalized by the ion inertial length $d_i = V_A/\Omega_i$, where $\Omega_i = \frac{eB}{m_p}$, is the proton gyrofrequency, e is the elementary charge, B is the mean magnetic field, and m_p is the mass of the proton (Huba, 2004). Additionally, for each identified event the temperature T_j was normalized by the average value $\tilde{T}_j$ within a window that spans $\delta\ell = 2 \cdot 10^5 d_i$ and is centered around the discontinuity under study. This allows us to

disentangle our observations from the effects of transients such as Heliospheric Current Sheet (HCS) crossings, usually associated with minima in solar wind temperature (Suess et al., 2009; Shi et al., 2022c), Switchback patches, observed to enhance the solar wind temperature (Shi et al., 2022a) etc. Additionally, it enables us to get a more direct estimate of the relative contribution of CSs to the internal energy of the charged particle species under investigation.

It appears that no significant proton and electron heating of the solar wind occurs at times when the magnetic field is relatively smooth, as indicated by the dip in the normalized mean temperature at lag equal to $t = 0$s for $PVI \leq 1$. Increasing the threshold value θ, however, results in a global maximum in normalized T_j close to zero lag, suggesting that both proton and electron temperatures will rise in the vicinity of coherent structures. It can be readily seen, however, that the heating process is less pronounced in the case of the electrons, since, T_e does not considerably deviate from the mean $\tilde{T}_e$. On the other hand, proton temperature considerably increases near CSs as illustrated in Figure 4.20b, with the enhancement being progressively more obvious as we consider higher PVI thresholds. There is a distinct rate of decrease for each bin, with the steepest gradients in T_p observed around the sharpest discontinuities, $PVI \geq 6$. T_p remains elevated near the main event, most likely because of the clustering of coherent structures (Yordanova et al., 2021; Sioulas et al., 2022).

4.2.4 Summary & Conclusions

In this work, we have analyzed magnetic field and particle data from the first six encounters of the PSP mission. Our goal was to study the statistics of intermittency and further elucidate the nature of turbulent dissipation in the neighborhood of the solar wind sources. As a first step, an effort was made to understand the nature of the mechanism that is responsible for the generation of intermittency and coherent structures in the solar wind. We have shown that coherent structures, corresponding to $PVI \geq 1$, constitute only $\approx 19\%$ of the dataset. As a follow-up to the study of (Chhiber et al., 2020a), we studied

the waiting time distributions by applying thresholds on the PVI time-series. We have confirmed that intermittent magnetic field structures are not evenly distributed in the solar wind but rather tend to strongly cluster, forming regions characterized by a high magnetic field variability followed by intervals for which the magnetic field is relatively smooth. This observation is also reinforced by the power-law nature of the waiting time distributions at low waiting times, indicating the presence of an intracluster population. The power law is followed by an exponential at longer waiting times, suggesting a second intercluster population of coherent structures in the solar wind's magnetic field. Additionally, the power-law scaling of the WT distributions is indicative of clusters that do not have a typical size or distance, except for the limiting size given by the exponential cutoff.

Focusing on observations from PSP's first encounter with the Sun, we investigated the relationship between the proton and electron heating with coherent magnetic structures in the young solar wind environment. Seeking to better understand turbulent dissipation in the vicinity of solar wind sources we have first identified coherent structures in our dataset using the PVI method (Greco et al., 2008). Subsequently, the effect of CSs on the heating of electrons and protons was examined. The electron temperature here is obtained from QTN-spectroscopy (Moncuquet et al., 2020a), which indicates the temperature of the distribution's core.

Our analysis corroborates previous theoretical and observational works (Greco et al., 2012b; Servidio et al., 2012; Osman et al., 2012; Sorriso-Valvo et al., 2019; Qudsi et al., 2020; Yordanova et al., 2021; Sioulas et al., 2022) and indicates that coherent structures can provide a channel for ion heating in the young solar wind. However, enhancements in electron temperature are considerably less significant and it would be challenging to imagine that intermittent heating could account for the non-adiabatic cooling profile of electrons in the solar wind. Qualitatively, the results are consistent with what numerical works have indicted in the past, namely enhanced heating of ions compared to electrons in the vicinity of coherent structures. (see, e.g., Parashar and Matthaeus, 2016). One possible explanation for the preferential intermittent heating of protons over electrons is the "helicity barrier" mechanism that prevents turbulence energy cascade to electron

scales so it can effectively heat the electrons (Squire et al., 2022a). In the case where the system is continuously driven, the large-scale energy will grow in time as the parallel correlation length decreases (Meyrand et al., 2021b). It is through this growth that turbulent energy is eventually funneled into a spectrum of high-frequency ion-cyclotron waves (ICWs), which end up primarily heating the ions.

As a result of our study, we gained a better understanding of how turbulent dissipation and heating of electrons and protons occur in the near Sun solar wind environment. The main finding of this study is that proton heating from coherent structures in the nascent solar wind is preferential to electron heating. However, our results present only a preliminary comparison of electron and proton heating in the near sun solar wind. A complete understanding of how particle heating and dissipation occur at inertial and kinetic scales, will require a more thorough statistical analysis considering a larger and higher resolution dataset. Additionally, strahl, and halo components of the electron distribution function will need to be studied to provide a more complete understanding on how different electron populations behave in the vicinity of CSs.

Our results will guide future works that model the heating of the nascent solar wind environment.

CHAPTER 5

Providing Observational Constraints for Phenomenological Models of MHD Turbulence

5.1 Higher-Order Analysis of Three-Dimensional Anisotropy in Imbalanced Alfvénic Turbulence

This section is based on work that has been submited for publication to the Astrophysical Journal and is available on the Arxiv (Sioulas et al., 2024):

5.1.1 Introduction

In this investigation, we endeavor to evaluate the consistency of the homogeneous models of balanced MHD turbulence by CSM15 and MS17, and discussed in Section 1.3.1, against in-situ observations sampled during the first perihelion (E1) of the Parker Solar Probe mission, (PSP, Fox et al., 2016). Our primary objective is to conduct a rigorous comparison between the predicted scalings of higher-order moments in these models and the corresponding empirical observations, with a specific focus on determining the presence and measurable impact of model-specific elements, such as SDDA and CB, on the observed characteristics. Through this analysis, our aim is to not only provide deeper insights into the higher-order statistics of magnetic turbulence but also to establish a robust benchmark for the testing and refinement of theoretical models addressing imbalanced MHD turbulence in the inhomogeneous solar wind.

We find that at the energy injection scales, (out)ingoing Alfvénic fluctuations undergo a weak cascade, $\chi_\lambda^\pm < 1$, $\chi_\lambda^\pm \equiv \tau_A^\pm/\tau_{nl}^\pm$, the ratio of linear to non-linear timescales. Outgoing

waves remain in the weak regime throughout the inertial range, $\chi_\lambda^+ \approx 0.2$; ingoing modes transition to $\chi_\lambda^- > 1$ at $\lambda \approx 3 \times 10^4 d_i$. This transition is accompanied by spectral scalings diverging from the expected behavior marking the shift from weak to strong turbulence - the discrepancy may be explained by "anomalous coherence' effects. What is normally considered as inertial range consists of two sub-inertial segments. At $\lambda \gtrsim 100 d_i$, the "average" eddy assumes a field-aligned tube topology, with SDDA signatures being weak–largely restricted to the highest amplitude fluctuations. The scaling exponents, ζ_n, of the structure functions, perpendicular to both the local mean field and fluctuation direction, conform to the (Chandran et al., 2015), (Mallet and Schekochihin, 2017) models, indicating "multifractal" statistics; parallel and fluctuation direction scalings are more concave than predicted. The different statistics of this range might be caused by expansion effects. Below $\lambda \approx 100 d_i$, eddies display increasing anisotropy, resembling thin current sheets. Concurrently, ζ_n scales linearly with order, signaling "monofractal" statistics. At $\lambda \approx 8 d_i$, the eddies transition to a quasi-isotropic state. This shift might be a signature of the "helicity barrier". We employ 5-point structure functions, shown to be more effective than the 2-point approach at small spatial scales.

The structure of the remainder of this section is as follows: Section 5.1.2 elaborates on the methodologies utilized in this analysis. Details regarding data selection and processing are outlined in Section 5.2.2. The study's findings are presented in Section 5.2.3. A comprehensive comparison with prior theoretical, observational, and numerical studies, which contextualizes our results, is provided in Section 5.2.4. The paper concludes with a summary of the main findings in Section 5.2.5.

5.1.2 Data Analysis

To investigate and quantify the three-dimensional anisotropy of higher-order magnetic field moments, we employ a methodology proposed by (Wang et al., 2022), which builds upon and extends the framework established in (Chen et al., 2012).

Adhering to the approach outlined in (Chen et al., 2012), we establish a locally-

defined, scale-dependent Cartesian coordinate system, represented as ($\hat{\xi}$, $\hat{\lambda}$, $\hat{\ell_{||}}$). In this coordinate system the "parallel" direction, $\hat{\ell_{||}}$, is aligned with the local magnetic field, $\boldsymbol{B_\ell}$, defined by Equation 2.0.4. Magnetic field increments are calculated using Equation 2.0.4. The amplitude of the field increment is denoted as $\delta b = |\delta \boldsymbol{b}|$. The local "displacement" direction, $\hat{\xi}$, aligns with the unit vector of the perpendicular component of the field increment, with $\delta \boldsymbol{b}_\perp$ defined as:

$$\delta \boldsymbol{b}_\perp = \boldsymbol{B_\ell} \times (\delta \boldsymbol{b} \times \boldsymbol{B_\ell}). \tag{5.1}$$

Lastly, the "perpendicular" direction, $\hat{\lambda}$, is orthogonal to both $\hat{\xi}$ and $\hat{\ell_{||}}$, $\hat{\lambda} = \hat{\ell_{||}} \times \hat{\xi}$. The Cartesian system can be converted into a spherical polar coordinate system (ℓ, θ_B, $\phi_{\delta \boldsymbol{B}_\perp}$), where θ_B is the angle between $\boldsymbol{B}_\ell$ and $\boldsymbol{\ell}$, and $\phi_{\delta \boldsymbol{B}_\perp}$ is the angle between $\hat{\xi}$ and the projection of $\boldsymbol{\ell}$ onto the plane orthogonal to $\boldsymbol{B}_\ell$.

In our analysis, we utilize the 5-point (5-point) increment method, which represents a significant advancement over the conventional 2-point (2-point) method, especially for examining turbulence statistics in sub-ion regimes. A critical benefit of the 5-point method is its reduced susceptibility to large-scale spectral leakage (Cho, 2019), rendering it more suitable and effective for our ensuing analysis.

For calculating 5-point structure functions, denoted as SF_5^n, a modified definition of $\delta \boldsymbol{b}$ is required, see Equation 2.0.4. Moreover, the local scale-dependent value $\boldsymbol{\psi}_\ell$ of a field $\boldsymbol{\psi}$ can be computed as a weighted average using a five-point stencil, Equation 2.0.4.

For example, the local scale-dependent magnetic and velocity fields are represented by $\boldsymbol{B}_\ell$ and $\boldsymbol{V}_\ell$, respectively.

The nth-order, structure functions conditioned on the pair of angles $\theta_B,\ \phi_{\delta \boldsymbol{B}_\perp}$, are defined as:

$$SF^n(\ell,\ \theta_B,\ \phi_{\delta \boldsymbol{B}_\perp}) = \langle (\delta B)^n |\ \theta_B,\ \phi_{\delta \boldsymbol{B}_\perp},\ \ell \rangle, \tag{5.2}$$

The conditional average in Equation 5.2 was calculated over the angle bin $\omega(i-1)^\circ \leq \theta_B \leq \omega i^\circ$, $\omega(j-1)^\circ \leq \phi_{\delta \boldsymbol{B}_\perp} \leq \omega j^\circ$, where $i = 1, ..., 9$ and $j = 1, ..., 9$. In the following, ω

takes the value of $\omega = 5$ for estimating lower-order moments and $\omega = 10$ for higher-order moments.

In the following, we focus mainly on three special cases, defining the components in

$$i = 1, \quad j = 1: \quad SF(\ell_{||})^n, \qquad \text{“parallel”}, \tag{5.3}$$

$$i = 9, \quad j = 1: \quad SF(\xi)^n, \quad \text{“displacement”}, \tag{5.4}$$

$$i = 9, \quad j = 9: \quad SF(\lambda)^n, \quad \text{“perpendicular”}, \tag{5.5}$$

directions, where $\ell_{||} = \boldsymbol{\ell} \cdot \hat{\boldsymbol{\ell}}_{||}$, $\lambda = \boldsymbol{\ell} \cdot \hat{\boldsymbol{\lambda}}$, and $\xi = \boldsymbol{\ell} \cdot \hat{\boldsymbol{\xi}}$.

To estimate a component structure function for the entire dataset, we adopt the methodology outlined in (Verdini et al., 2018). For each selected interval, j, within the dataset, we compute the structure functions $SF_j^n(\ell,\ \theta_B,\ \phi_{\delta \boldsymbol{B}_\perp})$ for the three orthogonal components, as defined by Equations 5.3 to 5.5. Considering the substantial variation in the root mean square (rms) of fluctuations between intervals, normalization is a critical step prior to averaging these intervals. The normalization involves selecting a specific scale, ℓ_*, and normalizing each SF_j^n by the energy of fluctuations at that scale. We determine an appropriate ℓ_* by estimating the trace structure function $S_j^n(\ell)$ for each interval and identifying a scale range where power-law behavior is consistent across all $S_j^n(\ell)$. The fluctuation energy at scale ℓ_* is given by the value of the trace structure function $S_i(\ell_*)$.

The normalized weighted average structure function for a given magnetic field component is then calculated as follows:

$$\tilde{SF}^n(\ell, \theta_B, \phi_{\delta \boldsymbol{B}_\perp}) = \sum_j \frac{SF_j^n(\ell, \theta_B, \phi_{\delta \boldsymbol{B}_\perp})}{S_j^n(\ell_*)} W_j, \tag{5.6}$$

where $W_j = n_j(\ell,\ \theta_B,\ \phi_{\delta \boldsymbol{B}_\perp})/n(\ell,\ \theta_B,\ \phi_{\delta \boldsymbol{B}_\perp})$ represents the weighting factor, with $n_j(\ell,\ \theta_B,\ \phi_{\delta \boldsymbol{B}_\perp})$ being the total number of measurements within each bin for the interval under consideration, divided by the count in each bin for the whole data set, $n = \sum_j n_j$.

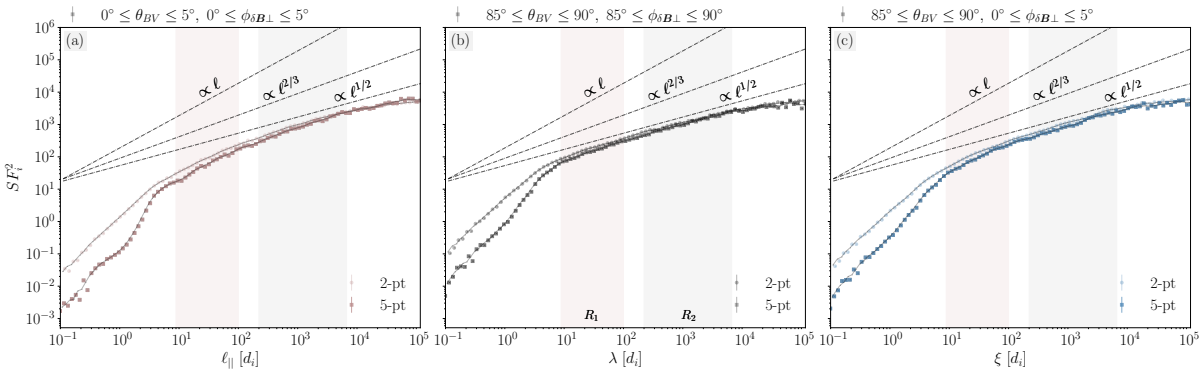

Figure 5.1: The local 2-point structure functions (circles) and 5-point structure functions (squares) averaged for the five most highly Alfvénic intervals within our dataset. The structure functions are displayed for the parallel, perpendicular, and displacement directions, indicated by red, black, and blue colors, respectively. Reference lines representing scalings of 1/2, 2/3, and 1 are included for comparison.

Our subsequent analysis, as discussed in Section 5.2.2, relies on these conditionally defined structure functions, utilizing data from the first perihelion of the Parker Solar Probe (PSP). Unless specified otherwise, the results in the following analysis are derived from estimating 5-point structure functions.[6]

5.1.3 Data Set

We analyze magnetic field and particle data collected during the first perihelion of the PSP mission, covering the period from November 1 to November 11, 2018. Specifically, we analyze magnetic field measurements obtained by the FIELDS instrument (Bale et al., 2016). In particular, we make use of the SCaM data product, which combines measurements from fluxgate and search-coil magnetometers (SCM) by using frequency-dependent merging coefficients. This approach allowed us to observe the magnetic field over a frequency range ranging from direct current (DC) to 1 MHz while achieving optimal signal-to-noise ratio (Bowen et al., 2020b). The FIELDS magnetometer suite is susceptible to narrow-band coherent noise stemming from the spacecraft reaction wheels, including their rotation frequencies, as well as harmonic and beat frequencies. To address potential

[6]The algorithm detailed in this section, along with a package for downloading, cleaning, and processing PSP data, is readily accessible in MHDTurbPy (Sioulas, 2023).

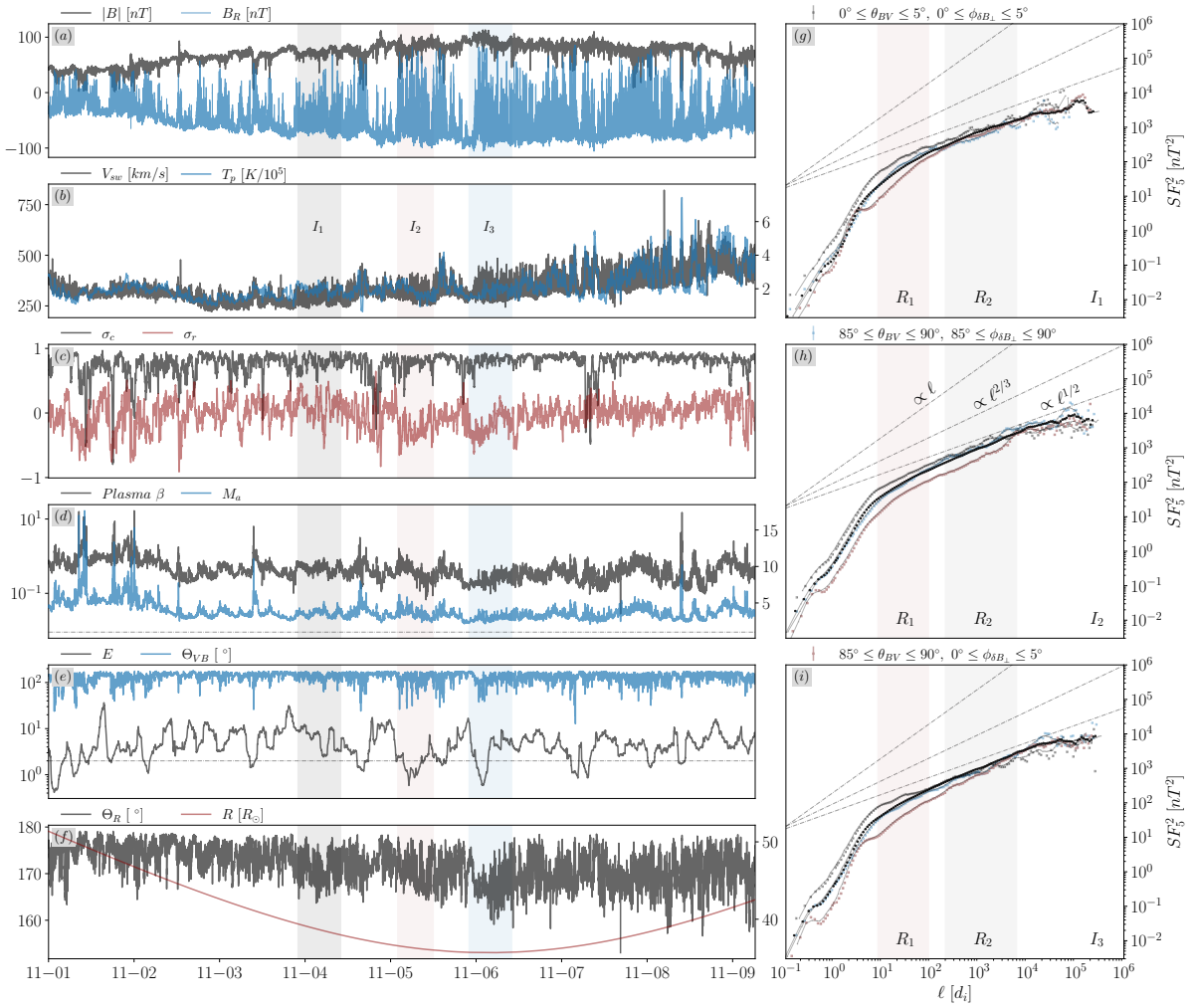

Figure 5.2: Overview of E1: (a) Magnetic field timeseries, radial component, B_R (blue) and magnitude, $|B|$ (black); (b) Solar wind speed, V_{sw} (black, left axis) and proton temperature, T_p (blue, right axis); (c) Normalized cross helicity, σ_c (black) and normalized residual energy, σ_r (red); (d) Plasma β (black, left axis) and Alfvénic Mach number, $M_a = V_R/|V_a|$ (blue, right axis); (e) Variance anisotropy, $E = (b_T^2 + b_N^2)/b_R^2$, where b represents the rms amplitude of fluctuations (black, left axis) and angle between the magnetic field and velocity flow, Θ_{VB} (blue); (f) Sampling angle, Θ_R, defined as the angle between $\hat{R}$ and $\boldsymbol{V}_{sc} - \boldsymbol{V}_{sw}$ (black, left axis), and radial distance from the Sun, R (red, right axis). Additionally, three intervals denoted as I_j, $j = 1, 2, 3$ and marked with black, pink, and cyan shadings on the main figure. The corresponding 5-point structure functions of the parallel, perpendicular, and displacement directions, denoted by red, transparent black, and blue colors, respectively, are shown in panels (g)-(i). In addition, the trace structure function is shown in black circles. Reference lines representing scalings of 1/2, 2/3, and 1 are included for comparison.

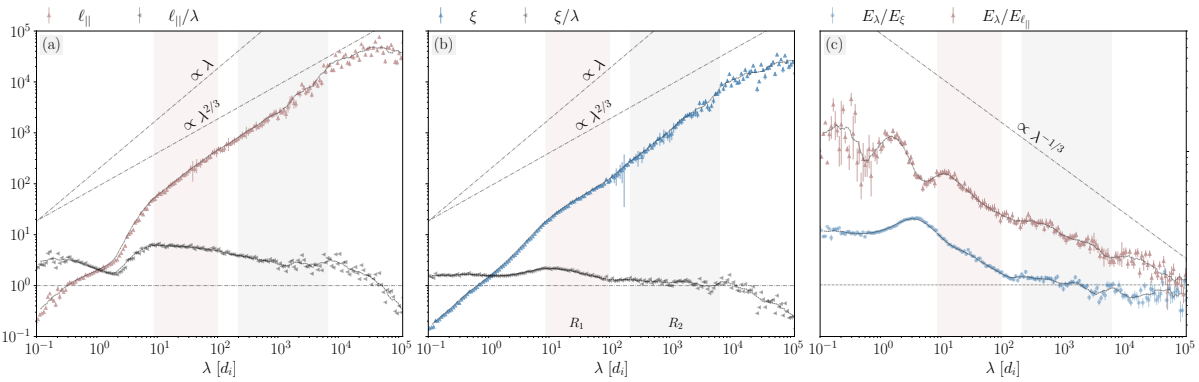

Figure 5.3: Wavevector anisotropy relationships: (a) $\ell_{||} = \ell_{||}(\lambda)$ (b) $\xi = \xi(\lambda)$, determined by equating pairs of $SF_5^2(\lambda)$ with $SF_5^2(\ell_{||})$, and $SF_5^2(\lambda)$ with $SF_5^2(\xi)$, respectively. The gray lines show the aspect ratios, $\ell_{||}/\lambda$ and ξ/λ plotted against λ in panels (a) and (b), respectively. For context, reference lines indicating scalings of 2/3 and 1 are also included. Panel (c) presents power anisotropy, with $E_\lambda/E_{\ell_{||}}$ depicted in red and E_λ/E_ξ in blue.

contamination of magnetic field measurements at ion-scales by the reaction wheels, for each interval, we implement a procedure involving the identification and elimination of reaction wheel noise using the method detailed in Shankarappa et al. (2023).

Moreover, we incorporated data from the Solar Probe Cup (SPC) instrument, which is part of the Solar Wind Electrons Alphas and Protons (SWEAP) suite (Kasper et al., 2016), to estimate bulk plasma properties. We also utilized Quasi Thermal Noise (QTN) electron density measurements (Moncuquet et al., 2020b; Pulupa et al., 2017). To enhance statistical robustness and expand the sample size, the data were segmented into 12-hour intervals. These intervals were designed to overlap by 6 hours to maximize data utilization. We then conditioned the intervals based on σ_c, selecting only those with an average value of $\sigma_c(\ell_*) \geq 0.75$, where $\ell_* = 10^4 d_i$. This methodology yielded a total of 82 intervals, sampled at distances ranging from 0.166 to 0.244 au.

5.1.4 Results

5.1.4.1 A Comparison of SF_5^n and SF_2^n

This section is dedicated to a comparative analysis aimed at substantiating our preference for the 5-point structure function method over the traditionally favored 2-point approach.

Table 5.1: The median values for the spectral indices of the trace, parallel, perpendicular, and displacement components of the magnetic field in the ranges R_1 and R_2. These indices are derived from the corresponding scaling indices of $SF^2_{5,\ i}$, utilizing the relationship $\alpha_i = -1 - \beta_i$ (Monin and Jaglom, 1987). The error values provided represent the standard deviation of the mean.

	α	$\alpha_{\ell_{\|\|}}$	α_λ	α_ξ
R_1	-1.79 ± 0.06	-1.97 ± 0.05	-1.64 ± 0.04	-1.94 ± 0.06
R_2	-1.53 ± 0.02	-1.66 ± 0.05	-1.49 ± 0.03	-1.56 ± 0.08

To this end, we calculated second-order structure functions for the parallel, perpendicular, and displacement components according to Equations 5.3 to 5.5, setting $\omega = 5$.

The local 2-point structure functions (circles) and 5-point structure functions (squares) averaged for the five most highly Alfvénic intervals within our dataset are illustrated in Figure 5.1. To highlight specific scale ranges, pink and gray shadings are employed for intervals $8-100d_i$ (labeled R_1) and $200-6000d_i$ (labeled R_2), respectively. At large scales, comparable results are obtained from both the 5-point and 2-point methods. However, a marked divergence is observed in the R_1 range. The 5-point method reveals steep scaling for parallel and displacement components, with indices $\beta_{\ell_{\|\|}} \approx \beta_\xi \approx 1$, aligning with wavelet-derived parallel component scaling of the same dataset reported in (Sioulas et al., 2023). In contrast, the 2-point method produces a notably flatter slope.

The distinction between the two methods becomes stark at kinetic scales, highlighting the 2-point method's limitations in detecting steep scalings. This shortfall is further evident when comparing $\boldsymbol{B}$-trace wavelet structure functions using both the SF^2_2 and SF^2_5 methods; only the 5-point approach produces scalings that align with wavelet analyses across scales from injection to kinetic (details not shown here). This inconsistency underscores potential inaccuracies when employing the 2-point method in scenarios characterized by steep scaling[7]. Therefore, for our further analyses, we have chosen to

[7]A cautionary note is warranted: when comparing SF^2_5 with wavelet-derived trace structure functions for intervals observed in later PSP encounters —characterized by shallower than $1/f$ energy injection scale power spectra (Huang et al., 2023; Davis et al., 2023)— SF^2_5 fails to replicate the wavelet scalings. This indicates that SF^2_5, similar to its SF^2_2 counterpart, is ineffective under conditions with scalings shallower than $1/f$.

rely on the 5-point method.

Across all examined intervals, the results remained qualitatively consistent. Three such intervals are illustrated in panels (g)-(h) of Figure 5.8. In addition to the component structure functions, these panels also illustrate the trace structure function estimated for the respective intervals. It can be observed that the perpendicular component can significantly diverge from the trace, while the latter typically shows remarkable overlap with the displacement component, with the difference becoming more pronounced towards smaller scales.

Table 5.1.3 presents the median SF_5^2 scalings estimated across the R_1 and R_2 ranges for the entire dataset.

5.1.4.2 Power & wavevector anisotropy

To examine the scale-dependent three-dimensional anisotropy in our dataset, we calculated $SF_5^2(\ell)$, following the methodology outlined in Equations 5.3 to 5.5, setting $\omega = 5$. Our analysis commenced by identifying the anisotropic relationships for individual intervals, then proceeded to compute a scale-dependent median for the entire dataset, utilizing 150 logarithmically spaced bins.

Panels (a) and (b) of Figure 5.3 illustrate the anisotropic relationships $\ell_{||}(\lambda)$, and $\xi(\lambda)$, derived by equating pairs of structure functions: $SF_5^2(\lambda)$ with $SF_5^2(\ell_{||})$, and $SF_5^2(\lambda)$ with $SF_5^2(\xi)$, respectively. The aspect ratios $\ell_{||}/\lambda$ and ξ/λ are represented by gray lines in their respective panels. Panel (c) focuses on power anisotropy, illustrating the ratios $SF_5^2(\lambda)/SF_5^2(\ell_{||})$ and $SF_5^2(\lambda)/SF_5^2(\xi)$ in red and blue, respectively. The median values of the dataset's anisotropic scalings are summarized in Table 5.1.4.2.

At large scales, our observations reveal a rough equipartition of the fluctuating energy between $SF_5^2(\lambda)$ and $SF_5^2(\ell_{||})$, with $SF_5^2(\xi)$ being slightly more energetic. The energy distribution is reflected in the wavevector anisotropy and aspect ratios, indicating that eddies tend to be slightly compressed along the fluctuation direction.

Within the R_2 range, we note that the fluctuating magnetic energy is distributed

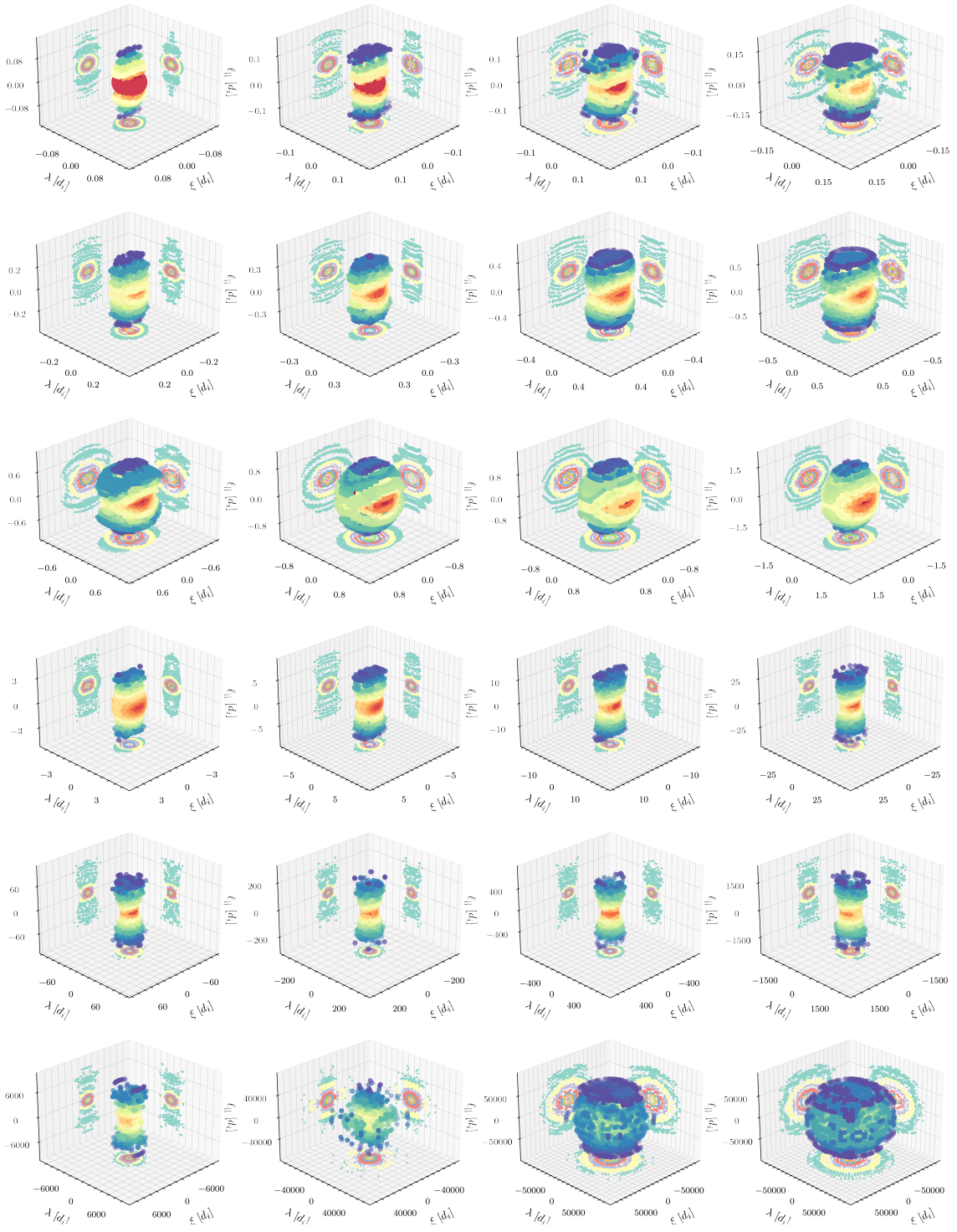

Figure 5.4: 3D representation of turbulence eddies obtained by estimating isosurfaces of constant energy of SF_5^2 at different levels, ranging from small scales (top left) to large scales (bottom right). The color scheme, although redundant, indicates the distance from the origin (0,0,0). Additionally, projections of the object onto each respective plane are displayed. While the projections share a common colormap to denote the distance from each plane's origin, the colormap for the 3D object differs.

Table 5.2: Median values of the scaling indices for wavevector anisotropies, specifically $\ell_{||} \propto \lambda^{w_{\ell_{||}}}$ and $\xi \propto \lambda^{w_\xi}$, and the power anisotropies $E_\lambda/E_{\ell_{||}} \propto \lambda^{p_{\ell_{||}}}$ and $E_\lambda/E_\xi \propto \lambda^{p_\xi}$. These indices were derived by applying a power-law fit to the curves obtained from individual intervals over the scale ranges R_1 and R_2. The table presents the median values along with their associated errors, represented as the standard deviation of the mean.

	$w_{\ell_{\|\|}}$	w_ξ	$p_{\ell_{\|\|}}$	p_ξ
R_1	0.89 ± 0.06	0.77 ± 0.05	-0.31 ± 0.04	-0.30 ± 0.07
R_2	0.86 ± 0.08	0.99 ± 0.06	-0.19 ± 0.05	-0.09 ± 0.06

almost evenly between the perpendicular and displacement components. This observation suggests rough axisymmetry of the turbulent eddies at these scales, i.e., approximate isotropy in the plane perpendicular to $\boldsymbol{B}_\ell$. The aspect ratio ξ/λ is observed to be close to, yet marginally greater than, unity, displaying only a slight increase within R_2. This trend is further emphasized by the scale-dependent power-anisotropy depicted in panel (c). In contrast, within this range, eddies exhibit elongation along $\boldsymbol{B}_\ell$, as indicated by the ratio $\ell_{||}/\lambda$, which is greater than 1 and shows a monotonic increase towards smaller scales. These findings collectively indicate that turbulent eddies within the R_2 range predominantly exhibit a field-aligned tube topology, consistent with the results presented in (Vinogradov et al., 2023). This is visually demonstrated in Figure 5.4. At scales smaller than $\lambda \lesssim 100 d_i$, a noticeable shift from isotropy in the plane perpendicular to $\boldsymbol{B}_\ell$ becomes evident. This shift is highlighted by a gradual increase in the aspect ratio ξ/λ, indicating a transition of eddy structures from tube-like to ribbon-like. The evolving eddies exhibit three-dimensional anisotropy, adhering to the relationship $\ell_{||} \gg \xi \gg \lambda$. This trend persists into the smaller-scale end of the R_1 range, where both power-anisotropy ratios follow a scaling of approximately -1/3. Additionally, within R_1, the ratio $\ell_{||}/\lambda$ continues to rise, albeit at a reduced rate compared to the $100 - 600 d_i$ range, where $\ell_{||} \propto \lambda^{0.72 \pm 0.04}$. This slower rate of increase within R_1 can be attributed to the steepening of $SF_5^2(\ell_{||})$ at scales marginally larger than R_1.

As we move below the R_1 range and into the transition region (Sahraoui et al., 2009; Bowen et al., 2020a), the previously observed trend of increasing anisotropy ceases. Within the scale range of $2 d_i \lesssim \lambda \lesssim 8 d_i$, the eddies start to demonstrate more isotropic

characteristics. This tendency towards isotropy peaks at $\lambda = 2d_i$, where the aspect ratio reaches $\lambda : \xi : \ell = 1.56 : 1 : 1$. Throughout this scale range, the anisotropic scaling relations —derived from fitting curves to individual intervals and estimating the median values, presented along with the standard deviation of the mean— conform to $\ell_{||} \propto \lambda^{2.01\pm0.06}$ and $\xi \propto \lambda^{1.25\pm0.05}$.

At even smaller scales, distinct scaling anisotropies characterize two separate ranges. Within $1d_i \lesssim \lambda \lesssim 2d_i$, the ratio $\ell_{||}/\lambda$ shows an upward trend, following $\ell_{||} \propto \lambda^{0.67\pm0.02}$, while the ratio ξ/λ remains relatively stable, adhering to $\xi \propto \lambda^{0.98\pm0.04}$. These findings stand in contrast to standard kinetic Alfvén wave (KAW) turbulence models (Howes et al., 2008; Schekochihin et al., 2009a) and deviate statistically from in-situ observations reported in (Duan et al., 2021; Zhang et al., 2022). However, they are in agreement with the intermittent KAW model proposed by (Boldyrev and Perez, 2012) and align with numerical kinetic simulations by (Cerri et al., 2019), as well as in-situ observations in the magnetosheath (Wang et al., 2020). At yet smaller scales, $0.5d_i \leq \lambda \leq 1d_i$, both $\ell_{||}/\lambda$ and ξ/λ ratios exhibit an increase, scaling as $\ell_{||} \propto \lambda^{0.5\pm0.05}$ and $\xi \propto \lambda^{0.87\pm0.04}$, respectively.

Figure 5.4 presents a three-dimensional representation of turbulence eddies, illustrating isosurfaces of SF_2^5 at various scales. This visualization was achieved by estimating conditional $SF_5^2(\ell,\ \theta_B,\ \phi_{\delta \boldsymbol{B}_\perp})$, according to Equation 5.2, and utilizing 5° angular bins. The spherical polar coordinates $(\ell,\ \theta_B,\ \phi_{\delta \boldsymbol{B}_\perp})$ obtained from this process were then converted into Cartesian coordinates $(\ell_{||},\ \xi,\ \lambda)$. Surfaces computed for the first octant were mirrored across to the other octants, based on the assumption of reflectional symmetry (Chen et al., 2012). In the 3D visualization, surface colors represent the distance from the origin, with cooler colors indicating larger distances. When these surfaces are projected onto different planes, the color denotes the distance from the origin of each respective plane. It is important to note that the colormap applied to these planar projections differs from the one used for the 3D representation. The color coding in these projections reflects the range of maximum and minimum distances observed across all three components.

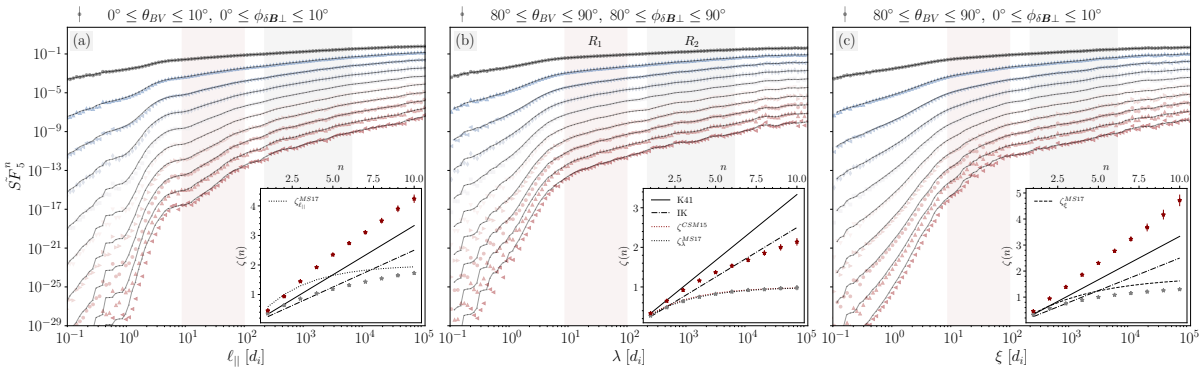

Figure 5.5: The main panels depict the normalized weighted average structure functions, $\tilde{SF}_5^n(\ell)$, for (a) parallel, (b) perpendicular, and (c) displacement components, each adjusted with a vertical offset for enhanced clarity. Prior to the weighted average estimation, each $SF_5^n(\ell)$ was normalized using the value of the trace $S_5^n(\lambda*)$, where $\lambda_* = 2 \times 10^3 d_i$. These normalized averages, $\tilde{SF}_5^n(\ell)$, displayed in the main figure, were used to estimate ζ_n for R_2, marked as gray asterisks in the insets. For ζ_n estimation in R_1, indicated by red asterisks in the insets, a similar normalization process was applied at $\lambda_* = 50 d_i$. It is important to note that the latter normalized $\tilde{SF}_5^n(\ell)$ for R_1 are not depicted in the figure. Error bars in the insets represent the uncertainty associated with the power-law fits. For comparison, the scaling behaviors as predicted by the K41, IK, CSM15, and MS17 models are also included.

5.1.4.3 Higher order statistics & Intermittency

We computed five-point structure functions, SF_5^n, for parallel, perpendicular, and displacement components, as per Equations 5.3 to 5.5, considering orders $n = 1, \ldots, 10$ with $\omega = 10$. Additionally, we evaluated $\boldsymbol{B}$-trace structure functions, S_5^n. Furthering our analysis, we derived thenormalized weighted average, $\tilde{SF}5^n$, for our dataset following Equation 5.6. After identifying two distinct sub-inertial ranges displaying clear power-law behavior, we calculated two sets of normalized structure functions. Within the R_1 domain, we normalized SF_5^n using $S_5^n(\lambda_*)$, where $\lambda_* = 50 d_i$.

For the R_2 domain, normalization employed a different scale, $\lambda_* = 2 \times 10^3 d_i$. The latter normalized structure functions, particularly for the parallel, perpendicular, and displacement components, are depicted in Figure 5.5 panels (a) to (c), respectively. To aid visualization, each n-th order moment was vertically offset by 10^{-n}. Fitting each component of $\tilde{SF}_5^n(\ell)$ to a power law, $\propto \ell^{\zeta_n}$, facilitated the estimation of scaling exponents, ζ_n. The resulting ζ_n are depicted by red asterisks for the R_1 domain and gray for R_2

within the insets of the corresponding figure panels. For comparison, scaling exponent predictions based on the theoretical models proposed by CSM15 and MS17 are also included.

In the R_2 range, the scaling exponent ζ_n^{λ} of the perpendicular component forms a convex function of n, indicative of multifractal statistics and strong intermittency. This scaling profile closely aligns with the theoretical predictions by CSM15 and MS17, showing notable correspondence to the latter model at lower n values. For $SF_5^n(\xi)$, the observed scaling exponents, ζ_n^{ξ}, slightly deviate towards shallower gradients compared to the MS17 model. The scaling exponents of the parallel component $\zeta_n^{\ell_{||}}$ exhibit a nonlinear dependence on n, though with less pronounced concavity than the perpendicular components, and notably diverge from the MS17 model, even at lower n values. A comprehensive discussion of these findings and their broader implications is provided in Section 5.2.4.

In the small-scale sub-inertial range, R_1, the scaling exponents for both the parallel and displacement components display a linear relationship with n. Conversely, the scaling exponent ζ_n^{λ} of the perpendicular component forms a convex function of n, albeit demonstrating a lesser extent of non-linearity relative to that observed in the R_2 range. Overall, R_1 is characterized by less pronounced intermittency signatures compared to R_2, with the observed ζ_n profiles deviating from the expectations set by established theoretical models.

To further investigate multifractality and deviations from Gaussian statistics in the magnetic field time series, we consider the Scale-Dependent Kurtosis, defined as $K(\ell) = SF^4(\ell)/[SF^2(\ell)]^2$ (Frisch, 1995; Bruno et al., 2003). As a normalized fourth-order moment, $K(\ell)$ is sensitive to extreme values of increments, allowing us to detect the tendency of PDFs in intermittency-affected time series to exhibit increasingly flared-out tails at smaller scales. In simpler terms, it quantifies how the "tailedness" of the distribution of increments in a turbulent field changes across various scales.

We employ both 2-point ($K_2(\ell)$) and 5-point ($K_5(\ell)$) methods to study the fractal properties of magnetic field time series. The resulting curves for the parallel, perpendicular,

and displacement components of the magnetic field are illustrated in panels (a) to (c) of Figure 5.6. At scales $\lambda \geq 100d_i$, an increase in $K(\ell)$ is observed for all components towards smaller scales, indicating a progressive deviation from Gaussianity in the underlying PDFs of increments, a hallmark of multifractal statistics (Sorriso-Valvo et al., 1999).

The limitations of the 2-point method are particularly evident in the R_1 range, where it notably diverges from the 5-point approach. In the case of the perpendicular component, $K_2(\lambda)$ appears to plateau at $\lambda < 20d_i$, consistent with the findings of (Chhiber et al., 2021a). Conversely, $K_5(\ell)$ maintains an increasing trend in R_1, albeit with a less steep slope compared to R_2. Within the R_1 range, both the parallel, $K_5(\ell_{||})$, and displacement, $K_5(\xi)$, components exhibit super-Gaussian but monofractal behavior, consistent with the linear $\zeta_n^{\ell_{||}}$ and ζ_n^{ξ} profiles illustrated in Figure 5.5.

At kinetic scales, both $K_5(\lambda)$ and $K_5(\xi)$ exhibit an increasing trend towards smaller scales, while the behavior of the parallel component remains less distinct. This trend in the perpendicular component diverges from the monofractal statistics observed at sub-ion scales in several observational studies using K_2 (Wu et al., 2013; Chen et al., 2014b; Chhiber et al., 2020a). However, our findings align with hybrid and fully kinetic simulations by (Cerri et al., 2019), where $K_5(\lambda)$ is demonstrated to increase above Gaussian values throughout the sub-ion scale range. Furthermore, qualitatively consistent trends were identified by (Alexandrova et al., 2008), who utilized wavelet-derived kurtosis to observe a gradual increase in this measure at kinetic scales.

5.1.4.4 Scale-Dependent Dynamic Alignment & Critical Balance

We begin by examining the scale-dependent behavior of the alignment angle between the perpendicular components of the increments, $\delta\boldsymbol{b}_\perp - \delta\boldsymbol{u}_\perp$ and $\delta\boldsymbol{z}_\perp^+ - \delta\boldsymbol{z}_\perp^-$. Elsässer variable increments were determined as $\delta\boldsymbol{z}_\perp^\pm = \delta\boldsymbol{v}_\perp \pm \mathrm{sign}(B_r^0)\delta\boldsymbol{b}_\perp$, where B_r^0 represents the 30-minute rolling average of the radial magnetic field component, B_r, used to determine the polarity of the background magnetic field. Here, $\boldsymbol{z}_\perp^-$ and $\boldsymbol{z}_\perp^+$ denote inward and outward propagating Alfvén waves, respectively. Magnetic field data were downsampled, following

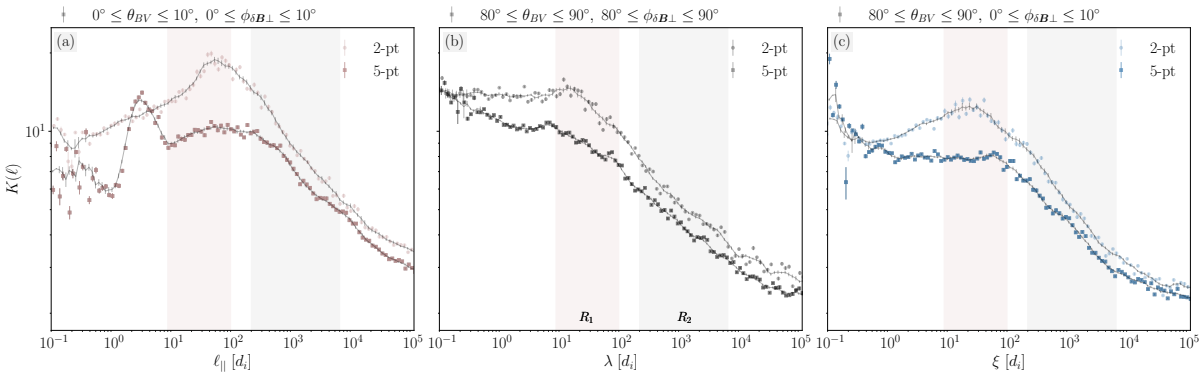

Figure 5.6: The scale-dependent kurtosis of the magnetic field, denoted as K_5 and K_2, is estimated using 5-point structure functions (SF_5^n) and 2-point structure functions (SF_2^n), respectively. These are plotted in red, gray and light-blue, respectively, as a function of scale in units of ion inertial length (d_i) for the parallel (a), perpendicular (b), and displacement (c) directions. Power-law fits have been applied to K_5 over the region R_2.

the application of a low-pass (Butterworth, 1930) filter to mitigate aliasing, to match the temporal resolution of the ion moment data. Magnetic field data were then normalized to velocity units using a 1-minute moving average applied to the proton density, n_p, time series.

Figure 5.7a,b illustrates two sets of alignment angles: $\theta_\perp^{ub(z)}$ in black, as defined by Equation 2.27, and $\tilde{\theta}_\perp^{ub(z)}$ in blue, calculated according to Equation 2.28. These sets are referred to as Θ^z when discussing Elsässer variables and Θ^{ub} in the context of velocity-magnetic field fluctuations, with the angle range confined to $0° - 90°$, consistent with (Podesta et al., 2009). The inset of Figure 5.7b illustrates the normalized residual energy, σ_r, in red, and the normalized cross helicity, σ_c, in gray.

At the energy injection range, $\lambda \gtrsim 2 \times 10^4 d_i$, a trend towards tighter alignment at smaller scales is observed, predominantly in Θ^{ub}. This is accompanied by a monotonic increase in σ_c and a shift of σ_r towards more negative values. These trends are more pronounced over longer observational intervals, although such extended periods are beyond the scope of this analysis.

Within the R_2 range, θ^z exhibits negligible variation with scale. Conversely, $\tilde{\theta}^z$ reveals subtle signatures of enhanced alignment at $\lambda \lesssim 2 \times 10^3 d_i$, coinciding with σ_r transitioning from negative to positive values. Simultaneously, Θ^{ub} steadily increases,

indicating progressive misalignment between the magnetic field and velocity increments at inertial scales.

The disparity between the two alignment definitions becomes more evident in the R_1 range, where $\tilde{\theta}^z \propto \lambda^{0.11}$. However, observations concerning this range should be approached cautiously due to potential instrumental noise, a matter further explored in Section 5.2.4.

What appears to solidly be the case, however, is that an inverse relationship holds between the alignment angle and the intensity of the field gradients. This relationship is depicted in the inset panel of Figure 5.7a, where θ^{ub} is plotted across various scale-dependent percentile bins of the Partial Variance of Increments (PVI) diagnostic, $\mathcal{I}_{\boldsymbol{B}}(t,\ell) = |\delta\boldsymbol{B}(t,\ell)|/\sigma_{\boldsymbol{B}}$, with $\sigma_{\boldsymbol{B}}$ representing the standard deviation calculated over a moving window of 1 hour, (Greco et al., 2018). Specifically, at $\lambda \gtrsim 2\times10^2 d_i$, higher-percentile $P(I_{\boldsymbol{B}})$ bins are characterized by lower average $\theta^{ub}_{\perp}$ values. Similar results were obtained when considering $\theta^z_{\perp}$ and segregating alignment angles based on the percentile bins of the PVI diagnostic applied to the $\boldsymbol{z}^+_{\perp}$ time-series, $I_{\boldsymbol{z}^+}$.

Under the assumption that the cascade is local in λ, we investigated the scale-dependence of the nonlinearity parameter $\chi^{\pm}$, according to the formulations by B06 and CSM15: $\chi^{\pm} = (\ell^{\pm}_{\parallel,\lambda}/\lambda^{\pm})/(\delta z^{\mp}_{\lambda}/V_a)sin\theta^z$. The analysis of outgoing (χ^+) and ingoing (χ^-) waves, depicted in gray and red respectively in panel (c) of Figure 5.7, reveals that both cascades start weak, with $\chi^{\pm} < 1$. As the cascade progresses towards smaller scales, a significant increase in the wave to nonlinear times ratio leads to a consistent rise in $\chi^{\pm}$, continuing until scales nearing the R_2 range onset.

For the ingoing waves, a transition from weak to strong wave turbulence is noted, with $\chi^- > 1$ at $\lambda \approx 3\times10^4 d_i$. The cascade remains strong throughout the resolvable portion of the inertial range, with χ^- being scale-independent, staying close to, yet slightly greater than, 1.

In contrast, the cascade of outwardly propagating waves remains weak within the R_2 range. More specifically, χ^+ shows a modest increase from approximately 0.1 at $\lambda = 10^4 d_i$

to around 0.2 at $\lambda = 2 \times 10^2 d_i$.

The potential inaccuracies in velocity measurements, exacerbated at smaller scales, along with the limited resolution of velocity field data, caution against drawing definitive conclusions about the cascades' nature in the R_1 range.

Lastly, it's noteworthy that the definition of $\chi^{\pm}$, as proposed by GS95, was also considered. This analysis revealed a scale dependence similar to that of $\chi^{\pm}$, but with both $\chi^{\pm}$ values being approximately twice as high.

5.1.5 Discussion

Recent in-situ observations indicate that the regime canonically identified as the inertial range comprises two sub-inertial segments, exhibiting distinct scaling behaviors (Wicks et al., 2011; Chhiber et al., 2021a; Sioulas et al., 2022b; Telloni, 2022; Wu et al., 2022; Sioulas et al., 2023; Sorriso-Valvo et al., 2023).

Building on this insight, our study investigates the anisotropic properties and higher-order statistics of the two sub-inertial ranges, utilizing a physically motivated, locally defined coordinate system. Concurrently, we focus on evaluating the predictions of homogeneous MHD turbulence models, grounded in the principles of *critical balance* and *dynamic alignment*, as proposed by CSM15 and MS17.

In the ensuing section, we embark on a detailed comparison with previous theoretical, observational, and numerical results that contextualizes our findings.

5.1.5.1 Investigating the Impact of Imbalance and Expansion on the Higher-Order Statistics

Phenomenological treatment of homogeneous MHD turbulence (e.g., GS95, B06, CSM15, MS17) is usually performed under the simplifying assumption of negligible cross helicity. However, the statistical properties of solar wind turbulence vary significantly with the degree of Elsässer and Alfvénic imbalance (Podesta and Borovsky, 2010; Chen et al.,

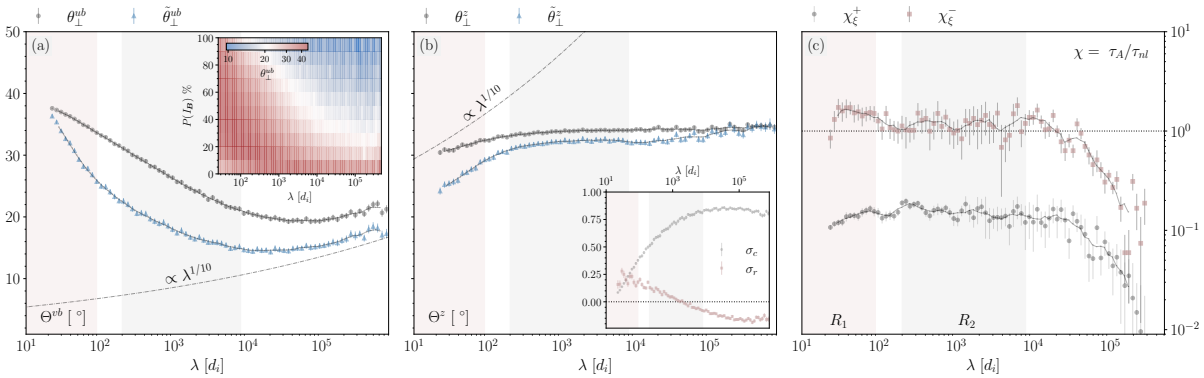

Figure 5.7: Alignment angles (a) $\Theta^{ub}(\lambda)$ and (b) $\Theta^{z}(\lambda)$, constrained to the range of $0° \leq \Theta^{ub(z)} \leq 90°$. The black curves depict alignment angles calculated with Equation 2.27, whereas the blue curves are based on Equation 2.28. The inset in panel (a) highlights the inverse relationship between alignment angle and field gradients by color-coding θ^{ub} across scale-dependent percentile bins of $I_{\boldsymbol{B}}$. The i-th bin at scale λ is defined as $[10(i-1), 10i)$, for $i = 1, ..., 10$. The inset in panel (b) displays $\sigma_r(\lambda)$, in red, and $\sigma_c(\lambda)$, in gray. Panel (c) shows the nonlinearity parameter, $\chi^{\pm}(\lambda)$, for outwardly (δz^{+}) and inwardly (δz^{-}) propagating waves, depicted with gray and red lines respectively. For all cases, results were derived by first calculating values for each interval independently and then computing a scale-dependent median.

2013; Wicks et al., 2011; Wicks et al., 2013b; Bowen et al., 2018b; Andrés et al., 2019; Sorriso-Valvo et al., 2021; Sioulas et al., 2023a; D'Amicis et al., 2022; McIntyre et al., 2023a). Various models have been proposed as modifications to the frameworks of GS95 and B06, incorporating different assumptions about the turbulent cascade to address the imbalance in oppositely directed Alfvénic fluxes (Lithwick et al., 2007; Beresnyak and Lazarian, 2008; Chandran, 2008; Perez and Boldyrev, 2009c; Podesta and Bhattacharjee, 2010; Schekochihin, 2022). As these models omit considerations of intermittency, they will not be elaborated upon in the ensuing discussion.

From an observational standpoint, the extent to which imbalance impacts higher-order statistics in MHD turbulence, is largely unexplored territory. Previous investigations have predominantly focused on categorizing findings based on wind speed or analyzing mixed Fast/Slow streams (Horbury and Balogh, 1997b; Mangeney, 2001b; Salem et al., 2009; Chhiber et al., 2021a; Wu et al., 2023), with a recent shift in interest towards magnetic compressibility (Palacios et al., 2022). However, these studies often do not explicitly detail the degree of Elsässer imbalance in the dataset, making direct comparisons

with our observations challenging. Nonetheless, it is worth pointing out that the scaling profiles observed in the R_2 range, especially for the parallel and perpendicular components, qualitatively align with results presented in (Osman et al., 2012).

In terms of numerical simulations, both homogeneous and inhomogeneous setups have been employed to examine the influence of imbalance on MHD turbulence statistics. Studies have primarily concentrated on spectral properties, revealing inertial range scalings of $\alpha_\lambda = -3/2$ (Perez et al., 2012; Chandran and Perez, 2019; Grappin et al., 2022; Meyrand et al., 2023).

(Shi et al., 2023a) investigated the effects of Elsässer imbalance on higher-order statistics using both homogeneous and EBM simulations, each initialized with varying degrees of imbalance. It was shown that EBM simulations initialized with $|\sigma_c| \approx 1$ result in higher-order moment scaling exponents consistent with the predictions of the CSM15 model. Conversely, simulations with lower values of σ_c exhibited scaling exponents showing a linear dependence on order n. The study also highlighted significant differences in higher-order scaling exponents between homogeneous and EBM simulations, even when initialized with identical levels of imbalance. For example, scaling exponents in homogeneous runs with $\sigma_c \approx 0$ were found to be convex functions of order and closely resembled the CSM15 model, in line with previous investigations (Chandran et al., 2015; Mallet et al., 2015; Palacios et al., 2022). Additionally, (Shi et al., 2023a) noted that in EBM simulations, the scaling properties displayed variations when higher-order moments were calculated from increments sampled in directions other than radial.

The latter observation is consistent with the findings of (Verdini and Grappin, 2015), who conducted a comparative analysis of balanced homogeneous and EBM simulations. They observed that while the homogeneous simulations displayed three-dimensional anisotropy, in agreement with B06—a finding further corroborated by (Mallet et al., 2016)—the EBM simulations demonstrated axisymmetry relative to $\boldsymbol{B}_\ell$ and did not exhibit three distinct inertial range scaling laws. Specifically, EBM simulations with increments measured along the radial direction demonstrated spectral scalings of $\alpha_\lambda \approx \alpha_\xi \approx -3/2$ in both the perpendicular and displacement components. However, measurements in the

transverse direction revealed scalings of $\alpha_\lambda \approx \alpha_\xi \approx -5/3$. In both cases, the parallel component lacked convincing scaling properties, although it exhibited a slightly steeper spectrum compared to the perpendicular components.

These findings lead to the following interpretation: The large-scale flow, being radial rather than uniform, cannot be negated by a Galilean transformation. Consequently, the expansion introduces an additional axis of symmetry and fosters a scale-dependent competition between the mean-field and radial axes (Völk and Aplers, 1973). Intuitively the effects of the expansion should be important when the non-linear time, τ_{nl} is slower than the expansion of the solar wind, $\tau_{exp} = R/V_{SW}$, $\tau_{exp} \leq \tau_{nl}$. Given that τ_{nl} is scale-dependent, it logically follows that the effects of expansion are more pronounced at larger scales[8]. From this discussion, it becomes evident that the expansion has the potential to modify the local 3D anisotropy in a scale-dependent manner.

At the resolution currently achievable in (R)MHD simulations, meaningful comparisons are possible with the larger-scale end of the inertial range, R_2, spanning $200 - 6000d_i$. Focusing on ζ_λ and setting aside anisotropy, our findings are consistent with (Shi et al., 2023a)'s imbalanced EBM results and, consequently, with the models of CSM15 and MS17. Nevertheless, the observed discrepancies in the scaling exponents of the parallel and displacement components within R_2 could hint at the influence of expansion effects, suggesting a scenario where the dominant axis of symmetry is a mix of both B_ℓ and the radial axis, with the contribution of each being scale-dependent.

Shifting focus to the scaling exponents in R_1 (spanning $8 - 100d_i$), recent theoretical work suggests that under conditions of strong imbalance, generalized helicity conservation may hinder turbulent energy transfer to kinetic scales (Passot et al., 2018; Passot and Sulem, 2019; Meyrand et al., 2021a; Passot et al., 2022). The "helicity barrier" effect could influence both spectral and potentially higher-order moment scalings at the smaller end of the inertial range. Homogeneous hybrid-kinetic simulations, initialized under strong imbalance conditions to capture this effect (Squire et al., 2022b), exhibit spectral

[8]Note, however, that observational evidence suggests that expansion can contaminate the turbulence statistics even within inertial scales (Verdini et al., 2018, 2019)

exponents for the parallel and perpendicular magnetic field components, $a_{\ell_{||}} \approx -2$ and $a_\lambda \approx -5/3$ respectively, in line with observations in the R_1 range.

While our current data does not definitively link our observations to the helicity barrier effect, it underscores the necessity for more comprehensive numerical studies focusing on the higher-order statistics of strongly imbalanced turbulence.

In conclusion, this discussion underscores the significant impact of imbalance and expansion effects on MHD turbulence statistics, indicating that the solar wind might not provide an ideal laboratory for evaluating homogeneous MHD turbulence models. This realization calls for a prudent application of homogeneous, balanced turbulence models in the analysis of solar wind observations and highlights the imperative for more sophisticated theoretical modeling and refined data interpretation techniques.

5.1.5.2 Critical Balance (CB)

Using balanced RMHD simulations, (Mallet et al., 2015) demonstrated that although the distributions of τ_{nl} and τ_A are not self-similar, their ratio, χ, maintains a scale-invariant distribution within the inertial range. (Chhiber et al., 2020) employed balanced incompressible MHD simulations to show that while the χ distribution peaks at $\chi \approx 1$, it is asymmetric and skewed towards $\chi \geq 1$. Further reinforcing the (Chhiber et al., 2020) findings, (Oughton and Matthaeus, 2020) highlighted that, despite RMHD simulations producing results claimed to support CB, the similarity between RMHD's $\chi \geq 1$ requirement and the CB condition of $\chi \approx 1$ has led to some confusion in differentiating these two theoretical frameworks.

(Chen, 2016a) utilized an extensive dataset of fast wind streams with moderate cross-helicity ($\sigma_c \approx 0.6$) from the outer heliosphere to investigate the scale dependence of the non-linearity parameter. They found χ to be scale-independent across the inertial range, maintaining a value around $\chi \sim 1$. Due to the lower resolution in velocity data and a less pronounced imbalance compared to our dataset, they assumed identical statistical properties for the two Elssässer fields, enabling them to estimate $\chi = (\ell_{||}/\lambda)(\delta b/V_A)$ using

solely magnetic field data.

However, numerical simulations by (Beresnyak and Lazarian, 2008, 2009) suggest that with increasing imbalance, statistical properties (i.e., amplitudes, coherence lengths) of the two Elsässer species diverge progressively. Considering the strong imbalance in our dataset, we employed a more refined approach, computing $\chi^{\pm} = (\ell^{\pm}_{||,\lambda}/\lambda^{\pm})/(\delta z^{\mp}_{\lambda}/V_a) sin\theta^z$.

Our analysis reveals a strong cascade for the inwardly propagating waves, with χ^- remaining scale-independent across the inertial range, maintaining a value slightly above unity. In contrast, the outwardly propagating waves exhibit a weaker cascade, with χ^+ increasing from 0.1 at $\lambda \approx 10^4 d_i$ to 0.2 at $\lambda \approx 10^2 d_i$

At this point, it's important to recognize two key factors that might affect the accuracy of our $\chi^{\pm}$ estimates. First, there's a prevailing assumption that $z^{\pm}$ structures are primarily sheared by counter-propagating $z^{\mp}$ wavepackets of similar perpendicular scale, which implies a cascade that is local in λ. However, this notion is challenged by the work of (Schekochihin, 2022) who put forward a model of imbalanced turbulence that consists of two strong, "semi-local" cascades: one local in λ for the stronger field and another, local in $\ell_{||}$, for the weaker field. The implications of this model cast doubt on our estimates of $\chi^{\pm}$ that is predicated on the concept of scale locality.

Furthermore, the transition from weak to strong turbulence, characterized by a change from $\chi \ll 1$ and $\alpha_\lambda \approx -2$ to $\chi \approx 1$ and $\alpha_\lambda \approx -3/2$, is a pivotal aspect of the CB discussion. This transition, observed in balanced RMHD shell-model simulations (Verdini and Grappin, 2012), 3D incompressible MHD simulations (Meyrand et al., 2016), and recently in the Earth's magnetosheath (Zhao et al., 2023), remains unreported in the solar wind [9].

Our results indicate a transition in the cascade of the ingoing wave from weak to strong turbulence, with $\chi^- > 1$ at $\lambda \approx 3 \times 10^4 d_i$, yet without capturing the anticipated scaling transition. We speculate, below, that this could be related to the effects of

[9]Even though such a transition was speculated in recent works (Telloni, 2022; Wu et al., 2022; Sioulas et al., 2023)

"anomalous coherence". More specifically, in the context of homogeneous MHD, nonlinear interactions between counterpropagating waves are uncorrelated and transient, limited to the duration of encounters. In the solar wind, however, nonlinear dynamics are complicated by *anomalous coherence*, a phenomenon arising from non-WKB reflection of outwardly propagating fluctuations (Velli et al., 1989; Velli et al., 1990; Hollweg and Isenberg, 2007). A key aspect of this effect is the presence of an "anomalous" reflected component, z_a^-, in addition to the "classical" component z_c^-, which remains stationary relative to the z^+ frame, coherently shearing it throughout its lifetime (Verdini et al., 2009; Chandran and Perez, 2019). Under strong imbalance and inhomogeneity, z_a^- can assume a leading role at large scales, altering the phenomenology of the energy cascade and leading to distinct spectral behaviors: a $1/f$ scaling for outwardly propagating waves and an $f^{-3/2}$ scaling for inwardly propagating waves (Velli et al., 1989; Perez and Chandran, 2013; Meyrand et al., 2023).

In summary, our results suggest that at inertial scales, outgoing waves experience a weak cascade, while ingoing waves undergo a strong one, closely resembling the CB condition ($\chi_\xi^- \approx 1$). However, given the complexities previously discussed and the uncertainties inherent in our measurements, we advise interpreting these findings with a degree of caution.

5.1.5.3 Scale Dependent Dynamic Alignment (SDDA)

Several numerical investigations into homogeneous (R)MHD (Mason et al., 2006; Perez et al., 2012, 2014; Cerri et al., 2022) have provided ample evidence for alignment signatures spanning a significant portion of the inertial range. However, (Beresnyak, 2012, 2014) have suggested that this observed alignment increase may be a finite-range phenomenon closely linked to dynamics at the outer scale.

Observational studies using data sampled at 1 AU have provided evidence of alignment at large, energy-containing scales. However, it has been observed that this trend towards increasing alignment diminishes at inertial scales (Podesta, 2009; Hnat et al., 2011; Wicks

et al., 2013a; Parashar et al., 2019). This trend persists even in data intervals specifically chosen to mitigate the effects of solar wind expansion (Verdini et al., 2018). It has been noted, however, that small errors in velocity vector measurements, due to instrumental limitations, can lead to significant errors in alignment angle measurements, even at large scales (Podesta et al., 2009).

Recently, (Parashar et al., 2020) explored the scale dependence of several alfvénicity diagnostics during E1 of PSP. Their findings suggest that σ_c starts decreasing, with σ_r increasing, at scales considerably larger than those observed at 1 AU (Podesta and Borovsky, 2010), despite high alfvénicity at large scales. This observation aligns with HELIOS observations (Tu et al., 1990) and has been attributed to the substantial energy found in velocity shears in the inner heliosphere (Ruffolo et al., 2020). Specifically, shear disrupts an initial spectrum of high cross helicity by injecting equal amounts of the two Elsässer energies (Roberts et al., 1987; Goldstein et al., 1989; Roberts et al., 1992).

The scale-dependence of the alignment angles correlates directly with that of σ_c and σ_r, as only two out of these four quantities are independent. Specifically, the formal relationship between imbalance, residual energy, and alignment, as described by $cos\theta^z_\perp = \sigma_r/(1-\sigma_c^2)^{1/2}$ and $cos\theta^{ub}_\perp = \sigma_c/(1-\sigma_r^2)^{1/2}$, indicates that the development of both Elsässer imbalance and residual energy, i.e., a monotonic increase in $|\sigma_c|$ and $|\sigma_r|$ towards smaller scales, is necessary for SDDA to emerge towards smaller scales (Wicks et al., 2013a; Schekochihin, 2022).

Such trend is evident in Figure 5.7, where alignment signatures become apparent only when σ_c exhibits a monotonic increase at scales $\lambda < 10^4 d_i$, or when σ_r becomes positive, leading to a monotonic increase in $|\sigma_r|$ at scales $\lambda < 2 \times 10^3 d_i$. Although instrumental noise might influence the latter trend, as discussed in (Bourouaine et al., 2020), the observed behavior at energy injection scales aligns with 1 AU observations (Wicks et al., 2013a). In contrast, in the inertial range, $\theta^z (\approx 35^\circ)$ remains roughly scale-independent.

These observations raise a critical question: Is the observed scale-dependence of the alignment a reflection of actual physical processes, or might it simply be a consequence of

instrument characteristics?

Potential physical mechanisms may encompass interactions between compressive and non-compressive modes (Cho and Lazarian, 2003; Chandran, 2005), ideal MHD instabilities manifesting in the solar wind, including the Kelvin-Helmholtz instability (Malagoli et al., 1996), the cessation of the aligning cascade due to the tearing instability (Mallet and Schekochihin, 2017; Boldyrev and Loureiro, 2017; Comisso et al., 2018), or even the solar wind's inherent inhomogeneity resulting in non-WKB reflections and a reduction in cross-helicity.

The extent to which instrumental noise influences these observations remains a crucial, yet unresolved, concern, emphasizing the necessity for a careful interpretation of observational data. While our analysis cannot definitively assert the nature of SDDA at small scales, it provides compelling observational evidence suggesting an inverse relationship between alignment angles and the intensity of field gradients, thereby corroborating the numerical results of (Mallet et al., 2015). As such, our observations lend support to the CSM15 model, suggesting that the physical basis of alignment lies in the mutual shearing of Elsässer fields during imbalanced collisions between counterpropagating wave packets.

Before concluding, another topic related to our findings deserves further discussion. Our observations indicate strong anti-alignment between Elsässer species at larger scales, with $\sigma_c \approx 1$ and typically small and negative σ_r, implying, as suggested by (Wicks et al., 2013a), $cos\theta^z_\perp \approx 180^\circ$ at $\lambda \approx 10^4 d_i$. It is natural, then, to inquire how this picture would be modified in the case of globally balanced streams. For instance, as emphasized in CSM15, outer-scale fluctuations in the context of globally balanced turbulence are not expected to be strongly aligned. This suggests that while imbalanced turbulence may exhibit alignment saturation at larger scales, balanced turbulence has the potential for further alignment, assuming that σ_c has room to increase at smaller scales. Thus, the dynamics of alignment across scales in balanced turbulence present an intriguing area for future research, particularly in comparing the extent of this alignment process with that in imbalanced streams. This aspect warrants further investigation and will be the focus of future work.

5.1.5.4 Exploring the Efficacy of the CSM15 & MS17 Models in the Context of Imbalanced Turbulence

Our results indicate that the intermittent scalings of the nth-order conditional structure functions in the direction perpendicular to both the local mean field and the fluctuation directions closely align with the theoretical frameworks proposed by CSM15 and MS17. However, our dataset exhibits notable characteristics that diverge from the assumptions underlying these models. These include strong imbalance in the fluxes of the Elsässer species and a prevalence of eddies conforming to a field-aligned tube topology, which, on average, do not display increasing alignment towards smaller scales. At first glance, these observations might seem contradictory to the expectations set forth in the aforementioned models. Nevertheless, upon closer examination of the model's fundamental assumptions, it becomes apparent that these empirical findings are not inconsistent with the model's theoretical framework.

In Section 1.3.6, we examine the foundational assumptions of the CSM15 and MS17 models. These assumptions encompass (1) negligible cross helicity at energy injection scales and (2) the formation of eddies following a current sheet topology, characterized by a volume filling factor $f_{cs} \propto \lambda$, alongside the dynamic alignment of vector field fluctuations at smaller scales. The models incorporate alignment as an intermittency effect, resulting in (1) the inherent introduction of local Elsässer imbalance and (2) the lack of a requirement for the "average" eddy to adhere to a 3D anisotropic current sheet topology. The models propose that it is the eddies in the tails of the PDFs that are expected to exhibit this topology, showing increased alignment at smaller scales. In essence, an inverse correlation between alignment and the intensity of field gradients is anticipated at any given scale.

When second-order moments are employed to examine the statistical shape of eddies, the high-amplitude, current-sheet-like structures found in the tails of the increment PDFs are typically obscured during the averaging process by more common, lower-amplitude, tube-like eddies. However, as higher moment orders are considered, these high-amplitude structures gain more prominence in the ensemble average, thereby significantly impacting

the profile of the scaling exponents.

Given that fluctuations in the perpendicular component are energetically dominant, any "side effects" stemming from the disruption of anisotropy due to expansion, and possibly from constraints imposed by spherical polarization (Matteini et al., 2024), do not seem to significantly impact the scaling characteristics of the perpendicular component. However, they do appear to influence the scaling profiles of the displacement and parallel components. Hence, incorporating these effects into the existing homogeneous models could potentially enhance the scaling predictions of these models and offer valuable insights into the nature of intermittent turbulence in the expanding solar wind.

5.1.5.5 Observations of the outer scale

At large energy-containing scales, as depicted in Figure 5.3, the parallel and perpendicular components display rough equipartition in fluctuating energy. However, the displacement component appears somewhat more energetic in comparison. Consequently, eddies deviate from isotropy, exhibiting a subtle compression along the fluctuation direction.

Our findings contrast with those of (Chen et al., 2012), who observed eddy elongation along the displacement direction ($\hat{\xi}$) at large scales in fast solar wind data at 1.4 AU.

To delve deeper into these findings, (Verdini and Grappin, 2015) conducted a comparative analysis using 3D MHD homogeneous and EBM simulations. They found isotropic eddies at energy injection scales in non-expanding simulations. However, in expanding simulations where increments were measured along the radial direction (typical for single-spacecraft missions at 1 AU), results aligned with those reported by (Chen et al., 2012). Interestingly, large-scale anisotropy disappeared, and eddies appeared isotropic when increments were measured in non-radial directions. This was interpreted as an effect of expansion, which preferentially dampens the radial component of magnetic field fluctuations relative to the azimuthal ones, confining fluctuations primarily to the plane orthogonal to the radial direction and leading to an anisotropic energy distribution among the field components. This phenomenon was observed in 3D EBM simulations (see e.g.,

Dong et al., 2014).

In a more recent study, (Verdini et al., 2018) analyzed a decade of data from the Wind spacecraft and identified a correlation between large-scale anisotropy and variance anisotropy, defined as $E = (b_T^2 + b_N^2)/b_R^2$, where b represents the rms amplitude of fluctuations. They found that intervals corresponding to the "strong" expansion dataset (defined by $E > 2$) exhibited eddy elongation along the displacement direction, consistent with (Chen et al., 2012). Conversely, intervals from the "weak" expansion dataset (with $E \leq 2$) showed eddy elongation along the perpendicular direction ($\hat{\lambda}$).

Based on these results, (Verdini et al., 2018) suggested that PSP, due to its unique orbit– allowing measurements perpendicular to the radial direction during its near-sun phase– would detect isotropic eddies at energy injection scales.

To overcome the limitations of single spacecraft measurements, (Vech and Chen, 2016) adopted a multispacecraft approach, enabling the separation of measurements along both radial and transverse directions. This strategy facilitated the isolation of expansion, solenoidality, and the mean magnetic field effects. Their investigation underscored the dominant role of the solenoidality constraint (Turner et al., 2011) over expansion in contributing to the observed variance anisotropy, E (see e.g., Horbury and Balogh, 2001). They further noted that while some anisotropy, as observed with radial increments, stemmed from expansion, a reduced yet noticeable degree of anisotropy persisted when measurements were conducted along the transverse direction. This suggests the involvement of additional mechanisms in shaping the large-scale 3D anisotropy.

Recent in-situ observations have shed light on the decay observed in the radial component within the inner heliosphere, indicating that it cannot be solely attributed to expansion effects. Specifically, analysis of data from PSP and HELIOS by (Tenerani et al., 2021) demonstrated that the rms of fluctuations in the radial component decays at a slower rate compared to that of the perpendicular component. This phenomenon was further clarified by (Matteini et al., 2024), who attributed it to the tendency of magnetic field fluctuations in the solar wind to evolve towards a state of spherical polarization. The

spherical polarization imposes constraints on the radial component's rms fluctuations, leading to a decay described, particularly at large scales, by $b_r \sim \boldsymbol{b}/2B$ (see also, Squire et al., 2020; Mallet et al., 2021).

Returning to our findings, we observe only a slight deviation from isotropy at the outer scale, which is notable considering that our dataset falls within the strong expansion category, with an average variance anisotropy of $E \approx 4.26 \pm 3.51$. Additionally, the sampling angle consistently falls within the range of $\theta_R \in [160°, 180°]$, indicating quasi-radial sampling. Despite identifying several intervals among multiple PSP encounters that exhibit isotropic large-scale eddies, no clear correlation has emerged from this preliminary analysis between prevailing plasma signatures (e.g., E, σ_c, σ_r, θ_R) and the occurrence of such intervals.

Taking into account the subtleties revealed by the recent observations discussed above, we must recognize our current inability to offer a satisfactory explanation for the observed configuration of the large-scale eddies in our dataset. However, the differences noted in the near-Earth and near-Sun eddies could indicate preferential damping in the fluctuations of the displacement component of the magnetic field. To clarify this aspect, it would be worthwhile to explore the development of the large-scale eddies at varying heliocentric distances.

5.1.5.6 Isotropization of eddies at small scales

Figure 5.4 illustrates that within the R_1 range, the eddies display increasing anisotropy, resembling ribbon-like structures towards smaller scales. However, the trend of increasing aspect ratio ceases at $\lambda \approx 2d_i$, at which point the eddies transition toward a quasi-isotropic state. In the following, we discuss two potential mechanisms that could explain these observations.

The observed transition towards isotropy at smaller scales is consistent with the idea that thin, long-lived current sheets generated by the turbulent cascade can be disrupted by the tearing instability and subsequent reconnection (Furth et al., 1963). Specifically,

when the maximum growth rate of the (Coppi et al., 1976) mode, γ_t, representing the fastest tearing mode in an MHD sheet, becomes comparable to the non-linear cascade time τ_{nl} ($\gamma_t \tau_{nl} \gtrsim 1$), the stability of the current sheets is compromised (Pucci and Velli, 2014; Uzdensky and Loureiro, 2016). The instability leads to the fragmentation of the dynamically forming sheets into flux ropes, which exhibit isotropy in the plane perpendicular to the magnetic field. This phenomenon is expected to occur at scale, λ_D, beyond which the nature of the MHD cascade undergoes a significant transformation. The disruption of the current sheets affects the dynamic alignment, accelerating the turbulent cascade and resulting in a noticeable steepening of the power spectrum (Mallet et al., 2017; Loureiro and Boldyrev, 2017; Boldyrev and Loureiro, 2017).

While this mechanism appears feasible for balanced turbulence, as evidenced by observations in the solar wind (Vech et al., 2018) and more recent findings in 3D fully-compressible (Dong et al., 2022) and reduced (Cerri et al., 2022) MHD simulations, it's important to acknowledge that the cutoff of the inertial range in imbalanced turbulence might also be influenced by kinetic effects. Therefore, despite the observation of a sub-ion-scale range mediated by magnetic reconnection in 2.5D hybrid-kinetic simulations (Cerri and Califano, 2017; Franci et al., 2017), other kinetic-scale mechanisms in imbalanced turbulence could potentially contribute to eddy isotropization. For instance, an alternative explanation for the isotropization of the eddies at small scales could be associated with the recently discovered "Helicity Barrier" mechanism (Passot et al., 2018; Passot and Sulem, 2019; Meyrand et al., 2021a; Passot et al., 2022).

As discussed in the introduction, strongly magnetized (low-beta) collisionless plasmas exhibit nonlinear conservation of both energy and cross helicity. However, the conserved quantity in reality is termed "generalized helicity." At $k_\perp \rho_i \lesssim 1$, this corresponds to the cross helicity following a forward cascade, which conservatively transforms into magnetic helicity at $k_\perp \rho_i \gtrsim 1$, undergoing an inverse cascade. Consequently, an imbalanced cascade arriving from the inertial range faces a complication—the sudden need to reverse the direction of the generalized helicity cascade. The helicity barrier impedes the viability of a constant-flux cascade, leading to an accumulation of energy in the stronger Elsässer

field. This accumulation shortens τ_{nl}, reducing the parallel correlation length, in line with the CB theory, to the extent that turbulent energy is redirected into an (ICW; (see, Stix, 1992)) spectrum. This mechanism opens up a new dissipation channel via the ion-cyclotron resonance (Squire et al., 2022c).

ICWs are commonly observed in the nascent solar wind, particularly during intervals marked by (anti)alignment between the mean magnetic field and solar wind flow direction (Bowen et al., 2020b). A strong correlation exists between the presence of ion-scale waves and the level of imbalance of fluctuations at inertial scales (Zhao et al., 2022; Bowen et al., 2023). The presence of ICWs can significantly impact the power spectra of magnetic fields at ion kinetic scales (Bowen et al., 2020b; Shankarappa et al., 2023). Specifically, the bump observed in the parallel spectrum just before the transition region has been attributed to the presence of ICWs, suggesting that the isotropization of the eddies could be a consequence of the helicity barrier mechanism.

The main emphasis of this analysis is on the inertial and energy injection scales. The extended interval size allows for more reliable estimates of second-order moments and, consequently, the anisotropic curves presented in Figure 5.3. However, no effort has been made to account for the energy contribution ICWs. Due to the strong correlation between the presence of ion-scale waves and Elsässer imbalance, simply disregarding intervals with ICW wave signatures (Duan et al., 2021; Zhang et al., 2022) may impede our investigation into kinetic-scale turbulence statistics in strongly imbalanced intervals. An alternative approach would entail identifying and eliminating the energy attributed to ICWs from the observed energy spectrum (see e.g., Shankarappa et al., 2023; Wang et al., 2023), and examining the resulting anisotropy based on the parallel and perpendicular spectra. This will be the focus of an upcoming study.

5.1.5.7 Can the trace PSD be interpreted as the perpendicular PSD ?

The theoretical models discussed in Section 1.3.5 provide scaling predictions for the parallel, perpendicular, and displacement components of fluctuating fields.

However, the angle between the solar wind flow and the magnetic field, as observed by spacecraft, can significantly influence whether fluctuations in measured quantities vary parallel or perpendicular to the magnetic field. Due to the Parker Spiral configuration (Parker and Tidman, 1958), the baseline value of the angle between the solar wind flow and the magnetic field, denoted as Θ_{VB}, increases with heliocentric distance. Consequently, spacecraft measuring magnetic field fluctuations at 1 AU are more likely to detect fluctuations perpendicular to the mean magnetic field direction.

Considering the strongly anisotropic nature of the turbulent cascade, with the majority of power associated with perpendicular wavenumbers (Shebalin et al., 1983; Montgomery and Turner, 1981; Horbury et al., 2008), observational studies have traditionally estimated the trace PSD and interpreted these measurements as representative of the perpendicular spectrum. However, as the PSP moves closer to the Sun, both the flow and the magnetic field become predominantly radial. Consequently, PSP often detects variations parallel -resulting in a deficit of measurements perpendicular- to the magnetic field. This can impact the statistical signatures of MHD turbulence, including intermittency (Sioulas et al., 2022b), estimates of correlation lengths (Cuesta et al., 2022), etc. As shown in Figure 5.8, the deficit caused by the sample size of the perpendicular fluctuations due to quasi-parallel sampling can also result in strong deviations between the perpendicular and trace PSD. This effect becomes even more important at later PSP encounters, and thus caution should be exercised when trying to utilize the trace PSD to compare with perpendicular PSD predictions of theoretical models.

5.1.5.8 Assessing 2-Point Structure Functions for Small-Scale Turbulence Analysis

The departure from monofractal statistics, exemplified by the adoption of SF_5^n, underscores the inadequacy of the SF_2^n method for statistical analysis of MHD turbulence at smaller spatial scales. Specifically, the SF_2^n method lacks accuracy in capturing the scaling behavior at these scales, where steep scaling in the power spectra and higher-order

moments are frequently seen. This deficiency can result in imprecise estimations of all associated intermittency metrics, leading to potentially erroneous interpretations of the nature of the turbulent cascade.

The prolonged duration of the intervals examined in this study, which may not be optimal for a concentrated analysis at kinetic scales, in conjunction with the limitations posed by the presence of ICWs as discussed in Section 5.1.4.2, underscores the need for further investigation. Future studies should consider employing either 5-point or wavelet-derived structure functions, with a specific emphasis on distinguishing between balanced and imbalanced turbulence streams (see, e.g., Bowen et al., 2023). This comprehensive exploration is essential for achieving a deeper and more precise comprehension of the fractal properties of MHD turbulence at kinetic scales.

5.1.5.9 Limitations

In addition to the limitations associated with velocity measurements discussed earlier, it is essential to acknowledge further inherent limitations in the analysis presented in this study.

5.1.5.10 Finite sample size effects

The proper study of MHD turbulence hinges on the ability to sample plasma from a common solar source, typically a single solar wind stream, and gather a sufficiently large sample size for statistical analysis. Spectral properties alone are insufficient for assessing scale invariance and fractal properties; higher-order moments are necessary. While evaluating structure functions is generally straightforward, estimating scaling exponents presents pitfalls. The primary concern arises from increased sensitivity to rare and large events as the order, p, increases. This can lead to finite sample effects dominating the analysis, especially as emphasis shifts to the poorly sampled tails of the distribution with higher orders. Consequently, higher-order moments become susceptible to outliers, rendering estimates of scaling exponents increasingly unreliable (Dudok de

Wit et al., 2013; Palacios et al., 2022). As a rule of thumb, it is generally deemed safe to compute structure functions up to a certain order, typically defined as $p_{\max} = \log N - 1$, where N represents the sample size (Dudok de Wit et al., 2013).

In our analysis, these challenges are further compounded by two factors. Firstly, we employ conditional analysis to estimate higher-order moments in three physically motivated directions, resulting in the exclusion of a significant portion of increments falling outside specified angle ranges. Secondly, we utilize 5-point structure functions, where the way increments are taken leads to a larger portion of the time series being discarded due to edge effects.

Moreover, PSP data introduces added complexity compared to 1AU measurements, as the distance from the Sun rapidly changes, causing large variations in the rms of fluctuations between intervals sampled at different heliocentric distances. Consequently, very long intervals cannot be utilized effectively.

Despite these limitations, the present analysis could be significantly improved by adopting the method described in (Palacios et al., 2022), where a large sample of increments from non-contiguous solar wind streams with similar characteristics can be utilized to construct the PDFs needed to obtain higher-order moments. This approach will be the focus of future work.

5.1.5.11 Scaling exponents of Elsässer fields.

In this study, our primary focus has been on the higher-order moments derived from the magnetic field timeseries. However, it's crucial to recognize that the fundamental variables in MHD are the Elsässer fields—rather than $\boldsymbol{B}$ and $\boldsymbol{V}$—due to their conservatively cascading energies. Indeed, the scaling predictions provided by the CSM15 and MS17 models pertain to the scaling exponents of the Elsässer field increment moments. Therefore, a more direct comparison with these models would entail estimating the moments of increments in $\boldsymbol{z}^{\pm}$ (see e.g., Palacios et al., 2022). However, adopting this approach would require downsampling the magnetic field timeseries to synchronize with the cadence of

the velocity field data. This would lead to a notable reduction in sample size, and render the estimation of anisotropic higher-order moments unfeasible with our current dataset.

Nevertheless, as discussed in CSM15, the regions contributing dominantly to both types of structure functions are those where $\delta \boldsymbol{z}^{\pm}$ exhibits exceptional magnitudes. In these regions, one Elsässer fluctuation, e.g., $\delta \boldsymbol{z}^{+}$, typically dominates over the other, leading to $\delta \boldsymbol{b} \approx (1/2)\delta \boldsymbol{z}^{+}$. Therefore, given the significant imbalance in our dataset, the scaling exponents estimated for the magnetic field timeseries can provide a reasonable approximation for the scaling exponents of the dominant (outgoing) Elsässer field.

5.1.5.12 Switchbacks

The near-Sun solar wind environment is characterized by the prevalent occurrence of Switchbacks, a subset of predominantly Alfvénic fluctuations with amplitudes significant enough to cause the magnetic field to reverse its direction abruptly, resulting in a local field polarity reversal and a corresponding radial velocity jet (Matteini et al., 2014; Horbury et al., 2018; Bale et al., 2019).

The question arises as to what extent these sudden reversals impact our ability to accurately estimate the local magnetic field, and consequently, the scaling exponents of the parallel and displacement components.

While excluding switchbacks from the analysis could potentially address this concern, it's noteworthy that the majority of our samples for the two perpendicular components originate from substantial kinks in the magnetic field time series, as these events lead to large Θ_{BV} angles. Therefore, no attempt has been made to further clarify this aspect. However, it is reassuring to note that the scaling exponent profiles obtained for a substantial dataset of imbalanced Wind observations at 1 AU, where significant kinks in the magnetic field time series typically diminish and switchbacks/switchback patches transition into microstreams (Horbury et al., 2023; Soni et al., 2024), are qualitatively consistent with those reported in the current analysis.

5.1.6 Conclusions and Summary

We analyzed in-situ observations from a highly Alfvénic stream captured during Parker Solar Probe's first perihelion to assess the predictions of MHD turbulence models grounded on the principles of "Critical Balance" and "Scale-Dependent Dynamic Alignment". Our objective was to assess the extent to which the conjectures made and predictions derived by these models align with in-situ solar wind observations and establish solid observational benchmarks for the testing and refinement of MHD turbulence phenomenologies.

The main findings of our study can be summarized as follows:

At the outer scale, $\lambda \gtrsim 2 \times 10^4 d_i$, we find:

(a1) Both (out)ingoing waves undergo a weak cascade, $\chi^{\pm} < 1$, that strengthens towards smaller scales. The trend is concurrent with tighter scale-dependent dynamic alignment (SDDA) of fluctuations, a monotonic increase in cross-helicity (σ_c), and a shift towards more negative residual energy (σ_r) values

(a2) The ingoing waves transition to a strong cascade ($\chi^{-} \gtrsim 1$) at $\lambda \approx 3 \times 10^4 d_i$; the associated spectral scalings deviate from the expected weak-to-strong turbulence transitions. We explore the possibility that "anomalous coherence' effects may account for this discrepancy in Section 5.2.4.

The domain canonically identified as the inertial range is comprised of two distinct sub-inertial segments that exhibit distinct turbulence statistics.

For the subinertial range spanning $200 - 6000 d_i$ and termed R_2 we find:

(b1) Spectral scaling indices for components parallel to the local mean field, fluctuation (displacement), and perpendicular directions assume values of $\alpha_{\ell_{||}} = -1.66 \pm 0.05$, $\alpha_{\xi} = -1.56 \pm 0.08$, and $\alpha_{\lambda} = -1.49 \pm 0.03$, respectively.

(b2) The "average" eddy assumes a field-aligned tube topology.

(b3) The alignment angle Θ^{ub} between velocity and magnetic-field fluctuations monotonically increases towards smaller scales, while the alignment Θ^{z} between the Elsässer fields remains roughly scale independent ($\approx 35°$). In both cases, an inverse relationship between alignment angles and the intensity of field gradients is observed, suggesting that the physical basis of alignment lies in the mutual shearing of Elsässer fields during imbalanced collisions between counterpropagating wave packets, as suggested in CSM15.

(b4) The cascade is strong for inwardly propagating waves ($\chi^{-} \gtrsim 1$) but weak for outwardly propagating ones, with χ^{+} increasing from 0.1 to 0.2 as scales decrease from $\lambda \approx 10^4 d_i$ to $10^2 d_i$.

(b5) The scaling exponents of the structure functions perpendicular to both $\boldsymbol{B}_\ell$ and the fluctuation direction conform to the theoretical models of CSM15 and MS17. However, the scaling profile in the parallel and displacement components deviates from theoretical predictions, possibly due to contamination from expansion effects.

For the subinertial range spanning $10 - 100 d_i$ (termed R_1), we find:

(c1) The spectrum steepens, with spectral scaling indices for components parallel to the local mean field, fluctuation (displacement), and perpendicular directions assuming values of $\alpha_{\ell_{||}} = -1.97 \pm 0.05$, $\alpha_\xi = -1.94 \pm 0.06$, and $\alpha_\lambda = -1.64 \pm 0.04$, respectively.

(c2) A shift from isotropy in the plane perpendicular to $\boldsymbol{B}_\ell$ becomes evident, indicating a shift in eddy structures from tube-like to ribbon-like, $\ell_{||} \gg \xi \gg \lambda$. While signatures of increasing SDDA are observed, the result is potentially susceptible to errors in particle data measurements.

(c3) The scaling exponents of the parallel and displacement components are a linear function of order, while the perpendicular component exhibits a weakly non-linear scaling profile. An overall transition towards "monofractal" statistics and a weakening of intermittency, compared to R_2, are evident.

(d) At $\lambda \approx 8d_i$, the increase in aspect ratio ceases, and the eddies transition to a quasi-isotropic state. This shift might be a signature of the tearing instability, potentially leading to reconnection of the thin current sheets, or it could result from turbulent energy being channeled into an ion-cyclotron wave spectrum, consistent with the "helicity barrier" effect.

(e) The 2-point structure function method SF_2^n is inadequate for capturing the essential properties of the turbulent cascade, at smaller scales. To accurately characterize steeper power laws at smaller spatial scales, the use of a more sophisticated method such as the 5-point structure function SF_5^n is essential.

While our study doesn't delve into the direct application of diagnostics for expansion and imbalance effects, it's interesting to note that preliminary findings using data from the Wind mission show a notable correspondence with the results from EBM simulations conducted by (Shi et al., 2023a). Specifically, the scaling exponents in R_2 are consistent with CSM15 when $\sigma_c \approx 1$, and become a linear function of order as the imbalance decreases to $\sigma_c \approx 0$. Furthermore, extending the work of (Verdini et al., 2018) to higher order moments it is found that when intervals are selected in such a way as to minimize the expansion effects the scaling exponents in all three components are in striking agreement with those predicted by the MS17 model (Sioulas et al. 2024, in progress).

In summary, our findings suggest that the models proposed by CSM15 and MS17, which integrate SDDA as an intermittency effect and account for local imbalance, possess the essential elements for a successful phenomenological representation of imbalanced MHD turbulence. This assertion stems from several key observations: firstly, the models provide scaling predictions for higher-order moments in the perpendicular component of the magnetic field that align well with our in-situ observations. Secondly, an inverse relationship between alignment angles and the intensity of field gradients suggests that the alignment mechanism originates from the mutual shearing of fields during imbalanced collisions of wavepackets. However, it's worth noting that certain aspects of solar wind turbulence, such as the presence of two sub-inertial ranges and anisotropic signatures,

remain unaddressed by the models. This suggests that incorporating additional effects, such as accounting for inhomogeneity or the spherical polarization of fluctuations, could enhance the models' scaling predictions.

5.2 Scale-Dependent Dynamic Alignment in Magnetohydrodynamic Turbulence: Insights into Intermittency, Compressibility, and Imbalance Effects

5.2.1 Introduction

In the framework of reduced Magnetohydrodynamics (RMHD), applied to highly conducting, magnetized plasmas threaded by a large-scale background magnetic field, $\boldsymbol{B}_0$, on scales larger than the ion gyroradius, ρ_i, the dynamics of (Alfvén, 1942) polarized fluctuations decouple from the compressive cascade and can be studied through (Kadomtsev and Pogutse, 1967; Schekochihin et al., 2009b)

$$\partial_t \boldsymbol{z}_\perp^\mp \pm V_A \partial_z \boldsymbol{z}_\perp^\mp + \boldsymbol{z}_\perp^\pm \cdot \nabla_\perp \boldsymbol{z}_\perp^\mp = -\nabla_\perp p, \tag{5.7}$$

where, $\boldsymbol{V}_a = \boldsymbol{B}_0/\sqrt{4\pi\rho}$ the Alfvén speed, $\boldsymbol{z}_\perp^\pm = \boldsymbol{u}_\perp - \boldsymbol{b}_\perp/\sqrt{4\pi\rho}$ are the (Elsasser, 1950) variables, $\boldsymbol{u}_\perp$ and $\boldsymbol{b}_\perp$ represent transverse, to $\boldsymbol{B}_0$, small amplitude $|\boldsymbol{b}_\perp|/|\boldsymbol{B}_0| \ll 1$ velocity and magnetic field perturbations, respectively, and the total pressure, p, can be determined by $\nabla_\perp \cdot \boldsymbol{z}_\perp^\pm = 0$. In this framework, non-linearity arises from the collisions of counterpropagating wave packets, resulting in their distortion and fragmentation (Iroshnikov, 1963; Kraichnan, 1965). The effectiveness of the non-linear interactions hinges on the relative importance of the linear and non-linear terms in Equation 5.2.1. It can be quantified by the non-linearity parameter $\chi^\pm \equiv \tau_A^\pm/\tau_{nl}^\pm \sim (k_\perp \delta u_k)(k_{||} V_A)$, which compares the linear wave propagation time $\tau_A^\pm = \ell_{||}^\pm/V_A$ and non-linear decorrelation time $\tau_{nl}^\pm \sim \lambda/\delta \boldsymbol{z}_\lambda^\mp$.

The interaction of Alfvénic wavepackets, described by the dispersion relation $\omega = k_{||} v_A$, where $k_{||}$ the wavevector parallel to B_0, gives rise to a distinctive feature of MHD turbulence wherein the flux of energy is primarily directed towards smaller scales perpendicular to the magnetic field. The cascade is strongly anisotropic, and even more so at smaller scales, resulting in structures characterized by coherence lengths parallel ($\ell_{||} \sim 1/k_{||}$) and perpendicular ($\lambda \sim 1/k_\perp$) to $\boldsymbol{B}_0$, which satisfy $\ell_{||} \gg \lambda$ (Robinson and Rusbridge, 1971;

Shebalin et al., 1983; Higdon, 1984; Oughton et al., 1994). The anisotropy amplifies the non-linearity of the interactions (Galtier et al., 2000). Consequently, even in the case where the system was forced at large scales such that $\chi \ll 1$ (referred to as the "weak turbulence" regime), it inevitably transitions, at sufficiently small scales, to a state where within a single collision, the wave packet undergoes deformation of a magnitude comparable to its own, $\chi \sim 1$, i.e., the cascade τ_c and dynamical $\tau_d = 1/wk_\perp$ timescales are similar. Since the perturbation frequency ω has a lower bound due to an uncertainty relation $\omega\tau_c > 1$, the cascade is forced to remain in the $\chi \sim 1$ regime. This realization foRMS the basis of what is formally known as the "critical balance" (CB) conjecture (Goldreich and Sridhar, 1995), denoted hereafter as (Goldreich and Sridhar, 1995). In the framework of *balanced* turbulence, i.e., assuming equal fluxes, $\epsilon^{\pm}$, in counterpropagating wavepackets, CB implies an anisotropic scaling relationship between the parallel and perpendicular wavevectors, specifically $\kappa_{||} \propto \kappa_\perp^{2/3}$, leading to expected field-perpendicular and field-parallel energy spectra of the form $E(k_\perp) \propto k_\perp^{-5/3}$ and $E(k_{||}) \propto k_{||}^{-2}$, resepectively.

While in situ observations of the solar wind appeared consistent with the phenomenology proposed by (Goldreich and Sridhar, 1995) (Horbury et al., 2008; Wicks et al., 2010), numerical simulations of homogeneous, incompressible MHD revealed a significant discrepancy. Specifically, the observed spectral index perpendicular to $\boldsymbol{B}_\ell$ was closer to $-3/2$ (Maron and Goldreich, 2001; Müller et al., 2003; Müller and Grappin, 2005). These findings prompted refinements to the (Goldreich and Sridhar, 1995) model (Boldyrev, 2005; Galtier et al., 2005; Beresnyak and Lazarian, 2006b; Gogoberidze, 2007).

One approach to addressing this discrepancy was the incorporation of scale-dependent dynamic alignment (SDDA) into the (Goldreich and Sridhar, 1995) framework. Specifically, (Boldyrev, 2006), henceforth (Boldyrev, 2006), proposed that non-linearity in MHD turbulence is reduced due to the increasing alignment between $\delta\boldsymbol{v}_\perp$ and $\delta\boldsymbol{b}_\perp$ as λ decreases, with $\theta_\lambda^{ub} \sim \delta b/v_A \propto \lambda^{1/4}$. At small scales, this leads to the emergence of three-dimensional anisotropic eddies characterized by $\ell_{||} \gg \xi \gg \lambda$, where ξ represents the coherence length in the direction of $\delta\boldsymbol{b}$. A self-consistent mechanism that results in increasing alignment would modify the spectral slope of the field-perpendicular inertial range energy spectrum

from the -5/3 Kolmogorov slope to the numerically observed -3/2 slope.

A substantial body of numerical studies on homogeneous MHD turbulence has provided evidence supporting the scale-dependence of certain alignment measures across a sizable portion of the inertial range (Mason et al., 2006; Perez et al., 2012, 2014; Mallet et al., 2015; Chandran et al., 2015; Cerri et al., 2022). However, concerns have been raised suggesting that the observed alignment may be a finite-range effect intrinsically linked to dynamics occurring at the outer scale (Beresnyak, 2012). For instance, Beresnyak (2012) interpret these signatures based on the idea that MHD turbulence is much less local in k-space compared to hydrodynamic turbulence (see, e.g., Beresnyak, 2011; Schekochihin, 2022). Consequently, the driving mechanism does not fully replicate the properties of the inertial range, and the transition to asymptotic statistics is broad, causing many quantities to appear scale-dependent as they adjust to the asymptotic regime. Moreover, the (Boldyrev, 2006) model has faced criticism for violating the rescaling symmetry of the RMHD equations (Beresnyak, 2012). As a result, an ongoing debate persists regarding whether this numerical evidence accurately reflects the scale-dependent dynamic alignment angle in the asymptotic state of the inertial range (Beresnyak, 2012; Perez et al., 2014).

The theory of SDDA has been revisited by Chandran et al. (2015, hereafter, (Chandran et al., 2015)), refining it in a manner that aligns SDDA with the rescaling symmetry of RMHD. Their model distinguishes between two archetypal types of alfvénic interactions: imbalanced ($\delta \boldsymbol{z}^{\pm} \gg \delta \boldsymbol{z}^{\mp}$) and balanced ($\delta \boldsymbol{z}^{\pm} \sim \delta \boldsymbol{z}^{\mp}$). They develop an approximate theory which demonstrates that in imbalanced interactions, the mutual shearing of the interacting wave packets leads to the rapid cascading of the subdominant field to smaller scales. This occurs as it rotates into alignment with the dominant field, notably without distorting their amplitudes. Consequently, at any given scale, wave packets subjected to the smallest number of balanced collisions—those that alter both amplitude and coherence lengths—roughly retain their outer scale amplitudes, resembling three-dimensional anisotropic current sheet structures (see also Howes, 2015; Mallet and Schekochihin, 2017). This indicates that as the cascade progresses toward smaller scales, the fluctuating energy becomes confined within an increasingly smaller volume fraction,

thus establishing a link between SDDA and intermittency (Oboukhov, 1962; Kolmogorov, 1962).

The framework established by (Chandran et al., 2015) has received substantial support from the studies of (Mallet et al., 2015, 2016), who utilized RMHD numerical simulations to demonstrate that the degree of alignment at any given scale increases with fluctuation amplitude. This result suggests that alignment angles exhibit intermittency rather than scale invariance (see also Beresnyak and Lazarian, 2006a). Furthermore, scaling predictions derived from these phenomenological models, particularly concerning higher-order moments and alignment angles, show strong agreement with numerical simulations of forced, homogeneous, and isotropic MHD turbulence (Chandran et al., 2015; Mallet et al., 2016; Mallet and Schekochihin, 2017; Shi et al., 2023a; Dong et al., 2022).

However, in-situ solar wind observations reveal certain deviations from the model predictions. For example, while inertial range scalings of the perpendicular components for highly Alfvénic intervals tend towards the predicted -3/2 value, for both magnetic field and velocity fluctuations, the former steepen towards -5/3 in balanced streams (Chen et al., 2013; Sioulas et al., 2022; McIntyre et al., 2023b). Moreover, emerging evidence indicates the presence of two sub-regimes within the traditionally defined inertial range, particularly prominent in strongly imbalanced streams and when considering anisotropic spectra in locally defined frames (Wicks et al., 2011; Sioulas et al., 2022b; Wu et al., 2022; Sioulas et al., 2023). Although 3D anisotropic eddies are evident at the smaller scale end of the inertial range, anisotropy qualitatively changes across scales (Chen et al., 2012; Verdini et al., 2018; Sioulas et al., 2024).

Finally, in-situ observations of SDDA in the solar wind remain inconclusive. While SDDA is evident at large, energy-containing scales in the *1/f* range, a shift occurs in the inertial range ($\lambda \approx 10^4 d_i$), demonstrating an increasing misalignment of fluctuations towards smaller scales (Podesta, 2009; Hnat et al., 2011; Wicks et al., 2013a; Parashar et al., 2018; Parashar et al., 2020). The increasing misalignment at inertial scales persists even in intervals selected to minimize solar wind expansion effects (Verdini et al., 2018), although in this case, the 3D anisotropic inertial range spectral scaling and topology of

eddies align with proposed models (Boldyrev, 2006; Chandran et al., 2015; Mallet and Schekochihin, 2017).

These observations could suggest that additional physical mechanisms beyond standard homogeneous MHD are necessary to fully explain the observed properties of solar wind turbulence. Such mechanisms include, but are not limited to, the breaking of local anisotropy due to the additional radial symmetry axis introduced by expansion (Dong et al., 2014; Verdini and Grappin, 2015; Verdini et al., 2018), the influence of non-Alfvénic interactions in the turbulent cascade (see, e.g., Bowen et al., 2021), the spherically polarized nature of Alfvénic fluctuations (Matteini et al., 2014; Mallet et al., 2021; Matteini et al., 2024), and the imbalance in the fluxes of counterpropagating wave packets (Lithwick et al., 2007; Chandran, 2008; Perez and Boldyrev, 2009a; Schekochihin, 2022).

In recent years, considerable efforts have been made to gauge the impact of imbalance, compressibility, intermittency, and expansion on the statistical properties of MHD turbulence (Lithwick and Goldreich, 2001; Hnat et al., 2005; Salem et al., 2009; Lithwick et al., 2007; Chandran, 2008; Podesta and Borovsky, 2010; Podesta and Bhattacharjee, 2010; Chen et al., 2013; Wicks et al., 2013a; Matteini et al., 2014; Bowen et al., 2018a,b; Shoda et al., 2019; Vech and Chen, 2016; Meyrand et al., 2021a; Sioulas et al., 2022b; Wang et al., 2023). However, previous investigations, particularly those focusing on in-situ observations, have not thoroughly explored these effects on the statistical properties of SDDA. This work aims to bridge this gap.

To this end, we conduct a statistical analysis of carefully selected solar wind intervals spanning a 28-year period from WIND observations. We utilize scale and time-dependent proxies to isolate the properties of interest, namely compressibility, intermittency, and imbalance, enabling us to quantify their effects on SDDA measurements.

5.2.2 Data Selection

We utilize data collected by instruments aboard the WIND spacecraft, positioned at Earth's L1 Lagrange point, approximately 1 AU from the Sun.

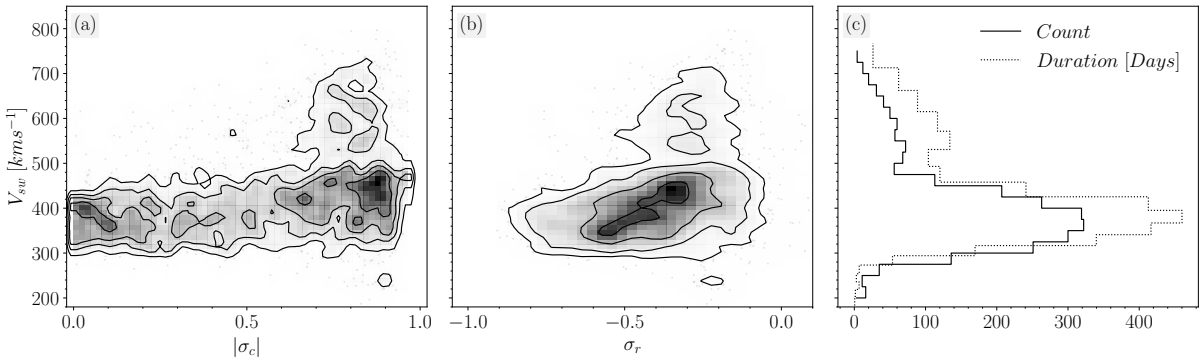

Figure 5.8: Joint probability distribution of $V_{\rm sw}$ and (a) σ_c, (b) σ_r for the homogeneous intervals selected for our analysis. σ_c and σ_r are computed based on fluctuations at the scale of $2 \cdot 10^4 d_i$. In Panel (d), a histogram displays interval counts and cumulative durations relative to $V_{\rm sw}$.

This study primarily analyzes magnetic field and ion measurements obtained from the MFI instrument (Lepping et al., 1995) and the 3DP/PESA-L instrument (Lin et al., 1995), which provide data with resolutions of 0.1 seconds and 3 seconds, respectively. It should be noted that, while a 3-second dataset is available for the magnetic field timeseries, an issue has been identified with this specific dataset, as detailed in 5.2.3.5. Consequently, the full-resolution MFI data were downsampled—following the application of a low-pass Butterworth filter to mitigate aliasing—to match the temporal resolution of the ion moment data.

In the preliminary phase of our analysis, we conducted a meticulous visual inspection of the WIND timeseries data spanning from January 1, 1995, to August 1, 2023. Based on this examination, we classified the data into three distinct categories:

1. Slow Alfvénic wind: $V_{sw} \leq 450$ km/s, $\sigma_c \geq 0.85$

2. Slow non-Alfvénic wind: $V_{sw} \leq 450$ km/s, $\sigma_c \leq 0.85$

3. Fast Alfvénic wind: $V_{sw} \geq 500$ km/s, $\sigma_c \geq 0.85$

Throughout the visual inspection, strict adherence was maintained to several selection criteria:

1. A minimum interval duration of 6 hours was mandated,

2. The stability of plasma parameters (V_{sw}, n_p, β, Θ_{VB}, σ_c, σ_r, sign(B_x)) was ensured throughout the selected interval,

3. Intervals showing clear indications of transient events, like Coronal Mass Ejections or Heliospheric Current Sheet crossings, were omitted,

4. Intervals were restricted to those with a maximum of 2

The selection process resulted in a total of 2335 intervals. The distribution of interval characteristics within our dataset is visualized in Fig. 5.8. Panels (a) to (c) depict 2D histograms illustrating the solar wind speed in correlation with normalized cross helicity (σ_c), normalized residual energy (σ_r), both evaluated at a scale of $\ell \approx 2 \cdot 10^4 d_i$. Finally, column (c) provides a histogram portraying the number of selected intervals (solid line) and their cumulative duration associated with different V_{sw} values.

Furthermore, to facilitate a more direct comparison with (Podesta, 2009) (hereinafter referred to as (Podesta, 2009)), we examined four intervals spanning: (a) January 1, 1995, to July 29, 1995, (b) May 15, 1996, to August 16, 1996, (c) January 8, 1997, to June 9, 1997, (d) August 23, 2000, to February 15, 2001. For an exhaustive discussion regarding the properties of the chosen intervals, readers are directed to (Podesta, 2009). An in-depth comparison between our results and those of (Podesta, 2009) is provided in Appendix 5.2.5.1.

5.2.2.1 Quantifying the Influence of Intermittency and Compressibility on SDDA

To assess the influence of intermittency and compressibility on alignment angle measurements, we utilize scale- and time-dependent proxies for these properties. Employing a scale-dependent conditional averaging technique enables us to isolate specific types of fluctuations, thus focusing on particular properties of interest.

To identify coherent structures, we employ the Partial Variance of Increments (PVI) method, which is effective for detecting sharp gradients within a turbulent field (Greco

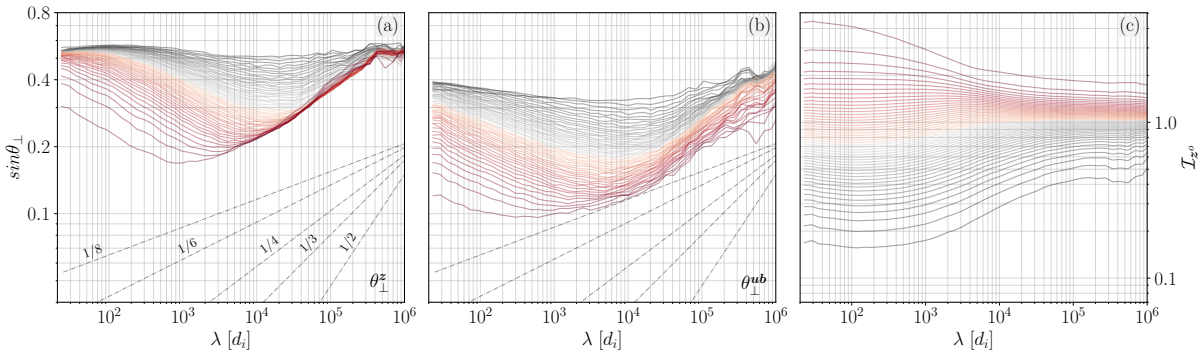

Figure 5.9: (a) $\theta_\perp^{\boldsymbol{z}}$, (b) $\theta_\perp^{\boldsymbol{ub}}$. Each subplot categorizes alignment angles into 50 bins based on $\mathcal{I}(\boldsymbol{z^o})$, as shown in panel (c). Specifically, the i-th bin at scale λ is defined as $[2(i-1), 2i]$, where $i = 1, ..., 50$. Reference lines depict the scaling parameter $\theta \propto \lambda^\alpha$, aiding comparative analysis.

et al., 2008; Servidio et al., 2012). The scale-dependent PVI time series can be estimated through Equation 2.29

To quantify the compressibility of fluctuations, we utilize

$$n_{\boldsymbol{q}}(t,\ \ell)\ = (\frac{\delta|\boldsymbol{q}(t,\ \ell)|}{|\delta\boldsymbol{q}(t,\ \ell)|})^2. \tag{5.8}$$

It's worth noting that alternative proxies for compressibility, such as C_{B^2} (Squire et al., 2020), have also been explored, yielding qualitatively similar results, although they are not presented here.

To conduct our analysis, we obtain $\delta\boldsymbol{b}_\perp(t,\ell)$ and $\delta\boldsymbol{v}_\perp(t,\ell)$ using the method detailed in Section 2.0.4. Additionally, we compute $\mathcal{I}_{\boldsymbol{q}}(t,\ell)$ and $n_{\boldsymbol{q}}(t,\ell)$ using equations 2.29 and 5.8, respectively, for a range of ℓ values, specifically $\ell = 1.2^j d_i$, where $j = 15, ..., 80$.

Here, d_i represents the ion inertial length, defined as $d_i = V_A/\Omega_i$, where Ω_i denotes the proton gyrofrequency, e is the elementary charge, $|B|$ is the magnetic field magnitude, and m_p is the proton mass.

Subsequently, we employ a scale-dependent conditional binning technique. This process entails partitioning $\mathcal{I}_{\boldsymbol{q}}(t,\ell)$, $n_{\boldsymbol{q}}(t,\ell)$, and their corresponding alignment angle values into $N = 50$ consecutive bins for each scale ℓ. More precisely, the i-th bin at scale ℓ is defined as the interval $[2(i-1),\ 2i)$, where $i = 1, ..., 50$. The results of this analysis are presented

in Section 5.2.3.1.

5.2.2.2 Quantifying Imbalance Effects on SDDA

The total energy $E_t = E^+ + E^-$ and cross-helicity $H_c = E^+ - E^-$, expressed in terms of the energy associated with fluctuations in $\boldsymbol{z}^\pm$, $E^\pm = \langle|\delta\boldsymbol{z}^\pm|^2\rangle/4$, are ideal (i.e., with zero viscosity and resistivity) invariants of the incompressible MHD equations. Elsässer imbalance can be quantified by the normalized cross-helicity, $\sigma_c = E_t/H_c$, which measures the relative fluxes of counterpropagating wavepackets in the system. In the context of solar wind turbulence, Elsässer imbalance is assessed by examining the relative magnitudes of inwardly and outwardly propagating Alfvén waves (Velli et al., 1991; Velli, 1993).

$$\sigma_c(t,\ \ell) = \frac{|\delta\boldsymbol{z}^o_\perp|^2 - |\delta\boldsymbol{z}^i_\perp|^2}{|\delta\boldsymbol{z}^o_\perp|^2 + |\delta\boldsymbol{z}^i_\perp|^2}. \tag{5.9}$$

In addition, we consider the normalized residual energy, σ_r, to investigate the effects of Alfvénic imbalance. This metric evaluates the relative energy in kinetic and magnetic fluctuations:

$$\sigma_r(t,\ \ell) = \frac{|\delta\boldsymbol{v}_\perp|^2 - |\delta\boldsymbol{b}_\perp|^2}{|\delta\boldsymbol{v}_\perp|^2 + |\delta\boldsymbol{b}_\perp|^2}. \tag{5.10}$$

To understand the influence of imbalance, we opted for an approach different from the one presented in Section 5.2.2.1. This decision was based on theresults presented Appendix 5.2.5.2. More specifically, among the variables σ_c, σ_r, $\theta^{ub}_\perp$, and $\theta^z_\perp$, only two are independent. Thus, using the previously described binning method would merely replicate the relationships shown in Figure 5.22. However, a more pressing question remains: how does global-scale imbalance affect SDDA measurements?

To address global imbalance, we adhered the following methodology: We computed the average values of $\sigma_c(\ell^*)$ and $\sigma_r(\ell^*)$ for each interval identified by visual inspection, where $\ell^* = 10^4\ d_i$. It is important to clarify that estimating $\sigma(\ell^*)$ involves more than simply calculating $\sigma(\ell^*) = \langle\sigma(t,\ell^*)\rangle$. Instead, we begin by estimating $\langle\delta\boldsymbol{\xi}_\perp(t,\ell^*)^2\rangle$ for all

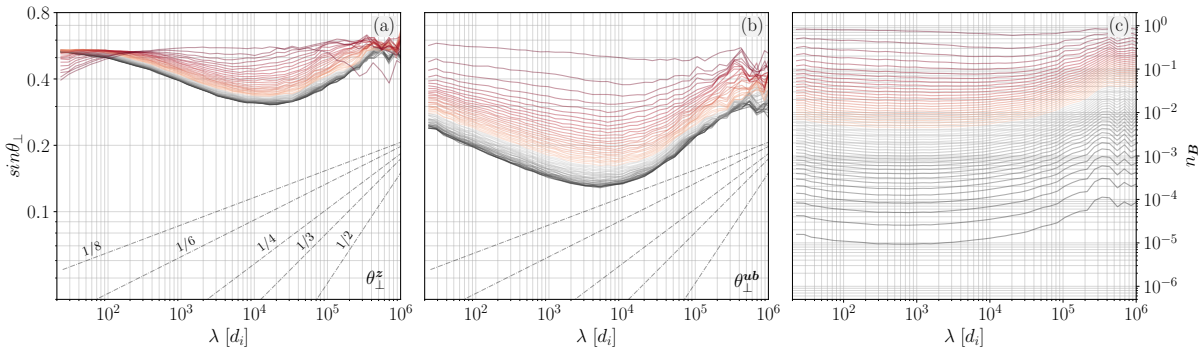

Figure 5.10: (a) $\theta_\perp^{\boldsymbol{z}}$, (b) $\theta_\perp^{\boldsymbol{ub}}$. These are categorized into scale-dependent percentiles based on $n_{\boldsymbol{B}}$.

fields involved in Equations 5.9-5.10 (see e.g., Shi et al., 2021). The former definition is applied only in cases requiring both temporal and spatial information to be retained, as illustrated in Figure 5.11.

Following this, we segregate our intervals into 10 linearly spaced bins, ranging from [0, 1] for Elsässer imbalance and [-1, 0] for Alfvénic imbalance, based on the values of $|\sigma_c(\ell_*)|$ and $\sigma_r(\ell^*)$, respectively. Within each bin, we calculate a scale-dependent weighted mean of the alignment angle, using the number of samples in each interval at that scale as the weighting factor. The results of this analysis are discussed in Section 5.2.3.3.

5.2.3 Results

In this section, our aim is to assess the impact of intermittency, compressibility, and global imbalance on SDDA measurements. However, before presenting our findings, it is essential to address a key aspect of our analysis.

We first investigated the scaling of SDDA for each stream type (slow Alfvénic, fast Alfvénic, slow non-Alfvénic) separately. Then, we aggregated all homogeneous intervals and applied the conditional averaging method outlined in Section 5.2.2.1. Interestingly, the trends observed when analyzing stream types with similar characteristics separately persisted when considering a mix of various interval types. This observation could be attributed to the inherently diverse nature of fluctuations across all wind streams. For instance, intervals primarily characterized as incompressible may still contain a fraction

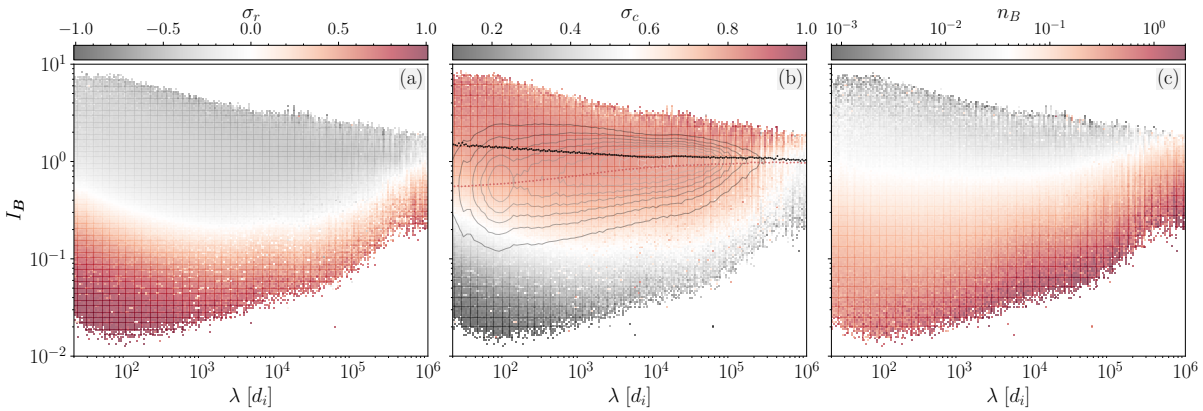

Figure 5.11: Distributions relative to λ, $\mathcal{I}_{\boldsymbol{B}}$ colored by the mean(a) σ_r. (b) σ_c. (c) n_B. Contours in panel (b) show the count levels of the distribution. In addition, mean (black) and median (red) curves of $\langle \mathcal{I}_{\boldsymbol{B}}^4 \rangle^{1/4}$, respectively, are shown.

of compressible fluctuations. Similarly, wind streams classified as generally balanced may exhibit localized patches of imbalance (Matthaeus et al., 2008b; Perez and Boldyrev, 2009a; Chen et al., 2013). The use of conditional averaging enables us to concentrate on specific types of fluctuations, facilitating an investigation into particular properties of interest, such as segregating fluctuations based on scale-dependent proxies for compressibility and intermittency.

Finally, it is important to point out that the conditional averaging analysis utilized here only considers normalized quantities like $\theta_\perp$, $I_{\boldsymbol{\xi}}$, and $n_{\boldsymbol{\xi}}$. Therefore, at this stage, we did not consider the polarization intermittency definition, $\tilde{\theta}_\perp$. This is because it entails averaging non-normalized quantities, and extreme values among different intervals, owing to significant variations in the root mean square of the fluctuations, could potentially dominate the mean. We will explore the polarization angle definition in Section 5.2.3.3, where we calculate averages among homogeneous intervals, ensuring that the previously mentioned concern does not hinder our analysis.

5.2.3.1 Influence of Intermittency & Compressibility on measurements of SDDA

In this section, we delve into the effects of intermittency and compressibility on SDDA using the conditional averaging method described in Section 5.2.2.1.

Figure 5.9 presents the results for intervals of mixed streams. The first two columns show $\theta_{\perp}^{\boldsymbol{z}}$ and $\theta_{\perp}^{\boldsymbol{ub}}$, conditioned on $\mathcal{I}_{\xi}(t,\ell)$ with $\xi = \boldsymbol{z}^o$, plotted against scales normalized in d_i units. Although analyses for $\xi = \boldsymbol{z}^i, \boldsymbol{B}, \boldsymbol{V}$ were also conducted, they are not shown here; key findings are discussed below.

Figure 5.9 clearly illustrates that the scaling of SDDA varies significantly depending on the percentile bin, the alignment angle definition, and the type of field gradient used to condition the alignment angles. However, it is evident that at any given scale, an inverse relationship exists between alignment angles and the intensity of field gradients.

More specifically, curves derived from averaging alignment angles for fluctuations with weak field gradients (black lines) tend to exhibit flat profiles, indicating negligible or weak SDDA at smaller scales. In contrast, curves for fluctuations with the strongest $\mathcal{I}_{\boldsymbol{z}^o}$ indices show steeper scaling laws, suggesting increasing alignment down to $\lambda \approx 8 \cdot 10^2 d_i$. While the anticorrelation holds in both cases, it is apparent that alignment in $\theta_{\perp}^{ub}$ is consistently tighter compared to $\theta_{\perp}^{z}$. This is likely because the intervals considered here are slightly skewed towards the globally Alfvénic side, as shown in Figure 5.8, primarily because such intervals were prioritized during the selection process. This was the only notable difference observed between the analyses of "pure" and "mixed" intervals. This effect will become more pronounced in Section 5.2.3.3, where we demonstrate that $\theta_{\perp}^{ub}$ and $\theta_{\perp}^{z}$ exhibit very similar behavior in balanced intervals, but they tend to diverge, with the former showing tighter alignment as the imbalance increases. Nonetheless, this does not affect the conclusions of this analysis. The primary objective here is to illustrate the relationship between alignment angles and field gradients, which, as explained earlier, shows consistent behavior in all cases.

It is also important to note that both $\theta_{\perp}^{z}$ and $\theta_{\perp}^{ub}$ exhibit an inverse relationship with

the gradients $\mathcal{I}_{\boldsymbol{B}}$. However, when conditioned on $\mathcal{I}_{\boldsymbol{V}}$, $\theta_{\perp}^{z}$ and $\theta_{\perp}^{ub}$ display forward and inverse correlations, respectively. Finally, $\theta_{\perp}^{z}$ and $\theta_{\perp}^{ub}$ are correlated and anti-correlated with $\mathcal{I}_{\boldsymbol{z}^i}$, respectively. This behavior primarily reflects a geometric effect, as discussed in Appendix 5.2.5.2. Nonetheless, even when forward correlation is observed, alignment angle curves derived from fluctuations with the strongest $\mathcal{I}_{\boldsymbol{\xi}}$ indices consistently exhibit the steepest power-law scaling.

As a final diagnostic, and for a more straightforward comparison with the numerical simulations by (Mallet et al., 2015), we also investigated the relationship between the alignment angle and the normalized Elsässer fluctuation magnitudes, $|\delta \boldsymbol{z^o}|/V_A$. The results, not shown here, reveal a trend qualitatively similar to those in Figure 5.9, as expected since the PVI diagnostics provide an estimate of fluctuation gradient intensity normalized by the standard deviation of local gradients.

We proceed to segregate fluctuations into percentile bins based on the compressibility diagnostic, n_ξ, illustrated in Figure 5.10, reveal a strong correlation between alignment and magnetic compressibility. Specifically, at the outer scale, strongly compressible fluctuations exhibit no signs of dynamic alignment, and the scaling of SDDA becomes progressively steeper as n_B decreases. Conditioning on $n_{\boldsymbol{V}}$ reveals only a weak and statistically insignificant correlation with alignment. It is worth noting, however, that the compressibility in the velocity field is considerably stronger than that in the magnetic field, with $n_{\boldsymbol{V}}(\ell) \gg n_{\boldsymbol{B}}(\ell)$ for the majority of intervals considered.

In general, curves derived from magnetically incompressible fluctuations exhibit behaviors at outer scales similar to those associated with the most intense coherent structures, suggesting a strong correlation between compressibility and intermittency (see also Vasko et al., 2022; Lotekar et al., 2022). However, unlike Figure 5.9, the quenching of SDDA, in most cases, occurs near the large-scale break of the power spectrum, approximately at the small-scale end of the outer range.

To quantify our findings, we applied a power-law fit to the curves representing the top 5% of fluctuations measured by $|\delta \boldsymbol{z}^{\pm}|$ and $\mathcal{I}_\xi$, with $\xi = \boldsymbol{z}^o, \boldsymbol{z}^i, \boldsymbol{B}, \boldsymbol{V}$, and to the

bottom 5% in terms of $n_{\boldsymbol{\xi}}$ for $\xi = \boldsymbol{B}, \boldsymbol{V}$. The derived scalings, evaluated over the range $4 \times 10^4 - 4 \times 10^5 d_i$, are summarized in Table 5.3.

5.2.3.2 Nature of fluctuations

In Section 5.2.2.1, our analysis revealed unexpected findings. While SDDA signatures persist within part of the inertial range for the strongest discontinuities, this is not the case when isolating the incompressible component of turbulence. Instead, a regime change was observed at the onset of the inertial range. To understand this discrepancy, we use here diagnostics to analyze the nature of fluctuations at inertial scales.

Figure 5.11 presents the results, showing $I_{\boldsymbol{B}}$ as a function of scale, color-coded by (a) σ_r, (b) σ_c, and (c) n_B. Panel (b) also includes a contour plot of the $I_{\boldsymbol{B}}$ distribution versus scale.

The distribution of $\langle I_{\boldsymbol{B}} \rangle$ shows a slight downward curvature at inertial scales, indicating a decrease in the median PVI index towards smaller scales. This may seem counterintuitive given in-situ observations of non-Gaussian increment distributions at smaller scales (see e.g., Sorriso-Valvo et al., 1999). However, examining $\langle \mathcal{I}_{\boldsymbol{B}}^n \rangle^{1/n}$ for $n = 2, ..., 6$ reveals that while the median curve bends downward, the mean curve trends upward at scales $\lambda \leq 10^4 d_i$. The steepness of the mean curve increases with n, reflecting intermittency in the magnetic field time series. For $n = 1$, the mean is influenced by median-amplitude eddies, while for larger n values, rare large-amplitude eddies dominate. The scale-dependent behavior of both the mean and median suggests a trend towards distributions that peak near zero but have heavier tails at smaller scales, consistent with previous findings (Sorriso-Valvo et al., 1999; Chhiber et al., 2021a).

Conversely, the roughly scale-independent behavior observed in both the mean and median curves at the outer range reflects the well-established phenomenon of Gaussian distributions of fluctuations at energy injection scales (Sorriso-Valvo et al., 1999; Bruno et al., 2003).

Interestingly, the shift from intermittent to Gaussian regimes appears to coincide with

Table 5.3: Power-law scaling of alignment angles within $4 \times 10^4 - 4 \times 10^5 d_i$ using top 5% fluctuations in $|\delta \boldsymbol{z}^{\pm}|$ and $\mathcal{I}_\xi$, where $\xi = \boldsymbol{B}, \boldsymbol{V}, \boldsymbol{z}^o, \boldsymbol{z}^i$, and bottom 5% in n_ξ for $\xi = \boldsymbol{B}, \boldsymbol{V}$.

	$\theta_\perp^z$	$\tilde{\theta}_\perp^z$	$\theta_\perp^{ub}$	$\tilde{\theta}_\perp^{ub}$
$\mathcal{I}_{\boldsymbol{z}^o}$	0.3 ± 0.02	0.32 ± 0.02	0.29 ± 0.02	0.33 ± 0.01
$\mathcal{I}_{\boldsymbol{z}^i}$	0.3 ± 0.02	0.28 ± 0.03	0.30 ± 0.02	0.35 ± 0.04
$\mathcal{I}_{\boldsymbol{B}}$	0.30 ± 0.01	0.30 ± 0.02	0.27 ± 0.01	0.31 ± 0.01
$\mathcal{I}_{\boldsymbol{V}}$	0.23 ± 0.01	0.25 ± 0.02	0.29 ± 0.02	0.30 ± 0.01
n_B	0.19 ± 0.01	0.26 ± 0.02	0.25 ± 0.03	0.32 ± 0.03
n_V	0.17 ± 0.03	0.25 ± 0.03	0.33 ± 0.04	0.38 ± 0.02

the scale at which we typically observe the rollover of the alignment curves. However, the extent to which this regime change affects the scaling of SDDA remains unclear.

In addition we can see that, at any given scale, fluctuations with the highest PVI index exhibit the lowest n_B and highest σ_c values, along with strongly negative residual energy indices. This implies an anticorrelation between σ_r and $I_{\boldsymbol{B}}$, a finding that aligns with the work by (Bowen et al., 2018b), who noted that intervals with large scale-dependent kurtosis, $K(\ell)$, predominantly exhibit negative σ_r. Our analysis confiRMS the persistence of this relationship across the observed spectrum, substantiating the claim that intermittency and residual energy are most likely interconnected.

Finally, we turn our attention to the nature of the compressible fluctuations. To this end, we consider the PVI diagnostic applied to the magnetic field magnitude and proton density timeseries, $I_{|\boldsymbol{B}|}$ and I_{n_p}, respectively. Figure 5.12 illustrates the distribution of I_{n_p}, binned by $I_{|B|}$ and scale λ. This method of visualizing the result has not been implemented before. Previous works have compared the magnetic and thermal pressure (Burlaga and Ogilvie, 1970; Thieme et al., 1990), used wavelet cross-coherence analysis (Kellogg and Horbury, 2005; Yao et al., 2011), or utilized the zero-lag cross-correlation between $|B|$ and n_p (Howes et al., 2012; Bowen et al., 2018a).

A well-established result is recovered: fluctuations in $|B|$ and n_p are anticorrelated at inertial scales, similar to observations by Thieme et al. (1990); Yao et al. (2011); Howes et al. (2012); Bowen et al. (2018a). However, this anticorrelation gradually fades at the

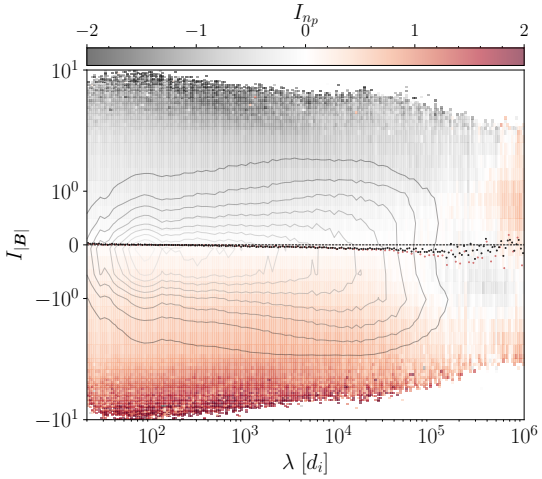

Figure 5.12: Distribution of I_{n_p}, binned by $I_{|B|}$ and scale λ (normalized to the ion inertial length d_i). The plot utilizes a color gradient to represent the mean values of I_{n_p} within each bin. Black and red dots show the mean and median values of $I_{|B|}$ as a function of scale.

outer scale, with clear correlation observed at $\lambda \geq 8 \times 10^4 d_i$ consistent witht the results of (Burlaga and Ogilvie, 1970). The observed inertial-range anticorrelations have been attributed to the presence of the kinetic slow-mode (Howes et al., 2012; Klein et al., 2012), while Verscharen et al. (2017) proposed that the MHD slow-mode provides a better fit to the observed properties of compressible fluctuations.

It is not clear whether this observation can provide any insights into the effects of compressible fluctuations on SDDA. Nevertheless, we present this finding for completeness without further discussion.

5.2.3.3 Influence of Imbalance on SDDA

In this section, we seek to understand the influence of global Alfvénic and Elsässer imbalance on alignment angle scaling using homogeneous intervals identified through visual inspection (see Section 5.2.2). To this end we employ the conditional averaging technique described in Section 5.2.2.2, and segregate intervals based on the outer scale values of either the cross-helicity or normalized residual energy $\sigma_c(\ell^*)$ and $\sigma_r(\ell^*)$, where $\ell^* = 10^4 d_i$.

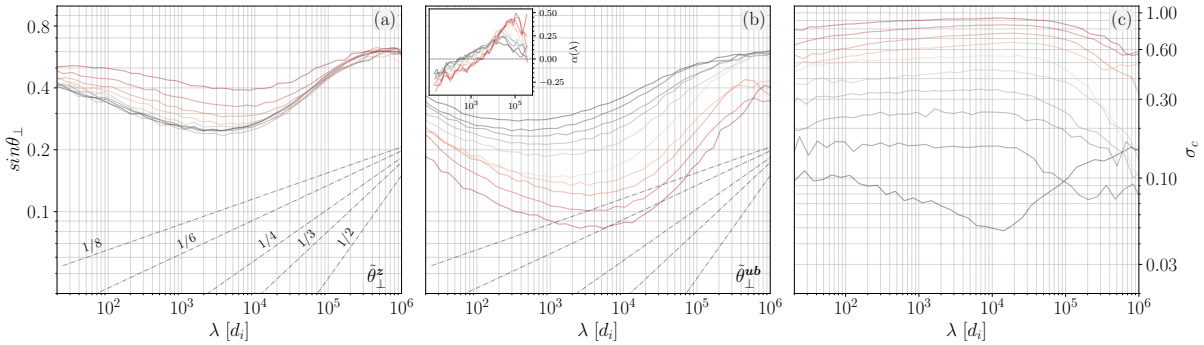

Figure 5.13: Weighted averages of (a) $\tilde{\theta}^{\boldsymbol{z}}_{\perp}$, (b) $\tilde{\theta}^{\boldsymbol{ub}}_{\perp}$, and (c) σ_c for the homogeneous intervals identified through visual inspection. After estimating these quantities as a function of scale for each identified interval, the curves are divided into $N = 10$ bins based on $\sigma_c(\ell^*)$, where $\ell^* = 2 \cdot 10^4 d_i$, and a scale-dependent weighted average of the curves is computed.

We first consider alignment curves conditioned on $\sigma_c(\ell^*)$. The results are shown in Figure 5.13. For $\sigma_c(\ell^*) < 0.7$, there is no clear trend in the scaling of $\tilde{\theta}^z_\perp$, as curves from all bins overlap. However, for $\sigma_c(\ell^*) > 0.7$, the scaling of $\tilde{\theta}^z_\perp$ becomes progressively shallower, especially at larger scales. In contrast, large-scale Elsässer imbalance organizes the $\tilde{\theta}^{ub}_\perp$ curves more clearly. As $\sigma_c(\ell^*)$ increases, (a) $\tilde{\theta}^{ub}_\perp$ shows steeper scaling, and (b) the quenching of the curves shifts towards larger scales. The local scaling index, $\alpha(\lambda)$, illustrated in the inset of Figure 5.13b, shows that $\alpha(\lambda) \approx 0.4$ for $\sigma_c(\ell^*) > 0.90$, while a shallower scaling of $\alpha(\lambda) \approx 0.2$ is observed for $\sigma_c(\ell^*) < 0.10$. The range of scales over which the slope remains positive increases as $\sigma_c(\ell^*) \to 0$. Additionally, there is a trend of increasing σ_c towards smaller scales, and the range of scales over which this behavior is observed widens with $\sigma_c(\ell^*) \to 0$.

It is worth noting that while alignment in $\tilde{\theta}^{ub}_\perp$ is considerably tighter compared to $\tilde{\theta}^z_\perp$ for strongly imbalanced intervals, the two definitions yield qualitatively similar results at $\sigma_c(\ell^*) \to 0$.

When intervals are segregated based on $\sigma_r(\ell^*)$, a similar trend is observed for $\tilde{\theta}^{ub}_\perp$. Additionally, as Alfvénic imbalance decreases ($\sigma_r(\ell^*) \to 0$), SDDA signatures in $\tilde{\theta}^z_\perp$ diminish, resulting in flatter curves between $10^2 - 10^6 d_i$. Conversely, with increasing magnetic energy dominance over kinetic energy, SDDA signatures become more pronounced, exhibiting steep power-law behavior, particularly at larger scales. In practice, this implies

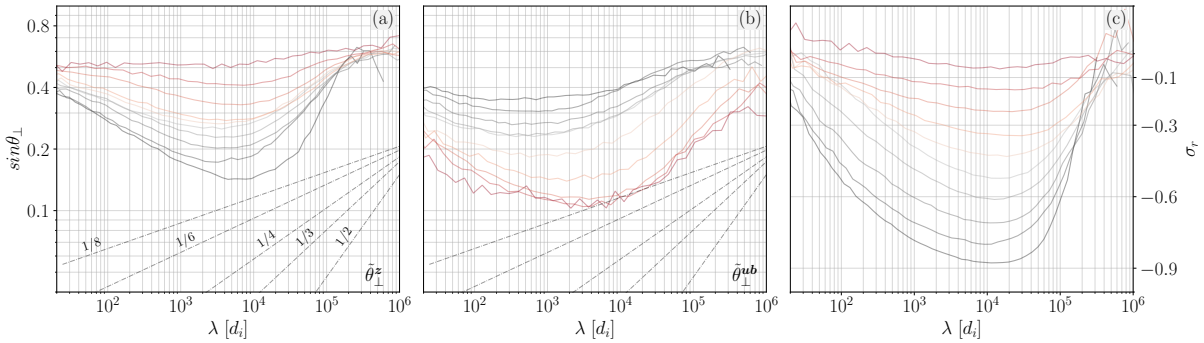

Figure 5.14: Columns 1 to 4 display $\theta^{\boldsymbol{z}}_\perp$, $\tilde{\theta}^{\boldsymbol{z}}_\perp$, $\theta^{\boldsymbol{ub}}_\perp$, and $\tilde{\theta}^{\boldsymbol{ub}}_\perp$, respectively. Homogeneous intervals, identified through visual inspection, are segregated into 50 bins based on $\sigma_c(\ell^*)$ and $\sigma_r(\ell^*)$, where $\ell^* = 2 \cdot 10^4 d_i$ and a scale-dependent weighted average of the curves is estimated shown in the top and bottom panels, respectively.

that equipartitioned intervals ($E_u \approx E_b$) show no signs of increasing alignment in the Elsässer field fluctuations, but at least at large scales still show increasing alignment in the polarizations of magnetic/velocity field fluctuations.

To summarize: (a) Large-scale Alfvénic imbalance is a good predictor for the expected behavior of both $\tilde{\theta}^{ub}_\perp$ and $\tilde{\theta}^{z}_\perp$. As $\sigma_r(\ell^*)$ approaches zero, the scalings of $\tilde{\theta}^{ub}_\perp$ become steeper, while the scalings of $\tilde{\theta}^{z}_\perp$ become shallower, extending to a narrower and wider range of scales, respectively. (b) Elsässer imbalance mostly correlates with the expected $\tilde{\theta}^{ub}_\perp$ scaling. SDDA signatures persist to smaller scales for globally balanced streams compared to their imbalanced counterparts, but with the scaling becoming progressively shallower.

5.2.3.4 High-Frequency Instrumental Noise

In this section, we investigate the extent to which high-frequency, small-amplitude noise in the velocity field measurements can affect our ability to reliably estimate alignment angles in the Elsässer field fluctuations, $\theta^{z}_\perp$.

Let $\delta\boldsymbol{b}$ denote the true value of the magnetic field fluctuation vector in velocity units. We assume that the error in its measurement is negligible. Although a more realistic assessment would incorporate an error term, especially since $\delta\boldsymbol{b}$ measurements may be contaminated by errors in proton density measurements, we assume for highly Alfvénic intervals that $\delta\rho/\rho$ is sufficiently small. This assumption is supported by observations

(Shi et al., 2021), allowing rolling averages of ρ to be used for Alfvénic normalization.

We define the real value of the velocity field as $\delta\boldsymbol{u}$ and introduce an error term $\boldsymbol{\Delta}$, where $\boldsymbol{\Delta}$ is a normally distributed random vector with mean $\mathbf{0}$ and standard deviation σ, represented by $\boldsymbol{\Delta} \sim \mathcal{N}(\mathbf{0}, \sigma)$. We assume that the magnitude of $\boldsymbol{\Delta}$ is significantly smaller than the magnitudes of $\delta\boldsymbol{b}$ and $\delta\boldsymbol{u}$ (i.e., $|\boldsymbol{\Delta}| \ll |\delta\boldsymbol{b}|, |\delta\boldsymbol{u}|$). For simplicity, we assume that the real vectors are perfectly aligned, $\delta\boldsymbol{u} = \alpha\delta\boldsymbol{b}$, and that $\delta\boldsymbol{z}_i = \epsilon\delta\boldsymbol{z}_o$.

We can then write:

$$\delta\boldsymbol{z}_o' = \delta\boldsymbol{z}_o + \boldsymbol{\Delta} \tag{5.11}$$

$$\delta\boldsymbol{z}_i' = \epsilon\delta\boldsymbol{z}_o + \boldsymbol{\Delta} \tag{5.12}$$

The quantity controlling the error in the measurements of $\delta\boldsymbol{z}_i$ can be represented by the dimensionless parameter Q:

$$Q = \frac{|\epsilon\delta\boldsymbol{z}_o|}{|\boldsymbol{\Delta}|} \tag{5.13}$$

We can estimate the alignment angles as follows:

$$\begin{aligned}\cos(\theta') &= \frac{\delta\boldsymbol{z}_o' \cdot \delta\boldsymbol{z}_i'}{\|\delta\boldsymbol{z}_o'\|\|\delta\boldsymbol{z}_i'\|} \\ &= \frac{\epsilon\delta z_o^2 + (1+\epsilon)\delta z_o\Delta + \Delta^2}{\epsilon\delta z_o^2\sqrt{1 + \frac{2\delta z_o\Delta}{\delta z_o^2} + \frac{\Delta^2}{z_o^2}}\sqrt{1 + \frac{2\delta z_o\Delta}{\epsilon\delta z_o^2} + \frac{\Delta^2}{\epsilon\delta z_o^2}}}\end{aligned}$$

Considering the case where $Q \gg 1$, we can estimate:

$$\cos(\theta') \approx 1 - O(Q^{-2}) \tag{5.14}$$

On the other hand, when $Q \ll 1$:

$$\cos(\theta') \approx 1 + \text{higher-order terms} \tag{5.15}$$

where higher-order terms include $O(Q)$, $O\left(\Delta/\delta z^o\right)$, and $O(\epsilon)$. Therefore, the accuracy of the angle measurement depends on the errors in the velocity compared to the true size of the δz_i signal. Specifically, when $Q \gg 1$, the alignment angle can be estimated reliably. Conversely, for $Q \ll 1$, a significant deviation is expected between the true and estimated values of the alignment angles.

5.2.3.5 Modeling High Frequency Instrumental Noise

To further investigate the impact of high-frequency noise on alignment angle measurements, we simulate the previous analysis by generating synthetic magnetic and velocity field data, which are subsequently polluted by artificial high-frequency white noise of specified amplitude.

To this end, we generate two sets of three-component time series for the magnetic field ($\mathbf{B}$) and the velocity field ($\mathbf{V}$), with the corresponding components being perfectly correlated ($\rho = 1$). To simplify our analysis, we assume—though this is strictly true only for the velocity field (Chen et al., 2012; Sioulas et al., 2023a; McIntyre et al., 2023b)—that the inertial-range trace power-spectral scalings of the two fields are independent of σ_c and scale as $a_b = a_v = -3/2$.

Initially, we generate a Gaussian white noise time series for each component of the magnetic and velocity fields. The duration of the time series is set to 48 hours ($d = 48$ hours), with a cadence of 3 seconds ($dt = 3$ s), mimicking the typical duration and cadence of our identified intervals. To shape the power-spectral density (PSD) of the time series, we apply filters in the frequency domain. For a given desired spectral exponent α, the filter response $H(f)$ is defined as:

$$H(f) = |f|^{\alpha/2}, \tag{5.16}$$

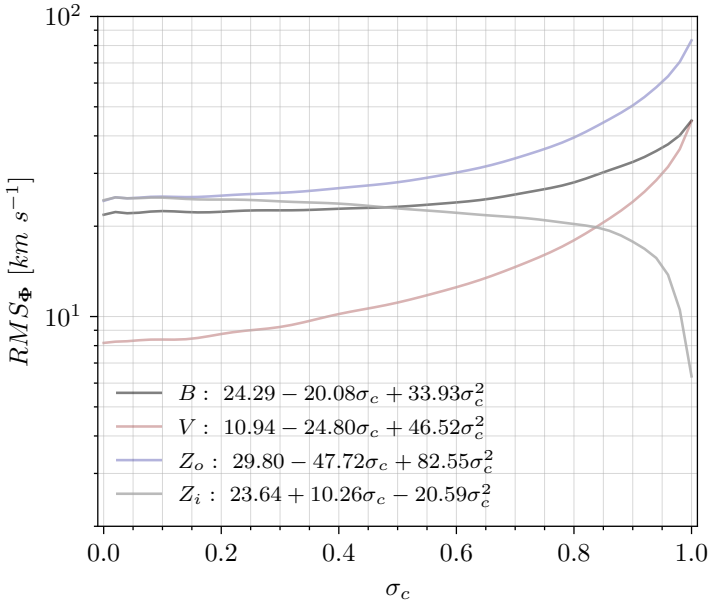

Figure 5.15: The empirical relationship for the RMS of the fluctuations is shown for (a) $\boldsymbol{B}$ (black line), (b) $\boldsymbol{V}$ (red line), (c) $\boldsymbol{z}_o$ (blue line), and (d) $\boldsymbol{z}_i$ (gray line), plotted against σ_c. Using the fluctuations estimated through Eq. 5.2.3.5, 1-minute moving averages of σ_c were also estimated, yielding a dataset of size $N \approx 7.5 \times 10^7$. The RMS quantities of the fields were plotted against σ_c, and an empirical fit was extracted by finding the best 12th-degree polynomial fit. The fits obtained for the different fields are plotted against σ_c, with the legends showing only the first three terms of the empirical fit.

where f denotes the frequency.

The base time series are transformed to the frequency domain using the Fast Fourier Transform (FFT). The spectral shaping filters are applied by multiplying the Fourier-transformed series by the filter response $H(f)$. The filtered series are then transformed back to the time domain using the inverse FFT. At this point, two time series with the desired correlation and spectral properties have been constructed.

Next, we need to properly normalize the two time series to model different levels of Elsässer imbalance. This requires input from in-situ observations. It is well known that the RMS of the fluctuations in both velocity and magnetic field increases with σ_c (Pi et al., 2020; Sioulas et al., 2023). To quantify this dependency, we estimate the RMS value of the fluctuations in the different fields for each of our selected intervals. For any given field $\mathbf{\Phi}$, fluctuations are estimated as:

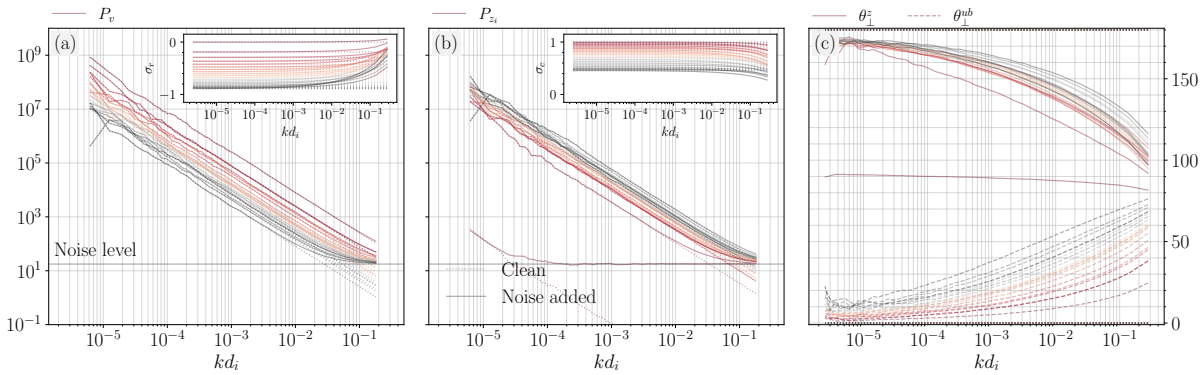

Figure 5.16: Synthetic power-spectra of (a) the velocity field ($P_{\boldsymbol{v}}$) and (b) the minor Elsässer field ($P_{\boldsymbol{z}_i}$) for different levels of imbalance. Dotted lines indicate the original time series, while solid lines represent the time series after adding white noise. Panel (c) shows the alignment angle of the Elsässer/Alfvén fields for the original time series (dotted lines), which remain constant at $\theta^z = 180°$, $\theta^{ub} = 0°$, respectively, independent of scale, and for the noise-affected time series (solid lines). The inset in panel (c) illustrates σ_c, σ_r for the different runs. Power-spectra obtained

$$\Delta\mathbf{\Phi} = \mathbf{\Phi} - \mathbf{\Phi}_0, \tag{5.17}$$

where $\mathbf{\Phi} = V_a, V, Z_o, Z_i$ and $\mathbf{\Phi}_0 = \langle \mathbf{\Phi} \rangle_D$ is a moving average with a window of duration $D = 8$ hours. Subsequently, the RMS of each field is estimated using $d = 1$ minute moving averages of the fluctuations:

$$\mathbf{\Phi}_{RMS} = \sqrt{\langle \Delta\mathbf{\Phi}^2 \rangle_d}. \tag{5.18}$$

Using the fluctuations estimated through Eq. 5.2.3.5, 1-minute moving averages of σ_c are then also estimated. This process yielded a dataset of size $N \approx 7.5 \times 10^7$ total measurements. $\mathbf{\Phi}_{RMS}$ are then then plotted against σ_c, and an empirical fit is extracted by finding the best 12th-degree polynomial fit. The fit obtained for the different fields is plotted against σ_c in Figure 5.15 with the legends showing only the first three terms.

Using the empirical relationship for the RMS of the fields as a function of σ_c, the time series are normalized such that the RMS of the synthetic data matches that of the real

data at different levels of imbalance while retaining the original correlation and desired spectral scalings.

Noise is then added to the $\boldsymbol{V}(t)$ series. We assume here, though not strictly true (see e.g., Ervin et al., 2024), that the noise floor in the velocity field measurements is the same for all intervals considered and independent of σ_c. Given that the RMS of the fluctuations peaks at $\sigma_c \approx 1$, we take the noise level to be $\Delta = 0.1\boldsymbol{V}^*_{RMS}(f_{\rm Nyq}) \times \mathcal{N}(0,1)$, where $\boldsymbol{V}^*_{RMS}(f_{\rm Nyq})$ is the RMS value of the velocity field at the Nyquist frequency for $\sigma_c = 1$.

For each simulated interval, the Fourier trace power spectral density $F(f)$ was calculated, smoothed by averaging over a sliding window with a factor of 2, and then transformed into a wavenumber spectrum expressed in physical units $P(kd_i)$:

$$P(kd_i) = \frac{V_{sw}}{2\pi d_i} F(f), \tag{5.19}$$

where $kd_i = (2\pi f d_i)/V_{sw}$ (Sioulas et al., 2023a). To perform this normalization, the ratio V_{sw}/d_i was estimated for all intervals in our dataset, resulting in a mean value of 3.95 ± 1.27. The mean value was used to normalize the synthetic spectra to enable a more meaningful comparison with the in-situ derived power spectra and spectral scaling indices.

The results of this analysis are illustrated in Figure 5.16. Panels (a)-(c) display the power-spectral density of the velocity field P_u, ingoing Elsässer fields P_{z_i}, and alignment angles $\theta^z_\perp$, $\theta^{ub}_\perp$, respectively. The insets in panels (a) and (b) show σ_r and σ_c, respectively. Different colors represent varying levels of Elsässer imbalance, with red lines indicating imbalanced intervals and black curves showing balanced intervals. Dotted lines represent the expected behavior, while solid lines show the impact of introducing white noise to the velocity field time series.

As $\sigma_c \to 1$, $\boldsymbol{V}_{RMS}$ increases and approaches that of $\boldsymbol{B}_{RMS}$. This results in a decrease in $\boldsymbol{z}_{i,\rm RMS}$, causing an artificial flattening of the power spectrum of $\boldsymbol{z}_i$ at lower frequencies. For the black curves, although the spectrum of $\boldsymbol{V}$ is flattened at lower frequencies, the

impact on $\boldsymbol{z}_i$ is subtle and mainly evident at high frequencies. More specifically, when Pu reaches the noise floor at a frequency f_n, the power spectrum of $\boldsymbol{z}_i$ becomes unmeasurable for $P_{z_i}(f > f^*)$, where $P_{z_i}(f^*) = P_u(f_n)$.

Although assuming the noise floor is independent of imbalance might be an over-simplification, our analysis demonstrates that small amplitude high-frequency noise can significantly affect P_{z_i}, thereby reducing the accuracy of P_{z_i} estimates as the Elsässer imbalance increases.

Noise has an even greater impact on alignment angle estimates. It distorts the phases of the velocity field measurements, causing them to decorrelate from the magnetic field phases without significantly altering their amplitude. The extent and frequency of these effects depend on the level of imbalance—$\theta^z_\perp$ is more affected during imbalanced intervals, while $\theta^{ub}_\perp$ is more affected during balanced intervals.

It is important to note that we have only examined the scenario where, for σ_c to decrease, the RMS of the velocity field fluctuations must decrease faster than that of the magnetic field fluctuations, with the alignment angle remaining independent of the imbalance. This assumption forces our time series to be perfectly correlated, limiting our analysis to the periphery of the circle plot shown in Figure 5.22. However, this is not always the case; in principle, we could maintain the RMS of both fields constant and adjust the alignment angles, or even use a combination of these factors. In fact, as shown in the inset of Figure 5.16b, this approach does not allow σ_c at large scales to decrease below $\sigma_c \lesssim 0.45$.

We therefore need to follow a more rigorous approach. To this end, we generate time series for the magnetic and velocity fields that meet three simultaneous conditions informed by our in-situ observations: (1) the fluctuations are correlated with a specified correlation coefficient, (2) their inertial-range spectral scaling, and (3) the RMS values of these time series align with those observed in-situ. Therefore, in addition to considering the RMS values of the fields, the inertial-range spectral-scalings, α_ϕ, where $\phi = \boldsymbol{B}, \boldsymbol{V}, \boldsymbol{Z}_i, \boldsymbol{Z}_o$ were estimated by finding the best-fit linear gradient in log–log space over the range

$kd_i \in [5 \times 10^{-4}, 10^{-2}]$. In addition, the correlation coefficient

$$C_\phi = \frac{\langle \Delta\boldsymbol{\phi} \cdot \Delta\boldsymbol{\psi} \rangle}{\sqrt{\langle \Delta\boldsymbol{\phi}^2 \rangle \langle \Delta\boldsymbol{\psi}^2 \rangle}}, \tag{5.20}$$

between either magnetic-velocity or Elsässer field fluctuations, was estimated and an empirical relationship was obtained for these quantities as a function of σ_c. The obtained functional form for the spectral scalings and the correlation coefficients between the magnetic-velocity fields, ρ_{ub}, and Elsässer fields, ρ_z, are illustrated in Figure 5.17.

While the third condition is straightforward to enforce and satisfying either of the first two conditions independently is also manageable, applying spectral shaping filters as described in Equation 5.16 to achieve the desired spectral scaling can disrupt the specified correlation coefficient, and vice-versa. Thus, imposing both conditions simultaneously in a rigorous manner is challenging.

To achieve this, we follow an iterative approach. Specifically, we generate time series for the magnetic field components B_i with the desired spectral scaling of $a_B = -1.74 + 0.26 \cdot \sigma_c$. Each component B_i of the magnetic field is paired with an initially uncorrelated component V_i of the velocity field. The desired scaling index for the velocity field is -1.5, independent of σ_c. However, the iterative process to achieve the desired correlation coefficient modifies the imposed scaling.

We have empirically found that if the initial scaling of the generated velocity time series is given by $a_v = -1.51 + 0.18 \cdot \sigma_c$, we can obtain both the desired scaling and correlation coefficient simultaneously through iterative adjustment. This process aims to match the desired correlation between the increments of B_i and V_i. The input velocity field component is given by

$$V_i = \rho \cdot B_i + \sqrt{1 - \rho^2} \cdot \eta_i, \tag{5.21}$$

where ρ is the desired correlation coefficient, and η_i is the initially generated velocity time series with the imposed scaling. This provides an initial guess for V_i.

For each iteration, the current correlation coefficient r between B_i and V_i increments over specified intervals is computed. If the absolute difference between the current and desired correlation coefficients is less than the specified tolerance, the iteration stops. Otherwise, an adjustment is applied to V_i based on the correlation error, defined as

$$\delta = \gamma \times (\rho - r) \times B_i, \tag{5.22}$$

where γ is the learning rate and r is the current correlation coefficient. This process is repeated until the desired correlation coefficient is achieved.

Once the desired correlation is achieved, we normalize the RMS values of the magnetic and velocity fields to ensure they meet the specified conditions.

By carefully balancing the spectral properties and correlation through this iterative process, we successfully produced time series for the magnetic and velocity fields that simultaneously satisfied the specified conditions and adhered to the desired spectral scalings and correlation coefficients.

The results of this analysis are presented in Figure 5.19, with a setup identical to Figure 5.16. In addition the inset of panel (c) illustrates the normalized diffrence of the alignemnt angle estimates of the clean and noise-affected timeseries. While the exact spectral scaling of the different fields does not make a big difference in the observed behavior, not shown here, allowing the correlation coefficient, to vary in a manner consitent with in-situ data, enables for a more realistic comparison between the synthetic and in-situ data.

To further clarify this aspect, we estimate the band-pass RMS value of the different fields within a specified frequency, or kd_i, range from the power spectral density through:

$$\mathcal{J}_{\boldsymbol{\xi}} = \sqrt{\int_{f_1}^{f_2} P_{\boldsymbol{\xi}}(f)\, df} \tag{5.23}$$

The results of this analysis are presented in Figure 5.18. Panels (a), (b), and (c) illustrate the variations of $\mathcal{J}_{\boldsymbol{z}_o}$, $\mathcal{J}_{\boldsymbol{z}_i}$, and $\mathcal{J}_{\boldsymbol{v}}/\mathcal{J}_{\boldsymbol{z}_i}$ as functions of kd_i and σ_c. These values

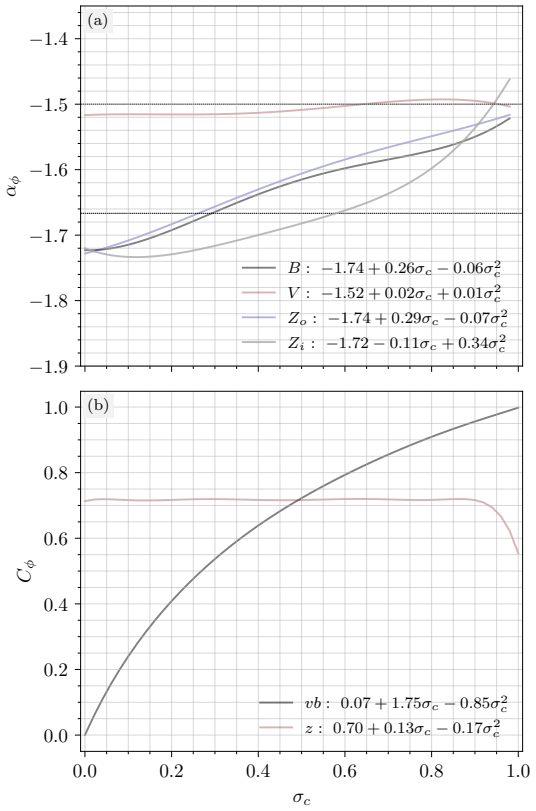

Figure 5.17: (a) The inertial-range power-spectral scalings for $\boldsymbol{B}$ (black line), $\boldsymbol{V}$ (red line), $\boldsymbol{z}_o$ (blue line), and $\boldsymbol{z}_i$ (gray line) plotted against σ_c, estimated by determining the best-fit linear gradient in log–log space over the range $kd_i \in [5 \times 10^4, 10^{-2}]$ for each selected interval in our dataset. (b) The correlation coefficient, C_ϕ, as defined in Equation 5.20, for the velocity/magnetic fields (black) and Elsässer fields (red) plotted against σ_c. In contrast to the scaling index in panel (a), C_ϕ is estimated using the 1-minute moving average, similar to Figure 5.15, from a dataset of size $N \approx 7.5 \times 10^7$.

are initially calculated for individual intervals in our dataset. Afterward, the weighted mean values for each kd_i and σ_c bin are determined, with the weights being the interval duration.

Panel (c) additionally includes estimates of the same quantities derived from the synthetic dataset, obtained by integrating the power-spectra shown in Figure 5.19. These synthetic estimates are represented as solid lines overlaid on the dots from the in-situ data.

The good agreement between the synthetic and in-situ data suggests that the noise level introduced in the synthetic dataset is roughly consistent with the quantization noise

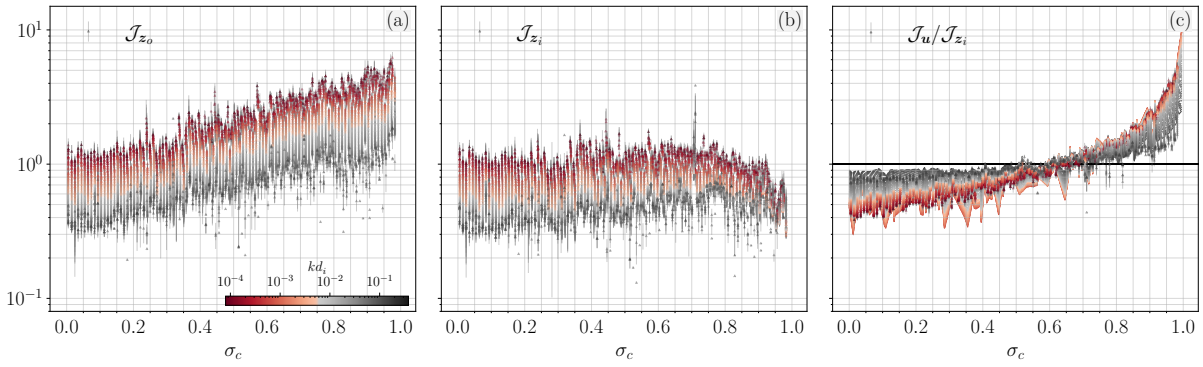

Figure 5.18: (a) $\mathcal{J}_{\boldsymbol{z}_o}$, (b) $\mathcal{J}_{\boldsymbol{z}_i}$, and (c) $\mathcal{J}_{\boldsymbol{v}}/\mathcal{J}_{\boldsymbol{z}_i}$ as functions of σ_c. Here, $\mathcal{J}_{\boldsymbol{\xi}}$ represents the band-pass RMS of the field $\boldsymbol{\xi}$, as defined in Equation 5.23. These values are initially estimated for individual intervals in our dataset. Subsequently, the weighted mean values at a given kd_i and σ_c bin are calculated, with the weights being the interval duration. Panel (c) also includes the estimates of the same quantities for the synthetic dataset obtained by integrating the power-spectra presented in Figure 5.19. These are shown as solid lines overlaid on the dots from the in-situ data.

observed in the in-situ data. This validation indicates that our method for simulating noise and comparing it to real data is reliable and accurate.

Overall, this analysis indicates that small amplitude high-frequency noise can cause significant deviations in observed alignment angles from their true values, even at low frequencies (large scales). However, reliable estimates of σ_c and σ_r can still be obtained at higher frequencies, as the distortion in amplitude is minimal, but the phase effects are significant.

5.2.4 Discussion

In recent years, the inertial-range scaling behavior of the alignment angle has ignited intense discussions and debate. SDDA, if related to the reduction of nonlinearities[10], holds the potential to flatten the inertial range spectrum from $E(k_\perp) \propto k_\perp^{-5/3}$ to $E(k_\perp) \propto k_\perp^{-3/2}$. Although the spectral exponents of -5/3 and -3/2 are numerically close, they signify fundamentally different physical mechanisms underlying the turbulent energy cascade. Therefore, a thorough understanding of the inertial range behavior of SDDA

[10]A dedicated discussion on why this may not be the case can be found in (Bowen et al., 2021)

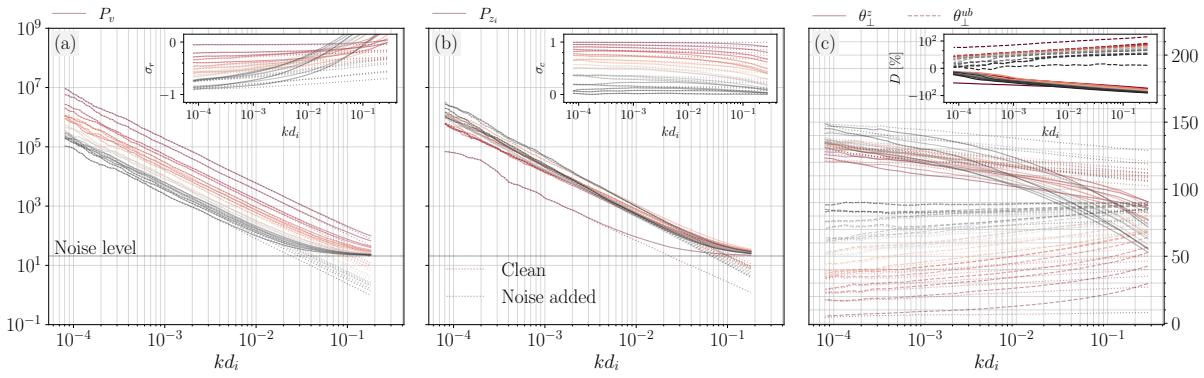

Figure 5.19: The setup is similar to that in Figure 5.16, but with the time series generated using the empirical relationships obtained for ρ, $\boldsymbol{B}_{\mathrm{RMS}}$, $\boldsymbol{V}_{\mathrm{RMS}}$, a_b, and a_u. Additionally, the inset in panel (c) features the normalized difference $D = 100(\theta - \theta_c)/\theta_c$, where θ and θ_c are the noise-affected and clean estimates of the alignment angles, respectively.

is crucial, particularly when applying MHD turbulence models to astrophysical systems with extensive inertial ranges. For example, predictions about the turbulent heating rate can deviate significantly between models that ingore and incorporate SDDA (**?**Chandran and Perez, 2019).

Nonetheless, in-situ observations have cast doubt on our comprehension of the role of SDDA in Alfvénic turbulence. While several aspects of model incorporating SDDA (Boldyrev, 2006; Chandran et al., 2015; Mallet and Schekochihin, 2017) are consistent with in-situ observations (Chen et al., 2012; Verdini et al., 2018; Shi et al., 2023a; Sioulas et al., 2024), signatures of increasing alignment usually fade within the inertial range (Podesta, 2009; Verdini et al., 2018; Parashar et al., 2019, 2020; Sioulas et al., 2024).

It is imperative to recognize, however, that the (Boldyrev, 2006) and (Chandran et al., 2015), models omit the potential effects of compressibility, imbalance, solar wind expansion, and various instabilities on field alignment. These factors have been deliberately neglected either because they were deemed negligible, given that these models focus on homogeneous alfvénic turbulence, or to simplify computations, e.g., by assuming negligible cross-helicity. Nonetheless, these effects often become significant in the solar wind, raising questions about the applicability of these models to such conditions (Verdini et al., 2018; Bowen et al., 2021).

In this work, we have cast our analysis within a framework that allows us to isolate and study the influence of effects such as compressibility, intermittency, and imbalance, which have not been adequately addressed in previous works.

Before drawing conclusions, we review related work and discuss the characteristics of solar wind turbulence that diverge from conventional models of homogeneous MHD turbulence. Additionally, we evaluate how instrumental noise might obscure the precise estimation of alignment angles in solar wind studies.

5.2.4.1 Wavepackets, shearing, alignment & residual energy

We have shown that the quenching of the alignment angle typically observed at inertial scales shifts toward smaller scales when fluctuations with strong gradients are isolated from residual fluctuations, as illustrated in Figure 5.9a. It is well known that the breadth of the inertial range narrows with Elsässer imbalance (Bruno and Carbone, 2013, and references therein). Nevertheless, at 1 AU, the inertial range begins, on average, at $\ell \approx 10^4 d_i$. Combining this observation with the results presented in Figure 5.9, it is clear that by carefully thresholding based on the field gradients, SDDA signatures can still be detected across a significant portion of the inertial range.

This latter observation is crucial because it is not the typical or median amplitude eddy that is expected—or required for the purposes of the (Chandran et al., 2015) model—to be strongly aligned at a given scale. Such wave packets have likely undergone several balanced collisions, which could impede increasing alignment. Instead, it is the "atypical," yet "dynamically relevant," eddies residing at the tails of the PDFs of increments that are expected to show such behavior for the model to work. This is indeed the case, at least down to the point where instrumental effects likely dominate the statistics (see analysis in Sections 5.2.3.5). These wave packets are characterized by strong field gradients, remain strongly incompressible, and have highly correlated velocity/magnetic field fluctuations, as evidenced by the low n_B and high σ_c indices, respectively. However, they exhibit a significant excess of magnetic over kinetic fluctuation energy and therefore deviate from

purely Alfvénic behavior.

Therefore, our observations support the following picture: The nonlinear, intermittent dynamics perpendicular to $\boldsymbol{B}_0$ produce highly aligned, strongly turbulent, current sheet structures that retain certain properties associated with the linear-wave response, given their high cross-helicity. Kinetic-magnetic energy equipartition is spontaneously broken due to imbalanced wave packet collisions, even if it is present initially at large scales, where $\delta\boldsymbol{u} \approx \pm\delta\boldsymbol{b}$. This process culminates in the formation of incompressible current sheet structures at smaller scales, residing at the periphery of the circle plot illustrated in Appendix 5.2.5.2, a result also recovered in homogeneous and EBM simulations (see e.g., Dong et al., 2014; Shi et al., 2023a). In this sense, our results provide observational support for the (Chandran et al., 2015) model, indicating that both excess residual energy and SDDA can be explained within the framework of strongly imbalanced wave packet collisions (see also, Boldyrev et al., 2012; Howes, 2015). As such, our results provide observational support for the in-situ generation of coherent structures as a by-product of the turbulent cascade. At the same time, however, our results cannot definitively rule out the presence of advected flux tube structures originating from the inner heliosphere (Borovsky, 2008).

5.2.4.2 Dependence of SDDA measurements to Elsässer and Alfvénic imbalance

In Section 5.2.3.3, we demonstrated that the scaling of Θ^z and Θ^{ub} is strongly correlated with the global Alfvénic and Elsässer imbalance, but with some nuances.

For instance, the large-scale value of normalized cross helicity, $\sigma_c(\ell^*)$, with $\ell^* = 2 \times 10^4 d_i$, shows a strong correlation with Θ^{ub}. As $\sigma_c(\ell^*) \to 1$, the scaling of Θ^{ub} becomes steeper and is observed over a progressively narrower range of scales. However, the scaling of Θ^z does not appear to change significantly with global Elsässer imbalance, at least for $\sigma_c(\ell^*) < 0.7$. This finding is in qualitative agreement with the incompressible, homogeneous MHD simulations by Beresnyak and Lazarian (2009), who found that the

scaling of Θ^z remains unaffected by the global Elsässer imbalance.

Conversely, large-scale Alfvénic imbalance correlates with both Θ^z and Θ^{ub}. As $\sigma_r(\ell^*) \to 0$, the scaling of Θ^{ub} becomes steeper and narrows in scale range; that is, the rollover of the curves shifts to smaller scales as $\sigma_r(\ell^*) \to -1$ or $\sigma_c(\ell^*) \to 0$. For Θ^z, the scaling becomes steeper as $\sigma_r(\ell^*) \to -1$, but there is no clear trend in the extent of Θ^z with $\sigma_r(\ell^*)$.

While our analysis clearly indicates that the scaling of SDDA depends strongly on the degree of large-scale imbalance in the system, the observation that the extent over which these signatures persist might also depend on imbalance is less convincing. It is tempting to assume that for globally imbalanced intervals, the fields are already tightly aligned at large scales, resulting in a strong depletion of nonlinearities. This would effectively halt the mechanism that results in SDDA and prevent the average value of the different alignment angles from becoming any tighter towards smaller scales. This could lead to a saturation of the alignment angles at some minimum value, or allow for other mechanisms that result in misalignment of the fields to become significant, as discussed in Section 5.2.4.6.

Another possible explanation could be instrumental effects. As discussed in Appendix 5.2.3.5, small uncertainties in high-frequency velocity field measurements can result in significant uncertainty in alignment angle measurements, with the effect becoming increasingly important as Elsässer imbalance increases. For example, it is clear from the inset in Figure 5.19c that as $\sigma_c \to 1$, the effects of high-frequency noise become increasingly important at larger scales for Θ^{ub}, consistent with the results presented in Figure 5.14b. Thus, the dependence of alignment angle contamination due to instrumental effects on the imbalance could provide an alternative explanation for the observed trend.

In any case, the extent to which SDDA persists deeper into the inertial range depending on the global imbalance in the system is an interesting area for future research. Further investigation with better quality particle measurements or high-resolution numerical simulations is necessary to conclusively address this matter.

5.2.4.3 Sensitivity of SDDA measurements to instrumental noise

In recent years, concerns have been raised regarding the extent to which our ability to estimate statistical quantities that depend on the sub-dominant Elsässer mode is hampered by uncertainty in velocity field measurements due to instrument characteristics (Podesta, 2009; Chen et al., 2012; Podesta et al., 2009; Gogoberidze et al., 2012; Bowen et al., 2021; Sioulas et al., 2024; Ervin et al., 2024).

For example, the velocity data from the Wind mission are quantized before transmission back to Earth, a process that involves rounding real, rational numbers to the nearest integer. A close inspection of the velocity field time series shows that almost every data point has a time-discontinuity. While these discontinuities are small—corresponding to the bit size of the data—they induce an artificial $\propto f^{-2}$ spectrum. This high-frequency quantization noise leads to a decoupling of velocity and magnetic field fluctuations near the Nyquist frequency, identified as the primary reason for the observed decrease in σ_c at high frequencies (Podesta and Borovsky, 2010). Other sources of uncertainty, including aliasing and Poisson noise, are further discussed by Chen et al. (2013).

Since good-quality, high-frequency velocity field measurements are not available at the moment, we have tried to quantify the uncertainty in our measurements to assess the degree of confidence we can place in our observations and to attribute them to physical mechanisms underlying the turbulent cascade.

In Section 5.2.3.5, we presented a simplified theoretical analysis along with an effort to model the effects of noise on SDDA measurements. Our analysis indicates that despite the fact that other quantities, e.g., P_u, σ_c, or even P_{zi}, may still be measurable for the largest portion of the inertial range, the effects of noise on alignment angle measurements can be dramatic at very low frequencies. The strong dependence on the level of Elsässer imbalance can render such measurements impossible even at scales as large as $5-10\times10^3 d_i$. Therefore, while we discuss other alternative mechanisms of physical origin that could result in misalignment of the fields in subsequent sections, we believe, based on the analysis presented in Section 5.2.3.5, that the increasing misalignment of the fields usually

observed at inertial scales is of instrumental origin.

5.2.4.4 Effects of compressibility in SDDA

As the cascade progresses toward smaller spatial scales, the topology and characteristics of turbulent fluctuations can change dramatically. Various types of coherent structures, both incompressible (such as current sheets and Alfvén vortices) and compressible (including magnetic holes and solitons), have been observed in different space-plasma environments (Alexandrova et al., 2006; Rees et al., 2006; Perrone et al., 2016; Vasko et al., 2022; Vinogradov et al., 2023). In many cases, compressive fluctuations have been shown to significantly impact the dynamics of the turbulent solar wind (Klein et al., 2012; Howes et al., 2012; Verscharen et al., 2017; Chandran, 2018; Shoda et al., 2019).

To bridge the gap between in-situ observations, theoretical predictions, and numerical evidence, we sought to quantify the effects of compressibility on SDDA. This involved a distinct examination of the dynamics of compressible and incompressible fluctuations to gain insights into the persistent observation of increasing misalignment at the inertial scale of solar wind turbulence.

As anticipated, our results indicated that strongly compressible fluctuations generally exhibit very weak to negligible signatures of increasing alignment, as shown in Figure 5.10. These fluctuations can, to some extent, affect the average scaling of SDDA when mixed with Alfvénic fluctuations. However, compressible fluctuations are usually associated with weak field gradients and have considerably lower amplitudes than incompressible fluctuations, Figure 5.11. Therefore, their impact on the average scaling behavior is minimal, especially when amplitude-weighted definitions of the alignment angle are considered.

In fact, though not shown here, the average behavior (i.e., without segregating compressible from incompressible fluctuations) of the alignment angles almost perfectly overlaps with the black (i.e., incompressible) lines in Figure 5.10, indicating that the effects of compressibility on SDDA are negligible and can thus not explain the trend of

misalignment at inertial scales.

5.2.4.5 Alignment at the Outer Scale: Assessing Consistency with Homogeneous, Incompressible MHD Phenomenologies

Our findings confirm a well-established result: increasing signatures of SDDA are observable for the majority of the intervals considered, irrespective of associated plasma parameters, at the outer scale. However, before concluding that the observed behavior aligns with the phenomenological models of homogeneous MHD turbulence discussed above, another aspect, which has not been extensively explored in the literature, warrants further discussion.

In homogeneous MHD, the turbulent cascade advances through uncorrelated collisions between counterpropagating wave packets. However, in the stratified solar wind, dynamics become more intricate due to linear couplings of outgoing waves with large-scale inhomogeneities, leading to non-WKB (Wentzel-Kramers-Brillouin) reflections. In this scenario, the Elsässer fields can be decomposed into primary and secondary components (Velli et al., 1989; Velli et al., 1990; Hollweg and Isenberg, 2007). The primary component, known as the "classical" component z_c^i, travels at the characteristic phase speed $V_{sw} - V_a$. The secondary, or "anomalous" component z_a^i, maintains the same phase function and thus propagating properties as the forcing, z^o. Consequently, z_a^i maintains a strong correlation with z^o, $\boldsymbol{z}^o \propto -\boldsymbol{z}_a^i$. Numerical demonstrations of this anomalous coherence effect in inhomogeneous MHD turbulence have been explored in (Verdini et al., 2009).

The nonlinear interactions between z^o and z_c^i are uncorrelated and transient, limited to the duration of their encounters. Conversely, in the frame of the outgoing wave, z_a^i appears stationary, and the shearing between z^o and z_a^i remains coherent over time. It is intuitive to anticipate that as the imbalance in the fluxes of counterpropagating wavepackets increases, the efficiency of z^o and z_c^i decreases—it becomes more difficult for a z_c^i fluctuation to locate and interact with the dominant z^o fluctuations. Consequently, the influence of the anomalous coherence effect would intensify with increasing Elsässer

imbalance.

The anomalous coherence of wave packets in the expanding solar wind enhances nonlinear interactions compared to the homogeneous scenario, thereby altering the phenomenology of the energy cascade. This results in $1/f$ and $f^{-3/2}$ outer range scalings for inwardly and outwardly propagating modes, respectively (Velli et al., 1989; Perez and Chandran, 2013). By selecting the most strongly imbalanced ($\sigma_c(\ell^*) > 0.95$) fast wind intervals—having similar levels of RMS—and calculating an average second-order moment, we demonstrate that this is indeed the case, as shown in Figure 5.20. herefore, the coherent nature of the interactions could potentially affect the scale-dependence of the alignment angle.

This discussion underscores the need for a comprehensive theoretical framework to understand the nature of SDDA in the solar wind, taking into account the relative contributions of z_a^i and z_c^i to the shearing of z^o across various scales. Nevertheless, regardless of whether SDDA derives primarily from "classical" or "anomalous" interactions, the underlying mechanism remains the same. Therefore, the conclusion that the physical origin of SDDA stems from the shearing of wave packets due to strongly imbalanced interactions remains valid, even though the exact scaling might deviate from the (Chandran et al., 2015) predictions, especially as $\sigma_c \to 1$.

5.2.4.6 Instabilities

An important question arising from our study concerns the regime change observed in the polarization alignment, which tends to plateau, at best, as inertial scales are approached. An additional explanation for the observed increasing misalignment at smaller spatial scales involves the idea that dynamically aligned structures of a particular amplitude become unstable to disruption by tearing instabilities and the onset of magnetic reconnection (Furth et al., 1963). Particularly, when the maximum growth rate of the (Coppi et al., 1976) mode, γ_t, becomes comparable to the non-linear cascade time τ_{nl}, $\gamma_t \tau_{nl} \gtrsim 1$, the current sheets can no longer remain stable (Pucci and Velli, 2014; Uzdensky

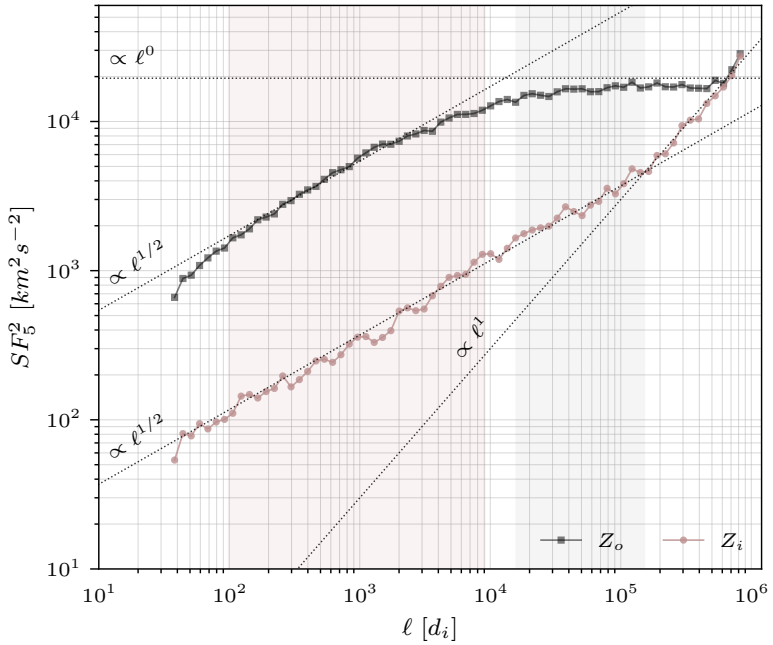

Figure 5.20: Averaged trace SF_5^2 of $\boldsymbol{z}_o$ (black) and $\boldsymbol{z}_i$ (red) for the fast, strongly Alfvénic ($\sigma_c > 0.95$) solar wind. At inertial scales, indicated by the pink shading, both fields follow a $-3/2$ spectral scaling. Two outer scale regimes may be observed: at scales $\ell \in [2 \times 10^4 - 2 \times 10^5]d_i$, spectral scalings for both fields, $P_{z_o} \propto k^{-1}$ and $P_{z_i} \propto k^{-3/2}$, are consistent with models based on "anomalous coherence" effects (Velli et al., 1989; Perez and Chandran, 2013). At even larger scales, a range with $P_{z_o} \propto k^{-1}$ and $P_{z_i} \propto k^{-2}$ scalings is observed, consistent with the model by Chandran (2018) based on PDI.

and Loureiro, 2016). The disruption of the current sheets, at a certain scale λ_D, interrupts dynamic alignment, accelerating the turbulent cascade and leading to a pronounced steepening of the power spectrum (Mallet et al., 2017; Loureiro and Boldyrev, 2017). In the tearing-dominated regime, the alignment angle is expected to increase with decreasing scale, $\theta^{ub} \sim \lambda^{-4/5}$ (Mallet and Schekochihin, 2017; Boldyrev and Loureiro, 2017).

Using three-dimensional gyrokinetic simulations, (Cerri et al., 2022) explored the dynamics of collisions between Alfvén waves (AW), revealing distinct behaviors in SDDA depending on whether the wave packets are colliding or well separated. When colliding, alignment demonstrates scale-dependent behavior likely induced by the packets shearing each other, whereas when well separated, a reconnection-mediated cascade dominates, leading to misalignment. This differentiation, as depicted in Figure 4 of (Cerri et al., 2022), is crucial; without it, the average curve lacks specific scaling and remains nearly

flat. This averaging effect could significantly impact in-situ measurements, especially when alignment is measured over extended periods, exacerbating as the measurements move towards smaller scales where turbulence evolution timescales become shorter.

In many astrophysical scenarios, MHD turbulence is typically driven by localized sources (e.g., shear, instabilities), leading to non-balanced states, i.e., non-negligible cross helicity. Indeed, localized regions of imbalance have been prominently observed even in globally imbalanced simulations of MHD turbulence (Matthaeus et al., 2008a; Perez and Boldyrev, 2009a). Patches of positive and negative cross-helicity are also evident in globally balanced solar wind streams (Chen et al., 2011; Wicks et al., 2013a). Considering these observations and based on their simulations (Cerri et al., 2022) propose that aligning thin, long-lived current sheets are generated by the turbulent cascade, then misaligning through tearing, in a patchy fashion in space and time, rather than stepwise in k-space. Taking these observations into account, we can conclude that while the tearing mediated regime is highly unlikely to occur at scales as large as $10^3 - 10^4 d_i$, the impact of tearing of the current sheets on the alignment angle at inertial scales warrants further investigation.

In addition, other types of ideal MHD instabilities, such as the Kelvin-Helmholtz instability (Malagoli et al., 1996), could potentially manifest in the solar wind. For example, it has been demonstrated that despite the highly Alfvénic nature of the fluctuations at large scales, the signatures of Alfvénicity (namely, σ_c, σ_r, θ^{ub}) diminish at considerably larger scales than those observed at 1 AU (Podesta and Borovsky, 2010).

(Parashar et al., 2020) interpret these observations as indicative of substantial energy found in velocity shears, which disrupt an initial spectrum of high cross helicity by injecting equal amounts of the two Elsässer energies (Roberts et al., 1987; Goldstein et al., 1989; Roberts et al., 1992) within the inner heliosphere (Ruffolo et al., 2020). Since both σ_c and σ_r are interdependent with the alignment angles, such effects could potentially influence the SDDA scalings. While it is not possible to rule out such effects, especially given recent in-situ observations (Paouris et al., 2024), it's essential to note that, as demonstrated in Section 5.2.4.3, high-frequency instrumental noise in velocity field measurements can contaminate the power spectrum of the ingoing Elsässer field even

at lower frequencies. This contamination becomes progressively more significant as the Elsässer imbalance increases, see 5.16b. Therefore, another plausible explanation for such observations may be contamination by high-frequency velocity field noise. Additionally, as pointed out in (Schekochihin, 2022), since the vortex stretching terms for the different Elsässer fields have opposite signs (Zhdankin et al., 2013), there will generally be more "current sheets" than "shear layers". In such sheets, at least in the homogeneous case, the Kelvin–Helmholtz instability will be suppressed (Taylor, 1938).

5.2.5 Summary & Conclusions

Using a large dataset of carefully selected homogeneous intervals from the WIND mission, we explored the impact of compressibility, intermittency, and imbalance on the statistical signatures of Scale-Dependent Dynamic Alignment (SDDA) in MHD turbulence within the solar wind (Boldyrev, 2006; Chandran et al., 2015).

Below, we summarize the key findings of our analysis. For clarity, we refer to the alignment angles of the Elsässer variables as (Θ^z) and the alignment between velocity and magnetic field fluctuations as (Θ^{ub}).

(1) SDDA in both Θ^z and Θ^{ub} is consistently evident at energy-containing scales, $\lambda \gtrsim 10^4 d_i$, and is observed concurrently with an increase in $|\sigma_c|$ and σ_r becoming more negative.

(2) Θ^z and Θ^{ub} exhibit an inverse correlation with the intensity of field gradients. This may stem from "anomalous" and/or "counterpropagating" wave packet interactions. Nevertheless, this observation indicates that the physical origin of alignment arises from the mutual shearing of the Elsässer fields during imbalanced wave-packet interactions (Chandran et al., 2015).

(2) Compressible fluctuations do not exhibit any signs of SDDA. However, their effects on the average behavior of SDDA are negligible due to their relatively low amplitude and

thus cannot explain the trend of misalignment at inertial scales.

(3) Stringent thresholding on proxies for intermittency reveals SDDA signatures within a portion of the inertial range. Regardless of the approach we follow increasing misalignment is consistently observed for scales $\lambda \geq 8 \times 10^2 d_i$. Based on analytical arguments and modeling, we believe this misalignment is not a physical phenomenon but rather an artifact caused by high-frequency noise in the velocity field measurements.

(4) The scaling of Θ^z/Θ^{ub} becomes steeper/shallower with increasing global Alfvénic imbalance ($\sigma_r(\ell^*) \to -1$), but only Θ^{ub} is correlated, becoming steeper, with the increasing global Elsässer imbalance ($\sigma_c(\ell^*) \to 1$).

(5) Signatures of increasing alignment in Θ^{ub} extend deeper into the inertial range of balanced intervals. This could be due to two factors: first, in globally imbalanced intervals, the fields are tightly aligned at large scales, depleting nonlinearities and halting the SDDA mechanism, causing alignment angles to saturate at a minimum value. Alternatively, instrumental noise may have a greater impact on alignment angle measurements as imbalance increases, leading to significant measurement errors.

While we do not disregard the need for theoretical advancements in existing turbulence models—especially to address the effects of imbalance and the expansion of the solar wind—it is more plausible that our results underscore the current limitations in precisely estimating alignment angles due to instrumental constraints, particularly in the context of highly Alfvénic, strongly imbalanced turbulence. Regrettably, the most intriguing cases are also the most difficult to investigate.

Alternative methods for studying the scaling of alignment angles should be considered. For example, using electric field measurements could enable the estimation of the perpendicular component of the magnetic field fluctuations, given by $\delta\mathbf{V}_\perp(\ell, t) = \delta\mathbf{E}_\perp(\ell, t) \times \mathbf{B}_0/c$, where $\delta\mathbf{E}_\perp(\ell, t)$ represents the perpendicular component of the electric field fluctuations and c is the speed of light. This approach is planned for future research.

Moreover, 3D expanding box simulations of compressible MHD, which include both balanced and imbalanced turbulence, will offer deeper insights and facilitate more precise quantification of these effects on alignment measurements (Shi et al., in prep).

5.2.5.1 Revisiting (Podesta et al., 2009)

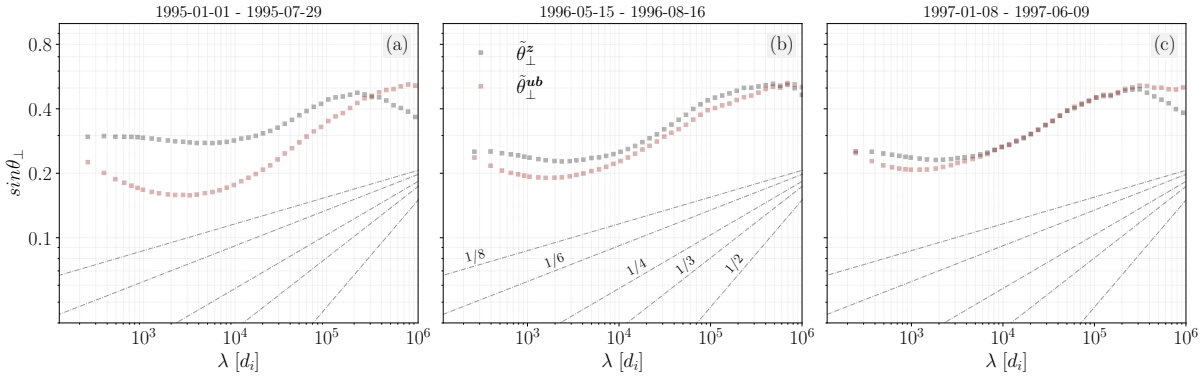

Figure 5.21: Alignment angle measurements as defined by Equations 2.27 and 2.28 in top and bottom panels, respectively, across the three (out of four) intervals studied in (Podesta et al., 2009).Black curves represent the alignment between Elsässer fields, while red curves illustrate the alignment between velocity and magnetic field fluctuations.

To verify the effectiveness of our modified alignment angle estimation method in comparison with (Podesta, 2009), we revisited the intervals analyzed in their study. Their investigation primarily focused on the alignment between $\delta\boldsymbol{v}_\perp$ and $\delta\boldsymbol{b}_\perp$, employing the definitions outlined in Equation 2.28. In addition they introduced a weighted average angle, defined in Equation 8 of (Podesta, 2009). Our analysis indicates that the latter definition results in scalings that are in most cases identical to the polarization alignment definiton. In line with the methodology proposed by (Chandran et al., 2015), we specifically examined the angles delineated by Equations 2.27 and 2.28.

2.27

Figure 5.21 showcases our findings for $\tilde{\theta}^{ub(z)}_{\perp}$, with each column representing one of the three (out of four) intervals analyzed by (Podesta, 2009). The Elsässer fields are denoted by black lines, while the angles between magnetic and velocity fields are depicted in red. In all instances, the scaling obtained aligns with those reported in (Podesta, 2009),

with both the 2-pt and 5-pt increment methods yielding very similar results, as detailed in Section 2.0.8. Thus, we can confidently proceed with our analysis utilizing the 5-pt increment method.

5.2.5.2 Geometrical Constrains and Types of Alignment

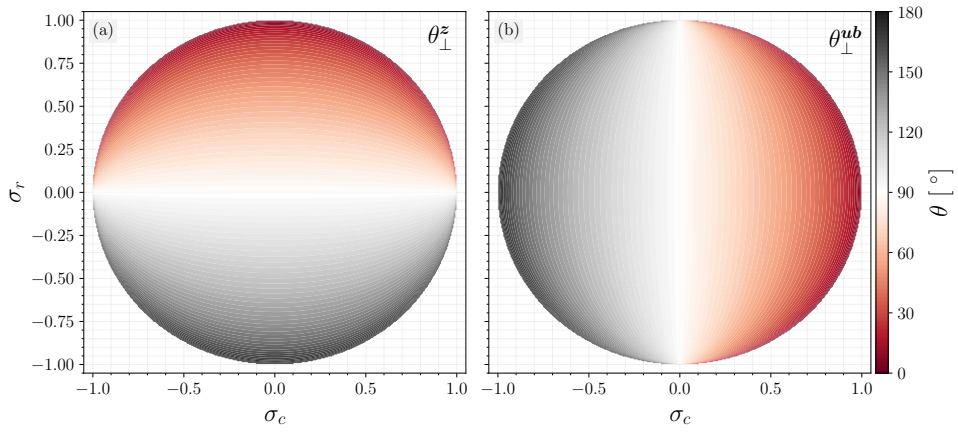

Figure 5.22: Graphical representation of Equations 5.24 illustrated in panels (a) and (b), respectively.

To provide a clear illustration of the interdependence between σ_c, σ_r, $\theta_\perp^{ub}$, and $\theta_\perp^z$ we provide a graphical representation of the equations:

$$\cos(\theta_\perp^z) = \frac{\sigma_r}{\sqrt{1-\sigma_c^2}}, \quad \cos(\theta_\perp^{ub}) = \frac{\sigma_c}{\sqrt{1-\sigma_r^2}}, \tag{5.24}$$

To generate random values for σ_c and σ_r within a unit circle on the Cartesian plane, constrained to the range of [-1, 1], we employed a random sampling approach. We independently selected values for σ_c and σ_r from a continuous uniform distribution spanning [-1, 1], while ensuring that the condition $\sigma_c^2 + \sigma_r^2 \leq 1$ was met to keep them within the unit circle. Subsequently, for each pair, we estimated the alignment angles according to Equation 5.24. The results are illustrated in Figure 5.22, colored by $\theta_\perp^z$ in panel (a), and $\theta_\perp^{ub}$ in panel (b).

CHAPTER 6

Conclusion

In this thesis I have investigated the statistical properties of MHD turbulence spanning the entire spectrum from the outer, to the inertial and in some cases the kinetic scales. I have combined observations from the PSP, SolO and WIND missions spanning several decades and heliocentric distances ranging from the boundary of the solar corona out to Earth's orbit at 1au.

Before summarizing the new physics learned from this work, it is important to highlight that this endeavor has revealed a significant limitation in a method widely used in experimental turbulence studies. More specifically, as discussed in Section 5.1, the susceptibility of 2-point structure functions to spectral leakage (Cho, 2019) can result in erroneous interpretations of the turbulent cascade. While negligible at inertial scales—validating the results in Section 4—this deficiency becomes significant at kinetic scales, Gaussianizing the distributions of increments and leading to imprecise estimations of intermittency-related metrics. Consequently, this work suggests that the well-established monofractal nature of the turbulent cascade at kinetic scales must be re-examined using wavelet or multipoint structure functions. This reconsideration is crucial for a deeper understanding of the fractal properties of MHD turbulence at kinetic scales, which can significantly impact our understanding of the mechanisms underlying magnetic turbulent energy dissipation into plasma heating. In future work, we will thoroughly investigate this topic, focusing on distinguishing between balanced and imbalanced turbulence streams (see, e.g., Bowen et al., 2023).

I first studied the evolution of statistical properties of magnetic field fluctuations in the inner heliosphere, published in (Sioulas et al., 2023a), and discussed in Section 3.1

of this thesis. Initially focusing on spectral properties, I aimed to identify the plasma parameters underlying the inertial-range steepening of the magnetic field power spectrum. The results indicate that closer to the Sun, the magnetic field power spectrum exhibits a poorly developed inertial range, characterized by a $-3/2$ spectral index. As the solar wind expands into the interplanetary medium, the inertial range extends to larger scales, with the spectral index steepening towards $-5/3$ (Chen et al., 2020). The main finding of this work is that the rate of steepening is strongly dependent on the degree of equipartition between the energy in magnetic field and velocity field fluctuations. Specifically, our results indicate that the shearing of counterpropagating wave packets results in a turbulent cascade producing highly aligned coherent structures with an excess of residual magnetic over kinetic energy, leading to steeper magnetic field spectra. Conversely, nonlinearities are suppressed in strongly imbalanced intervals, allowing them to retain their near-sun shallower scaling of $-3/2$ at Earth's orbit.

Focusing on the anisotropic properties of the magnetic field power spectra (Sioulas et al., 2023), and discussed in Section 3.2, we provided strong evidence suggesting that the domain canonically identified as the inertial range comprises two distinct sub-inertial segments exhibiting different turbulence statistics. The presence of the two sub-ranges is evident closer to the Sun, with the small-scale sub-range extending between $10 - 100 d_i$ and gradually extending to larger scales with increasing heliocentric distance. Turbulence in the large-scale sub-inertial range is roughly isotropic, and thus close to the Sun, the anisotropy in both the scaling and power gradually diminishes and deviates significantly from the canonical behavior expected from the phenomenological models discussed in Section 1.3.1. Additionally, this work highlights that the lack of a well-defined inertial range close to the Sun could be partly attributed to the scarcity of perpendicular fluctuations due to quasi-parallel sampling, leading to significant discrepancies between the perpendicular and trace power spectra. This study underscores the importance of using conditional analysis to separately estimate the field-parallel and field-perpendicular power spectra. Without this careful analysis, results cannot be accurately interpreted based on the phenomenological models discussed in Section 1.3.1, which only offer scaling predictions

in the three physically important directions, as elaborated in Section **??**. Finally, this work has shown that close to the Sun, the outer range of the spectrum is characterized a remarkably extended and relatively shallow scaling of $\alpha_B \approx -0.8$ that steepens towards $\alpha_B \approx -1$ with distance. This is particularly noteworthy as previous research has shown that the coupling of large amplitude outwardly propagating waves to slow magnetosonic wave through the parametric decay instability (Galeev and Oraevskii, 1963b; Goldstein, 1978; Pruneti and Velli, 1997; Réville et al., 2018; Malara et al., 2022; Chandran, 2018) which results in two daughter waves; an antisunward propagating slow wave and a sunward propagating alfven wave, of frequency slightly lower than the mother wave. This process may lead an inverse energy cascade and to the development of a $k_{||}^{-1}$ spectrum for outward-propagating AWs by the time they reach a heliocentric distance of 0.3 au in the fast solar wind (Chandran, 2018).

To elucidate the mechanisms behind the slow decay of electron and proton temperatures in the solar wind, compared to spherically symmetric adiabatic expansion models (i.e., $T \sim r^{-4/3}$), I investigated the characteristics and radial evolution of coherent structures and their role in magnetic energy dissipation and plasma heating. Focusing on the perihelia of PSP, we found that coherent structures tend to form clusters rather than being evenly distributed. Regions with strong magnetic field gradients, which are expected to enhance stochastic heating rates based on critically balanced Alfvénic turbulence (Mallet et al., 2019), are associated with significantly higher proton temperatures but only slightly elevated electron temperatures. The results suggest a heating mechanism in the nascent solar wind driven by a nonlinear turbulent cascade that preferentially heats protons over electrons. This could be interpreted through the recently discovered "helicity barrier" mechanism (Meyrand et al., 2021a; Squire et al., 2022b), which posits that under conditions of strong imbalance, generalized helicity conservation may impede energy transfer to electron scales, resulting in preferential proton heating. Further work is needed to understand whether heating rates among different species change between balanced and imbalanced solar wind intervals. This could be investigated using high-quality electron temperature data from the quasithermal-noise estimate of the SolO mission.

Following the solar wind further into the inner heliosphere, I investigated the dynamic evolution of magnetic coherent structures and how their statistical is that the strengthening of intermittency with increasing distance from the Sun (Bruno et al., 2003) should be re-examined. This is because intermittency properties exhibit strong anisotropy relative to the background magnetic field, and the angle between the solar wind flow and the magnetic field, as observed by spacecraft, can significantly influence whether fluctuations in measured quantities vary parallel or perpendicular to the magnetic field. Due to the Parker Spiral configuration (Parker and Tidman, 1958), the baseline angle between the solar wind flow and the magnetic field, denoted as Θ_{VB}, increases with heliocentric distance. Consequently, spacecraft measuring magnetic field fluctuations at 1 AU are more likely to detect fluctuations perpendicular to the mean magnetic field direction, resulting in an observational bias when Θ_{VB} is not taken into account, leading to a perceived radial increase in intermittency. However, when the sampling becomes quasi-perpendicular and the fraction of parallel intervals becomes statistically insignificant, a decrease in the fraction of the dataset occupied by coherent structures is evident. This observation provides a simple explanation for the observed weakening of intermittency beyond 1 AU (Parashar et al., 2019; Cuesta et al., 2022b).

Given the unexpected observation of the two sub-inertial ranges in the domain cnaonically identified as the inertial range, I have then tried to understand the physical mechanisms underlying this transition. In the process an effort was made to on determining the presence and measurable impact of model-specific elements, such as SDDA and CB, on the observed characteristics. It was shown, for the first time, through in situ observations that the two Alfvénic species undergo distinct turbulent cascades. While both start weak at large scales, outgoing modes remain in the weak regime throughout the inertial range, while ingoing modes transition to a strong cascade at the onset of the inertial range. This transition is accompanied by spectral scalings diverging from the expected behavior marking the shift from weak to strong turbulence, an effect we have atributed to "anomalous coherence' effects taking place in the solar wind (Velli et al., 1989).

While several findings came out of this work, the most important realization, is that the models proposed by CSM15 and MS17, which integrate SDDA as an intermittency effect and account for local imbalance, possess the essential elements for a successful phenomenological representation of imbalanced MHD turbulence. However, the models do not address certain aspects of solar wind turbulence, such as the presence of two sub-inertial ranges and anisotropic signatures. THerefore Incorporating additional effects, like accounting for inhomogeneity or the spherical polarization of fluctuations, proves necessary to enhance the models' scaling predictions.

While important, the previous work only considers a specific case of MHD turbulence, namely imbalanced turbulence. It is essential to understand how these statistical signatures change depending on the global imbalance. To address this, the study was extended using a large statistical dataset from the WIND mission. Although this work is not yet fully completed, the initial focus has been on a topic that has proven controversial in recent years.

SDDA in the polarization of Elsässer field fluctuations is posited to suppress nonlinearities and modulate the energy spectrum. Despite its theoretical significance, empirical evidence for SDDA within the inertial range of solar wind turbulence has been sparse. I revisited the topic analyzed homogeneous intervals from 28 years of WIND mission data to assess the effects of compressibility, intermittency, and imbalance on SDDA. The results indicate that alignment at the largest scales tightens regardless of plasma parameters. As imbalance increases, the scaling of SDDA becomes steeper; however, SDDA signatures are observed deeper within the inertial range of balanced intervals. Minor uncertainties in high-frequency velocity field measurements can significantly affect estimates of low-frequency alignment angles, and such effects intensify with imbalance. An observed anticorrelation between the intensity of field gradients and alignment angles supports the hypothesis that SDDA may originate from the mutual shearing of Elsässer fields in highly imbalanced collisions ($\delta \boldsymbol{z}^{\pm} \gg \delta \boldsymbol{z}^{\mp}$) between counterpropagating wave packets. By applying stringent thresholds on proxies for intermittency and compressibility, we identified SDDA signatures extending into a portion of the inertial range. This work

highlights another limitation of in-situ observations and suggests that a satisfactory answer to the question of how deep into the inertial range SDDA affects the turbulent spectra will not be provided using solely velocity field data.

Alternative methods for studying the scaling of alignment angles warrant consideration. For instance, using electric field measurements could allow for the estimation of the perpendicular component of the magnetic field fluctuations, $\delta\mathbf{V}_\perp(\ell,t) = \delta\mathbf{E}_\perp(\ell,t) \times \mathbf{B}_0/c$, where $\delta\mathbf{E}_\perp(\ell,t)$ denotes the perpendicular component of the electric field fluctuations and c is the speed of light. This area of study is slated for future research. Finally, 3D expanding box simulations of compressible MHD, including both balanced and imbalanced turbulence, will provide deeper insights and facilitate a more precise quantification of these effects on alignment measurements (Shi et al., in prep).

Finally, using the WIND dataset, the 3D anisotropic higher-order scalings of the different fields will be studied and an effort will be made to further understand the degree to which effects happening, but are not accounted for by MHD turbulence phenomenologies, modfy the turbent cascade and in turn affect the magentic energy dissipation and plasm heting in the solar wind.

SDDA in the polarization of Elsässer field fluctuations is posited to suppress nonlinearities and modulate the energy spectrum. Despite its theoretical significance, empirical evidence for SDDA within the inertial range of solar wind turbulence has been sparse. Revisiting this topic, I analyzed homogeneous intervals from 28 years of data from the WIND mission, selected through visual inspection, to assess the effects of compressibility, intermittency, and imbalance on SDDA. The results indicate that, at any given scale, the alignment angle is anticorrelated with the intensity of field gradients, supporting the hypothesis that the physical origin of SDDA may stem from the mutual shearing of Elsässer fields in highly imbalanced collisions ($\delta\boldsymbol{z}^\pm \gg \delta\boldsymbol{z}^\mp$) between counterpropagating wave packets. Compressible fluctuations do not show any increasing alignment and, when mixed with Alfvénic ones, can pollute the average behavior. By applying stringent thresholds on proxies for intermittency and compressibility, I have identified SDDA signatures extending into a portion of the inertial range. As imbalance increases, the scaling of

SDDA becomes steeper; however, SDDA signatures are observed deeper within the inertial range of balanced intervals. However, by modeling the influence of minor uncertainties in high-frequency velocity field measurements, demonstrating their substantial impact on low-frequency alignment angle estimates, with these effects intensifying with Elsässer imbalance. Therefore, this work highlights another limitation of in-situ observations and suggests that a satisfactory answer to how deep into the inertial range SDDA affects the turbulent spectra will not be provided using solely velocity field data.

Alternative methods for studying the scaling of alignment angles warrant consideration. For instance, using electric field measurements could allow for the estimation of the perpendicular component of the magnetic field fluctuations, $\delta\mathbf{V}_\perp(\ell,t) = \delta\mathbf{E}_\perp(\ell,t) \times \mathbf{B}_0/c$, where $\delta\mathbf{E}_\perp(\ell,t)$ denotes the perpendicular component of the electric field fluctuations and c is the speed of light. This area of study is slated for future research. Additionally, 3D expanding box simulations of compressible MHD, including both balanced and imbalanced turbulence, will provide deeper insights and facilitate a more precise quantification of these effects on alignment measurements (Shi et al., in prep).

Finally, using the WIND dataset, the 3D anisotropic higher-order scalings of the different fields will be studied. Efforts will be made to understand the degree to which unaccounted effects in MHD turbulence phenomenologies modify the turbulent cascade and, in turn, affect magnetic energy dissipation and plasma heating in the solar wind.

Acuña, M. H., Curtis, D., Scheifele, J. L., Russell, C. T., Schroeder, P., Szabo, A., and Luhmann, J. G. (2008). The STEREO/IMPACT Magnetic Field Experiment. , 136(1-4):203–226. 107

Alberti, T., Laurenza, M., Consolini, G., Milillo, A., Marcucci, M. F., Carbone, V., and Bale, S. D. (2020). On the Scaling Properties of Magnetic-field Fluctuations through the Inner Heliosphere. *The Astrophysical Journal*, 902(1):84. Publisher: American Astronomical Society. 100, 122

Alexandrova, O., Carbone, V., Veltri, P., and Sorriso-Valvo, L. (2008). Small-Scale Energy Cascade of the Solar Wind Turbulence. , 674(2):1153–1157. 176

Alexandrova, O., Mangeney, A., Maksimovic, M., Cornilleau-Wehrlin, N., Bosqued, J. M., and André, M. (2006). Alfvén vortex filaments observed in magnetosheath downstream of a quasi-perpendicular bow shock. *Journal of Geophysical Research (Space Physics)*, 111(A12):A12208. 235

Alfvén, H. (1942). Existence of Electromagnetic-Hydrodynamic Waves. , 150(3805):405–406. 30, 35, 202

Andrés, N., Sahraoui, F., Galtier, S., Hadid, L. Z., Ferrand, R., and Huang, S. Y. (2019). Energy cascade rate measured in a collisionless space plasma with mms data and compressible hall magnetohydrodynamic turbulence theory. *Phys. Rev. Lett.*, 123:245101. 180

Angelopoulos, V. (2008). The THEMIS Mission. , 141(1-4):5–34. 58

Bale, S. D., Badman, S. T., Bonnell, J. W., Bowen, T. A., Burgess, D., Case, A. W., Cattell, C. A., Chandran, B. D. G., Chaston, C. C., Chen, C. H. K., Drake, J. F., de Wit, T. D., Eastwood, J. P., Ergun, R. E., Farrell, W. M., Fong, C., Goetz, K., Goldstein, M., Goodrich, K. A., Harvey, P. R., Horbury, T. S., Howes, G. G., Kasper, J. C., Kellogg, P. J., Klimchuk, J. A., Korreck, K. E., Krasnoselskikh, V. V., Krucker, S., Laker, R., Larson, D. E., MacDowall, R. J., Maksimovic, M., Malaspina, D. M., Martinez-Oliveros, J., McComas, D. J., Meyer-Vernet, N., Moncuquet, M., Mozer, F. S., Phan, T. D., Pulupa, M., Raouafi, N. E., Salem, C., Stansby, D., Stevens, M., Szabo, A., Velli, M., Woolley, T., and Wygant, J. R. (2019). Highly structured slow solar wind emerging from an equatorial coronal hole. *Nature*, pages 1–6. 66, 197

Bale, S. D., Badman, S. T., Bonnell, J. W., Bowen, T. A., Burgess, D., Case, A. W., Cattell, C. A., Chandran, B. D. G., Chaston, C. C., Chen, C. H. K., Drake, J. F., de Wit, T. D., Eastwood, J. P., Ergun, R. E., Farrell, W. M., Fong, C., Goetz, K., Goldstein, M., Goodrich, K. A., Harvey, P. R., Horbury, T. S., Howes, G. G., Kasper, J. C., Kellogg, P. J., Klimchuk, J. A., Korreck, K. E., Krasnoselskikh, V. V., Krucker, S., Laker, R., Larson, D. E., MacDowall, R. J., Maksimovic, M., Malaspina, D. M., Martinez-Oliveros, J., McComas, D. J., Meyer-Vernet, N., Moncuquet, M., Mozer, F. S.,

Phan, T. D., Pulupa, M., Raouafi, N. E., Salem, C., Stansby, D., Stevens, M., Szabo, A., Velli, M., Woolley, T., and Wygant, J. R. (2019). Highly structured slow solar wind emerging from an equatorial coronal hole. , 576(7786):237–242. 103

Bale, S. D., Goetz, K., Harvey, P. R., Turin, P., Bonnell, J. W., Dudok de Wit, T., Ergun, R. E., MacDowall, R. J., Pulupa, M., Andre, M., Bolton, M., Bougeret, J. L., Bowen, T. A., Burgess, D., Cattell, C. A., Chandran, B. D. G., Chaston, C. C., Chen, C. H. K., Choi, M. K., Connerney, J. E., Cranmer, S., Diaz-Aguado, M., Donakowski, W., Drake, J. F., Farrell, W. M., Fergeau, P., Fermin, J., Fischer, J., Fox, N., Glaser, D., Goldstein, M., Gordon, D., Hanson, E., Harris, S. E., Hayes, L. M., Hinze, J. J., Hollweg, J. V., Horbury, T. S., Howard, R. A., Hoxie, V., Jannet, G., Karlsson, M., Kasper, J. C., Kellogg, P. J., Kien, M., Klimchuk, J. A., Krasnoselskikh, V. V., Krucker, S., Lynch, J. J., Maksimovic, M., Malaspina, D. M., Marker, S., Martin, P., Martinez-Oliveros, J., McCauley, J., McComas, D. J., McDonald, T., Meyer-Vernet, N., Moncuquet, M., Monson, S. J., Mozer, F. S., Murphy, S. D., Odom, J., Oliverson, R., Olson, J., Parker, E. N., Pankow, D., Phan, T., Quataert, E., Quinn, T., Ruplin, S. W., Salem, C., Seitz, D., Sheppard, D. A., Siy, A., Stevens, K., Summers, D., Szabo, A., Timofeeva, M., Vaivads, A., Velli, M., Yehle, A., Werthimer, D., and Wygant, J. R. (2016). The FIELDS Instrument Suite for Solar Probe Plus. Measuring the Coronal Plasma and Magnetic Field, Plasma Waves and Turbulence, and Radio Signatures of Solar Transients. *ßr*, 204(1-4):49–82. 87, 101, 123, 153, 166

Bale, S. D., Goetz, K., Harvey, P. R., Turin, P., Bonnell, J. W., Dudok de Wit, T., Ergun, R. E., MacDowall, R. J., Pulupa, M., Andre, M., Bolton, M., Bougeret, J. L., Bowen, T. A., Burgess, D., Cattell, C. A., Chandran, B. D. G., Chaston, C. C., Chen, C. H. K., Choi, M. K., Connerney, J. E., Cranmer, S., Diaz-Aguado, M., Donakowski, W., Drake, J. F., Farrell, W. M., Fergeau, P., Fermin, J., Fischer, J., Fox, N., Glaser, D., Goldstein, M., Gordon, D., Hanson, E., Harris, S. E., Hayes, L. M., Hinze, J. J., Hollweg, J. V., Horbury, T. S., Howard, R. A., Hoxie, V., Jannet, G., Karlsson, M., Kasper, J. C., Kellogg, P. J., Kien, M., Klimchuk, J. A., Krasnoselskikh, V. V., Krucker, S., Lynch, J. J., Maksimovic, M., Malaspina, D. M., Marker, S., Martin, P., Martinez-Oliveros, J., McCauley, J., McComas, D. J., McDonald, T., Meyer-Vernet, N., Moncuquet, M., Monson, S. J., Mozer, F. S., Murphy, S. D., Odom, J., Oliverson, R., Olson, J., Parker, E. N., Pankow, D., Phan, T., Quataert, E., Quinn, T., Ruplin, S. W., Salem, C., Seitz, D., Sheppard, D. A., Siy, A., Stevens, K., Summers, D., Szabo, A., Timofeeva, M., Vaivads, A., Velli, M., Yehle, A., Werthimer, D., and Wygant, J. R. (2016). The FIELDS Instrument Suite for Solar Probe Plus. Measuring the Coronal Plasma and Magnetic Field, Plasma Waves and Turbulence, and Radio Signatures of Solar Transients. , 204(1-4):49–82. 151

Bale, S. D., Horbury, T. S., Velli, M., Desai, M. I., Halekas, J. S., McManus, M. D., Panasenco, O., Badman, S. T., Bowen, T. A., Chandran, B. D. G., Drake, J. F., Kasper, J. C., Laker, R., Mallet, A., Matteini, L., Phan, T. D., Raouafi, N. E., Squire, J., Woodham, L. D., and Woolley, T. (2021a). A Solar Source of Alfvénic Magnetic Field Switchbacks: In Situ Remnants of Magnetic Funnels on Supergranulation Scales. , 923(2):174. 66

Bale, S. D., Horbury, T. S., Velli, M., Desai, M. I., Halekas, J. S., McManus, M. D., Panasenco, O., Badman, S. T., Bowen, T. A., Chandran, B. D. G., Drake, J. F., Kasper, J. C., Laker, R., Mallet, A., Matteini, L., Phan, T. D., Raouafi, N. E., Squire, J., Woodham, L. D., and Woolley, T. (2021b). A Solar Source of Alfvénic Magnetic Field Switchbacks: In Situ Remnants of Magnetic Funnels on Supergranulation Scales. , 923(2):174. 156

Bandyopadhyay, R., Matthaeus, W. H., McComas, D. J., Chhiber, R., Usmanov, A. V., Huang, J., Livi, R., Larson, D. E., Kasper, J. C., Case, A. W., Stevens, M., Whittlesey, P., Romeo, O. M., Bale, S. D., Bonnell, J. W., Dudok de Wit, T., Goetz, K., Harvey, P. R., MacDowall, R. J., Malaspina, D. M., and Pulupa, M. (2022). Sub-Alfvénic Solar Wind Observed by the Parker Solar Probe: Characterization of Turbulence, Anisotropy, Intermittency, and Switchback. , 926(1):L1. 122

Bandyopadhyay, R., Matthaeus, W. H., Parashar, T. N., Chhiber, R., Ruffolo, D., Goldstein, M. L., Maruca, B. A., Chasapis, A., Qudsi, R., McComas, D. J., Christian, E. R., Szalay, J. R., Joyce, C. J., Giacalone, J., Schwadron, N. A., Mitchell, D. G., Hill, M. E., Wiedenbeck, M. E., McNutt, R. L., Desai, M. I., Bale, S. D., Bonnell, J. W., Wit, T. D. d., Goetz, K., Harvey, P. R., MacDowall, R. J., Malaspina, D. M., Pulupa, M., Velli, M., Kasper, J. C., Korreck, K. E., Stevens, M., Case, A. W., and Raouafi, N. (2020). Observations of Energetic-particle Population Enhancements along Intermittent Structures near the Sun from the Parker Solar Probe. *The Astrophysical Journal Supplement Series*, 246(2):61. Publisher: American Astronomical Society. 51, 82, 150

Bandyopadhyay, R. and McComas, D. J. (2021). Geometry of magnetic fluctuations near the sun from the parker solar probe. *The Astrophysical Journal*, 923(2):193. 42, 113

Barnes, A. and Hollweg, J. V. (1974). Large-amplitude hydromagnetic waves. *Journal of Geophysical Research (1896-1977)*, 79(16):2302–2318. _eprint: https://agupubs.onlinelibrary.wiley.com/doi/pdf/10.1029/JA079i016p02302. 66, 70

Batchelor, G. K., Townsend, A. A., and Jeffreys, H. (1949). The nature of turbulent motion at large wave-numbers. *Proceedings of the Royal Society of London. Series A. Mathematical and Physical Sciences*, 199(1057):238–255. 49

Bavassano, B., Dobrowolny, M., Mariani, F., and Ness, N. F. (1982). Radial evolution of power spectra of interplanetary Alfvénic turbulence. *Journal of Geophysical Research: Space Physics*, 87(A5):3617–3622. _eprint: https://agupubs.onlinelibrary.wiley.com/doi/pdf/10.1029/JA087iA05p03617. 66, 67, 68, 69

Belcher, J. W. and Davis Jr., L. (1971). Large-amplitude Alfvén waves in the interplanetary medium, 2. *Journal of Geophysical Research (1896-1977)*, 76(16):3534–3563. _eprint: https://agupubs.onlinelibrary.wiley.com/doi/pdf/10.1029/JA076i016p03534. 42, 64, 69

Beresnyak, A. (2011). Spectral slope and kolmogorov constant of mhd turbulence. *Phys. Rev. Lett.*, 106:075001. 48, 204

Beresnyak, A. (2012). Basic properties of magnetohydrodynamic turbulence in the inertial range. , 422(4):3495–3502. 48, 185, 204

Beresnyak, A. (2014). Spectra of Strong Magnetohydrodynamic Turbulence from High-resolution Simulations. , 784(2):L20. 185

Beresnyak, A. (2015). On the Parallel Spectrum in Magnetohydrodynamic Turbulence. , 801(1):L9. 53

Beresnyak, A. (2019). MHD turbulence. *Living Reviews in Computational Astrophysics*, 5(1):2. 2

Beresnyak, A. and Lazarian, A. (2006a). Polarization Intermittency and Its Influence on MHD Turbulence. , 640(2):L175–L178. 47, 82, 205

Beresnyak, A. and Lazarian, A. (2006b). Polarization Intermittency and Its Influence on MHD Turbulence. , 640(2):L175–L178. 203

Beresnyak, A. and Lazarian, A. (2008). Strong Imbalanced Turbulence. , 682(2):1070–1075. 180, 184

Beresnyak, A. and Lazarian, A. (2009). Comparison of Spectral Slopes of Magnetohydrodynamic and Hydrodynamic Turbulence and Measurements of Alignment Effects. , 702(2):1190–1198. 184, 232

Beresnyak, A. and Lazarian, A. (2010). SCALING LAWS AND DIFFUSE LOCALITY OF BALANCED AND IMBALANCED MAGNETOHYDRODYNAMIC TURBULENCE. *The Astrophysical Journal*, 722(1):L110–L113. 42

Bieber, J. W., Wanner, W., and Matthaeus, W. H. (1996). Dominant two-dimensional solar wind turbulence with implications for cosmic ray transport. *Journal of Geophysical Research: Space Physics*, 101(A2):2511–2522. 42

Biskamp, D. (2003). *Magnetohydrodynamic Turbulence*. 16, 34

Biskamp, D. (2003). *Magnetohydrodynamic Turbulence*. 28, 98

Biskamp, D. and Müller, W.-C. (2000). Scaling properties of three-dimensional isotropic magnetohydrodynamic turbulence. *Physics of Plasmas*, 7(12):4889–4900. 146

Boldyrev, S. (2002). Kolmogorov-Burgers Model for Star-forming Turbulence. , 569(2):841–845. 51

Boldyrev, S. (2005). On the spectrum of magnetohydrodynamic turbulence. *The Astrophysical Journal*, 626(1):L37. 47, 203

Boldyrev, S. (2006). Spectrum of magnetohydrodynamic turbulence. *Phys. Rev. Lett.*, 96:115002. xi, 47, 48, 53, 68, 86, 100, 118, 178, 179, 180, 181, 203, 204, 206, 230, 240

Boldyrev, S., Forest, C., and Egedal, J. (2020). Electron temperature of the solar wind. *Proceedings of the National Academy of Science*, 117(1):9232–9240. 58

Boldyrev, S. and Loureiro, N. F. (2017). Magnetohydrodynamic turbulence mediated by reconnection. *The Astrophysical Journal*, 844(2):125. 187, 192, 238

Boldyrev, S. and Perez, J. C. (2012). Spectrum of kinetic-alfvÉn turbulence. *The Astrophysical Journal Letters*, 758(2):L44. 173

Boldyrev, S., Perez, J. C., and Zhdankin, V. (2012). Residual energy in MHD turbulence and in the solar wind. In Heerikhuisen, J., Li, G., Pogorelov, N., and Zank, G., editors, *Physics of the Heliosphere: A 10 Year Retrospective*, volume 1436 of *American Institute of Physics Conference Series*, pages 18–23. AIP. 232

Borovsky, J. E. (2008). Flux tube texture of the solar wind: Strands of the magnetic carpet at 1 AU? *Journal of Geophysical Research (Space Physics)*, 113(A8):A08110. 69, 232

Borovsky, J. E. (2021). Solar-Wind Structures That Are Not Destroyed by the Action of Solar-Wind Turbulence. *Frontiers in Astronomy and Space Sciences*, 8. 51

Borovsky, J. E., Denton, M. H., and Smith, C. W. (2019). Some properties of the solar wind turbulence at 1 au statistically examined in the different types of solar wind plasma. *Journal of Geophysical Research: Space Physics*, 124(4):2406–2424. 103

Bourouaine, S. and Perez, J. C. (2019). On the Interpretation of Parker Solar Probe Turbulent Signals. *apjl*, 879(1):L16. _eprint: 1906.05644. 61

Bourouaine, S., Perez, J. C., Klein, K. G., Chen, C. H. K., Martinović, M., Bale, S. D., Kasper, J. C., and Raouafi, N. E. (2020). Turbulence Characteristics of Switchback and Nonswitchback Intervals Observed by Parker Solar Probe. , 904(2):L30. 86, 186

Bowen, T. A., Badman, S., Hellinger, P., and Bale, S. D. (2018a). Density Fluctuations in the Solar Wind Driven by Alfvén Wave Parametric Decay. , 854(2):L33. 68, 206, 216

Bowen, T. A., Badman, S. T., Bale, S. D., de Wit, T. D., Horbury, T. S., Klein, K. G., Larson, D., Mallet, A., Matteini, L., McManus, M. D., and Squire, J. (2021). Nonlinear interactions in spherically polarized alfvénic turbulence. 69, 71, 206, 229, 230, 234

Bowen, T. A., Bale, S. D., Bonnell, J. W., Dudok de Wit, T., Goetz, K., Goodrich, K., Gruesbeck, J., Harvey, P. R., Jannet, G., Koval, A., MacDowall, R. J., Malaspina, D. M., Pulupa, M., Revillet, C., Sheppard, D., and Szabo, A. (2020a). A merged search-coil and fluxgate magnetometer data product for parker solar probe fields. *Journal of Geophysical Research: Space Physics*, 125(5):e2020JA027813. e2020JA027813 10.1029/2020JA027813. 101, 153

Bowen, T. A., Bale, S. D., Bonnell, J. W., Dudok de Wit, T., Goetz, K., Goodrich, K., Gruesbeck, J., Harvey, P. R., Jannet, G., Koval, A., MacDowall, R. J., Malaspina, D. M., Pulupa, M., Revillet, C., Sheppard, D., and Szabo, A. (2020b). A merged search-coil and fluxgate magnetometer data product for parker solar probe fields. *Journal of Geophysical Research: Space Physics*, 125(5):e2020JA027813. e2020JA027813 10.1029/2020JA027813. 166

Bowen, T. A., Bale, S. D., Chandran, B. D. G., Chasapis, A., Chen, C. H. K., de Wit, T. D., Mallet, A., Meyrand, R., and Squire, J. (2023). Mediation of collisionless turbulent dissipation through cyclotron resonance. 69, 193, 195, 244

Bowen, T. A., Mallet, A., Bale, S. D., Bonnell, J. W., Case, A. W., Chandran, B. D. G., Chasapis, A., Chen, C. H. K., Duan, D., Dudok de Wit, T., Goetz, K., Halekas, J. S., Harvey, P. R., Kasper, J. C., Korreck, K. E., Larson, D., Livi, R., MacDowall, R. J., Malaspina, D. M., McManus, M. D., Pulupa, M., Stevens, M., and Whittlesey, P. (2020c). Constraining Ion-Scale Heating and Spectral Energy Transfer in Observations of Plasma Turbulence. *Phys. Rev. Lett.*, 125(2):025102. Publisher: American Physical Society. 131

Bowen, T. A., Mallet, A., Bale, S. D., Bonnell, J. W., Case, A. W., Chandran, B. D. G., Chasapis, A., Chen, C. H. K., Duan, D., Dudok de Wit, T., Goetz, K., Halekas, J. S., Harvey, P. R., Kasper, J. C., Korreck, K. E., Larson, D., Livi, R., MacDowall, R. J., Malaspina, D. M., McManus, M. D., Pulupa, M., Stevens, M., and Whittlesey, P. (2020a). Constraining Ion-Scale Heating and Spectral Energy Transfer in Observations of Plasma Turbulence. , 125(2):025102. 172

Bowen, T. A., Mallet, A., Bonnell, J. W., and Bale, S. D. (2018b). Impact of Residual Energy on Solar Wind Turbulent Spectra. , 865(1):45. 69, 94, 96, 180, 206, 216

Bowen, T. A., Mallet, A., Huang, J., Klein, K. G., Malaspina, D. M., Stevens, M., Bale, S. D., Bonnell, J. W., Case, A. W., Chandran, B. D. G., Chaston, C. C., Chen, C. H. K., Dudok de Wit, T., Goetz, K., Harvey, P. R., Howes, G. G., Kasper, J. C., Korreck, K. E., Larson, D., Livi, R., MacDowall, R. J., McManus, M. D., Pulupa, M., Verniero, J. L., and Whittlesey, P. (2020b). Ion-scale Electromagnetic Waves in the Inner Heliosphere. , 246(2):66. 193

Bretherton, F. P. and Garrett, C. J. R. (1968). Wavetrains in inhomogeneous moving media. *Proceedings of the Royal Society of London. Series A. Mathematical and Physical Sciences*, 302(1471):529–554. 65

Bruno, R., Bavassano, B., Bianchini, L., Pietropaolo, E., Villante, U., Carbone, V., and Veltri, P. (1999). Solar Wind Intermittency Studied via Local Intermittency Measure. In Wilson, A. and et al., editors, *Magnetic Fields and Solar Processes*, volume 9 of *ESA Special Publication*, page 1147. 82

Bruno, R. and Carbone, V. (2013). The Solar Wind as a Turbulence Laboratory. *Living Reviews in Solar Physics*, 10(1):2. 2, 56, 68, 69, 231

Bruno, R., Carbone, V., Sorriso-Valvo, L., and Bavassano, B. (2003). Radial evolution of solar wind intermittency in the inner heliosphere. *Journal of Geophysical Research (Space Physics)*, 108(A3):1130. _eprint: astro-ph/0303578. 68, 69, 103, 121, 141, 175, 215, 247

Bruno, R., Carbone, V., Veltri, P., Pietropaolo, E., and Bavassano, B. (2001). Identifying intermittency events in the solar wind. , 49(12):1201–1210. 66, 70

Burch, J. L., Moore, T. E., Torbert, R. B., and Giles, B. L. (2016). Magnetospheric Multiscale Overview and Science Objectives. , 199:5–21. 58

Burlaga, L. F. (1991). Intermittent turbulence in the solar wind. , 96(A4):5847–5851. 49

Burlaga, L. F. and Ogilvie, K. W. (1970). Magnetic and Thermal Pressures in the Solar Wind. , 15(1):61–71. 216, 217

Butterworth, S. (1930). On the theory of filter amplifiers. the wireless engineer. *From 1923 to 1930, the journal was called Experimental Wireless and the Radio Engineer*, 7:536–541. 177

Castaing, B., Gagne, Y., and Hopfinger, E. J. (1990). Velocity probability density functions of high Reynolds number turbulence. *Physica D Nonlinear Phenomena*, 46(2):177–200. 49, 121

Cerri, S. S. and Califano, F. (2017). Reconnection and small-scale fields in 2D-3V hybrid-kinetic driven turbulence simulations. , 19(2):025007. 192

Cerri, S. S., Grošelj, D., and Franci, L. (2019). Kinetic plasma turbulence: recent insights and open questions from 3D3V simulations. *Frontiers in Astronomy and Space Sciences*, 6:64. 173, 176

Cerri, S. S., Passot, T., Laveder, D., Sulem, P. L., and Kunz, M. W. (2022). Turbulent Regimes in Collisions of 3D Alfvén-wave Packets. , 939(1):36. 48, 185, 192, 204, 238, 239

Chandran, B. D. G. (2005). Weak Compressible Magnetohydrodynamic Turbulence in the Solar Corona. , 95(26):265004. 68, 70, 187

Chandran, B. D. G. (2008). Strong Anisotropic MHD Turbulence with Cross Helicity. , 685(1):646–658. 68, 180, 206

Chandran, B. D. G. (2018). Parametric instability, inverse cascade and the $1/f$ range of solar-wind turbulence. *Journal of Plasma Physics*, 84(1):905840106. xxii, 67, 70, 111, 118, 235, 238, 246

Chandran, B. D. G. and Perez, J. C. (2019). Reflection-driven magnetohydrodynamic turbulence in the solar atmosphere and solar wind. *Journal of Plasma Physics*, 85(4):905850409. 42, 86, 181, 185, 230

Chandran, B. D. G., Schekochihin, A. A., and Mallet, A. (2015). INTERMITTENCY AND ALIGNMENT IN STRONG RMHD TURBULENCE. *The Astrophysical Journal*, 807(1):39. Publisher: American Astronomical Society. xix, 48, 51, 53, 68, 70, 82, 162, 174, 175, 178, 179, 181, 182, 187, 188, 196, 197, 199, 200, 204, 205, 230, 231, 232, 237, 240, 242, 248

Chandran, B. D. G., Schekochihin, A. A., and Mallet, A. (2015). Intermittency and Alignment in Strong RMHD Turbulence. , 807(1):39. 86, 119, 163, 181, 206, 230

Chasapis, A., Retinò, A., Sahraoui, F., Vaivads, A., Khotyaintsev, Y. V., Sundkvist, D., Greco, A., Sorriso-Valvo, L., and Canu, P. (2015). Thin Current Sheets and Associated Electron Heating in Turbulent Space Plasma. , 804:L1. 150

Chasapis, A., Retinò, A., Sahraoui, F., Vaivads, A., Khotyaintsev, Y. V., Sundkvist, D., Greco, A., Sorriso-Valvo, L., and Canu, P. (2015). Thin Current Sheets and Associated Electron Heating in Turbulent Space Plasma. *apjl*, 804:L1. 69, 82

Chen, C. H. K. (2016a). Recent progress in astrophysical plasma turbulence from solar wind observations. *Journal of Plasma Physics*, 82(6):535820602. 2, 42, 183

Chen, C. H. K. (2016b). Recent progress in astrophysical plasma turbulence from solar wind observations. *Journal of Plasma Physics*, 82(6):535820602. _eprint: 1611.03386. 69

Chen, C. H. K., Bale, S. D., Bonnell, J. W., Borovikov, D., Bowen, T. A., Burgess, D., Case, A. W., Chandran, B. D. G., Wit, T. D. d., Goetz, K., Harvey, P. R., Kasper, J. C., Klein, K. G., Korreck, K. E., Larson, D., Livi, R., MacDowall, R. J., Malaspina, D. M., Mallet, A., McManus, M. D., Moncuquet, M., Pulupa, M., Stevens, M. L., and Whittlesey, P. (2020). The Evolution and Role of Solar Wind Turbulence in the Inner Heliosphere. *The Astrophysical Journal Supplement Series*, 246(2):53. Publisher: American Astronomical Society. 68, 69, 71, 87, 93, 100, 121, 144, 245

Chen, C. H. K., Bale, S. D., Salem, C. S., and Maruca, B. A. (2013). Residual Energy Spectrum of Solar Wind Turbulence. , 770(2):125. 68, 69, 94, 205, 234

Chen, C. H. K., Bale, S. D., Salem, C. S., and Maruca, B. A. (2013). Residual energy spectrum of solar wind turbulence. *The Astrophysical Journal*, 770(2):125. 179

Chen, C. H. K., Bale, S. D., Salem, C. S., and Maruca, B. A. (2013). Residual Energy Spectrum of Solar Wind Turbulence. , 770(2):125. 206, 212

Chen, C. H. K., Chandran, B. D. G., Woodham, L. D., Jones, S. I., Perez, J. C., Bourouaine, S., Bowen, T. A., Klein, K. G., Moncuquet, M., Kasper, J. C., and Bale, S. D. (2021). The near-Sun streamer belt solar wind: turbulence and solar wind acceleration. *åp*, 650:L3. _eprint: 2101.00246. 86

Chen, C. H. K., Horbury, T. S., Schekochihin, A. A., Wicks, R. T., Alexandrova, O., and Mitchell, J. (2010). Anisotropy of solar wind turbulence between ion and electron scales. *Phys. Rev. Lett.*, 104:255002. 99

Chen, C. H. K., Leung, L., Boldyrev, S., Maruca, B. A., and Bale, S. D. (2014a). Ion-scale spectral break of solar wind turbulence at high and low beta. , 41(22):8081–8088. 95

Chen, C. H. K., Mallet, A., Schekochihin, A. A., Horbury, T. S., Wicks, R. T., and Bale, S. D. (2012). Three-dimensional Structure of Solar Wind Turbulence. , 758(2):120. 68, 163, 173, 189, 190, 205, 221, 230, 234

Chen, C. H. K., Mallet, A., Yousef, T. A., Schekochihin, A. A., and Horbury, T. S. (2011). Anisotropy of Alfvénic turbulence in the solar wind and numerical simulations. , 415(4):3219–3226. 46, 79, 96, 239

Chen, C. H. K., Sorriso-Valvo, L., Šafránková, J., and Němeček, Z. (2014b). Intermittency of Solar Wind Density Fluctuations From Ion to Electron Scales. , 789(1):L8. 176

Chhiber, R. (2022). Anisotropic magnetic turbulence in the inner heliosphere—radial evolution of distributions observed by parker solar probe. *The Astrophysical Journal*, 939(1):33. 43

Chhiber, R., Goldstein, M. L., Maruca, B. A., Chasapis, A., Matthaeus, W. H., Ruffolo, D., Bandyopadhyay, R., Parashar, T. N., Qudsi, R., de Wit, T. D., Bale, S. D., Bonnell, J. W., Goetz, K., Harvey, P. R., MacDowall, R. J., Malaspina, D., Pulupa, M., Kasper, J. C., Korreck, K. E., Case, A. W., Stevens, M., Whittlesey, P., Larson, D., Livi, R., Velli, M., and Raouafi, N. (2020a). Clustering of intermittent magnetic and flow structures near parker solar probe's first perihelion—a partial-variance-of-increments analysis. *The Astrophysical Journal Supplement Series*, 246(2):31. 155, 156, 159, 176

Chhiber, R., Goldstein, M. L., Maruca, B. A., Chasapis, A., Matthaeus, W. H., Ruffolo, D., Bandyopadhyay, R., Parashar, T. N., Qudsi, R., Wit, T. D. d., Bale, S. D., Bonnell, J. W., Goetz, K., Harvey, P. R., MacDowall, R. J., Malaspina, D., Pulupa, M., Kasper, J. C., Korreck, K. E., Case, A. W., Stevens, M., Whittlesey, P., Larson, D., Livi, R., Velli, M., and Raouafi, N. (2020b). Clustering of Intermittent Magnetic and Flow Structures near Parker Solar Probe's First Perihelion—A Partial-variance-of-increments Analysis. *The Astrophysical Journal Supplement Series*, 246(2):31. Publisher: American Astronomical Society. 51, 82, 153

Chhiber, R., Matthaeus, W. H., Bowen, T. A., and Bale, S. D. (2021a). Subproton-scale Intermittency in Near-Sun Solar Wind Turbulence Observed by the Parker Solar Probe. , 911(1):L7. 176, 179, 180, 215

Chhiber, R., Matthaeus, W. H., Oughton, S., and Parashar, T. N. (2020). A detailed examination of anisotropy and timescales in three-dimensional incompressible magnetohydrodynamic turbulence. *Physics of Plasmas*, 27(6):062308. 183

Chhiber, R., Matthaeus, W. H., Usmanov, A. V., Bandyopadhyay, R., and Goldstein, M. L. (2022). An extended and fragmented Alfvén zone in the Young Solar Wind. *Monthly Notices of the Royal Astronomical Society*, 513(1):159–167. 122

Chhiber, R., Usmanov, A. V., Matthaeus, W. H., and Goldstein, M. L. (2021b). Large-scale Structure and Turbulence Transport in the Inner Solar Wind: Comparison of Parker Solar Probe's First Five Orbits with a Global 3D Reynolds-averaged MHD Model. , 923(1):89. 148

Chiuderi, C. and Velli, M. (2015). *Basics of Plasma Astrophysics*. 16, 28

Cho, J. (2019). A Technique for Removing Large-scale Variations in Regularly and Irregularly Spaced Data. , 874(1):75. 164, 244

Cho, J. and Lazarian, A. (2003). Compressible magnetohydrodynamic turbulence: mode coupling, scaling relations, anisotropy, viscosity-damped regime and astrophysical implications. , 345(12):325–339. 70, 187

Cho, J. and Vishniac, E. T. (2000). The Anisotropy of Magnetohydrodynamic Alfvénic Turbulence. , 539(1):273–282. 45, 46, 99

Coleman, Paul J., J. (1968). Turbulence, Viscosity, and Dissipation in the Solar-Wind Plasma. *apj*, 153:371. 64, 68, 86

Comisso, L., Huang, Y. M., Lingam, M., Hirvijoki, E., and Bhattacharjee, A. (2018). Magnetohydrodynamic Turbulence in the Plasmoid-mediated Regime. , 854(2):103. 187

Coppi, B., Galvao, R., Pellat, R., Rosenbluth, M., and Rutherford, P. (1976). Resistive internal kink modes. *Soviet Journal of Plasma Physics*, 2:533–535. 192, 237

Cranmer, S. R. and van Ballegooijen, A. A. (2005). On the Generation, Propagation, and Reflection of Alfvén Waves from the Solar Photosphere to the Distant Heliosphere. *apjs*, 156(2):265–293. _eprint: astro-ph/0410639. 66

Cuesta, M. E., Chhiber, R., Roy, S., Goodwill, J., Pecora, F., Jarosik, J., Matthaeus, W. H., Parashar, T. N., and Bandyopadhyay, R. (2022). Isotropization and Evolution of Energy-containing Eddies in Solar Wind Turbulence: Parker Solar Probe, Helios 1, ACE, WIND, and Voyager 1. , 932(1):L11. 78, 194

Cuesta, M. E., Chhiber, R., Roy, S., Goodwill, J., Pecora, F., Jarosik, J., Matthaeus, W. H., Parashar, T. N., and Bandyopadhyay, R. (2022a). Isotropization and evolution of energy-containing eddies in solar wind turbulence: Parker solar probe, helios 1, ace, wind, and voyager 1. 148

Cuesta, M. E., Parashar, T. N., Chhiber, R., and Matthaeus, W. H. (2022b). Intermittency in the Expanding Solar Wind: Observations from Parker Solar Probe (0.16 au), Helios 1 (0.3–1 au), and Voyager 1 (1–10 au). *The Astrophysical Journal Supplement Series*, 259(1):23. Publisher: American Astronomical Society. 87, 122, 148, 247

D'Amicis, R., Alielden, K., Perrone, D., Bruno, R., Telloni, D., Raines, J. M., Lepri, S. T., and Zhao, L. (2021). Solar wind Alfvénicity during solar cycle 23 and 24. Perspective for future observations with Parker Solar Probe and Solar Orbiter. , 654:A111. 70

D'Amicis, R., Matteini, L., and Bruno, R. (2019). On the slow solar wind with high Alfvénicity: from composition and microphysics to spectral properties. , 483(4):4665–4677. 69

D'Amicis, R., Perrone, D., Velli, M., Sorriso-Valvo, L., Telloni, D., Bruno, R., and De Marco, R. (2022). Investigating Alfvénic Turbulence in Fast and Slow Solar Wind Streams. *Universe*, 8(7):352. 180

Dasso, S., Milano, L. J., Matthaeus, W. H., and Smith, C. W. (2005). Anisotropy in Fast and Slow Solar Wind Fluctuations. , 635(2):L181–L184. 108

Davies, L. and Gather, U. (1993a). The Identification of Multiple Outliers. *Journal of the American Statistical Association*, 88(423):782–792. Publisher: Taylor & Francis _eprint: https://www.tandfonline.com/doi/pdf/10.1080/01621459.1993.10476339. 88, 103, 126

Davies, L. and Gather, U. (1993b). The identification of multiple outliers. *Journal of the American Statistical Association*, 88(423):782–792. 152

Davis, N., Chandran, B. D. G., Bowen, T. A., Badman, S. T., de Wit, T. D., Chen, C. H. K., Bale, S. D., Huang, Z., Sioulas, N., and Velli, M. (2023). The Evolution of the 1/f Range within a Single Fast-solar-wind Stream between 17.4 and 45.7 Solar Radii. , 950(2):154. 111, 169

DeForest, C. E., Howard, R. A., Velli, M., Viall, N., and Vourlidas, A. (2018). The Highly Structured Outer Solar Corona. *apj*, 862(1):18. 121

Del Zanna, L., Velli, M., and Londrillo, P. (2001). Parametric decay of circularly polarized Alfvén waves: Multidimensional simulations in periodic and open domains. , 367:705–718. 67

Dmitruk, P., Matthaeus, W. H., and Oughton, S. (2005). Direct comparisons of compressible magnetohydrodynamics and reduced magnetohydrodynamics turbulence. *Physics of Plasmas*, 12(11):112304. 47

Dmitruk, P., Matthaeus, W. H., and Seenu, N. (2004). Test Particle Energization by Current Sheets and Nonuniform Fields in Magnetohydrodynamic Turbulence. *apj*, 617(1):667–679. 69

Dobrowolny, M., Mangeney, A., and Veltri, P. (1980). Fully Developed Anisotropic Hydromagnetic Turbulence in Interplanetary Space. *Phys. Rev. Lett.*, 45(2):144–147. Publisher: American Physical Society. 48

Dong, C., Wang, L., Huang, Y.-M., Comisso, L., Sandstrom, T. A., and Bhattacharjee, A. (2022). Reconnection-driven energy cascade in magnetohydrodynamic turbulence. *Science Advances*, 8(49):eabn7627. 43, 47, 192, 205

Dong, Y., Verdini, A., and Grappin, R. (2014). Evolution of turbulence in the expanding solar wind, a numerical study. *The Astrophysical Journal*, 793(2):118. 67, 71, 190, 206, 232

Drake, J. F., Agapitov, O., Swisdak, M., Badman, S. T., Bale, S. D., Horbury, T. S., Kasper, J. C., MacDowall, R. J., Mozer, F. S., Phan, T. D., Pulupa, M., Szabo, A., and Velli, M. (2021). Switchbacks as signatures of magnetic flux ropes generated by interchange reconnection in the corona. , 650:A2. 66

Duan, D., He, J., Bowen, T. A., Woodham, L. D., Wang, T., Chen, C. H. K., Mallet, A., and Bale, S. D. (2021). Anisotropy of solar wind turbulence in the inner heliosphere at kinetic scales: PSP observations. *The Astrophysical Journal Letters*, 915(1):L8. 78, 90, 95, 105, 173, 193

Dudok de Wit, T., Alexandrova, O., Furno, I., Sorriso-Valvo, L., and Zimbardo, G. (2013). Methods for Characterising Microphysical Processes in Plasmas. , 178(2-4):665–693. 108, 130, 195, 196

Dudok de Wit, T., Krasnoselskikh, V. V., Bale, S. D., Bonnell, J. W., Bowen, T. A., Chen, C. H. K., Froment, C., Goetz, K., Harvey, P. R., Jagarlamudi, V. K., Larosa, A., MacDowall, R. J., Malaspina, D. M., Matthaeus, W. H., Pulupa, M., Velli, M., and Whittlesey, P. L. (2020). Switchbacks in the Near-Sun Magnetic Field: Long Memory and Impact on the Turbulence Cascade. , 246(2):39. 156

Dunn, C., Bowen, T., Mallet, A., Badman, S., and Bale, S. (2023). Effect of Spherical Polarization on the Magnetic Spectrum of the Solar Wind. *arXiv e-prints*, page arXiv:2305.09763. 71

D'Amicis, R. and Bruno, R. (2015). On the origin of highly alfvÉnic slow solar wind. *The Astrophysical Journal*, 805(1):84. 57, 69

D'Amicis, R., Perrone, D., Bruno, R., and Velli, M. (2021). On alfvénic slow wind: A journey from the earth back to the sun. *Journal of Geophysical Research: Space Physics*, 126(4):e2020JA028996. e2020JA028996 2020JA028996. 57

Elsasser, W. M. (1950). The hydromagnetic equations. *Phys. Rev.*, 79:183–183. 34, 202

Ervin, T., Bale, S. D., Badman, S. T., Bowen, T. A., Riley, P., Paulson, K., Rivera, Y. J., Romeo, O., Sioulas, N., Larson, D. E., Verniero, J. L., Dewey, R. M., and Huang, J. (2024). Near subsonic solar wind outflow from an active region. *arXiv e-prints*, page arXiv:2405.15844. 224, 234

Escoubet, C. P., Fehringer, M., and Goldstein, M. (2001). Introduction: The Cluster mission. *Annales Geophysicae*, 19:1197–1200. 58

Feller, W. (1968). *An Introduction to Probability Theory and Its Applications*, volume 1. Wiley. 12

Fisk, L. A. and Kasper, J. C. (2020). Global Circulation of the Open Magnetic Flux of the Sun. , 894(1):L4. 66

Fox, N. J., Velli, M. C., Bale, S. D., Decker, R., Driesman, A., Howard, R. A., Kasper, J. C., Kinnison, J., Kusterer, M., Lario, D., Lockwood, M. K., McComas, D. J., Raouafi, N. E., and Szabo, A. (2016). The Solar Probe Plus Mission: Humanity's First Visit to Our Star. *ßr*, 204(1-4):7–48. 2, 69, 87, 122, 150, 162

Franci, L., Cerri, S. S., Califano, F., Landi, S., Papini, E., Verdini, A., Matteini, L., Jenko, F., and Hellinger, P. (2017). Magnetic Reconnection as a Driver for a Sub-ion-scale Cascade in Plasma Turbulence. , 850:L16. 192

Franz, M. and Harper, D. (2002). Heliospheric coordinate systems. *Planetary and Space Science*, 50(2):217–233. 81

Fredricks, R. W. and Coroniti, F. V. (1976). Ambiguities in the deduction of rest frame fluctuation spectrums from spectrums computed in moving frames. , 81(A31):5591–5595. 61

Frisch, U. (1995). *Turbulence: The Legacy of A.N. Kolmogorov*. Publication Title: Astrophysical Letters and Communications. 9, 10, 49, 50, 84, 85, 121, 175

Frisch, U., Sulem, P. L., and Nelkin, M. (1978). A simple dynamical model of intermittent fully developed turbulence. *Journal of Fluid Mechanics*, 87:719–736. 51

Furth, H. P., Killeen, J., and Rosenbluth, M. N. (1963). Finite-Resistivity Instabilities of a Sheet Pinch. *The Physics of Fluids*, 6(4):459–484. 191, 237

Galeev, A. A. and Oraevskii, V. N. (1963a). The Stability of Alfvén Waves. *Soviet Physics Doklady*, 7:988. 111

Galeev, A. A. and Oraevskii, V. N. (1963b). The Stability of Alfvén Waves. *Soviet Physics Doklady*, 7:988. 246

Galtier, S., Nazarenko, S. V., Newell, A. C., and Pouquet, A. (2000). A weak turbulence theory for incompressible magnetohydrodynamics. *Journal of Plasma Physics*, 63(5):447–488. 99, 203

Galtier, S., Pouquet, A., and Mangeney, A. (2005). On spectral scaling laws for incompressible anisotropic magnetohydrodynamic turbulence. *Physics of Plasmas*, 12(9):092310. 203

Gerick, F., Saur, J., and von Papen, M. (2017). The uncertainty of local background magnetic field orientation in anisotropic plasma turbulence. *The Astrophysical Journal*, 843(1):5. 45, 46, 77, 78, 99

Gogoberidze, G. (2007). On the nature of incompressible magnetohydrodynamic turbulence. *Physics of Plasmas*, 14(2):022304–022304. 203

Gogoberidze, G., Chapman, S. C., Hnat, B., and Dunlop, M. W. (2012). Impact of measurement uncertainties on universal scaling of MHD turbulence. , 426(2):951–955. 234

Goldreich, P. and Sridhar, S. (1995). Toward a Theory of Interstellar Turbulence. II. Strong Alfvenic Turbulence. *apj*, 438:763. xi, 44, 46, 47, 68, 86, 99, 179, 180, 203

Goldreich, P. and Sridhar, S. (1997). Magnetohydrodynamic Turbulence Revisited. *apj*, 485(2):680–688. _eprint: astro-ph/9612243. 86, 99, 118

Goldstein, M. L. (1978). An instability of finite amplitude circularly polarized Afvén waves. , 219:700–704. 246

Goldstein, M. L., Roberts, D. A., and Matthaeus, W. H. (1989). Numerical simulation of interplanetary and magnetospheric phenomena: the Kelvin-Helmholtz instability. *Geophysical Monograph Series*, 54:113–125. 186, 239

Grappin, R. and Velli, M. (1996a). Waves and streams in the expanding solar wind. , 101(A1):425–444. 65

Grappin, R. and Velli, M. (1996b). Waves and streams in the expanding solar wind. , 101(A1):425–444. 67, 71

Grappin, R., Velli, M., and Mangeney, A. (1991). "Alfvénic" versus "standard" turbulence in the solar wind. *Annales Geophysicae*, 9:416–426. 69

Grappin, R., Velli, M., and Mangeney, A. (1993). Nonlinear wave evolution in the expanding solar wind. *Phys. Rev. Lett.*, 70:2190–2193. 67, 71

Grappin, R., Verdini, A., and Müller, W.-C. (2022). Modeling the solar wind turbulent cascade including cross helicity: With and without expansion. *The Astrophysical Journal*, 933(2):246. 181

Grauer, R., Krug, J. H. A., and Marliani, C. (1994). Scaling of high-order structure functions in magnetohydrodynamic turbulence. *Physics Letters A*, 195:335–338. 51

Greco, A., Chuychai, P., Matthaeus, W. H., Servidio, S., and Dmitruk, P. (2008). Intermittent MHD structures and classical discontinuities. *Geophysical Research Letters*, 35(19). _eprint: https://agupubs.onlinelibrary.wiley.com/doi/pdf/10.1029/2008GL035454. 82, 133, 142, 160, 208

Greco, A., Matthaeus, W. H., D'Amicis, R., Servidio, S., and Dmitruk, P. (2012a). EVIDENCE FOR NONLINEAR DEVELOPMENT OF MAGNETOHYDRODYNAMIC SCALE INTERMITTENCY IN THE INNER HELIOSPHERE. *The Astrophysical Journal*, 749(2):105. Publisher: American Astronomical Society. 69, 122

Greco, A., Matthaeus, W. H., Perri, S., Osman, K. T., Servidio, S., Wan, M., and Dmitruk, P. (2018). Partial Variance of Increments Method in Solar Wind Observations and Plasma Simulations. *ßr*, 214(1):1. 83, 178

Greco, A., Matthaeus, W. H., Servidio, S., and Dmitruk, P. (2009). Waiting-time distributions of magnetic discontinuities: Clustering or poisson process? *Phys. Rev. E*, 80:046401. 155

Greco, A., Perri, S., and Zimbardo, G. (2010). Stochastic Fermi acceleration in the magnetotail current sheet: A numerical study. *Journal of Geophysical Research: Space Physics*, 115(A2). _eprint: https://agupubs.onlinelibrary.wiley.com/doi/pdf/10.1029/2009JA014690. 51

Greco, A., Perri, S., and Zimbardo, G. (2010). Stochastic Fermi acceleration in the magnetotail current sheet: A numerical study. *Journal of Geophysical Research (Space Physics)*, 115:A02203. 155

Greco, A., Valentini, F., Servidio, S., and Matthaeus, W. H. (2012b). Inhomogeneous kinetic effects related to intermittent magnetic discontinuities. *Phys. Rev. E*, 86:066405. 160

Gurland, J. and Tripathi, R. C. (1971a). A simple approximation for unbiased estimation of the standard deviation. *The American Statistician*, 25(4):30–32. 51, 109, 157

Gurland, J. and Tripathi, R. C. (1971b). A Simple Approximation for Unbiased Estimation of the Standard Deviation. *The American Statistician*, 25(4):30–32. Publisher: [American Statistical Association, Taylor & Francis, Ltd.]. 127

Hada, T., Koga, D., and Yamamoto, E. (2003). Phase coherence of MHD waves in the solar wind. *ßr*, 107(1):463–466. 82

Halekas, J. S., Whittlesey, P., Larson, D. E., McGinnis, D., Maksimovic, M., Berthomier, M., Kasper, J. C., Case, A. W., Korreck, K. E., Stevens, M. L., Klein, K. G., Bale, S. D., MacDowall, R. J., Pulupa, M. P., Malaspina, D. M., Goetz, K., and Harvey, P. R. (2020). Electrons in the young solar wind: First results from the iparker solar probe/i. *The Astrophysical Journal Supplement Series*, 246(2):22. 153

He, J., Tu, C., Marsch, E., Bourouaine, S., and Pei, Z. (2013). Radial evolution of the wavevector anisotropy of solar wind turbulence between 0.3 and 1 au. *The Astrophysical Journal*, 773(1):72. 113

Heinemann, M. and Olbert, S. (1980). Non-wkb alfvén waves in the solar wind. *Journal of Geophysical Research: Space Physics*, 85(A3):1311–1327. 61, 65, 70

Hellinger, P., Matteini, L., Štverák, Š., Trávníček, P. M., and Marsch, E. (2011). Heating and cooling of protons in the fast solar wind between 0.3 and 1 AU: Helios revisited. *Journal of Geophysical Research (Space Physics)*, 116(A9):A09105. 152

Higdon, J. C. (1984). Density fluctuations in the interstellar medium: Evidence for anisotropic magnetogasdynamic turbulence. I - Model and astrophysical sites. , 285:109–123. 44, 99, 203

Hnat, B., Chapman, S. C., Gogoberidze, G., and Wicks, R. T. (2011). Scale-free texture of the fast solar wind. *Phys. Rev. E*, 84:065401. 185, 205

Hnat, B., Chapman, S. C., and Rowlands, G. (2005). Compressibility in solar wind plasma turbulence. *Phys. Rev. Lett.*, 94:204502. 69, 206

Hollweg, J. V. and Isenberg, P. A. (2007). Reflection of alfvén waves in the corona and solar wind: An impulse function approach. *Journal of Geophysical Research: Space Physics*, 112(A8). 185, 236

Horbury, T. S., Bale, S. D., McManus, M. D., Larson, D., Kasper, J. C., Laker, R., Matteini, L., Raouafi, N. E., Velli, M., Woodham, L. D., Woolley, T., Fedorov, A., Louarn, P., Kieokaew, R., Durovcova, T., Chandran, B., and Owen, C. J. (2023). Switchbacks, microstreams, and broadband turbulence in the solar wind. *Physics of Plasmas*, 30(8):082905. 197

Horbury, T. S. and Balogh, A. (1997a). Structure function measurements of the intermittent MHD turbulent cascade. *Nonlinear Processes in Geophysics*, 4(3):185–199. 51

Horbury, T. S. and Balogh, A. (1997b). Structure function measurements of the intermittent MHD turbulent cascade. *Nonlinear Processes in Geophysics*, 4(3):185–199. 180

Horbury, T. S. and Balogh, A. (2001). Evolution of magnetic field fluctuations in high-speed solar wind streams: Ulysses and Helios observations. , 106(A8):15929–15940. 190

Horbury, T. S., Forman, M., and Oughton, S. (2008). Anisotropic Scaling of Magnetohydrodynamic Turbulence. *prl*, 101(17):175005. _eprint: 0807.3713. xi, 46, 61, 68, 69, 96, 99, 113, 115, 137, 194, 203

Horbury, T. S., Matteini, L., and Stansby, D. (2018). Short, large-amplitude speed enhancements in the near-Sunfast solar wind. , 478(2):1980–1986. 66, 197

Horbury, T. S., O'Brien, H., Carrasco Blazquez, I., Bendyk, M., Brown, P., Hudson, R., Evans, V., Oddy, T. M., Carr, C. M., Beek, T. J., Cupido, E., Bhattacharya, S., Dominguez, J. A., Matthews, L., Myklebust, V. R., Whiteside, B., Bale, S. D., Baumjohann, W., Burgess, D., Carbone, V., Cargill, P., Eastwood, J., Erdös, G., Fletcher, L., Forsyth, R., Giacalone, J., Glassmeier, K. H., Goldstein, M. L., Hoeksema, T., Lockwood, M., Magnes, W., Maksimovic, M., Marsch, E., Matthaeus, W. H., Murphy, N., Nakariakov, V. M., Owen, C. J., Owens, M., Rodriguez-Pacheco, J., Richter, I., Riley, P., Russell, C. T., Schwartz, S., Vainio, R., Velli, M., Vennerstrom, S., Walsh, R., Wimmer-Schweingruber, R. F., Zank, G., Müller, D., Zouganelis, I., and Walsh, A. P. (2020). The Solar Orbiter magnetometer. *åp*, 642:A9. 88, 101, 125

Horbury, T. S., Wicks, R. T., and Chen, C. H. K. (2012). Anisotropy in Space Plasma Turbulence: Solar Wind Observations. *ssr*, 172(1-4):325–342. 43, 96

Howes, G. G. (2015). A dynamical model of plasma turbulence in the solar wind. *Philosophical Transactions of the Royal Society A: Mathematical, Physical and Engineering Sciences*, 373(2041):20140145. 51, 53, 204, 232

Howes, G. G., Bale, S. D., Klein, K. G., Chen, C. H. K., Salem, C. S., and TenBarge, J. M. (2012). The Slow-mode Nature of Compressible Wave Power in Solar Wind Turbulence. *apjl*, 753(1):L19. _eprint: 1106.4327. 70, 216, 217

Howes, G. G., Bale, S. D., Klein, K. G., Chen, C. H. K., Salem, C. S., and TenBarge, J. M. (2012). The Slow-mode Nature of Compressible Wave Power in Solar Wind Turbulence. , 753(1):L19. 216, 235

Howes, G. G., Cowley, S. C., Dorland, W., Hammett, G. W., Quataert, E., and Schekochihin, A. A. (2008). A model of turbulence in magnetized plasmas: Implications for the dissipation range in the solar wind. *Journal of Geophysical Research (Space Physics)*, 113(A5):A05103. 173

Howes, G. G., Klein, K. G., and TenBarge, J. M. (2014). Validity of the Taylor Hypothesis for Linear Kinetic Waves in the Weakly Collisional Solar Wind. , 789(2):106. 61

Huang, J., Kasper, J. C., Vech, D., Klein, K. G., Stevens, M., Martinović, M. M., Alterman, B. L., Ďurovcová, T., Paulson, K., Maruca, B. A., Qudsi, R. A., Case, A. W., Korreck, K. E., Jian, L. K., Velli, M., Lavraud, B., Hegedus, A., Bert, C. M., Holmes, J., Bale, S. D., Larson, D. E., Livi, R., Whittlesey, P., Pulupa, M., MacDowall, R. J., Malaspina, D. M., Bonnell, J. W., Harvey, P., Goetz, K., and de Wit, T. D. (2020). Proton temperature anisotropy variations in inner heliosphere estimated with the first parker solar probe observations. *The Astrophysical Journal Supplement Series*, 246(2):70. 152

Huang, S. Y., Xu, S. B., Zhang, J., Sahraoui, F., Andrés, N., He, J. S., Yuan, Z. G., Deng, X. H., Jiang, K., Wei, Y. Y., Xiong, Q. Y., Wang, Z., Yu, L., and Lin, R. T. (2022). Anisotropy of magnetic field spectra at kinetic scales of solar wind turbulence as revealed by the parker solar probe in the inner heliosphere. *The Astrophysical Journal Letters*, 929(1):L6. 114

Huang, Z., Sioulas, N., Shi, C., Velli, M., Bowen, T., Davis, N., Chandran, B. D. G., Matteini, L., Kang, N., Shi, X., Huang, J., Bale, S. D., Kasper, J. C., Larson, D. E., Livi, R., Whittlesey, P. L., Rahmati, A., Paulson, K., Stevens, M., Case, A. W., de Wit, T. D., Malaspina, D. M., Bonnell, J. W., Goetz, K., Harvey, P. R., and MacDowall, R. J. (2023). New Observations of Solar Wind 1/f Turbulence Spectrum from Parker Solar Probe. , 950(1):L8. 169

Huba, J. (2004). NRL: Plasma Formulary. page 73. 158

Iroshnikov, P. S. (1963). Turbulence of a Conducting Fluid in a Strong Magnetic Field. *Astronomicheskii Zhurnal*, 40:742. ADS Bibcode: 1963AZh....40..742I. xix, 37, 40, 50, 57, 68, 99, 174, 202

Isliker, H., Archontis, V., and Vlahos, L. (2019). Particle Acceleration and Heating in Regions of Magnetic Flux Emergence. *The Astrophysical Journal*, 882(1):57. 51

Jacques, S. A. (1977). Momentum and energy transport by waves in the solar atmosphere and solar wind. *ApJ*, 215:942–951. 65

Kadomtsev, B. B. and Pogutse, O. P. (1967). Plasma Instability Due to Particle Trapping in a Toroidal Geometry. *Soviet Journal of Experimental and Theoretical Physics*, 24:1172. 46, 202

Karimabadi, H., Roytershteyn, V., Wan, M., Matthaeus, W. H., Daughton, W., Wu, P., Shay, M., Loring, B., Borovsky, J., Leonardis, E., Chapman, S. C., and Nakamura, T. K. M. (2013). Coherent structures, intermittent turbulence, and dissipation in high-temperature plasmas. *Physics of Plasmas*, 20(1):012303. 51, 69, 150

Kasper, J. C., Abiad, R., Austin, G., Balat-Pichelin, M., Bale, S. D., Belcher, J. W., Berg, P., Bergner, H., Berthomier, M., Bookbinder, J., Brodu, E., Caldwell, D., Case, A. W., Chandran, B. D. G., Cheimets, P., Cirtain, J. W., Cranmer, S. R., Curtis, D. W., Daigneau, P., Dalton, G., Dasgupta, B., DeTomaso, D., Diaz-Aguado, M., Djordjevic, B., Donaskowski, B., Effinger, M., Florinski, V., Fox, N., Freeman, M., Gallagher, D., Gary, S. P., Gauron, T., Gates, R., Goldstein, M., Golub, L., Gordon, D. A., Gurnee, R., Guth, G., Halekas, J., Hatch, K., Heerikuisen, J., Ho, G., Hu, Q., Johnson, G., Jordan, S. P., Korreck, K. E., Larson, D., Lazarus, A. J., Li, G., Livi, R., Ludlam, M., Maksimovic, M., McFadden, J. P., Marchant, W., Maruca, B. A., McComas, D. J., Messina, L., Mercer, T., Park, S., Peddie, A. M., Pogorelov, N., Reinhart, M. J., Richardson, J. D., Robinson, M., Rosen, I., Skoug, R. M., Slagle, A., Steinberg, J. T., Stevens, M. L., Szabo, A., Taylor, E. R., Tiu, C., Turin, P., Velli, M., Webb, G., Whittlesey, P., Wright, K., Wu, S. T., and Zank, G. (2016). Solar Wind Electrons Alphas and Protons (SWEAP) Investigation: Design of the Solar Wind and Coronal Plasma Instrument Suite for Solar Probe Plus. *ßr*, 204(1-4):131–186. 101, 123, 150, 153, 168

Kasper, J. C., Abiad, R., Austin, G., Balat-Pichelin, M., Bale, S. D., Belcher, J. W., Berg, P., Bergner, H., Berthomier, M., Bookbinder, J., Brodu, E., Caldwell, D., Case, A. W., Chandran, B. D. G., Cheimets, P., Cirtain, J. W., Cranmer, S. R., Curtis, D. W., Daigneau, P., Dalton, G., Dasgupta, B., DeTomaso, D., Diaz-Aguado, M., Djordjevic, B., Donaskowski, B., Effinger, M., Florinski, V., Fox, N., Freeman, M., Gallagher, D., Gary, S. P., Gauron, T., Gates, R., Goldstein, M., Golub, L., Gordon, D. A., Gurnee, R., Guth, G., Halekas, J., Hatch, K., Heerikuisen, J., Ho, G., Hu, Q., Johnson, G., Jordan, S. P., Korreck, K. E., Larson, D., Lazarus, A. J., Li, G., Livi, R., Ludlam, M., Maksimovic, M., McFadden, J. P., Marchant, W., Maruca, B. A., McComas, D. J., Messina, L., Mercer, T., Park, S., Peddie, A. M., Pogorelov, N., Reinhart, M. J., Richardson, J. D., Robinson, M., Rosen, I., Skoug, R. M., Slagle, A., Steinberg, J. T., Stevens, M. L., Szabo, A., Taylor, E. R., Tiu, C., Turin, P., Velli, M., Webb, G., Whittlesey, P., Wright, K., Wu, S. T., and Zank, G. (2016). Solar Wind Electrons Alphas and Protons (SWEAP) Investigation: Design of the Solar Wind and Coronal Plasma Instrument Suite for Solar Probe Plus. , 204(1-4):131–186. 152

Kasper, J. C., Klein, K. G., Lichko, E., Huang, J., Chen, C. H. K., Badman, S. T., Bonnell, J., Whittlesey, P. L., Livi, R., Larson, D., Pulupa, M., Rahmati, A., Stansby,

D., Korreck, K. E., Stevens, M., Case, A. W., Bale, S. D., Maksimovic, M., Moncuquet, M., Goetz, K., Halekas, J. S., Malaspina, D., Raouafi, N. E., Szabo, A., MacDowall, R., Velli, M., Dudok de Wit, T., and Zank, G. P. (2021). Parker solar probe enters the magnetically dominated solar corona. *Phys. Rev. Lett.*, 127:255101. 122

Kellogg, P. J. and Horbury, T. S. (2005). Rapid density fluctuations in the solar wind. *Annales Geophysicae*, 23(12):3765–3773. 216

Khabarova, O., Sagitov, T., Kislov, R., and Li, G. (2021). Automated Identification of Current Sheets—A New Tool to Study Turbulence and Intermittency in the Solar Wind. *Journal of Geophysical Research (Space Physics)*, 126(8):e29099. _eprint: 2101.02804. 82

Klein, K. G. (2013). *The kinetic plasma physics of solar wind turbulence*. PhD thesis, University of Iowa. 26

Klein, K. G., Howes, G. G., and TenBarge, J. M. (2014). The Violation of the Taylor Hypothesis in Measurements of Solar Wind Turbulence. , 790(2):L20. 61

Klein, K. G., Howes, G. G., TenBarge, J. M., Bale, S. D., Chen, C. H. K., and Salem, C. S. (2012). Using Synthetic Spacecraft Data to Interpret Compressible Fluctuations in Solar Wind Turbulence. , 755(2):159. 70, 217, 235

Klein, K. G., Perez, J. C., Verscharen, D., Mallet, A., and Chandran, B. D. G. (2015). A MODIFIED VERSION OF TAYLOR's HYPOTHESIS FOR SOLAR PROBE PLUS OBSERVATIONS. *The Astrophysical Journal*, 801(1):L18. 61, 88

Klein, K.-L., Trottet, G., Samwel, S., and Malandraki, O. (2011). Particle Acceleration and Propagation in Strong Flares without Major Solar Energetic Particle Events. , 269:309–333. 65

Kolmogorov, A. (1941). The Local Structure of Turbulence in Incompressible Viscous Fluid for Very Large Reynolds' Numbers. *Akademiia Nauk SSSR Doklady*, 30:301–305. xix, 4, 41, 50, 174

Kolmogorov, A. N. (1962). A refinement of previous hypotheses concerning the local structure of turbulence in a viscous incompressible fluid at high Reynolds number. *Journal of Fluid Mechanics*, 13(1):82–85. Publisher: Cambridge University Press. 49, 50, 120, 205

Kraichnan, R. H. (1965). Inertial-range spectrum of hydromagnetic turbulence. *The Physics of Fluids*, 8(7):1385–1387. Publisher: American Institute of Physics. 37, 57, 68, 99, 202

Krishna Jagarlamudi, V., Dudok de Wit, T., Krasnoselskikh, V., and Maksimovic, M. (2019). Inherentness of Non-stationarity in Solar Wind. , 871(1):68. 152

Landi, S., Hellinger, P., and Velli, M. (2006). Heliospheric magnetic field polarity inversions driven by radial velocity field structures. , 33(14):L14101. 67

Langmuir, I. (1928). Oscillations in Ionized Gases. *Proceedings of the National Academy of Science*, 14(8):627–637. 16

Lemoine, M. (2021). Particle acceleration in strong mhd turbulence. *Phys. Rev. D*, 104:063020. 51

Lepping, R. P., Acũna, M. H., Burlaga, L. F., Farrell, W. M., Slavin, J. A., Schatten, K. H., Mariani, F., Ness, N. F., Neubauer, F. M., Whang, Y. C., Byrnes, J. B., Kennon, R. S., Panetta, P. V., Scheifele, J., and Worley, E. M. (1995). The Wind Magnetic Field Investigation. , 71(1-4):207–229. 2, 207

Lin, R. P., Anderson, K. A., Ashford, S., Carlson, C., Curtis, D., Ergun, R., Larson, D., McFadden, J., McCarthy, M., Parks, G. K., Rème, H., Bosqued, J. M., Coutelier, J., Cotin, F., D'Uston, C., Wenzel, K. P., Sanderson, T. R., Henrion, J., Ronnet, J. C., and Paschmann, G. (1995). A Three-Dimensional Plasma and Energetic Particle Investigation for the Wind Spacecraft. , 71(1-4):125–153. 207

Lithwick, Y. and Goldreich, P. (2001). Compressible Magnetohydrodynamic Turbulence in Interstellar Plasmas. , 562(1):279–296. 206

Lithwick, Y., Goldreich, P., and Sridhar, S. (2007). Imbalanced Strong MHD Turbulence. , 655(1):269–274. 68, 99, 180, 206

Lotekar, A. B., Vasko, I. Y., Phan, T., Bale, S. D., Bowen, T. A., Halekas, J., Artemyev, A. V., Khotyaintsev, Y. V., and Mozer, F. S. (2022). Kinetic-scale Current Sheets in Near-Sun Solar Wind: Properties, Scale-dependent Features and Reconnection Onset. , 929(1):58. 82, 214

Loureiro, N. F. and Boldyrev, S. (2017). Role of Magnetic Reconnection in Magnetohydrodynamic Turbulence. , 118(24):245101. 192, 238

Maksimovic, M., Bale, S. D., Berčič, L., Bonnell, J. W., Case, A. W., Dudok de Wit, T., Goetz, K., Halekas, J. S., Harvey, P. R., Issautier, K., Kasper, J. C., Korreck, K. E., Jagarlamudi, V. K., Lahmiti, N., Larson, D. E., Lecacheux, A., Livi, R., MacDowall, R. J., Malaspina, D. M., Martinović, M. M., Meyer-Vernet, N., Moncuquet, M., Pulupa, M., Salem, C., Stevens, M. L., Štverák, Š., Velli, M., and Whittlesey, P. L. (2020). Anticorrelation between the Bulk Speed and the Electron Temperature in the Pristine Solar Wind: First Results from the Parker Solar Probe and Comparison with Helios. , 246(2):62. 115

Maksimovic, M., Zouganelis, I., Chaufray, J. Y., Issautier, K., Scime, E. E., Littleton, J. E., Marsch, E., McComas, D. J., Salem, C., Lin, R. P., and Elliott, H. (2005). Radial evolution of the electron distribution functions in the fast solar wind between 0.3 and 1.5 AU. *Journal of Geophysical Research (Space Physics)*, 110(A9):A09104. 58

Malagoli, A., Bodo, G., and Rosner, R. (1996). On the Nonlinear Evolution of Magnetohydrodynamic Kelvin-Helmholtz Instabilities. , 456:708. 187, 239

Malara, F., Primavera, L., and Veltri, P. (2001). Nonlinear evolution of the parametric instability: numerical predictions versus observations in the heliosphere. *Nonlinear Processes in Geophysics*, 8(3):159–166. 146

Malara, F., Primavera, L., and Veltri, P. (2022). Parametric instability: An evolutive mechanism for the alfveacute;nic turbulence in the solar wind. *Universe*, 8(8). 111, 246

Mallet, A., Klein, K. G., Chandran, B. D. G., Grošelj, D., Hoppock, I. W., Bowen, T. A., Salem, C. S., and Bale, S. D. (2019). Interplay between intermittency and dissipation in collisionless plasma turbulence. *Journal of Plasma Physics*, 85(3):175850302. 246

Mallet, A. and Schekochihin, A. A. (2017). A statistical model of three-dimensional anisotropy and intermittency in strong Alfvénic turbulence. , 466(4):3918–3927. xix, 53, 68, 119, 162, 163, 174, 175, 179, 182, 187, 188, 196, 199, 200, 204, 205, 206, 230, 238, 248

Mallet, A., Schekochihin, A. A., and Chandran, B. D. G. (2015). Refined critical balance in strong Alfvenic turbulence. , 449:L77–L81. 48, 53, 181, 183, 187, 204, 205, 214

Mallet, A., Schekochihin, A. A., and Chandran, B. D. G. (2017). Disruption of Alfvénic turbulence by magnetic reconnection in a collisionless plasma. *Journal of Plasma Physics*, 83(6):905830609. 192, 238

Mallet, A., Schekochihin, A. A., Chandran, B. D. G., Chen, C. H. K., Horbury, T. S., Wicks, R. T., and Greenan, C. C. (2016). Measures of three-dimensional anisotropy and intermittency in strong Alfvénic turbulence. , 459(2):2130–2139. 47, 70, 181, 205

Mallet, A., Squire, J., Chandran, B. D. G., Bowen, T., and Bale, S. D. (2021). Evolution of Large-amplitude Alfvén Waves and Generation of Switchbacks in the Expanding Solar Wind. , 918(2):62. 68, 191, 206

Mangeney, A. (2001a). Intermittency in the Solar Wind Turbulence and the Haar Wavelet Transform. In Warmbein, B., editor, *Sheffield Space Plasma Meeting: Multipoint Measurements versus Theory*, volume 492 of *ESA Special Publication*, page 53. 68

Mangeney, A. (2001b). Intermittency in the Solar Wind Turbulence and the Haar Wavelet Transform. In Warmbein, B., editor, *Sheffield Space Plasma Meeting: Multipoint Measurements versus Theory*, volume 492 of *ESA Special Publication*, page 53. 180

Maron, J. and Goldreich, P. (2001). Simulations of Incompressible Magnetohydrodynamic Turbulence. , 554(2):1175–1196. 42, 44, 46, 47, 203

Marsch, E. and Liu, S. (1993). Structure functions and intermittency of velocity fluctuations in the inner solar wind. *Annales Geophysicae*, 11(4):227–238. 121

Marsch, E. and Tu, C.-Y. (1990a). On the radial evolution of MHD turbulence in the inner heliosphere. *Journal of Geophysical Research: Space Physics*, 95(A6):8211–8229. _eprint: https://agupubs.onlinelibrary.wiley.com/doi/pdf/10.1029/JA095iA06p08211. 57

Marsch, E. and Tu, C. Y. (1990b). Spectral and spatial evolution of compressible turbulence in the inner solar wind. *jgr*, 95(A8):11945–11956. 68, 69

Martinović, M. M., Klein, K. G., Huang, J., Chandran, B. D. G., Kasper, J. C., Lichko, E., Bowen, T., Chen, C. H. K., Matteini, L., Stevens, M., Case, A. W., and Bale, S. D. (2021). Multiscale Solar Wind Turbulence Properties inside and near Switchbacks Measured by the Parker Solar Probe. *The Astrophysical Journal*, 912(1):28. Publisher: American Astronomical Society. 86

Mason, J., Cattaneo, F., and Boldyrev, S. (2006). Dynamic alignment in driven magnetohydrodynamic turbulence. *Phys. Rev. Lett.*, 97:255002. 48, 82, 100, 185, 204

Matteini, L., Horbury, T. S., Neugebauer, M., and Goldstein, B. E. (2014). Dependence of solar wind speed on the local magnetic field orientation: Role of alfvénic fluctuations. *Geophysical Research Letters*, 41(2):259–265. 66, 69, 70, 103, 197, 206

Matteini, L., Tenerani, A., Landi, S., Verdini, A., Velli, M., Hellinger, P., Franci, L., Horbury, T. S., Papini, E., and Stawarz, J. E. (2024). Alfvénic fluctuations in the expanding solar wind: Formation and radial evolution of spherical polarization. *Physics of Plasmas*, 31(3):032901. 67, 189, 190, 206

Matthaeus, W. H. and Goldstein, M. L. (1982). Measurement of the rugged invariants of magnetohydrodynamic turbulence in the solar wind. *jgr*, 87(A8):6011–6028. 10, 59, 60, 69

Matthaeus, W. H. and Goldstein, M. L. (1982a). Measurement of the rugged invariants of magnetohydrodynamic turbulence in the solar wind. , 87(A8):6011–6028. 149

Matthaeus, W. H. and Goldstein, M. L. (1982b). Stationarity of magnetohydrodynamic fluctuations in the solar wind. , 87(A12):10347–10354. 152

Matthaeus, W. H., Goldstein, M. L., and Roberts, D. A. (1990). Evidence for the presence of quasi-two-dimensional nearly incompressible fluctuations in the solar wind. , 95:20673–20683. 42

Matthaeus, W. H. and Montgomery, D. (1980). Selective decay hypothesis at high mechanical and magnetic Reynolds numbers. *Annals of the New York Academy of Sciences*, 357:203–222. 51

Matthaeus, W. H., Pouquet, A., Mininni, P. D., Dmitruk, P., and Breech, B. (2008a). Rapid alignment of velocity and magnetic field in magnetohydrodynamic turbulence. *Phys. Rev. Lett.*, 100:085003. 48, 239

Matthaeus, W. H., Pouquet, A., Mininni, P. D., Dmitruk, P., and Breech, B. (2008b). Rapid alignment of velocity and magnetic field in magnetohydrodynamic turbulence. *Phys. Rev. Lett.*, 100:085003. 212

Matthaeus, W. H., Servidio, S., Dmitruk, P., Carbone, V., Oughton, S., Wan, M., and Osman, K. T. (2012). Local Anisotropy, Higher Order Statistics, and Turbulence Spectra. , 750(2):103. 46

Matthaeus, W. H. and Velli, M. (2011). Who Needs Turbulence?. A Review of Turbulence Effects in the Heliosphere and on the Fundamental Process of Reconnection. *Space Science Reviews*, 160:145–168. 2, 68, 69

Matthaeus, W. H. and Velli, M. (2011). Who Needs Turbulence?. A Review of Turbulence Effects in the Heliosphere and on the Fundamental Process of Reconnection. *Space Science Reviews*, 160:145–168. 51, 57, 122

Matthaeus, W. H., Wan, M., Servidio, S., Greco, A., Osman, K. T., Oughton, S., and Dmitruk, P. (2015). Intermittency, nonlinear dynamics and dissipation in the solar wind and astrophysical plasmas. *Philosophical Transactions of the Royal Society of London Series A*, 373(2041):20140154–20140154. 51

McComas, D. J., Bame, S. J., Barraclough, B. L., Feldman, W. C., Funsten, H. O., Gosling, J. T., Riley, P., Skoug, R., Balogh, A., Forsyth, R., Goldstein, B. E., and Neugebauer, M. (1998). Ulysses' return to the slow solar wind. , 25(1):1–4. 57

McIntyre, J. R., Chen, C. H. K., and Larosa, A. (2023a). Properties underlying the variation of the magnetic field spectral index in the inner solar wind. *The Astrophysical Journal*, 957(2):111. 180

McIntyre, J. R., Chen, C. H. K., and Larosa, A. (2023b). Properties underlying the variation of the magnetic field spectral index in the inner solar wind. 205, 221

Meyrand, R., Galtier, S., and Kiyani, K. H. (2016). Direct evidence of the transition from weak to strong magnetohydrodynamic turbulence. *Phys. Rev. Lett.*, 116:105002. 44, 116, 184

Meyrand, R., Squire, J., Mallet, A., and Chandran, B. D. G. (2023). Reflection-driven turbulence in the super-alfvénic solar wind. 181, 185

Meyrand, R., Squire, J., Schekochihin, A., and Dorland, W. (2021a). On the violation of the zeroth law of turbulence in space plasmas. *Journal of Plasma Physics*, 87(3):535870301. 182, 192, 206, 246

Meyrand, R., Squire, J., Schekochihin, A. A., and Dorland, W. (2021b). On the violation of the zeroth law of turbulence in space plasmas. *Journal of Plasma Physics*, 87(3). 161

Mininni, P. D. and Pouquet, A. (2009). Finite dissipation and intermittency in magnetohydrodynamics. *Phys. Rev. E*, 80:025401. 96

Moncuquet, M., Meyer-Vernet, N., Issautier, K., Pulupa, M., Bonnell, J. W., Bale, S. D., de Wit, T. D., Goetz, K., Griton, L., Harvey, P. R., MacDowall, R. J., Maksimovic, M., and Malaspina, D. M. (2020a). First in situ measurements of electron density and temperature from quasi-thermal noise spectroscopy with iparker solar probe/i/FIELDS. *The Astrophysical Journal Supplement Series*, 246(2):44. 88, 101, 153, 160

Moncuquet, M., Meyer-Vernet, N., Issautier, K., Pulupa, M., Bonnell, J. W., Bale, S. D., Wit, T. D. d., Goetz, K., Griton, L., Harvey, P. R., MacDowall, R. J., Maksimovic, M., and Malaspina, D. M. (2020b). First In Situ Measurements of Electron Density and Temperature from Quasi-thermal Noise Spectroscopy with Parker Solar Probe/FIELDS. *The Astrophysical Journal Supplement Series*, 246(2):44. Publisher: The American Astronomical Society. 168

Monin, A. S. and Jaglom, A. M. (1987). *Statistical fluid mechanics. 2.* MIT Pr, Cambridge, Mass., 3. print edition. xxiii, 169

Montgomery, D. and Matthaeus, W. H. (1995). Anisotropic Modal Energy Transfer in Interstellar Turbulence. , 447:706. 42, 99

Montgomery, D. and Turner, L. (1981). Anisotropic magnetohydrodynamic turbulence in a strong external magnetic field. *The Physics of Fluids*, 24(5):825–831. 42, 99

Montgomery, D. and Turner, L. (1981). Anisotropic magnetohydrodynamic turbulence in a strong external magnetic field. *Physics of Fluids*, 24(5):825–831. 194

Müller, W.-C. and Biskamp, D. (2000). Scaling properties of three-dimensional magnetohydrodynamic turbulence. *Phys. Rev. Lett.*, 84:475–478. 51

Müller, W.-C., Biskamp, D., and Grappin, R. (2003). Statistical anisotropy of magnetohydrodynamic turbulence. , 67(6):066302. 47, 203

Müller, W.-C. and Grappin, R. (2005). Spectral energy dynamics in magnetohydrodynamic turbulence. *Phys. Rev. Lett.*, 95:114502. 47, 203

Müller, D., St. Cyr, O. C., Zouganelis, I., Gilbert, H. R., Marsden, R., Nieves-Chinchilla, T., Antonucci, E., Auchère, F., Berghmans, D., Horbury, T. S., Howard, R. A., Krucker, S., Maksimovic, M., Owen, C. J., Rochus, P., Rodriguez-Pacheco, J., Romoli, M., Solanki, S. K., Bruno, R., Carlsson, M., Fludra, A., Harra, L., Hassler, D. M., Livi, S., Louarn, P., Peter, H., Schühle, U., Teriaca, L., del Toro Iniesta, J. C., Wimmer-Schweingruber, R. F., Marsch, E., Velli, M., De Groof, A., Walsh, A., and Williams, D. (2020). The Solar Orbiter mission. Science overview. *åp*, 642:A1. _eprint: 2009.00861. 2, 69, 87, 122

Neugebauer, M. and Snyder, C. W. (1966). Mariner 2 Observations of the Solar Wind, 1, Average Properties. , 71:4469. 56

Ng, C. S. and Bhattacharjee, A. (1996). Interaction of Shear-Alfven Wave Packets: Implication for Weak Magnetohydrodynamic Turbulence in Astrophysical Plasmas. , 465:845. 99

Němeček, Z., Šafránková, J., Němec, F., Ďurovcová, T., Pitňa, A., Alterman, B. L., Voitenko, Y. M., Pavlů, J., and Stevens, M. L. (2021). Spectra of temperature fluctuations in the solar wind. *Atmosphere*, 12(10):1277. 108

Oboukhov, A. M. (1962). Some specific features of atmospheric turbulence. *Journal of Fluid Mechanics*, 13:77–81. 50, 119, 205

Osman, K. T., Matthaeus, W. H., Wan, M., and Rappazzo, A. F. (2012). Intermittency and Local Heating in the Solar Wind. *Phys. Rev. Lett.*, 108(26):261102. Publisher: American Physical Society. 42, 51, 69, 96, 137, 146, 150, 157, 160, 181

Oughton, S. and Matthaeus, W. H. (2020). Critical Balance and the Physics of Magnetohydrodynamic Turbulence. , 897(1):37. 46, 183

Oughton, S., Matthaeus, W. H., and Dmitruk, P. (2017). Reduced MHD in Astrophysical Applications: Two-dimensional or Three-dimensional? , 839(1):2. 46

Oughton, S., Matthaeus, W. H., and Dmitruk, P. (2017). Reduced mhd in astrophysical applications: Two-dimensional or three-dimensional? *The Astrophysical Journal*, 839(1):2. 47

Oughton, S., Matthaeus, W. H., Wan, M., and Osman, K. T. (2015a). Anisotropy in solar wind plasma turbulence. *Philosophical Transactions of the Royal Society A: Mathematical, Physical and Engineering Sciences*, 373(2041):20140152. 96

Oughton, S., Matthaeus, W. H., Wan, M., and Osman, K. T. (2015b). Anisotropy in solar wind plasma turbulence. *Philosophical Transactions of the Royal Society A: Mathematical, Physical and Engineering Sciences*, 373(2041):20140152. 99

Oughton, S., Matthaeus, W. H., Wan, M., and Osman, K. T. (2015). Anisotropy in solar wind plasma turbulence. *Philosophical Transactions of the Royal Society of London Series A*, 373(2041):20140152–20140152. 137

Oughton, S., Priest, E. R., and Matthaeus, W. H. (1994). The influence of a mean magnetic field on three-dimensional magnetohydrodynamic turbulence. *Journal of Fluid Mechanics*, 280:95–117. 203

Owen, C. J., Bruno, R., Livi, S., Louarn, P., Al Janabi, K., Allegrini, F., Amoros, C., Baruah, R., Barthe, A., Berthomier, M., Bordon, S., Brockley-Blatt, C., Brysbaert, C., Capuano, G., Collier, M., DeMarco, R., Fedorov, A., Ford, J., Fortunato, V., Fratter, I., Galvin, A. B., Hancock, B., Heirtzler, D., Kataria, D., Kistler, L., Lepri, S. T., Lewis, G., Loeffler, C., Marty, W., Mathon, R., Mayall, A., Mele, G., Ogasawara, K., Orlandi, M., Pacros, A., Penou, E., Persyn, S., Petiot, M., Phillips, M., Přech, L., Raines, J. M., Reden, M., Rouillard, A. P., Rousseau, A., Rubiella, J., Seran, H., Spencer, A., Thomas, J. W., Trevino, J., Verscharen, D., Wurz, P., Alapide, A., Amoruso, L., André, N., Anekallu, C., Arciuli, V., Arnett, K. L., Ascolese, R., Bancroft, C., Bland, P., Brysch, M., Calvanese, R., Castronuovo, M., Čermák, I., Chornay, D., Clemens, S., Coker, J., Collinson, G., D'Amicis, R., Dandouras, I., Darnley, R., Davies, D., Davison,

G., De Los Santos, A., Devoto, P., Dirks, G., Edlund, E., Fazakerley, A., Ferris, M., Frost, C., Fruit, G., Garat, C., Génot, V., Gibson, W., Gilbert, J. A., de Giosa, V., Gradone, S., Hailey, M., Horbury, T. S., Hunt, T., Jacquey, C., Johnson, M., Lavraud, B., Lawrenson, A., Leblanc, F., Lockhart, W., Maksimovic, M., Malpus, A., Marcucci, F., Mazelle, C., Monti, F., Myers, S., Nguyen, T., Rodriguez-Pacheco, J., Phillips, I., Popecki, M., Rees, K., Rogacki, S. A., Ruane, K., Rust, D., Salatti, M., Sauvaud, J. A., Stakhiv, M. O., Stange, J., Stubbs, T., Taylor, T., Techer, J. D., Terrier, G., Thibodeaux, R., Urdiales, C., Varsani, A., Walsh, A. P., Watson, G., Wheeler, P., Willis, G., Wimmer-Schweingruber, R. F., Winter, B., Yardley, J., and Zouganelis, I. (2020). The Solar Orbiter Solar Wind Analyser (SWA) suite. *åp*, 642:A16. 88, 102, 125

Palacios, J. C., Bourouaine, S., and Perez, J. C. (2022). On the Statistics of Elsasser Increments in Solar Wind and Magnetohydrodynamic Turbulence. , 940(1):L20. 70, 180, 181, 196

Paouris, E., Stenborg, G., Linton, M. G., Vourlidas, A., Howard, R. A., and Raouafi, N. E. (2024). First Direct Imaging of a Kelvin–Helmholtz Instability by PSP/WISPR. , 964(2):139. 239

Parashar, T. N., Chasapis, A., Bandyopadhyay, R., Chhiber, R., Matthaeus, W. H., Maruca, B., Shay, M. A., Burch, J. L., Moore, T. E., Giles, B. L., Gershman, D. J., Pollock, C. J., Torbert, R. B., Russell, C. T., Strangeway, R. J., and Roytershteyn, V. (2018). Kinetic Range Spectral Features of Cross Helicity Using the Magnetospheric Multiscale Spacecraft. , 121(26):265101. 205

Parashar, T. N., Cuesta, M., and Matthaeus, W. H. (2019). Reynolds number and intermittency in the expanding solar wind: Predictions based on ivoyager/i observations. *The Astrophysical Journal*, 884(2):L57. 122, 148, 186, 230, 247

Parashar, T. N., Goldstein, M. L., Maruca, B. A., Matthaeus, W. H., Ruffolo, D., Bandyopadhyay, R., Chhiber, R., Chasapis, A., Qudsi, R., Vech, D., Roberts, D. A., Bale, S. D., Bonnell, J. W., de Wit, T. D., Goetz, K., Harvey, P. R., MacDowall, R. J., Malaspina, D., Pulupa, M., Kasper, J. C., Korreck, K. E., Case, A. W., Stevens, M., Whittlesey, P., Larson, D., Livi, R., Velli, M., and Raouafi, N. (2020). Measures of Scale-dependent Alfvénicity in the First PSP Solar Encounter. , 246(2):58. 153

Parashar, T. N., Goldstein, M. L., Maruca, B. A., Matthaeus, W. H., Ruffolo, D., Bandyopadhyay, R., Chhiber, R., Chasapis, A., Qudsi, R., Vech, D., Roberts, D. A., Bale, S. D., Bonnell, J. W., de Wit, T. D., Goetz, K., Harvey, P. R., MacDowall, R. J., Malaspina, D., Pulupa, M., Kasper, J. C., Korreck, K. E., Case, A. W., Stevens, M., Whittlesey, P., Larson, D., Livi, R., Velli, M., and Raouafi, N. (2020). Measures of scale-dependent alfvénicity in the first psp solar encounter. *The Astrophysical Journal Supplement Series*, 246(2):58. 186, 205, 230, 239

Parashar, T. N. and Matthaeus, W. H. (2016). PROPINQUITY OF CURRENT AND VORTEX STRUCTURES: EFFECTS ON COLLISIONLESS PLASMA HEATING. *The Astrophysical Journal*, 832(1):57. 160

Parashar, T. N., Shay, M. A., Cassak, P. A., and Matthaeus, W. H. (2009). Kinetic dissipation and anisotropic heating in a turbulent collisionless plasma. *Physics of Plasmas*, 16(3):032310. 150

Parker, E. N. (1958). Dynamics of the Interplanetary Gas and Magnetic Fields. *The Astrophysical Journal*, 128:664. ADS Bibcode: 1958ApJ...128..664P. 55

Parker, E. N. (1979). *Cosmical magnetic fields. Their origin and their activity*. 98

Parker, E. N. and Tidman, D. A. (1958). Suprathermal Particles. *Physical Review*, 111:1206–1211. 194, 247

Passot, T. and Sulem, P. L. (2019). Imbalanced kinetic Alfvén wave turbulence: from weak turbulence theory to nonlinear diffusion models for the strong regime. *Journal of Plasma Physics*, 85(3):905850301. 182, 192

Passot, T., Sulem, P. L., and Laveder, D. (2022). Direct kinetic Alfvén wave energy cascade in the presence of imbalance. *Journal of Plasma Physics*, 88(3):905880312. 182, 192

Passot, T., Sulem, P. L., and Tassi, E. (2018). Gyrofluid modeling and phenomenology of low-β_e Alfvén wave turbulence. *Physics of Plasmas*, 25(4):042107. 182, 192

Pecora, F., Servidio, S., Greco, A., and Matthaeus, W. H. (2021). Identification of coherent structures in space plasmas: the magnetic helicity-PVI method. *A&A*, 650:A20. 82

Perez, J. C. and Boldyrev, S. (2009a). Role of cross-helicity in magnetohydrodynamic turbulence. *Phys. Rev. Lett.*, 102:025003. 68, 206, 212, 239

Perez, J. C. and Boldyrev, S. (2009b). Role of cross-helicity in magnetohydrodynamic turbulence. *Phys. Rev. Lett.*, 102:025003. 100

Perez, J. C. and Boldyrev, S. (2009c). Role of cross-helicity in magnetohydrodynamic turbulence. *Phys. Rev. Lett.*, 102:025003. 180

Perez, J. C., Bourouaine, S., Chen, C. H. K., and Raouafi, N. E. (2021). Applicability of Taylor's hypothesis during Parker Solar Probe perihelia. , 650:A22. 61

Perez, J. C. and Chandran, B. D. G. (2013). Direct numerical simulations of reflection-driven, reduced magnetohydrodynamic turbulence from the sun to the alfvÉn critical point. *The Astrophysical Journal*, 776(2):124. xxii, 185, 237, 238

Perez, J. C., Mason, J., Boldyrev, S., and Cattaneo, F. (2012). On the energy spectrum of strong magnetohydrodynamic turbulence. *Phys. Rev. X*, 2:041005. 47, 48, 181, 185, 204

Perez, J. C., Mason, J., Boldyrev, S., and Cattaneo, F. (2014). Scaling properties of small-scale fluctuations in magnetohydrodynamic turbulence. *The Astrophysical Journal Letters*, 793(1):L13. 48, 185, 204

Perrone, D., Alexandrova, O., Mangeney, A., Maksimovic, M., Lacombe, C., Rakoto, V., Kasper, J. C., and Jovanovic, D. (2016). Compressive Coherent Structures at Ion Scales in the Slow Solar Wind. , 826(2):196. 235

Perrone, D., Stansby, D., Horbury, T. S., and Matteini, L. (2019). Radial evolution of the solar wind in pure high-speed streams: HELIOS revised observations. , 483(3):3730–3737. 142

Pi, G., PitÅa, A., Němeček, Z., Šafránková, J., Shue, J.-H., and Yang, Y.-H. (2020). Long- and Short-Term Evolutions of Magnetic Field Fluctuations in High-Speed Streams. , 295(6):84. 104, 222

Pine, Z. B., Smith, C. W., Hollick, S. J., Argall, M. R., Vasquez, B. J., Isenberg, P. A., Schwadron, N. A., Joyce, C. J., Sokół, J. M., Bzowski, M., Kubiak, M. A., Hamilton, K. E., McLaurin, M. L., and Leamon, R. J. (2020). Solar Wind Turbulence from 1 to 45 au. III. Anisotropy of Magnetic Fluctuations in the Inertial Range Using Voyager and ACE Observations. , 900(2):93. 42

Podesta, J. J. (2009). DEPENDENCE OF SOLAR-WIND POWER SPECTRA ON THE DIRECTION OF THE LOCAL MEAN MAGNETIC FIELD. *The Astrophysical Journal*, 698(2):986–999. 45, 68, 69, 77, 96, 99, 106, 107, 113, 115, 185, 205, 208, 230, 234, 242

Podesta, J. J. and Bhattacharjee, A. (2010). Theory of Incompressible Magnetohydrodynamic Turbulence with Scale-dependent Alignment and Cross-helicity. , 718(2):1151–1157. 68, 180, 206

Podesta, J. J. and Borovsky, J. E. (2010). Scale invariance of normalized cross-helicity throughout the inertial range of solar wind turbulence. *Physics of Plasmas*, 17(11):112905. 69, 96, 179, 186, 206, 234, 239

Podesta, J. J., Chandran, B. D. G., Bhattacharjee, A., Roberts, D. A., and Goldstein, M. L. (2009). Scale-dependent angle of alignment between velocity and magnetic field fluctuations in solar wind turbulence. *Journal of Geophysical Research (Space Physics)*, 114(4):A01107. xxii, 80, 177, 186, 234, 242

Politano, H. and Pouquet, A. (1995). Model of intermittency in magnetohydrodynamic turbulence. *Phys. Rev. E*, 52:636–641. 51

Pruneti, F. and Velli, M. (1997). Parametric Decay of Large Amplitude Alfven Waves in the Solar Atmosphere. In Wilson, A., editor, *Fifth SOHO Workshop: The Corona and Solar Wind Near Minimum Activity*, volume 404 of *ESA Special Publication*, page 623. 67, 246

Pucci, F. and Velli, M. (2014). Reconnection of Quasi-singular Current Sheets: The "Ideal" Tearing Mode. , 780(2):L19. 192, 237

Pulupa, M., Bale, S. D., Bonnell, J. W., Bowen, T. A., Carruth, N., Goetz, K., Gordon, D., Harvey, P. R., Maksimovic, M., Martínez-Oliveros, J. C., Moncuquet, M., Saint-Hilaire, P., Seitz, D., and Sundkvist, D. (2017). The Solar Probe Plus Radio Frequency Spectrometer: Measurement requirements, analog design, and digital signal processing. *Journal of Geophysical Research: Space Physics*, 122(3):2836–2854. _eprint: https://onlinelibrary.wiley.com/doi/pdf/10.1002/2016JA023345. 168

Qudsi, R. A., Maruca, B. A., Matthaeus, W. H., Parashar, T. N., Bandyopadhyay, R., Chhiber, R., Chasapis, A., Goldstein, M. L., Bale, S. D., Bonnell, J. W., Dudok de Wit, T., Goetz, K., Harvey, P. R., MacDowall, R. J., Malaspina, D., Pulupa, M., Kasper, J. C., Korreck, K. E., Case, A. W., Stevens, M., Whittlesey, P., Larson, D., Livi, R., Velli, M., and Raouafi, N. (2020). Observations of Heating along Intermittent Structures in the Inner Heliosphere from PSP Data. *apjs*, 246(2):46. _eprint: 1912.05483. 51, 160

Rees, A., Balogh, A., and Horbury, T. S. (2006). Small-scale solitary wave pulses observed by the Ulysses magnetic field experiment. *Journal of Geophysical Research (Space Physics)*, 111(A10):A10106. 235

Réville, V., Tenerani, A., and Velli, M. (2018). Parametric Decay and the Origin of the Low-frequency Alfvénic Spectrum of the Solar Wind. , 866(1):38. 67, 246

Reynolds, O. (1883). An Experimental Investigation of the Circumstances Which Determine Whether the Motion of Water Shall Be Direct or Sinuous, and of the Law of Resistance in Parallel Channels. [Abstract]. *Proceedings of the Royal Society of London Series I*, 35:84–99. 7

Richardson, J. D., Paularena, K. I., Lazarus, A. J., and Belcher, J. W. (1995). Radial evolution of the solar wind from imp 8 to voyager 2. *Geophysical Research Letters*, 22(4):325–328. 58

Roberts, D. A., Goldstein, M. L., Klein, L. W., and Matthaeus, W. H. (1987). Origin and evolution of fluctuations in the solar wind: Helios observations and helios-voyager comparisons. *Journal of Geophysical Research: Space Physics*, 92(A11):12023–12035. 69, 70, 186, 239

Roberts, D. A., Goldstein, M. L., Matthaeus, W. H., and Ghosh, S. (1992). Velocity shear generation of solar wind turbulence. *jgr*, 97(A11):17115–17130. 93, 121, 186, 239

Robinson, D. C. and Rusbridge, M. G. (1971). Structure of Turbulence in the Zeta Plasma. *Physics of Fluids*, 14(11):2499–2511. 202

Ruffolo, D., Matthaeus, W. H., Chhiber, R., Usmanov, A. V., Yang, Y., Bandyopadhyay, R., Parashar, T. N., Goldstein, M. L., DeForest, C. E., Wan, M., Chasapis, A., Maruca, B. A., Velli, M., and Kasper, J. C. (2020). Shear-driven Transition to Isotropically Turbulent Solar Wind Outside the Alfvén Critical Zone. , 902(2):94. 186, 239

Russell, C. T., Luhmann, J. G., and Strangeway, R. J. (2016). *Space Physics: An Introduction*. Cambridge University Press. 56

Ruzmaikin, A. A., Feynman, J., Goldstein, B. E., Smith, E. J., and Balogh, A. (1995). Intermittent turbulence in solar wind from the south polar hole. , 100(A3):3395–3404. 51

Sahraoui, F., Goldstein, M. L., Robert, P., and Khotyaintsev, Y. V. (2009). Evidence of a Cascade and Dissipation of Solar-Wind Turbulence at the Electron Gyroscale. , 102(23):231102. 172

Salem, C., Mangeney, A., Bale, S. D., and Veltri, P. (2009). Solar Wind Magnetohydrodynamics Turbulence: Anomalous Scaling and Role of Intermittency. , 702(1):537–553. 68, 180, 206

Schekochihin, A. A. (2022). MHD turbulence: a biased review. *Journal of Plasma Physics*, 88(5):155880501. 2, 48, 54, 68, 69, 99, 180, 184, 186, 204, 206, 240

Schekochihin, A. A., Cowley, S. C., Dorland, W., Hammett, G. W., Howes, G. G., Quataert, E., and Tatsuno, T. (2009a). ASTROPHYSICAL GYROKINETICS: KINETIC AND FLUID TURBULENT CASCADES IN MAGNETIZED WEAKLY COLLISIONAL PLASMAS. *The Astrophysical Journal Supplement Series*, 182(1):310–377. 2, 42, 96, 99, 173

Schekochihin, A. A., Cowley, S. C., Dorland, W., Hammett, G. W., Howes, G. G., Quataert, E., and Tatsuno, T. (2009b). Astrophysical Gyrokinetics: Kinetic and Fluid Turbulent Cascades in Magnetized Weakly Collisional Plasmas. *apjs*, 182(1):310–377. _eprint: 0704.0044. 26, 44, 202

Servidio, S., Matthaeus, W. H., Shay, M. A., Cassak, P. A., and Dmitruk, P. (2009). Magnetic Reconnection in Two-Dimensional Magnetohydrodynamic Turbulence. *Physical Review Letters*, 102(11):115003. 83

Servidio, S., Valentini, F., Califano, F., and Veltri, P. (2012). Local Kinetic Effects in Two-Dimensional Plasma Turbulence. *prl*, 108(4):045001. 157, 160, 209

Shankarappa, N., Klein, K. G., and Martinović, M. M. (2023). Estimation of turbulent proton and electron heating rates via landau damping constrained by parker solar probe observations. *The Astrophysical Journal*, 946(2):85. 168, 193

She, Z.-S. and Leveque, E. (1994). Universal scaling laws in fully developed turbulence. , 72(3):336–339. 51

Shebalin, J. V., Matthaeus, W. H., and Montgomery, D. (1983). Anisotropy in mhd turbulence due to a mean magnetic field. *Journal of Plasma Physics*, 29(3):525–547. 42, 99, 194, 203

Shi, C., Panasenco, O., Velli, M., Tenerani, A., Verniero, J. L., Sioulas, N., Huang, Z., Brosius, A., Bale, S. D., Klein, K., Kasper, J., de Wit, T. D., Goetz, K., Harvey, P. R., MacDowall, R. J., Malaspina, D. M., Pulupa, M., Larson, D., Livi, R., Case, A., and Stevens, M. (2022a). Patches of magnetic switchbacks and their origins. *The Astrophysical Journal*, 934(2):152. 86, 159

Shi, C., Sioulas, N., Huang, Z., Velli, M., Tenerani, A., and Réville, V. (2023a). Evolution of MHD turbulence in the expanding solar wind: residual energy and intermittency. *arXiv e-prints*, page arXiv:2308.12376. 47, 181, 182, 200, 205, 230, 232

Shi, C., Velli, M., Lionello, R., Sioulas, N., Huang, Z., Halekas, J. S., Tenerani, A., Réville, V., Dakeyo, J.-B., Maksimović, M., and Bale, S. D. (2023b). Proton and electron temperatures in the solar wind and their correlations with the solar wind speed. *arXiv e-prints*, page arXiv:2301.00852. 115

Shi, C., Velli, M., Panasenco, O., Tenerani, A., Réville, V., Bale, S. D., Kasper, J., Korreck, K., Bonnell, J. W., Dudok de Wit, T., Malaspina, D. M., Goetz, K., Harvey, P. R., MacDowall, R. J., Pulupa, M., Case, A. W., Larson, D., Verniero, J. L., Livi, R., Stevens, M., Whittlesey, P., Maksimovic, M., and Moncuquet, M. (2021). Alfvénic versus non-Alfvénic turbulence in the inner heliosphere as observed by Parker Solar Probe. *åp*, 650:A21. _eprint: 2101.00830. 69, 71, 81, 87, 93, 96, 100, 103, 114, 115, 121, 144, 211, 220

Shi, C., Velli, M., Tenerani, A., Réville, V., and Rappazzo, F. (2022b). Influence of the heliospheric current sheet on the evolution of solar wind turbulence. _eprint: 2201.02894. 86, 121

Shi, C., Velli, M., Tenerani, A., Réville, V., and Rappazzo, F. (2022c). Influence of the heliospheric current sheet on the evolution of solar wind turbulence. *arXiv:2201.02894 [astro-ph, physics:physics]*. arXiv: 2201.02894. 93, 159

Shoda, M., Suzuki, T. K., Asgari-Targhi, M., and Yokoyama, T. (2019). Three-dimensional Simulation of the Fast Solar Wind Driven by Compressible Magnetohydrodynamic Turbulence. , 880(1):L2. 93, 206, 235

Sioulas, N. (2023). Mhdturbpy. 166

Sioulas, N., Huang, Z., Shi, C., Velli, M., Tenerani, A., Bowen, T. A., Bale, S. D., Huang, J., Vlahos, L., Woodham, L. D., Horbury, T. S., de Wit, T. D., Larson, D., Kasper, J., Owen, C. J., Stevens, M. L., Case, A., Pulupa, M., Malaspina, D. M., Bonnell, J. W., Livi, R., Goetz, K., Harvey, P. R., MacDowall, R. J., Maksimović, M., Louarn, P., and Fedorov, A. (2023a). Magnetic Field Spectral Evolution in the Inner Heliosphere. , 943(1):L8. 86, 114, 180, 221, 224, 244

Sioulas, N., Huang, Z., Shi, C., Velli, M., Tenerani, A., Vlahos, L., Bowen, T. A., Bale, S. D., Bonnell, J. W., Harvey, P. R., Larson, D., Pulupa, a., Livi, R., Woodham, L. D., Horbury, T. S., Stevens, M. L., de Wit, T. D., MacDowall, R. J., Malaspina, D. M., Goetz, K., Huang, J., Kasper, J., Owen, C. J., Maksimović, M., Louarn, P., and Fedorov, A. (2022a). Magnetic field spectral evolution in the inner heliosphere. 71, 100, 105, 115, 116

Sioulas, N., Huang, Z., Velli, M., Chhiber, R., Cuesta, M. E., Shi, C., Matthaeus, W. H., Bandyopadhyay, R., Vlahos, L., Bowen, T. A., Qudsi, R. A., Bale, S. D., Owen, C. J., Louarn, P., Fedorov, A., Maksimović, M., Stevens, M. L., Case, A., Kasper, J.,

Larson, D., Pulupa, M., and Livi, R. (2022b). Magnetic field intermittency in the solar wind: Parker solar probe and SolO observations ranging from the alfvén region up to 1 AU. *The Astrophysical Journal*, 934(2):143. 43, 87, 96, 103, 114, 120, 179, 194, 205, 206

Sioulas, N., Isliker, H., and Vlahos, L. (2020a). Stochastic Turbulent Acceleration in a Fractal Environment. *apjl*, 895(1):L14. _eprint: 2005.02668. 51, 150

Sioulas, N., Isliker, H., and Vlahos, L. (2022c). Particle heating and acceleration by reconnecting and nonreconnecting current sheets. *åp*, 657:A8. _eprint: 2107.08314. 51, 157

Sioulas, N., Isliker, H., Vlahos, L., Koumtzis, A., and Pisokas, T. (2020b). Superdiffusive stochastic Fermi acceleration in space and energy. *mnras*, 491(3):3860–3869. _eprint: 1911.07973. 150

Sioulas, N., Shi, C., Huang, Z., and Velli, M. (2022). Preferential Heating of Protons over Electrons from Coherent Structures during the First Perihelion of the Parker Solar Probe. , 935(2):L29. 150, 205

Sioulas, N., Velli, M., Chhiber, R., Vlahos, L., Matthaeus, W. H., Bandyopadhyay, R., Cuesta, M. E., Shi, C., Bowen, T. A., Qudsi, R. A., Stevens, M. L., and Bale, S. D. (2022). Statistical analysis of intermittency and its association with proton heating in the near Sun environment. _eprint: 2201.10067. 51, 142, 150, 159, 160

Sioulas, N., Velli, M., Huang, Z., Shi, C., Bowen, T. A., Chandran, B. D. G., Liodis, I., Bale, S. D., Horbury, T. S., Dudok de Wit, T., Larson, D., Kasper, J., Owen, C. J., Stevens, M. L., Case, A., Pulupa, M., Bonnell, J. W., Goetz, K., Harvey, P. R., and MacDowall, R. J. (2023b). On the evolution of the Anisotropic Scaling of Magnetohydrodynamic Turbulence in the Inner Heliosphere. *arXiv e-prints*, page arXiv:2301.03896. 98

Sioulas, N., Velli, M., Huang, Z., Shi, C., Bowen, T. A., Chandran, B. D. G., Liodis, I., Davis, N., Bale, S. D., Horbury, T. S., de Wit, T. D., Larson, D., Stevens, M. L., Kasper, J., Owen, C. J., Case, A., Pulupa, M., Malaspina, D. M., Livi, R., Goetz, K., Harvey, P. R., MacDowall, R. J., and Bonnell, J. W. (2023). On the evolution of the anisotropic scaling of magnetohydrodynamic turbulence in the inner heliosphere. *The Astrophysical Journal*, 951(2):141. 169, 179, 184, 205, 222, 245

Sioulas, N., Zikopoulos, T., Shi, C., Velli, M., Bowen, T., Mallet, A., Sorriso-Valvo, L., Verdini, A., Chandran, B. D. G., Martinović, M. M., Cerri, S. S., Davis, N., and Dunn, C. (2024). Higher-order analysis of three-dimensional anisotropy in imbalanced alfvénic turbulence. 162, 205, 230, 234

Soni, S. L., Akhavan-Tafti, M., Suen, G. H. H., Kasper, J., Velli, M., Marco, R. D., and Owen, C. (2024). Switchback patches evolve into microstreams via magnetic relaxation. 197

Sorriso-Valvo, L., Carbone, F., Perri, S., Greco, A., Marino, R., and Bruno, R. (2018). On the statistical properties of turbulent energy transfer rate in the inner heliosphere. *Solar Physics*, 293. 158

Sorriso-Valvo, L., Carbone, V., Veltri, P., Consolini, G., and Bruno, R. (1999). Intermittency in the solar wind turbulence through probability distribution functions of fluctuations. *Geophysical Research Letters*, 26(13):1801–1804. 49, 68, 176, 215

Sorriso-Valvo, L., De Vita, G., Fraternale, F., Gurchumelia, A., Perri, S., Nigro, G., Catapano, F., Retinò, A., Chen, C. H. K., Yordanova, E., Pezzi, O., Chargazia, K., Kharshiladze, O., Kvaratskhelia, D., Vásconez, C. L., Marino, R., Le Contel, O., Giles, B., Moore, T. E., Torbert, R. B., and Burch, J. L. (2019). Sign Singularity of the Local Energy Transfer in Space Plasma Turbulence. *Frontiers in Physics*, 7. 160

Sorriso-Valvo, L., Marino, R., Foldes, R., Lévêque, E., D'Amicis, R., Bruno, R., Telloni, D., and Yordanova, E. (2023). Helios 2 observations of solar wind turbulence decay in the inner heliosphere. , 672:A13. 179

Sorriso-Valvo, L., Yordanova, E., Dimmock, A. P., and Telloni, D. (2021). Turbulent cascade and energy transfer rate in a solar coronal mass ejection. *The Astrophysical Journal Letters*, 919(2):L30. 180

Squire, J., Chandran, B. D. G., and Meyrand, R. (2020). In-situ switchback formation in the expanding solar wind. *The Astrophysical Journal Letters*, 891(1):L2. 68, 70, 191, 209

Squire, J., Meyrand, R., Kunz, M. W., Arzamasskiy, L., Schekochihin, A. A., and Quataert, E. (2022a). High-frequency heating of the solar wind triggered by low-frequency turbulence. *Nature Astronomy*. 161

Squire, J., Meyrand, R., Kunz, M. W., Arzamasskiy, L., Schekochihin, A. A., and Quataert, E. (2022b). High-frequency heating of the solar wind triggered by low-frequency turbulence. *Nature Astronomy*, 6:715–723. 182, 246

Squire, J., Meyrand, R., Kunz, M. W., Arzamasskiy, L., Schekochihin, A. A., and Quataert, E. (2022c). High-frequency heating of the solar wind triggered by low-frequency turbulence. *Nature Astronomy*, 6:715–723. 193

Sridhar, S. and Goldreich, P. (1994). Toward a Theory of Interstellar Turbulence. I. Weak Alfvenic Turbulence. , 432:612. 99, 116

Stansby, D., Salem, C., Matteini, L., and Horbury, T. (2018). A New Inner Heliosphere Proton Parameter Dataset from the Helios Mission. , 293(11):155. 58

Stix, T. H. (1992). *Waves in plasmas*. 193

Strauss, H. R. (1976). Nonlinear, three-dimensional magnetohydrodynamics of noncircular tokamaks. *Physics of Fluids*, 19(1):134–140. 46

Suess, S. T., Ko, Y. K., von Steiger, R., and Moore, R. L. (2009). Quiescent current sheets in the solar wind and origins of slow wind. *Journal of Geophysical Research (Space Physics)*, 114(A4):A04103. 159

Taylor, G. I. (1938). The Spectrum of Turbulence. *Proceedings of the Royal Society of London. Series A - Mathematical and Physical Sciences*, 164(919):476–490. 59, 79, 82, 88

Taylor, G. I. (1938). The Spectrum of Turbulence. *Proceedings of the Royal Society of London Series A*, 164(919):476–490. 158, 240

Telloni, D. (2022). Frequency transition from weak to strong turbulence in the solar wind. *Frontiers in Astronomy and Space Sciences*, 9. 116, 179, 184

Telloni, D., Sorriso-Valvo, L., Woodham, L. D., Panasenco, O., Velli, M., Carbone, F., Zank, G. P., Bruno, R., Perrone, D., Nakanotani, M., Shi, C., D'Amicis, R., De Marco, R., Jagarlamudi, V. K., Steinvall, K., Marino, R., Adhikari, L., Zhao, L., Liang, H., Tenerani, A., Laker, R., Horbury, T. S., Bale, S. D., Pulupa, M., Malaspina, D. M., MacDowall, R. J., Goetz, K., de Wit, T. D., Harvey, P. R., Kasper, J. C., Korreck, K. E., Larson, D., Case, A. W., Stevens, M. L., Whittlesey, P., Livi, R., Owen, C. J., Livi, S., Louarn, P., Antonucci, E., Romoli, M., O'Brien, H., Evans, V., and Angelini, V. (2021). Evolution of Solar Wind Turbulence from 0.1 to 1 au during the First Parker Solar Probe-Solar Orbiter Radial Alignment. , 912(2):L21. 69, 100, 122

TenBarge, J. M. and Howes, G. G. (2013). CURRENT SHEETS AND COLLISIONLESS DAMPING IN KINETIC PLASMA TURBULENCE. *The Astrophysical Journal*, 771(2):L27. Publisher: American Astronomical Society. 69

Tenerani, A., González, C., Sioulas, N., Shi, C., and Velli, M. (2023). Dispersive and kinetic effects on kinked Alfvén wave packets: A comparative study with fluid and hybrid models. *Physics of Plasmas*, 30(3):032101. 66

Tenerani, A., Sioulas, N., Matteini, L., Panasenco, O., Shi, C., and Velli, M. (2021). Evolution of switchbacks in the inner heliosphere. *The Astrophysical Journal Letters*, 919(2):L31. 67, 146, 190

Tenerani, A., Velli, M., and Hellinger, P. (2017). The Parametric Instability of Alfvén Waves: Effects of Temperature Anisotropy. , 851(2):99. 93, 111

Tessein, J. A., Matthaeus, W. H., Wan, M., Osman, K. T., Ruffolo, D., and Giacalone, J. (2013a). ASSOCIATION OF SUPRATHERMAL PARTICLES WITH COHERENT STRUCTURES AND SHOCKS. *The Astrophysical Journal*, 776(1):L8. Publisher: American Astronomical Society. 51, 82

Tessein, J. A., Matthaeus, W. H., Wan, M., Osman, K. T., Ruffolo, D., and Giacalone, J. (2013b). ASSOCIATION OF SUPRATHERMAL PARTICLES WITH COHERENT STRUCTURES AND SHOCKS. *The Astrophysical Journal*, 776(1):L8. 158

Tessein, J. A., Smith, C. W., and MacBride, B. T. (2009). Spectral Indices for Multi-Dimensional Interplanetary Turbulence at 1 AU. In *Solar Heliospheric and INterplanetary Environment (SHINE 2009*, page 70. 96

Thieme, K. M., Marsch, E., and Schwenn, R. (1990). Spatial structures in high-speed streams as signatures of fine structures in coronal holes. *Annales Geophysicae*, 8:713–723. 216

Tu, C. Y., Marsch, E., and Rosenbauer, H. (1990). The dependence of MHD turbulence spectra on the inner solar wind stream structure near solar minimum. , 17(3):283–286. 186

Turner, A. J., Gogoberidze, G., Chapman, S. C., Hnat, B., and Müller, W. C. (2011). Nonaxisymmetric Anisotropy of Solar Wind Turbulence. , 107(9):095002. 190

Uzdensky, D. A. and Loureiro, N. F. (2016). Magnetic reconnection onset via disruption of a forming current sheet by the tearing instability. *Phys. Rev. Lett.*, 116:105003. 192, 237

Vasko, I. Y., Alimov, K., Phan, T., Bale, S. D., Mozer, F. S., and Artemyev, A. V. (2022). Kinetic-scale Current Sheets in the Solar Wind at 1 au: Scale-dependent Properties and Critical Current Density. , 926(2):L19. 82, 214, 235

Vasquez, B. J., Smith, C. W., Hamilton, K., MacBride, B. T., and Leamon, R. J. (2007). Evaluation of the turbulent energy cascade rates from the upper inertial range in the solar wind at 1 au. *Journal of Geophysical Research: Space Physics*, 112(A7). 104

Vech, D. and Chen, C. H. K. (2016). Testing the effects of expansion on solar wind turbulence. *The Astrophysical Journal Letters*, 832(1):L16. 190, 206

Vech, D., Mallet, A., Klein, K. G., and Kasper, J. C. (2018). Magnetic reconnection may control the ion-scale spectral break of solar wind turbulence. *The Astrophysical Journal Letters*, 855(2):L27. 192

Velli, M. (1993). On the propagation of ideal, linear alfven waves in radially stratified stellar atmospheres and winds. *A&A*, 270(1-2):304–314. 65, 81, 210

Velli, M., Grappin, R., and Mangeney, A. (1989). Turbulent cascade of incompressible unidirectional Alfv\'en waves in the interplanetary medium. *Physical Review Letters*, 63(17):1807–1810. Publisher: American Physical Society. xxii, 57, 68, 86, 185, 236, 237, 238, 247

Velli, M., Grappin, R., and Mangeney, A. (1990). Solar wind expansion effects on the evolution of hydromagnetic turbulence in the interplanetary medium. *Computer Physics Communications*, 59(1):153–162. 185, 236

Velli, M., Grappin, R., and Mangeney, A. (1991). Waves from the sun? *Geophysical & Astrophysical Fluid Dynamics*, 62(1-4):101–121. 65, 70, 81, 119, 210

Velli, M., Grappin, R., and Mangeney, A. (1992). MHD turbulence in an expanding atmosphere. In Spicer, D. S. and MacNeice, P., editors, *Electromechanical Coupling of the Solar Atmosphere*, volume 267 of *American Institute of Physics Conference Series*, pages 154–159. AIP. 67

Velli, M., Harra, L. K., Vourlidas, A., Schwadron, N., Panasenco, O., Liewer, P. C., Müller, D., Zouganelis, I., St Cyr, O. C., Gilbert, H., Nieves-Chinchilla, T., Auchère, F., Berghmans, D., Fludra, A., Horbury, T. S., Howard, R. A., Krucker, S., Maksimovic, M., Owen, C. J., Rodríguez-Pacheco, J., Romoli, M., Solanki, S. K., Wimmer-Schweingruber, R. F., Bale, S., Kasper, J., McComas, D. J., Raouafi, N., Martinez-Pillet, V., Walsh, A. P., De Groof, A., and Williams, D. (2020a). Understanding the origins of the heliosphere: integrating observations and measurements from Parker Solar Probe, Solar Orbiter, and other space- and ground-based observatories. , 642:A4. 70

Velli, M., Harra, L. K., Vourlidas, A., Schwadron, N., Panasenco, O., Liewer, P. C., Müller, D., Zouganelis, I., St Cyr, O. C., Gilbert, H., Nieves-Chinchilla, T., Auchère, F., Berghmans, D., Fludra, A., Horbury, T. S., Howard, R. A., Krucker, S., Maksimovic, M., Owen, C. J., Rodríguez-Pacheco, J., Romoli, M., Solanki, S. K., Wimmer-Schweingruber, R. F., Bale, S., Kasper, J., McComas, D. J., Raouafi, N., Martinez-Pillet, V., Walsh, A. P., De Groof, A., and Williams, D. (2020b). Understanding the origins of the heliosphere: integrating observations and measurements from Parker Solar Probe, Solar Orbiter, and other space- and ground-based observatories. , 642:A4. 122

Veltri, P. (1999). MHD turbulence in the solar wind: self-similarity, intermittency and coherent structures. *Plasma Physics and Controlled Fusion*, 41(3A):A787–A795. Publisher: IOP Publishing. 51

Verdini, A. and Grappin, R. (2012). Transition from weak to strong cascade in mhd turbulence. *Phys. Rev. Lett.*, 109:025004. 44, 184

Verdini, A. and Grappin, R. (2015). Imprints of Expansion on the Local Anisotropy of Solar Wind Turbulence. , 808(2):L34. 47, 181, 189, 206

Verdini, A., Grappin, R., Alexandrova, O., Franci, L., Landi, S., Matteini, L., and Papini, E. (2019). Three-dimensional local anisotropy of velocity fluctuations in the solar wind. , 486(3):3006–3018. 69, 182

Verdini, A., Grappin, R., Alexandrova, O., and Lion, S. (2018). 3D Anisotropy of Solar Wind Turbulence, Tubes, or Ribbons? , 853(1):85. 68, 69, 79, 165, 182, 186, 190, 200, 205, 206, 230

Verdini, A. and Velli, M. (2007). Alfvén Waves and Turbulence in the Solar Atmosphere and Solar Wind. *The Astrophysical Journal*, 662(1):669. Publisher: IOP Publishing. 66

Verdini, A., Velli, M., and Buchlin, E. (2009). Turbulence in the Sub-Alfvénic Solar Wind Driven by Reflection of Low-Frequency Alfvén Waves. , 700(1):L39–L42. 185, 236

Verscharen, D., Chen, C. H. K., and Wicks, R. T. (2017). On Kinetic Slow Modes, Fluid Slow Modes, and Pressure-balanced Structures in the Solar Wind. , 840(2):106. 217, 235

Vinogradov, A., Alexandrova, O., Démoulin, P., Artemyev, A., Maksimovic, M., Mangeney, A., Vasiliev, A., Petrukovich, A., and Bale, S. (2023). Embedded coherent structures from mhd to sub-ion scales in turbulent solar wind at 0.17 au. 172, 235

Vlahos, L., Isliker, H., Kominis, Y., and Hizanidis, K. (2008). Normal and Anomalous Diffusion: A Tutorial. *arXiv e-prints*, page arXiv:0805.0419. 150

Völk, H. J. and Aplers, W. (1973). The Propagation of Alfvén Waves and Their Directional Anisotropy in the Solar Wind. , 20(2):267–285. 71, 182

Wan, M., Matthaeus, W. H., Karimabadi, H., Roytershteyn, V., Shay, M., Wu, P., Daughton, W., Loring, B., and Chapman, S. C. (2012). Intermittent Dissipation at Kinetic Scales in Collisionless Plasma Turbulence. , 109(19):195001. 150

Wan, M., Oughton, S., Servidio, S., and Matthaeus, W. H. (2009). Generation of non-Gaussian statistics and coherent structures in ideal magnetohydrodynamics. *Physics of Plasmas*, 16(8):080703. 146

Wang, T., He, J., Alexandrova, O., Dunlop, M., and Perrone, D. (2020). Observational Quantification of Three-dimensional Anisotropies and Scalings of Space Plasma Turbulence at Kinetic Scales. , 898(1):91. 173

Wang, X., Fan, X., Wang, Y., Wu, H., and Zhang, L. (2023). Effect of intermittent structures on the spectral index of the magnetic field in the slow solar wind. *Annales Geophysicae*, 41(1):129–145. 206

Wang, X., Huang, L., Wang, Y., and Yuan, H. (2023). Influence of alfvén ion–cyclotron waves on the anisotropy of solar wind turbulence at ion kinetic scales. *Universe*, 9(9). 193

Wang, Y., Chhiber, R., Adhikari, S., Yang, Y., Bandyopadhyay, R., Shay, M. A., Oughton, S., Matthaeus, W. H., and Cuesta, M. E. (2022). Strategies for determining the cascade rate in mhd turbulence: isotropy, anisotropy, and spacecraft sampling. 79, 163

Weygand, J. M., Kivelson, M. G., Khurana, K. K., Schwarzl, H. K., Walker, R. J., Balogh, A., Kistler, L. M., and Goldstein, M. L. (2006). Non-self-similar scaling of plasma sheet and solar wind probability distribution functions of magnetic field fluctuations. *Journal of Geophysical Research (Space Physics)*, 111(A11):A11209. 141

Weygand, J. M., Matthaeus, W. H., Dasso, S., Kivelson, M. G., Kistler, L. M., and Mouikis, C. (2009). Anisotropy of the taylor scale and the correlation scale in plasma sheet and solar wind magnetic field fluctuations. *Journal of Geophysical Research: Space Physics*, 114(A7). 42

Wicks, R. T., Horbury, T. S., Chen, C. H. K., and Schekochihin, A. A. (2010). Power and spectral index anisotropy of the entire inertial range of turbulence in the fast solar wind. *mnras*, 407(1):L31–L35. xi, 46, 69, 77, 106, 113, 115, 116, 118, 203

Wicks, R. T., Horbury, T. S., Chen, C. H. K., and Schekochihin, A. A. (2011). Anisotropy of Imbalanced Alfvénic Turbulence in Fast Solar Wind. , 106(4):045001. 69, 179, 180, 205

Wicks, R. T., Mallet, A., Horbury, T. S., Chen, C. H. K., Schekochihin, A. A., and Mitchell, J. J. (2013a). Alignment and scaling of large-scale fluctuations in the solar wind. *Phys. Rev. Lett.*, 110:025003. 42, 113, 185, 186, 187, 205, 206, 239

Wicks, R. T., Roberts, D. A., Mallet, A., Schekochihin, A. A., Horbury, T. S., and Chen, C. H. K. (2013b). Correlations at large scales and the onset of turbulence in the fast solar wind. *The Astrophysical Journal*, 778(2):177. 180

Witham, G. (1965). A general approach to linear and non-linear dispersive waves. *J. Fluid Mech*, 22:273–283. 65

Woodham, L. (2019a). *Characterising Solar Wind Fluctuations at Ion-kinetic Scales*. PhD thesis. 95

Woodham, L. (2019b). *Characterising Solar Wind Fluctuations at Ion-kinetic Scales*. PhD thesis. 107

Wu, H., He, J., Yang, L., Wang, X., Huang, S., and Yuan, Z. (2022). On the scaling and anisotropy of two subranges in the inertial range of solar wind turbulence. 114, 116, 117, 179, 184, 205

Wu, H., Huang, S., Wang, X., Yuan, Z., He, J., and Yang, L. (2023). Intermittency of magnetic discontinuities in the near-sun solar wind turbulence. *The Astrophysical Journal Letters*, 947(2):L22. 180

Wu, P., Perri, S., Osman, K., Wan, M., Matthaeus, W. H., Shay, M. A., Goldstein, M. L., Karimabadi, H., and Chapman, S. (2013). Intermittent Heating in Solar Wind and Kinetic Simulations. , 763(2):L30. 176

Yao, S., He, J. S., Marsch, E., Tu, C. Y., Pedersen, A., Rème, H., and Trotignon, J. G. (2011). Multi-scale Anti-correlation Between Electron Density and Magnetic Field Strength in the Solar Wind. , 728(2):146. 216

Yordanova, E., Vörös, Z., Sorriso-Valvo, L., Dimmock, A. P., and Kilpua, E. (2021). A Possible Link between Turbulence and Plasma Heating. , 921(1):65. 150, 157, 159, 160

Zank, G. P., Nakanotani, M., Zhao, L.-L., Adhikari, L., and Telloni, D. (2020). Spectral anisotropy in 2d plus slab magnetohydrodynamic turbulence in the solar wind and upper corona. *The Astrophysical Journal*, 900(2):115. 100, 116

Zank, G. P., Zhao, L. L., Adhikari, L., Telloni, D., Kasper, J. C., Stevens, M., Rahmati, A., and Bale, S. D. (2022). Turbulence in the Sub-Alfvénic Solar Wind. , 926(2):L16. 43, 61

Zhang, J., Huang, S. Y., He, J. S., Wang, T. Y., Yuan, Z. G., Deng, X. H., Jiang, K., Wei, Y. Y., Xu, S. B., Xiong, Q. Y., Lin, R. T., and Yu, L. (2022). Three-dimensional anisotropy and scaling properties of solar wind turbulence at kinetic scales in the inner heliosphere: Parker solar probe observations. *The Astrophysical Journal Letters*, 924(2):L21. 173, 193

Zhao, G. Q., Meyrand, R., Feng, H. Q., Wu, D. J., and Kasper, J. C. (2022). Cross-scale correlations in imbalanced solar wind turbulence: Parker solar probe observations. *The Astrophysical Journal*, 938(2):124. 113, 193

Zhao, L. L., Zank, G. P., Adhikari, L., Nakanotani, M., Telloni, D., and Carbone, F. (2020). Spectral Features in Field-aligned Solar Wind Turbulence from Parker Solar Probe Observations. , 898(2):113. 103, 148

Zhao, L. L., Zank, G. P., Telloni, D., Stevens, M., Kasper, J. C., and Bale, S. D. (2022). The Turbulent Properties of the Sub-Alfvénic Solar Wind Measured by the Parker Solar Probe. , 928(2):L15. 122

Zhao, S., Yan, H., Liu, T. Z., Yuen, K. H., and Wang, H. (2023). Satellite Observations of the Alfvénic Transition from Weak to Strong Magnetohydrodynamic Turbulence. *arXiv e-prints*, page arXiv:2301.06709. 184

Zhdankin, V., Boldyrev, S., and Chen, C. H. K. (2016). Intermittency of energy dissipation in Alfvénic turbulence. , 457(1):L69–L73. 53

Zhdankin, V., Uzdensky, D. A., Perez, J. C., and Boldyrev, S. (2013). Statistical Analysis of Current Sheets in Three-dimensional Magnetohydrodynamic Turbulence. *Astrophs. J.*, 771:124. _eprint: 1302.1460. 240